A Novel Infrared Thermography Technique for Measuring Heat Transfer in Transonic Turbine Blades



Manuela Sisti

Wolfson College

University of Oxford

A thesis submitted for the degree of

Doctor of Philosophy

Hilary 2024

To all the women who were told

'you don't look like an engineer'

Acknowledgements

On 19 July 2023, the first successful test employing Infrared Thermography in the Oxford Turbine Research Facility was recorded. As I reflect on this chapter of my academic journey, I cannot avoid mentioning the individuals who were instrumental in achieving this milestone.

First, I must thank my supervisor Dr. Paul F. Beard who offered me the opportunity to work on such a groundbreaking project. His insightful feedback was fundamental to the success of this endeavour. I also want to recognise Dr. Chiara Falsetti, my unofficial supervisor during her time at the University of Oxford, who generously shared her expertise on Infrared Thermography. Our collaboration has been both enjoyable and enlightening. Special thanks are due to David Cardwell and Sunny Chana, the OTRF test controllers who made this campaign possible.

From the Oxford Thermofluids Institute, my gratitude extends to Jamie Saw, my first desk-mate. Our brainstorming sessions were crucial in surviving daily academic crises. I am also grateful to the 11 o'clock tea break crew: Michael van de Noort, Alexander Bebb, Matthew Stokes, for lending a sympathetic ear to my endless rambling. A sincere thanks to Maïlys Buquet, my kindred spirit in the lab, for offering a great deal of emotional support; our walks around Oxford and our friendship have been a source of joy. Heartfelt thanks to Simla Saglam for bringing cake on my birthday.

From the Physics department, I would like to acknowledge Emily Archer who kept me accountable during the final months with our Bodleian Old Library and Radcliffe Camera sessions, where we both wrote our DPhil thesis away. I will always treasure the memory of our serendipitous encounter.

I must acknowledge Mariano Galante, my greatest supporter throughout this adventure and beyond. His belief in my potential has motivated me to strive for the best, and his generous Matlab consulting was greatly appreciated.

I would like to express my appreciation for my siblings, especially Aurora, my compass and first point of reference, along with Chiara and Elena, always just a phone call away. I am also grateful to my sisters: Francesca, Claudia, Silvia, Beatrice, and my brothers: Matteo, and Marco, all of whom have contributed to my journey. Finally, I am grateful to my parents: my mother, Fiorella Tofani, who instilled in me the value of hard work and the power of will, my father, Marcello Sisti, who nurtured my academic curiosity with his ability to simplify complex physics concepts.

I had my share of fun among the ups and downs of this doctoral odyssey and I am now curious to see what the future holds.

Ad Maiora Semper.

Abstract

This thesis presents a new measurement methodology aimed at accelerating progress in the Aviation industry while ensuring reliable results. A novel measurement system employing Infrared (IR) Thermography was developed for the Oxford Turbine Research Facility (OTRF), a national engine-representative high-pressure turbine test facility operating with rotational speed of $300\,\mathrm{m\,s^{-1}}$ and transonic flow.

The literature review evidences that there is still considerable work to do to thoroughly understand the applicability of IR thermography to fast moving targets, and particularly to accurately quantify and minimise the sources of error. The work in this dissertation sought to fill this gap by conceiving accurate and novel calibration and processing methods. The methodology and design requirements, described in the thesis, were used and validated in the OTRF.

The infrared data of blades captured in the OTRF and processed to full surface heat transfer quantities were validated against thin-film gauges experimental data and CFD simulation, in both instances a good agreement was found, proving that the methodology surpassed standard point-based measurement techniques, and demonstrating a step change in heat transfer measurements. Scalable Nusselt number on the rotor blade, not previously possible with thin-film gauges, was achieved using the developed IR thermography methodology. Finally, the results proved the need to carefully select the camera integration time to balance image quality and accuracy.

Contents

1 Introduction **1**

1.1 Motivation 1

1.2 Cycle Performance 3

1.3 Modelling and Testing of Turbomachinery Flows 10

1.4 Research Aims 12

1.5 Structure of the Thesis 14

2 Review of Heat Transfer Measurement Techniques **17**

2.1 Review of testing facilities 19

2.1.1 Short Duration Facilities 21

2.2 Review of Heat Transfer Instrumentation: Thin Film Gauges 23

2.2.1 Single Layer Semi-Infinite Gauges 24

2.2.2 Two Layer Single-Sided Gauges 27

2.3 Review of Heat Transfer Instrumentation: Thermochromic Liquid Crystals 28

2.4 Review of Heat Transfer Instrumentation: Infrared Thermography . . 31

2.4.1 Theory of Thermal Radiation Heat Transfer 31

2.4.1.1 Emissivity of the Target 34

2.4.1.2 Reflectivity of the Target 35

2.4.1.3 Absorption/Transmission of the Optical Path 36

2.4.2 Infrared Thermography Calibration Techniques 38

2.4.3 Turbine Heat Transfer Studies using Infrared Thermography in Engine Scale Rotating Facilities 51
2.5 Review of Blade Tip Heat Transfer Studies 54
2.6 Summary 59

3 Development of an Infrared Thermography Measurement Methodology for Fast Moving Targets 63
3.1 Infrared Thermography Measurements in the OTRF 65
3.2 Infrared Detector Selection 69
3.3 Steady System Calibration 73
3.3.1 Detector Calibration 75
3.3.2 Surface Emissivity Calibration 80
3.3.2.1 Emissivity roughness dependence 84
3.3.3 Transmittance Calibration 87
3.3.4 Reflection Calibration 88
3.4 Calibration Performance on High Speed Objects 89
3.4.1 Emissivity and Reflections Correction with Blur 92
3.5 Quantifying Uncertainty in Target Temperature and Metal Effectiveness 98
3.6 Summary 100

4 Development of an Infrared Thermography System for Transient Heat Transfer Measurements in a Rotating Facility 103
4.1 The Oxford Turbine Research Facility 105
4.1.1 The SILOET HP Turbine Stage 106
4.1.2 Combustor Simulator 107
4.1.3 Data Acquisition and Instrumentation 109
4.1.4 Rig Conditions Processing 113
4.1.5 Mass-Averaged Inlet Total Temperature 117

4.2 Test Programme During IR Experiments: Rotor Casing Effusion Cooling 119
4.2.1 Cooling Module 120
4.2.2 Coolant Delivery to Effusion Segment 122
4.3 Designing the Optical Access 125
4.3.1 Optical Materials and the Choice of Zinc Selenide 126
4.3.2 Optical Access for OTRF Experiments 130
4.3.3 Observation Angles 131
4.3.4 Transmittance of the Optical Path in the OTRF 134
4.4 Designing the Composite Blade 135
4.4.1 Tensile Load and Fatigue Tests 137
4.5 Infrared Camera Synchronisation System 143
4.6 Blades Instrumented with Thin-Film Gauges 146
4.7 Summary 150

5 Infrared Thermography of Rotor Tip Heat Transfer 153
5.1 Background 154
5.2 Experimental Setup 154
5.3 Effect of Integration Time 157
5.4 Processing of Thermal Data 163
5.4.1 Target Temperature and Run Characteristics 165
5.4.2 Dynamic Synchronisation and Vibration Instabilities 172
5.4.3 Heat Flux and Nusselt Number Processing 176
5.5 Validation Cases 180
5.5.1 Comparison with Heat Flux Gauges 180
5.5.2 Comparison to validated CFD 185
5.5.3 Uncertainty Comparison 187
5.5.3.1 Uncertainty of Surface Temperature Measurement . . 187
5.5.3.2 Uncertainty of Heat Flux Calculation 189

5.6 Summary 190

6 Conclusions **193**

Bibliography **200**

List of Figures

1.1 CO_2 emission from international aviation for the period 2005 to 2050 2
1.2 Gas turbine engine cross-section 3
1.3 Aircraft gas turbine thermal, propulsive and overall efficiencies 4
1.4 Specific Fuel Consumption, thermal, and propulsive efficiency 4
1.5 Schematic on the Brayton cycle 5
1.6 Analysis of the Brayton thermodynamic efficiency 7
1.7 Specific core power as a function of turbine rotor inlet temperature . 7
1.8 Example of high pressure turbine blades failures due to overheating . 8
1.9 Variation of turbine entry temperature over years 9

2.1 Schematic of a thin-film heat flux gauge on semi-infinite layer 24
2.2 Analysis of thermal penetration depth for a selection of materials . . 26
2.3 Schematic of a two layer single-sided thin-film heat flux gauge 27
2.4 Colour response for temperature sensitive liquid crystals 29
2.5 Blackbody emissive power distribution 32
2.6 Infrared transmission spectrum of the atmosphere at Sea Level 37
2.7 Sketch of an IR thermography system in a section of a 1.5 turbine stage 39
2.8 Signal detected by the IR camera in a typical turbomachinery experiment 43
2.9 Nusselt number and uncertainty in adiabatic wall temperature on vane endwall from IR thermography 45
2.10 Reflective markers array study 47
2.11 Example of offset radiance distribution using a correction field 49
2.12 Thermocouple installation to reduce instrumentation induced error . 51
2.13 IR thermography employed in a engine scale rig at ETH Zurich. . . . 52
2.14 IR thermography employed in a engine scale rig at Ohio State University 53
2.15 IR thermography employed in a engine scale rig at Penn State University 54
2.16 Schematic of tip leakage flow over a flat tip 55
2.17 Typical patterns of leakage flow over an unshrouded flat tip blade . . 56
2.18 Typical patterns of leakage flow over an unshrouded squealer tip blade 57
2.19 Heat transfer coefficient on a squealer tip compared to a flat tip at different tip gaps 58
2.20 Heat transfer coefficient on a squealer tip compared to a flat tip at different turbulence intensity levels 58

3.1 Photograph of OTRF and Schematic of the IR thermography system 66

3.2 Target, surroundings, and optics contributions to total detected spectral radiance . . . 67
3.3 Impact of emissivity on influence coefficients . . . 69
3.4 Blackbody emissive power for three absolute temperature (K) values as a function of wavelength. . . . 72
3.5 Steady calibration bench-top facility . . . 74
3.6 Comparison of uncertainties associated with two blackbody calibrators 75
3.7 Equivalent blackbody temperature and spectral radiance at five camera integration times . . . 77
3.8 IR camera temporal noise analysis showing raw signal and signal-to-noise ratio . . . 79
3.9 Equivalent blackbody temperature and absolute error . . . 80
3.10 Maximum absolute temporal error function of target temperature and camera integration time . . . 80
3.11 Surface emissivity calibration showing equivalent blackbody temperature and emissivity maps . . . 82
3.12 Emissivity ε of the black matt coating . . . 83
3.13 Polar plot of the measured directional emissivity. . . . 84
3.14 Key results from analysis of emissivity on different samples of paint showing impact of surface roughness . . . 85
3.15 Photograph of the Alicona Infinite Focus 3D Profilometer . . . 86
3.16 Photograph of the rotating disc facility . . . 90
3.17 Exemplary equivalent blackbody temperature data of the flat disc . . 91
3.18 Effect of rotation on IR images of the flat disc . . . 93
3.19 Identification of high and low emissivity regions on IR images of the flat disc . . . 95
3.20 Maps of reconstructed target and reflected temperatures . . . 95
3.21 Equivalent blackbody and target temperatures at location $y = 311$ . . 95
3.22 Equivalent blackbody and target temperatures at location $y = 480$ . . 96
3.23 Errors after calibration at locations $y = 311$ and $y = 480$ . . . 98

4.1 Schematic of the Oxford Turbine Research Facility . . . 105
4.2 SILOET turbine NGV and blades . . . 106
4.3 CAD model of the combustor simulator . . . 108
4.4 Radial inlet temperature profile achievable in the OTRF . . . 108
4.5 Measurement locations away from the working section in the OTRF . 110
4.6 Measurement locations in the OTRF working section . . . 112
4.7 Typical pressure, temperature and speed time traces in the OTRF . . 114
4.8 Typical mass flow rate time traces from the OTRF . . . 117
4.9 Typical mean level temperature traces during a run in the OTRF . . 119
4.10 Photographs of the casing effusion cooling segment . . . 120
4.11 CAD model of the casing effusion cooling segment . . . 121
4.12 Schematic of the effusion cooling feed system . . . 122
4.13 Photographs of effusion cooling feed system . . . 122
4.14 Schematic of the experiments for the orifice calibrations . . . 124

4.15 Calibration curves for effusion cooling feed orifices 124
4.16 Index of refraction and absorption coefficient of yttria 127
4.17 Transmission regions in a selection of optical materials 128
4.18 Infrared transmittance in a selection of optical materials 129
4.19 Transmission of ZnS, ZnSe and Ge at temperature from 20 °C to 200 °C 129
4.20 CAD model of the IR transparent window designed for the OTRF . . 132
4.21 Finite Element stress analysis on window designed for the OTRF . . 132
4.22 Photographs and schematic of the OTRF test section for IR thermography testing 133
4.23 Analysis of the observation angles on rotor blades 133
4.24 Schematic of the manufacturing process for composite blade 136
4.25 Thermophysical properties of PEEK 137
4.26 Simplified models of composite blade for tensile load and fatigue tests 138
4.27 Composite blade sample installed on the load cell 140
4.28 Results of tensile load test on the baseline design 140
4.29 Results of tensile load tests on composite blade samples 141
4.30 Results from fatigue test on composite blade sample D3 142
4.31 Photograph of composite blade insert, moulding and final machining . 142
4.32 Infrared camera triggering and synchronisation system block diagram 143
4.33 Rotor revolution, blade passing and camera synchronisation signals . 145
4.34 Raw total pressure and camera record trigger signals 146
4.35 Photographs of a rotor blade instrumented with thin-film heat flux gauges 147
4.36 Photograph of calibration facility for thin-film heat flux gauges 150
4.37 Exemplary calibration data for best and worst thin-film gauge 150

5.1 Rotor assembly and FOV for IR thermography measurements in the OTRF 156
5.2 Camera detector calibration for integration times of 20, 10, 5, 2, 1 µs 158
5.3 Analysis on the effect of camera integration time in OTRF tests . . . 159
5.4 Equivalent blackbody temperature readings and absolute temporal errors from a single pixel over a range of integration times 161
5.5 Maximum absolute temporal error in temperature reading as a function of integration time and target temperature 162
5.6 Photographs of FOV 1 for T_{cam1} and FOV 2 for T_{cam2} 164
5.7 Workflow block diagram to process IR data in the OTRF 164
5.8 Single frame blackbody equivalent temperature, showing T_{cam1} and T_{cam2} 166
5.9 Evolution of the blackbody equivalent temperature T_{cam1} during the stages of a test run with uniform inlet condition 168
5.10 Results from the transient heat convection simulation on the IR transparent window used in the OTRF 170
5.11 Exemplary results and the correction of blade tip IR thermal data captured in the OTRF, showing blackbody equivalent, target, and reflected temperatures 171
5.12 Contrast enhancement procedure, showing original and enhanced images 173

5.13 Raw digital counts history of a pixel on the blade tip for a dataset acquired with an integration time of 5 µs 174
5.14 Example of feature tracking analysis in Blender 175
5.15 Results from the motion tracking algorithm 175
5.16 (a) Full FOV of temperature T_t at frame 392 during test 6076 corrected with test 6080. One pixel highlighted for point analysis; (b) Temperature T_t of blade tip at frame 392 during test 6076 corrected with 6080. One pixel highlighted for point analysis. 177
5.17 Key results from analysis of heat transfer for one pixel on the blade tip 178
5.18 Adiabatic wall temperature and Nusselt number on the rotor blade tip 180
5.19 Photograph of the blade instrumented with thin-film heat transfer gauges showing the gauge used for the IR data validation 181
5.20 IR thermography data corrected to target temperature looking at the blade pressure side 181
5.21 Key results from the analysis of heat transfer from gauge 1 on the blade pressure side 183
5.22 Key results from the analysis of heat transfer from one pixel on the blade pressure side 184
5.23 View of the domain used for the CFD simulation for the cooled and uncooled case 186
5.24 Adiabatic wall temperature obtained with IR thermography and CFD simulation 187

List of Tables

2.1 Main studies on calibration techniques for IR camera measurements. . 62

3.1 Influence coefficients C_i of each variable to the final T_t of expected value 500 K. 68
3.2 Infrared camera specifications. 72
3.3 Symbols and abbreviations of quantities used to define roughness of different samples of paint. 87
3.4 Results of roughness and emissivity study on different samples of paint. 87
3.5 Emissivity and reflection correction applied to an experimental case. . 89
3.6 Calibration uncertainty analysis, assuming $\tau = 0.95$, $\varepsilon = 0.95$, $T_r = 298\,\mathrm{K}$, $T_{opt} = 298\,\mathrm{K}$. 99
3.7 Target temperature uncertainty analysis, assuming $\tau = 0.95$, $\varepsilon_1 = 0.94$, $\varepsilon_2 = 0.04$, $T_r = 550\,\mathrm{K}$, $T_{opt} = 430\,\mathrm{K}$. 99
3.8 Metal effectiveness uncertainty analysis. 100

4.1 SILOET turbine design conditions in the OTRF. 107
4.2 Thermophysical properties of PEEK. Density at room temperature $\rho = 1.31\,\mathrm{g/cm^3}$ 137
4.3 Example of annealing procedure for a blade with thin-film gauges . . 148

5.1 Relevant testing conditions in the OTRF during IR thermography rotor tip heat transfer measurements. 156
5.2 Blur levels as a function of integration time for nominal speed condition in the OTRF. 158
5.3 Boundary conditions types used for CFD simulation. 186
5.4 Comparing the uncertainty in surface temperature between thin-film gauges and IR camera. 189
5.5 Comparing the uncertainty in heat flux between thin-film gauges and IR camera 190

Nomenclature

Latin Letters

$\dot{m}$	Mass flow rate	$\mathrm{kg\,s^{-1}}$
c_p	Heat capacity at constant pressure	
r	Turbine radius	m
v_t	Tangential velocity	$\mathrm{m\,s^{-1}}$
C	Influence coefficient	
c	Velocity	$\mathrm{m\,s^{-1}}$
h	Specific enthalpy	$\mathrm{J\,kg^{-1}}$
p	Pressure	
Q	Heat	J
R	Pixel digital count	
T	Temperature, K	
U	Uncertainty	
W	Work	J
w	Specific work	$\mathrm{J\,kg^{-1}}$
z	Altitude	m

Chemical Formulae

GaSb	Gallium antimonide
InAs	Indium arsenide

InSb	Indium antimony	
CO_2	Carbon dioxide	
ZnSe	Zinc selenide	

Greek Letters

α	Thermal Diffusivity	$\mathrm{mm\,s^{-1}}$
β	Pressure ratio	
η	Efficiency	
γ	Heat capacity ratio	
λ	Wavelength	µm
ω	Angular velocity	$\mathrm{rad\,s^{-1}}$
τ	Transmittance	
θ	Observation angle	
ε	Emissivity	

Abbreviations

BPR	Bypass Ratio
FOV	Field of View
FPA	Focal Plane Array
HP	High Pressure
HPV	High Pressure Vane
IR	Infrared
IT	Integration Time
LE	Leading Edge
LWIR	Long wavelength infrared spectral band
MWIR	Middle wavelength infrared spectral band

NGV	Nozzle Guide Vane
NUC	Non-Uniformity Correction
OTRF	Oxford Turbine Research Facility
PEEK	Polyether ether ketone
PS	Pressure Side
ROI	Region of Interest
SFC	Specific Fuel Consumption
SNR	Signal to Noise Ratio
SS	Suction Side
TET	Turbine Entry Temeperature
TRL	Technology Readiness Level
UDF	Unducted Fan

Physics Constants

h	Planck constant	$6.62607015 \times 10^{-34}\,\mathrm{J\,Hz^{-1}}$
g	Gravity	

Subscripts

bb	blackbody
c	Coolant
cam	Camera
comp	Compressor
corr	Corrected
g	Gas
i	blackbody source temperature
id	Ideal

opt	Optical path
r	Reflected
s	Isentropic
s	Shaft
t	Target
TC	Thermocouple
turb	Turbine
w	Wall
x,y	Pixel location in array

Chapter 1

Introduction

1.1 Motivation

Climate change is the most significant threat currently faced by humanity. The aim of reducing CO_2 emissions has led to tighter regulation across many industries, including aviation [1]. With globalization, international air travel has become increasingly important, yet is clearly conflicted or at odds with the goal of combating climate change. Approximately $2-3\%$ of CO_2 global emissions is attributed to global aviation [2]. Several organisations have set targets to reduce emissions: the Aviation Research and Innovation in Europe (ACARE) has defined the Flightpath 2050 [3] with a goal to reduce CO_2 emissions by 75% by 2050, while other organisations such as the International Civil Aviation Organization (ICAO) are targeting achieving net zero emissions by the year 2050 [4], a goal supported by several countries worldwide. Figure 1.1 depicts the CO_2 emissions in Megaton from 2005 to 2050 [5]. The analysis shows emissions reduction from technological improvements, as well as air traffic management and infrastructure use. To help the industry meet the 2050 emission target, alternative measurements are being examined such as implementing sustainable fuels, electric and hydrogen propulsion, and battery technology [6]. However, these new technologies require the development of new fields and infrastructure, which is time-consuming and expensive [7]. Optimising and redesigning existing engine technologies for greater efficiency is essential to reduce the impact of aviation and is the

most effective short term solution. In an endeavour to develop the next generation of air vehicles and to meet the net zero target, researchers and designers work to improve the efficiency in the conversion of energy from fuel into thrust, essentially improving engine efficiency. There is significant potential for improving gas turbine engines, possibly leading to a 30% increase in overall efficiency compared to current best-in-service engines [8], with consequential reduction of CO_2 emissions. New generation aircraft generate 20 to 25% less CO_2 compared to the previous generation [5]. The Rolls Royce Trent XWB in service on the Airbus A350 is an example of how continuous innovation and pursuit of higher efficiencies have made an impact on emissions: the engine has resulted in a 15% reduction in fuel consumption compared to the first Trent engine [9]. This in turn has played a crucial role in achieving a 25% reduction in fuel burn from the aircraft compared to previous-generation models [10].

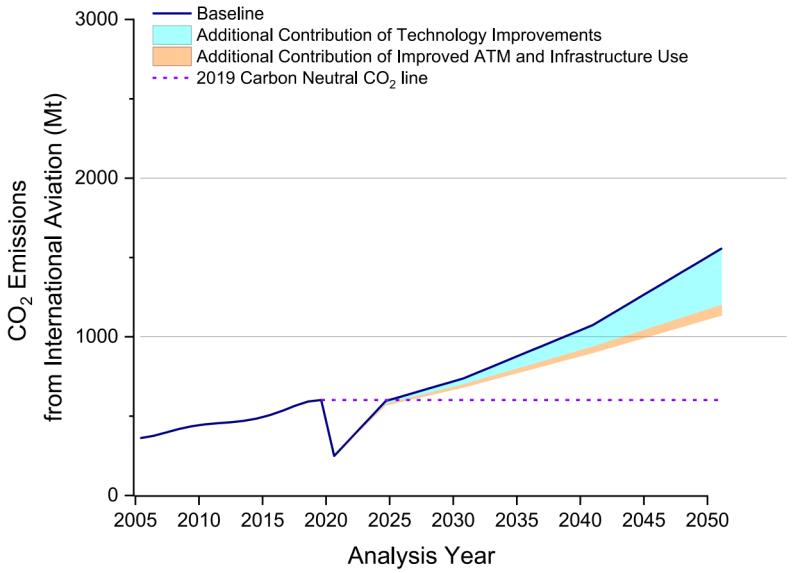

Figure 1.1: CO_2 emission from international aviation for the period 2005 to 2050 [5].

1.2 Cycle Performance

All modern commercial aircrafts are equipped with gas turbine engines, making their efficiency a crucial consideration for reducing carbon emission in the aviation industry. All gas turbine engines comprise compressor, combustor, and turbine sections, as shown in the cross-section in Figure 1.2. An engine efficiency reflects how well it can convert fuel energy into propulsive energy. This process is influenced by both thermodynamic and propulsive efficiencies. Figure 1.3 illustrates the evolving trends in these engine efficiencies, with the combined product of the two efficiencies represented as arcs. These arcs illustrate the overall efficiency of converting chemical energy from the fuel into propulsive power [12]. Since the inception of Whittle's engine, the thermodynamic efficiency has made substantial progress, increasing from approximately 10% to approximately 50%, as inferred from Figure 1.3. Concurrently, propulsive efficiency has also witnessed enhancements, progressing from 50% to 70%. As a result, the overall efficiency of gas turbine engines has risen from a modest 10% to nearly 40%. Figure 1.4 depicts the relationship between the two cycle efficiencies and specific fuel consumption (SFC) and highlights the fundamental limitations at play. Thermal

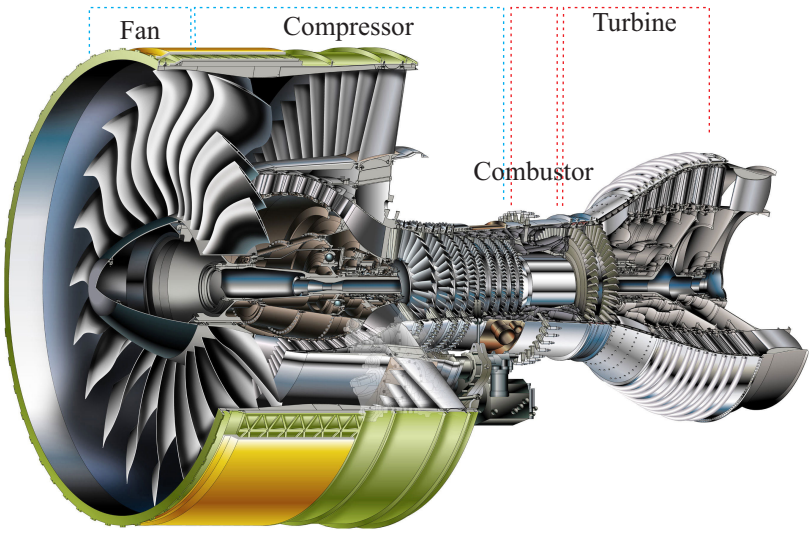

Figure 1.2: Gas turbine engine cross-section [11].

efficiency is constrained by a theoretical limit that entails stoichiometric combustion temperature, and lossless components. Propulsive efficiency is theoretically capable of nearing 100%. However, in the context of existing gas turbine engines, there is significant room for progress before reaching these limits.

Achieving this level of progress requires advancement in various fields. In terms of thermodynamic efficiency, this primarily translates into advancements in performance by which the jet engine increases the kinetic energy of the fluid, allowing thrust generation. This energy transfer consists of a series of transformations which wholly constitute the engine cycle: the Brayton (or Joule) cycle.

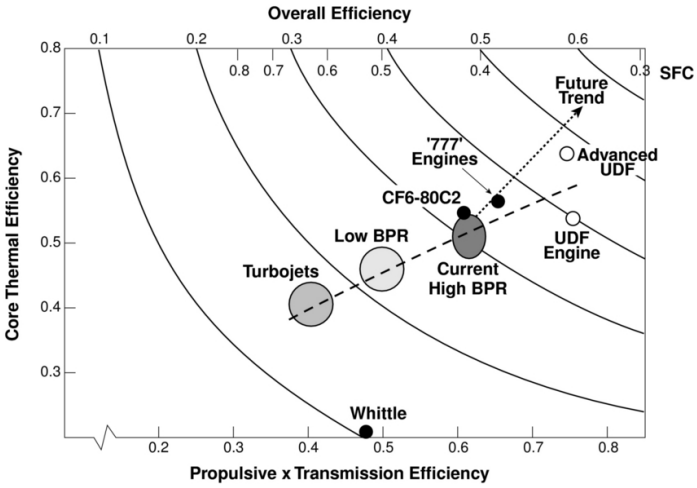

Figure 1.3: Aircraft gas turbine thermal, propulsive and overall efficiencies. Adapted from Epstein [12] and Koff [13].

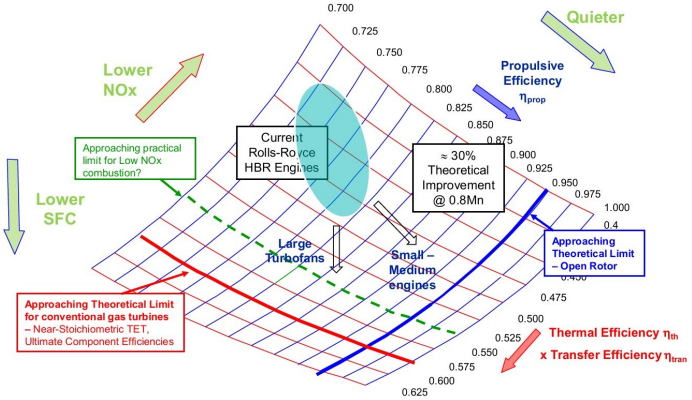

Figure 1.4: Specific Fuel Consumption (SFC), thermal, and propulsive efficiency [9].

The Brayton cycle [14], i.e. cycle $1 \rightarrow 2s \rightarrow 3 \rightarrow 4s$ shown in Figure 1.5, enables the study of the thermodynamic behaviour of the engine in ideal conditions. The four transformations are the following:

$1 \rightarrow 2s$	Isentropic compression (both adiabatic and reversible)
$2s \rightarrow 3$	Isobaric heat addition
$3 \rightarrow 4s$	Isentropic expansion
$4 \rightarrow 1$	Isobaric heat rejection

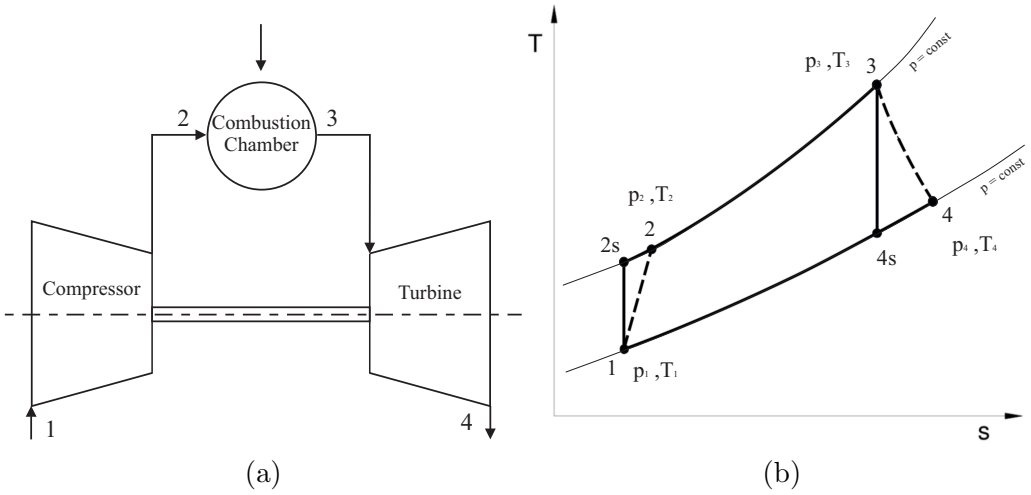

(a) (b)

Figure 1.5: The Brayton cycle including (a) schematic showing key stages of combustion for a jet engine and (b) T-S graph for the thermodynamic cycle, ideal and real transformations are shown.

The thermodynamic efficiency of the idealised cycle, knowing: i) the steady flow energy equation $Q - W = \dot{m}[(h_2 - h_1) + 1/2(c_2^2 - c_1^2) + g(z_2 - z_1)]$, which becomes $\dot{q} - w_s = (h_2 - h_1) + 1/2(c_2^2 - c_1^2) + g(z_2 - z_1)$ ($g(z_2 - z_1)$ neglected for gases), where w_s is the shaft work, ii) knowing that for an isentropic transformation $p^{(\gamma-1)/\gamma}/T = \text{const}$, and iii) assuming ideal gas behaviour $h = c_p T$, can be given by [14]

$$\eta_{cycle,id} = \frac{\text{net work out}}{\text{heat in}} = \frac{W_{34s} - W_{12s}}{Q_{2s3}} = \frac{c_p(T_3 - T_{4s}) - c_p(T_{2s} - T_1)}{c_p(T_3 - T_{2s})} = 1 - \frac{1}{\beta^{\frac{\gamma-1}{\gamma}}} \tag{1.1}$$

Hence, the ideal efficiency is only a function of pressure ratio β and the nature of the working fluid γ. However, in reality, while it is still possible to consider the compression and expansion process adiabatic, these are not reversible. Consequently, on

the T-S diagram shown in Figure 1.5b the final states of the compression and expansion will have an increased entropy, shown with points 2 and 4 in the cycle. Thus, isentropic efficiencies are defined for the compressor and the turbine as follows [14]

$$\eta_{comp} = \frac{T_{2s} - T_1}{T_2 - T_1} \quad \text{and} \quad \eta_{turb} = \frac{T_3 - T_4}{T_3 - T_{4s}} \tag{1.2}$$

The thermodynamic efficiency of the real cycle is defined as the ratio between the net work output from the cycle and the heat addition (stages 2-3), where the net work output is obtained from the difference between the turbine power output and the compressor power requirement, and can be expressed as

$$\eta_{cycle,real} = \frac{\dot{w}_{net}}{\dot{Q}_{in}} = \frac{\dot{w}_{turb} - \dot{w}_{comp}}{\dot{Q}_{in}} = \frac{c_p(T_3 - T_4) - c_p(T_2 - T_1)}{c_p(T_3 - T_2)} \tag{1.3}$$

If the compressor and turbine stage efficiencies (given by Eqs. 1.2) are substituted into the previous expression (Eq. 1.3), the following equation can be derived

$$\begin{aligned} \eta_{cycle,real} &= \frac{c_p\,\eta_{turb}(T_3 - T_{4s}) - c_p\frac{1}{\eta_{comp}}(T_{2s} - T_1)}{c_p(T_3 - T_2)} = \\ &= \frac{T_1\left[\eta_{turb}\frac{T_3}{T_1}\left(1 - \frac{1}{\beta^{\frac{\gamma-1}{\gamma}}}\right) - \frac{1}{\eta_{comp}}\beta^{\frac{\gamma-1}{\gamma}}\right]}{(T_3 - T_2)} \end{aligned} \tag{1.4}$$

From Equation 1.1 and 1.4, it can be observed that the idealised efficiency is only a function of pressure ratio, with the former increasing as the latter increases. However, the influence of pressure ratio on real efficiency is more complicated. This relationship is graphically illustrated in Figure 1.6. From the plot, it can be inferred that an increase in pressure ratio requires a corresponding increase in temperature ratio to maintain similar efficiencies. This translates in an increase of Turbine Entry Temperature (TET) – often referred to as turbine inlet temperature, T_3 in the analysis. This is also illustrated in Figure 1.7, which shows specific core power production as a function of the turbine inlet temperature. As improvements in cycle efficiency have a direct impact on specific fuel consumption and, consequently, emissions, studies on how to maximise the TET for a given cycle are strongly motivated.

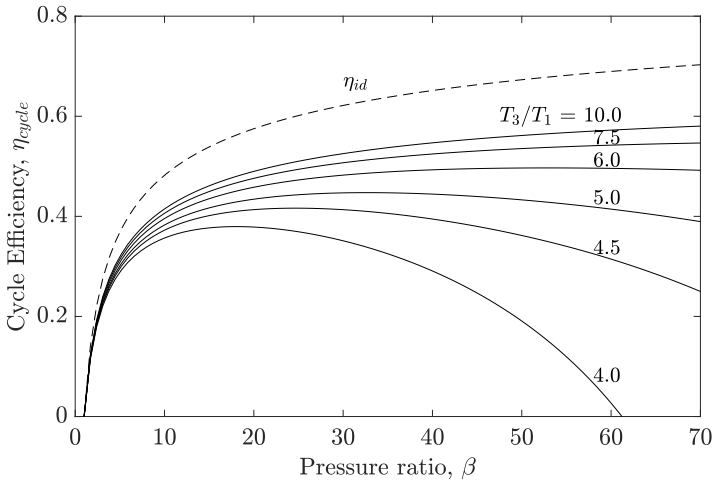

Figure 1.6: Analysis of the Brayton thermodynamic efficiency considering non-isentropic compressor and turbine at different temperature ratios. The isentropic efficiencies used are $\eta_c = 0.9$, $\eta_t = 0.9$.

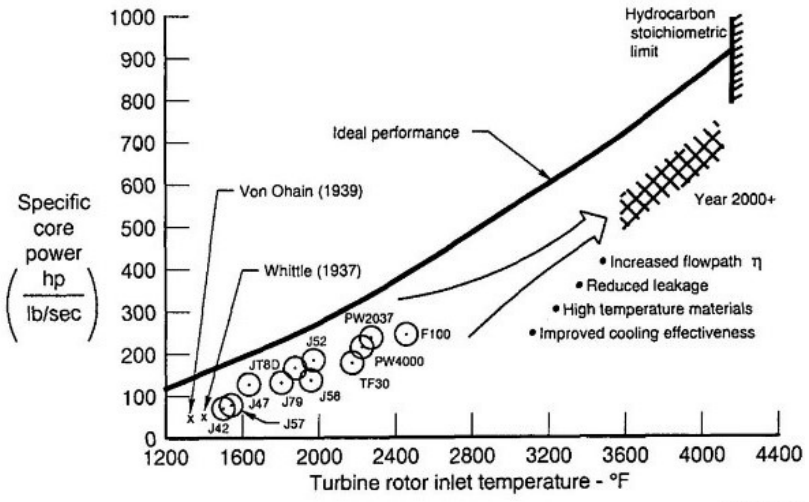

Figure 1.7: Specific core power as a function of turbine rotor inlet temperature [15].

Ultimately, achieving higher turbine entry temperatures primarily revolves around attaining efficient combustion, more advanced thermal management systems, and improved material capabilities to endure high temperatures. Metallurgical constraints limit the maximum TET by determining the maximum allowable temperature to ensure adequate components lifetime. Indeed, the trend of increasing turbine inlet temperature leads to a marked decrease in durability of the components in the hot section. Components which in the past required only modest cooling could now limit the lifetime of the whole gas turbine engine without improvements to the cooling system. One such component is the high-pressure (HP) turbine stage. The combustion process taking place in the combustion chamber upstream the HP turbine employs swirling action to aid combustion stability and better fuel-air mixing, both pivotal for optimising combustion efficiency. As a result, the temperature profile seen by the high-pressure turbine not only registers gas temperature beyond the materials melting threshold, exceeding 1700 °C [18], but that is also characterised by radial and circumferential variations. This intricate interaction subjects the high-pressure turbine stage to substantial cyclic thermal and mechanical stresses. Figure 1.8 illus-



(a) (b)

Figure 1.8: Example of turbine blades failures due to overheating (a) from [16], and (b) from [17].

trates the consequences of enduring such heat loads on turbine HP rotor blades. The damage, known as tip burnout, predominantly affects the tip region . In addition to the obvious issue of material failure, the progressive erosion of the tip diminishes the stage efficiency as the increased gap between rotor tip and casing leads to higher aerodynamic losses (see leakage flow loss in Denton [19]).

The main strategy employed to overcome the limitation on increasing TET due to component failure is the implementation of cooling technologies. Figure 1.9 illustrates the progression of TET through the utilization of various technologies in aircraft engines. Since 1965, advances in material and cooling technologies have nearly doubled TET. This emphasised that cooling methods are crucial to operate the engine at temperature significantly higher than the metal melting temperature, and are important not only to avoid the melting of the material, but also to reduce thermal stresses.

As a final observation, the importance of accurately predicting the thermal loads that turbine components undergo has been stressed by Han et al. [21], who observed

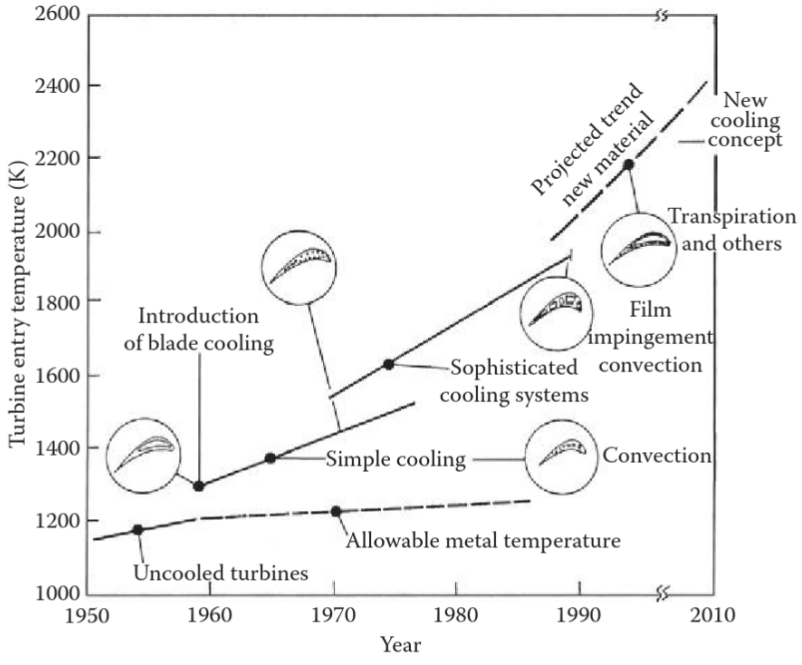

Figure 1.9: Variation of turbine entry temperature over years. Adapted from Clifford [20], collected in Han et al. [21].

that an error in blade metal temperature prediction of approximately 20 K can result in halving blades life.

It is noteworthy to mention that, besides the TET, also component efficiencies, and reducing the amount of compressor bleed air used for turbine cooling, have a notable impact on the overall engine efficiency.

1.3 Modelling and Testing of Turbomachinery Flows

The internal flow fields in turbomachinery are inherently three-dimensional, characterised by high levels of unsteadiness. The research that focus on comprehending such flows has started with the use of simplified facilities and continued increasing the complexity to achieve a close replica of the flow conditions in a real engine. These facilities include cascade linear or annular facilities and rotating facilities [22].

Cascade rigs consist of a limited number of blades positioned inside a wind tunnel. Cascade facilities can be linear [23] or annular [24]. In linear cascade facilities the blades are linearly positioned, while in an annular cascade test rig the blades are housed inside a space delimited by two concentric cylinders (annulus). The tested blade geometry can either be a replica of actual engine blades or scaled-up version for increased measurement resolution and to facilitate detailed three-dimensional flow investigations. The role of cascade testing has been pivotal in understanding the fundamental flow mechanisms within axial turbomachinery blade rows, and they can successfully investigate the influence of parameters such as Mach and Reynolds number on the aerodynamics and heat transfer of a blade. However, they cannot capture the true physics of a jet engine. The effects of relative movement of casing, buoyancy in the mainstream flow and cooling flow within blades, and temperature and pressure profiles downstream of high-pressure vanes are not entirely captured in cascade facilities. This is where rotating facilities come into play, providing a closer represen-

tation of the unsteady nature of flow quantities in jet engines. Rotating facilities are fundamentally a rotating annulus cascade. They can include one or more stages of a turbine, with a general configuration of high-pressure vane (HPV), also referred to as nozzle guide vane (NGV), upstream of a high-pressure rotor blade row, an example of such facilities is the Oxford Turbine Research Facility (OTRF) [25]. Cascade facilities have a crucial role in the development phase of new concepts, enabling the testing of several designs within a short timeframe. Concepts downselected in cascade facilities can then be evaluated in rotating facilities, before progressing to the final stage of design development, which is an engine test. The absence of rotating facilities as a connecting bridge between cascade testing and engine testing would create a significant, if not dangerous, gap. One of the primary advantage of rotating cascades lies in their capability to emulate the impact of tip clearance flows, an extensive area of research especially important for the tip burn-out phenomenon previously discussed.

Having established the importance of rotating testing to study phenomena such as tip flows, we now delve into discussing the instrumentation necessary to capture the flow thermal quantities.

Over the years, several techniques for measuring temperature have been conceived with the purpose of achieving accurate readings of thermal interactions. Widely used methods include: thermocouples, thin-film gauges, thermochromic liquid crystals, temperature and pressure sensitive paints, and infrared thermography. While thermocouples and thin-film gauges are extensively used to perform single-point measurements on stationary components, they both present a list of challenges when used on rotating or fast moving components. Both measurement techniques require wiring access, and thin film gauges in particular require time consuming soldering and complicated calibration and data processing. Sensor integrity is also often an issue, for example under the high centrifugal forces on the rotor blade. The introduction of optical measurement techniques has offered new prospects to overcome these chal-

lenges. However, thermocouples and thin-film gauges are still vital measurements, for instance thermocouples are often used as a reference for IR and optical methods, and both techniques offer measurement when optical access in not possible. Optical measurement techniques are non-intrusive (no thermal or fluid dynamic interference of a sensor with the flow) and permit the assessment of the temperature field over the entirety two-dimensional specimen surface. In this category, pressure sensitive paints and liquid crystals permit to correlate the colour change to temperature and have been used in the past for research in jet engines and gas turbines [26, 27, 28]. The main downside of these two techniques is their operational temperature limit of 200 °C and 120 °C, respectively. In contrast, infrared (IR) thermography is non-intrusive, provides a high-resolution two-dimensional temperature field, and does not present a upper temperature limit of operation. In addition, modern IR cameras can achieve very low integration time and high frame rate, enabling measurement on object traveling at high velocities. These aspects make infrared thermography a viable candidate to study heat transfer phenomena in the HP turbine section of a rotating facility. A full review of temperature measurement techniques will be given in the literature review developed in Chapter 2.

1.4 Research Aims

In this introduction, the need to reduce CO_2 emissions in the aviation sector is emphasised. A key strategy to achieve this reduction involves pursuing higher Turbine Entry Temperatures (TET) and implementing more efficient cooling technologies. The discussion highlights the necessity for representative data obtainable in rotating facilities, such as the Oxford Turbine Research Facility (OTRF). It is stressed that accurate temperature measurements are crucial for component design development. Historically, thermal measurements in high-speed, rotating facilities like the OTRF relied on sensors with limited spatial resolution, and incurring in substantial instal-

lation time. The discussion underlines the superiority of IR infrared thermography over these conventional techniques, though acknowledging the challenges it presents in the context of high-speed rotating engine facilities.

The thesis aims to address these challenges by conceiving an innovative infrared measurement technique to improve the prediction and understanding of thermal loads on turbine blades. This approach offers benefits such as repeatability and cost-effectiveness, enabling early diagnostics of novel cooling systems. The research specifically focuses on examining aerodynamics and heat transfer in the first stage of a high-pressure unshrouded turbine designed for the next generation of low-emission aircraft engines. The objective is to develop a highly accurate infrared thermography measurement system for assessing surface temperature and heat transfer in the OTRF. Ultimately, this system aims to provide measurements of surface temperature at Technology Readiness Level (TRL) 5 [29], streamlining technology development by rapidly identifying the most efficient cooling designs. The proposed technique will allow rainbow testing with different designs, facilitating down-selection before proceeding to the thermal paint test. This test, which evaluates achieved versus expected temperatures of engine parts, is crucial for obtaining certification from the Federal Aviation Administration (FAA). Infrared thermography tests at the OTRF level provide an additional, more economical stage for manufacturers to test multiple designs before the thermal paint test, aiding in the efficient transition of designs into products. Finally, the research aims to generate a bank of experimental data for validating and improving predictive models and numerical simulation techniques contributing to the advancement of turbine technology.

The output of this work includes three publications. These are:

i) Infrared thermography and calibration techniques for gas turbine applications: A review [30].

ii) Infrared temperature measurements on high pressure turbine blades in the Oxford Turbine Research Facility: calibration and image processing techniques [31].

iii) Infrared temperature measurements on fast moving targets: A novel calibration approach [32].

The first paper presents a review of the calibration techniques for infrared (IR) measurements in the field of gas turbines and laid the foundation for the Literature Review in Chapter 2. The second and the third papers evolved from a deep understanding of state-of-the-art calibration techniques for infrared thermography, coupled with understanding of the sources of error. Based on this analysis, a comprehensive calibration was developed for an IR thermography system designed for fast moving targets, such as turbine blades in the OTRF. This calibration is discussed in details in Chapter 3.

1.5 Structure of the Thesis

A succinct description of the content of each chapter is given below.

Chapter 2

Review of Heat Transfer Measurement Techniques

In this chapter, representative engine experiments and accurate temperature measurements are contextualised in the literature. The chapter starts from a short review of different types of rotating facilities for heat transfer studies and moves to different types of heat transfer instrumentation. Particular attention is paid to the current state of the art in IR camera calibration methods. Many developments and recent advances are presented, including numerous calibration methods and advanced image processing techniques. The relative strengths and limitations are outlined by comparing past studies in the literature. Finally, a brief review of turbine blade tip heat transfer studies is given.

Chapter 3

Development of an Infrared Measurement Methodology for Fast Moving Targets Techniques

In this chapter, a methodology for accurate IR thermography measurements on fast moving targets is presented. The chapter starts by framing the use of IR thermography in the Oxford Turbine Research Facility (OTRF), with attention to the sources of error that arise in this situation. Subsequently, the reasoning behind the choice of the best IR detector for this application is discussed. Finally, a calibration approach for measurements on fast moving targets is described. This calibration addresses the need for emissivity, reflection and transmittance corrections and its performance is tested on an high-speed rotating object. The uncertainty of the calibration is included at the end of the chapter.

Chapter 4

Development of an Infrared Thermography System for Transient Heat Transfer Measurements in a Rotating Facility

In this chapter, the experimental Oxford Turbine Research Facility (OTRF), the test programme during the IR experiments, and the designing of the IR thermography components are delineated. The chapter stars describing the facility turbine geometry as well as the working principle of the combustor simulator component. The facility data acquisition system and location of instrumentation are also described. A brief account of the test program conducted during the IR experiments is provided. The final part of the chapter delves into the design of the components implemented on the facility for IR thermography measurements. Starting from the design of the optical access and of composite blade, and moving onto the camera synchronisation system. The chapter closes with the description of the thin-film heat flux gauges instrumentation used on two aluminium blades.

Chapter 5

Infrared Thermography of Rotor Tip Heat Transfer

In this chapter, the results of heat transfer measurements obtained using IR thermography in the Oxford Turbine Research Facility are introduced. The chapter starts with a qualitative comparison of datasets acquired at different camera integration times. The processing of one dataset from raw camera digital counts to heat flux and Nusselt number is then developed. Finally, two validation cases are reported: a CFD simulation and experimental data acquired with thin-film heat flux gauges. The chapter concludes with an uncertainty evaluation in surface temperature and heat flux for thin-film gauges and IR thermography data.

Chapter 6

Conclusions

In this chapter, the motivation and aim of the work presented in this thesis, as well as the main findings are summarised. A few suggestions for further improvements in the methodology and future experiments are given.

Chapter 2

Review of Heat Transfer Measurement Techniques

This literature review focuses on two key aspects of heat transfer research: testing facilities and heat transfer measurement instrumentation.

The first section provides an overview of annular rotating facilities, with focus on short duration facilities akin to the Oxford Turbine Research Facility (OTRF), the facility where the studies presented in this thesis were carried out.

The second part of the chapter delves into heat transfer measurement instrumentation. Traditional sensors and a range of optical techniques are reviewed, with the scope of highlighting the merits and limitations for each. Among the sensors, thin-film heat flux gauges are discussed given their long-standing history as the predominant sensor in heat transfer turbomachinery measurement. Turning to optical techniques, a brief overview of thermochromic liquid crystals is provided, acknowledging their historical significance in the field. However, their limitation for measurements on rotor blades in a transient facility, the experimental focus of this study, are outlined. Thus, infrared thermography is examined in greater detail as the primary technique chosen for this study.

The theoretical aspects of thermal radiation heat transfer are explained, including the emissivity of the target, reflectivity of the target, and transmission of the optical path. The review extends to infrared thermography calibration and correction

techniques, aiming to provide an overview of the current state-of-the-art methodologies. This becomes fundamental as accurate temperature measurements with infrared thermography on fast moving targets require fine-tuned calibration and correction procedures.

The subsequent discussion delves into application of infrared thermography for temperature measurements in large-scale turbine rigs.

Finally, the chapter ends with a concise review of blade tip heat transfer studies, the primary focus of the measurements presented in this thesis.

2.1 Review of testing facilities

As turbine designs continue to evolve, understanding the underlying flow physics of an operating turbine becomes increasingly important for further advancements. The hot section of a turbine presents a complex flow environment, characterized by unsteadiness, three-dimensionality, and high temperature and mechanical loads. To predict the consequences of these factors in the design phase, it is essential to accurately measure and comprehend their impact. In recent years, simulation codes have been validated against various measurements. However, aerothermal predictions for gas turbine environments remain challenging given the fast pace required in design process. Modelling of phenomena, such as film cooling, requires simulation times that can go from 5 weeks up to 10 for one solution, depending on the computation power employed. Hence, a distinct gap exists at TRL 5 for component development that increases the risk to engine project, and simultaneously limits the advancement of technologies into product. The ability to predict both the aerodynamics and heat transfer associated with turbine stages poses a significant challenge for designers and it is the experimental researchers role to aid solving this challenge providing accurate data. The first attempts were carried out with simplified geometries in the shape of flat plates in low speed wind tunnels, or with linear cascade facilities replicating a few blade/vane passages. A good reference that collects expertise on cascade testing techniques gathered over the years from various institution is the AGARDograph [22]. Aerothermal research on flat plates and cascades has contributed greatly to heat transfer predictions, however, these experiments do not fully represent the unsteady flow field environment of a complete turbine stage. Phenomena such as wakes interaction, mainstream turbulence, coolant ingestion, and secondary flows typical of a real engine environment may not be replicable in these simplified experiments. Nonetheless, this type of fundamental research played a pivotal role in the development of theories that improved understanding of turbine flows and were used in the

first computational fluid dynamics (CFD) prediction codes.

The natural advancement to annular cascade and rotating facility testing was guided by the need to validate these hypotheses at correct Mach number, Reynolds number and radial pressure gradient. Annular cascades permitted to investigate the influence of Mach and Reynolds numbers on blade aerodynamics and heat transfer at the correct radial pressure gradient. With the addition of the rotor, and the advent of engine-scale rotating facility, the rotor-vane interactions as well as unsteady rotating phenomena, including rotor boundary layers, and tip leakage flow could be investigated.

The functions of these facilities have evolved alongside progress made in measurement techniques and data acquisition methods. Presently, flat plate and cascade facilities have the capability to incorporate comprehensive two-dimensional surface measurements, while engine-scale rotating rigs typically provide more localised point measurements. Technologies that have been developed in the cascade facilities are being adapted for use in the engine-scale facilities, with ongoing efforts focused on equipping engine-scale rotating facility with fully two-dimensional surface measurements, specifically optical measurements. Additionally, rotating facilities present opportunities for examining internal flow characteristics, such as blade cooling passages, at design speeds. The insights gained from these facilities have greatly contributed to turbine research, playing a pivotal role in advancing the turbine industry. The data generated by these facilities are actively employed in the validation process of computational fluid dynamics (CFD) simulations, thereby driving progress in the field.

Engine-scale rotating rigs can be classified into two categories based on the duration of a run: continuous and transient facilities. Continuous facilities have long run times, typically lasting hours, and operate under steady-state conditions. These facilities provide a continuous and sustained flow environment for testing. On the

other hand, transient facilities are characterized by short run times, ranging from fractions of seconds to seconds. In these facilities, the test article never reaches an equilibrium temperature. Long duration facilities are well-suited for conducting aerodynamics and efficiency studies, whereas short duration facilities are better suited for investigating heat transfer phenomena. The advantages of measuring heat transfer in transient facilities have been extensively discussed in literature [33, 34, 35]. The thermal transients achievable in the short duration facilities provide opportunities to determine the heat flux rate by recording the time-temperature history. There are three main types of these facilities currently in use: shock tunnel, blowdown and isentropic light piston tube facilities. These are briefly described in the following section.

2.1.1 Short Duration Facilities

Shock tunnels generate high-velocity and high-enthalpy flows using a strong shock wave. A diaphragm separates the tube into a high-pressure and a low-pressure region; when the diaphragm bursts, the high-pressure driver gas expands into the low-pressure chamber creating a shock wave. The shock wave propagates in the tube compressing the low-pressure driven test gas. This concept, initially presented at Cornell Aeronautical Laboratories to generate and study hypersonic flows [36], has been extended to turbine research. The Turbine Test Facility at the Ohio State University is one of the facilities at the forefront of turbine research using shock tube technology. The facility was firstly commissioned at Calspan, where the first turbine measurements were performed in 1977 [37, 38]. It was upgraded in 1986 to reproduce the temperature profiles typical of the combustor exit section and operating with fully cooled turbine stages and subsequently moved to OSU in 1996. The history of the facility was reported by Dunn and Mathison in 2013 [35].

Blowdown facilities rely on the rapid release of high-pressure gas from the supply

tank to the dump tank. The MIT blowdown turbine facility is an example of this type of operating conditions. Developed in 1984 [39], the facility features an oil jacket around the supply tank to heat up the system. Prior to a run, vacuum level is achieved in the facility, subsequently, the supply tank is heated up to temperature and the high pressure gas injected with the fast acting valve closed. The turbine is brought up to speed using an air motor and an eddy current brake is used to keep the turbine speed constant during the run. Very similar to the MIT facility, the Air Force Research Laboratory Turbine Research Facility is characterised by long blowdown duration: the size of the supply tanks allows running time for vane-only tests of typically 3 to 5 seconds, which are reduced to 2-2.5 seconds for vane and rotor tests [40]. The downside of blowdown facilities is the difficulty of keeping a constant inlet total pressure, as this pressure decreases when the gas is released into the dump tank, causing a drop in inlet Reynolds number.

Piston tunnel facilities were developed to model the flow conditions in a gas turbine engine as closely as possible. In particular, they are able to match Mach and Reynolds numbers, as well as gas to wall temperature ratio. The theory of operation of an Isentropic Light Piston Tunnel (ILPT) was firstly presented by Jones et al. in 1973 [41], and used in 1977 to develop the Oxford University transient cascade facility [42]. A high pressure (HP) reservoir is connected to the pump tube containing a light weight piston, which starts its travel at the HP reservoir end. As high pressure air is injected behind the piston, this is driven down the tube, thereby compressing the gas within the piston tube. A bursting diaphragm or fast acting valve isolates the pump tube from the test section, and this is triggered to open when the desired pressure in the test gas has been achieved. When this valve opens, the test gas flows through the test section and by matching the volumetric flow rate exiting the piston tube with the one entering the tube from the HP reservoir behind the piston, the test gas conditions remain constant throughout the run. The capability of ensuring steady

conditions thanks to a constant pressure within the piston tube represents the main innovation of piston tunnel facilities. The same theory was applied to develop the Isentropic Light Piston Cascade at Pyestock in 1985 [43], which was upgraded in 1994 to include a high pressure turbine stage [44], and moved to Oxford in 2010 where it was renamed the Oxford Turbine Research Facility [45, 25]. Another notable ILPT facility is the von Karman Institute Compression Tube Facility [46].

2.2 Review of Heat Transfer Instrumentation
Thin-Film Gauges

Among the different types of heat flux sensors, thin-film heat flux gauges are most widely used due to their high temporal response, low thickness, and ability to measure a value close to the true surface temperature [33]. Initially developed for use in hypersonic wind tunnels [47, 33], thin-film gauges have been an important tool in turbomachinery research since the 1970s. Thin-film heat flux gauges are fabricated by depositing a thin layer of conductive material, typically platinum or nickel, onto an insulating film with thickness typically between 0.01 and 0.1 µm, and using copper tracks to form the electrical connections. When a constant electrical current is passed through the thin-film, the voltage drop across the element provides a way of monitoring the element temperature. Subsequently, Fourier's law of heat conduction can be used to calculate the heat flux based on the temperature history of the film.

The resistance of the film is a function of the temperature, as follows

$$R_T = R_0(1 + \alpha T) \tag{2.1}$$

where R_0 is the resistance at temperature T_0 and α is the temperature coefficient of resistance. If a current I is passed through the gauge, the voltage change across the film is proportional to its temperature. Hence, temperature values can be inferred from voltage measurements. With prior knowledge of the material's thermal properties and a measurement of the temperature, the heat flux can be obtained by Fourier's

law:

$$\dot{q} = -k\nabla T \tag{2.2}$$

Where k is the thermal conductivity. This enables the determination of the heat transfer coefficient and adiabatic wall temperature.

2.2.1 Single Layer Semi-Infinite Gauges

Gauges operating on the semi-infinite hypothesis for use in short-duration facilities were first proposed by Vidal in 1956 [47] and a thorough theoretical monograph was presented by Schultz and Jones in 1973 [33]. A schematic of a single layer thin-film gauge mounted on a semi-infinite substrate is shown in Figure 2.1. Schultz and

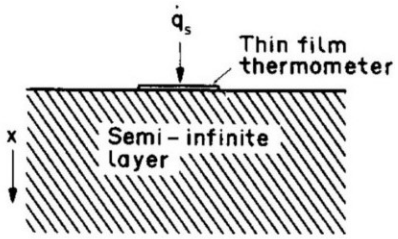

Figure 2.1: Schematic of a thin-film heat flux gauge on semi-infinite layer [48].

Jones [33] demonstrated that the presence of the thin-film gauge has a negligible effect on the heat transfer. With a film thickness of 0.1 µm, the heat transfer rate was measured with an error of 5% after 0.4 µs and 1% after 120 µs. In other words, the low thickness of the film enables a temperature measure very close to the true surface temperature.

Assuming 1D heat conduction and negligible impact of the thin-film gauge on the heat transfer, the Fourier equation that governs the heat transfer is as follows [49]

$$\frac{\partial^2 T}{\partial x^2} = \frac{1}{\alpha}\frac{\partial T}{\partial t} \tag{2.3}$$

where T is the temperature of the substrate at a distance x from the surface at time t, and α is the thermal diffusivity of the material, defined in terms of thermal conductivity, k, density, ρ, and specific heat, c: $\alpha = k/\rho c$.

If the heat transfer rate to the surface is $\dot{q}$, given the following boundary conditions

$$\dot{q} = -k\frac{\partial T}{\partial x} \qquad \text{at } x = 0 \tag{2.4}$$

$$T = 0 \qquad \text{at } x = \infty \tag{2.5}$$

then the Fourier equation can be solved to obtain the Laplace transform of the surface heat transfer rate [33]

$$\overline{\dot{q}} = \sqrt{\rho c k}\sqrt{s}\,\overline{T} \tag{2.6}$$

where s is the Laplace transform variable. Inverting the transform for the more general case where the heat transfer rate is not constant, this may be obtained from

$$\dot{q}(t) = \sqrt{\frac{\rho c k}{\pi}}\left[\frac{T(t)}{\sqrt{t}} + \frac{1}{2}\int_0^t \frac{T(t) - T(\tau)}{(t-\tau)^{3/2}} d\tau\right] \tag{2.7}$$

Equation 2.7 demonstrates that it is possible to calculate $\dot{q}$ from a digitally recorded temperature signal, however this cannot be done in the time-continuous domain given the singularity contained in the integral at $t = \tau$, such that evaluation of the heat transfer from the surface temperature signal needs to be carried out numerically. The use of numerical methods however brings in a numerical error [50]. A way around this was found in the use of electrical analogues to convert the film voltage into a current proportional to the heat transfer [51, 33, 50, 52]. An alternative approach was proposed by Oldfield in 2008. [53], who developed an impulse response processing.

The solution of the heat transfer equation in thin-film gauge theory is based on the assumption that the heat transfer under the thin film layer can be considered one-dimensional and the substrate semi-infinite. For the assumption to be valid, the penetration depth of the thermal impulse in the substrate needs to be sufficiently small. The depth, x, at which the substrate can be considered to be semi-infinite is a function of flow duration, t, and material properties. To quantify the validity of this assumption, the solution of the heat transfer equation for the temperature T_x at a depth x can be considered. This leads to an equation for the depth at which the

heat transfer rate is 1% of the surface value: $x = 3.47\sqrt{\alpha\, t}$. Figure 2.2 shows the penetration depth as a function of time for a selection of materials calculated assuming constant thermal properties. It can be inferred that at 1 s flow duration, the layer depth varies from 1 mm for glass materials such as porcelain RTV and epoxy, to 3 cm for metals such as aluminium, which is practically excessive. Thus, since the use of glass machined blades is limited to stationary cascade facility for obvious structural reasons, the use thin film gauges in fully rotating turbine test rigs is limited to flow duration shorter than 1 s. For nickel a thickness of 3 mm would be satisfactory for a flow duration of 10 ms.

The single layer semi-infinite gauges technique has been refined to a great extent in stationary turbine cascades by manufacturing complete airfoils from ceramic material to eliminate flow disruption issues. Nevertheless, this method is limited to ceramic or plastic test specimens, which are frequently difficult to manufacture or unsuitable for use in rotating facilities. This challenge has provided scope for development of multi layer thin-film gauges.

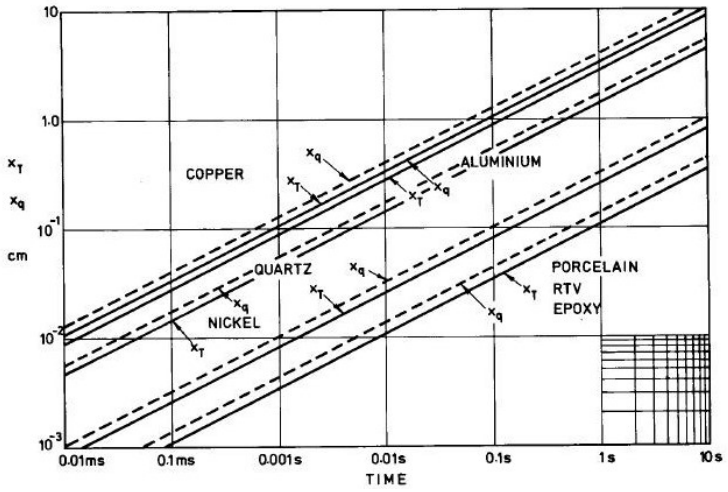

Figure 2.2: Analysis of thermal penetration depth for a selection of materials, defined as depths at which 1% heat loss at the rear face is found as a function of time; x_T is the depth at which temperature is 1% of surface value and x_q is the depth at which heat transfer rate is 1% of surface value [33].

2.2.2 Two Layer Single-Sided Gauges

Measuring the heat transfer on blades within rotating turbine test rigs requires instrumentation that can tolerate high stresses without affecting any aspect of the aero-thermodynamics of the system. Such stringent requirements led to the development of two layer gauges composed of the metal substrate of the model, and an insulator. A schematic of two layer single-sided thin-film gauges is shown in Figure 2.3. At Oxford, Doorly in 1985 [54] developed a procedure which involved the firing of a 140 µm layer of vitreous enamel, an electrically insulating medium, onto mild steel, with the thin-film hand painted on top.

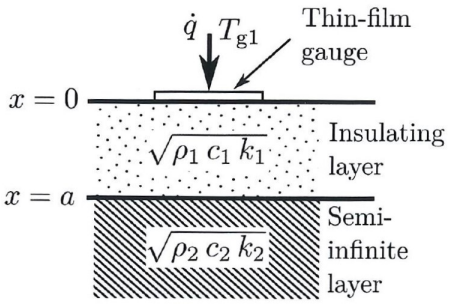

Figure 2.3: Schematic of a two layer single-sided thin-film heat flux gauge [53].

According to theory of two layer thin-film gauges, reported by Doorly et al. [48], the relationship between heat transfer rate and surface temperature (Equation 2.6 for single layer gauges) becomes

$$\overline{\dot{q}} = \sqrt{\rho_1 c_1 k_1}\sqrt{s}\frac{1 - A\exp(-2a\sqrt{s/\alpha_1})}{1 + A\exp(-2a\sqrt{s/\alpha_1})}\,\overline{T} \tag{2.8}$$

where a is the thickness of the insulating layer, and

$$A = \frac{\sqrt{\rho_1 c_1 k_1} - \sqrt{\rho_2 c_2 k_2}}{\sqrt{\rho_1 c_1 k_1} + \sqrt{\rho_2 c_2 k_2}} \tag{2.9}$$

where 1 indicates the insulating layer, and 2 the semi-infinite metal. Similarly to the solution for single layer thin-film gauges, it is difficult to solve such equation

analytically, and either numerical methods or an electrical analogue are used, and more recently the impulse response method was able to offer a more computationally efficient and simpler processing solution [53].

While the two layer single-sided gauges broaden the validity of the 1D assumption, this is still an issue when the gauges are applied to thin walls or to highly curved geometries, such as blades' trailing or leading edges, respectively.

2.3 Review of Heat Transfer Instrumentation
Thermochromic Liquid Crystals

Thermochromic liquid crystals (TLCs) are organic compounds with a unique phase change behaviour during the transition from a crystalline solid to an isotropic liquid that makes them useful for surface temperature measurement [55]. These molecules exhibit an ability to selectively reflect wavelength bands of the incident electromagnetic spectrum as a function of their temperature in their optically active range; in other words, if the reflected wavelength is in the visible spectrum, it will be seen as a colour change of the crystal. TLCs are available in an encapsulated form, housed within a sealed polymeric spherical shell with a diameter ranging between 10 and 20 µm, providing a protective shield [56], when these are applied to a surface and monitored with a video camera, the colour changes observed provide insights into the spatial distribution of surface temperature. This technique has been widely used for heat transfer measurements [57, 58, 59], offering the advantage of high spatial resolution. However, they present a number of limitations as discussed by Ireland and Jones [26]: chemical contamination sensitivity, temperature operating range, response time, and maximum heat flux.

Thermochromic liquid crystals are susceptible to damage resulting from contamination by organic compounds and the degrading effects of exposure to ultraviolet light, leading to the destruction of their colour play [26].

The operational absolute temperature range of TLCs span from −30 to 115 °C [26]. Additionally, TLCs are characterised by a 'colour play' range where the crystals are optically active. This is a transitional temperature range where the material is in the transition between solid and liquid state. The narrowest and widest colour play range reported by Ireland and Jones [26] are approximately 1 °C and 20 °C, respectively. Over the colour play bandwidth, with increasing temperature, the reflected light changes from "red" and passes through the visible spectrum to "violet" before reaching the optically inactive phase (liquid), this is visually summarised in Figure 2.4 [60, 61]. Yan and Owen [62] explained that TLCs characterised by narrower colour play ranges offer higher precision in temperature measurements. Consequently, employing multiple TLC coatings, each with a distinct and narrow colour play range, becomes a desirable practice. Each type of TLC coating becomes optically active at a different temperature, expanding the range of measurable temperatures while keeping high temperature measurement accuracy.

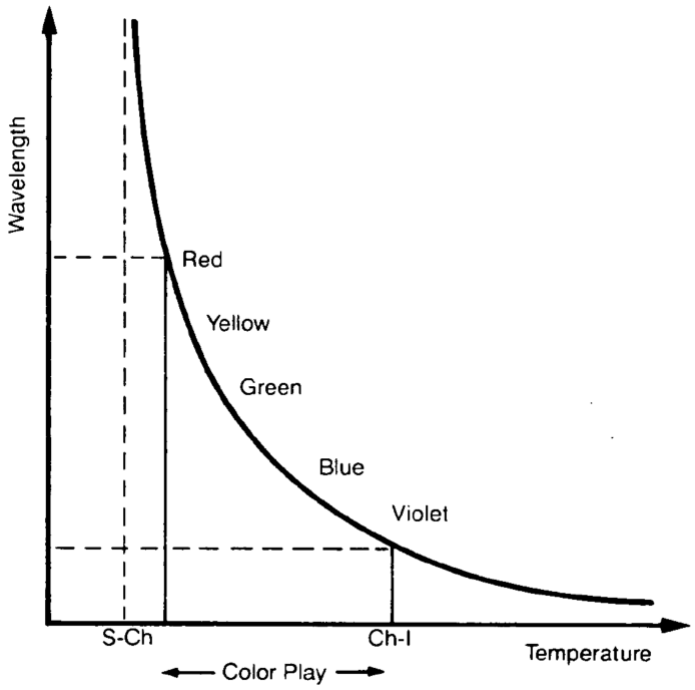

Figure 2.4: Diagram of colour response with temperature for temperature sensitive liquid crystals [61].

Ireland and Jones [56] quantified the response time of an encapsulated liquid crystal device when subjected to a linearly increasing surface temperature. In this experiment, a thin aluminium foil, coated with a 10 µm thick layer of TLCs, underwent rapid heating through an electrical current, employing temperature increase rates of up to 2600 °C/s. The determined delay between the moment the surface reached the steady-state colour display temperature and the actual onset of the colour display was approximately 3 ms. This temporal lag was found to be insensitive to the the rate at which the surface temperature rose. However, the researchers emphasised that at higher rates of temperature increase, this constant temporal lag led to a more substantial error in temperature readings: they concluded that if the temperature difference across the film is significant enough to result in only a small portion of the film being at the colour display temperature, the light received at the photodiode would be diminished. Furthermore, the authors observed a reduction in the intensity of the colour play at higher heating rates.

A similar problem arises when the TLCs layer is subjected to high heat fluxes, requiring consideration related to the maximum heat flux that maintain accurate surface temperature measurements. The minimum thickness of a TLCs layer is constrained by the capsule diameter, and per findings by Ireland and Jones [26], a 20 µm layer typically exhibits a thermal conductivity of $0.2\,\mathrm{W\,m^{-1}\,K}$. For a heat flux of $2 \times 10^4\,\mathrm{W\,m^{-2}}$, a temperature drop of 2 °C across the layer is anticipated. The authors recommended not to exceed this specified heat flux, as exceeding it may result in a significant difference between the average crystal temperature and the actual surface temperature.

Both the response time delay and the maximum heat flux, limit the use of TLCs in wind tunnel tests where an appreciable temperature difference across the layer is expected.

2.4 Review of Heat Transfer Instrumentation
Infrared Thermography

Infrared (IR) thermography is a powerful tool in turbomachinery research, since it allows for measurements with high spatial resolution under both transient and steady conditions. Moreover, being a non-intrusive techniques, it is a particularly interesting option for measurements on rotating targets. Nevertheless, its working principles need to be clearly understood to achieve high accuracy measurements. In the following sections, the theory of infrared thermography is presented and the possible sources of error are discussed. Finally, methods to calibrate IR cameras and the results for gas turbine applications are reviewed.

2.4.1 Theory of Thermal Radiation Heat Transfer

The goal of radiation thermometry is to relate spectral radiance to thermodynamic temperature. This is possible because temperature causes excitation of the electrons bound to the atoms and molecules of the material, whose movement results in energy emitted in form of electromagnetic radiation.

The energy of the emitted radiation can be expressed as $E = hc/\lambda$, where h is Planck's constant, c is the speed of light and λ is the radiation wavelength [63]. From this relationship, it is possible to observe that the emitted energy per photon is inversely proportional to the wavelength.

The concept of a blackbody plays an important role in radiation theory. A blackbody is an idealised body that absorbs and emits all incident radiation. In other words a blackbody is a perfect absorber and emitter [49]. The electromagnetic radiation emitted by a blackbody is a function of temperature and wavelength, and as described by *Planck's law*, visually presented in Figure 2.5

$$E_{\lambda,bb}(\lambda, T) = \frac{c_1}{\lambda^5(e^{\frac{c_2}{\lambda T}} - 1)} \tag{2.10}$$

where E is the power emitted per unit area per unit wavelength ($Wm^{-2}\mu m^{-1}$), $c_1 = 2\pi hc^2$ and $c_2 = hc/k$ are the first and second radiation constants, h and k are the Planck's and Boltzmann's constant respectively, and T is the absolute temperature of the blackbody in Kelvin.

By integrating Equation 2.10 across all wavelengths (from 0 to ∞), the *Stefan-Boltzmann law* is obtained. This gives the total hemispherical radiant intensity of a blackbody at a given temperature T_{bb}

$$E_{bb} = \sigma T_{bb}^4 \tag{2.11}$$

where σ is the *Stefan-Boltzmann* constant.

Infrared thermography measures the spectrum of radiation emitted from a body to infer its temperature by mean of Equation 2.10. The wavelength at which the radiant intensity is maximised is calculated by differentiating the *Planck's law* in Equation 2.10 with respect to λ, obtaining *Wien's law*: $\lambda_{peak} = 0.0029/T$. Equation 2.10 is plotted in Figure 2.5 for a range of temperatures. The two wavelength

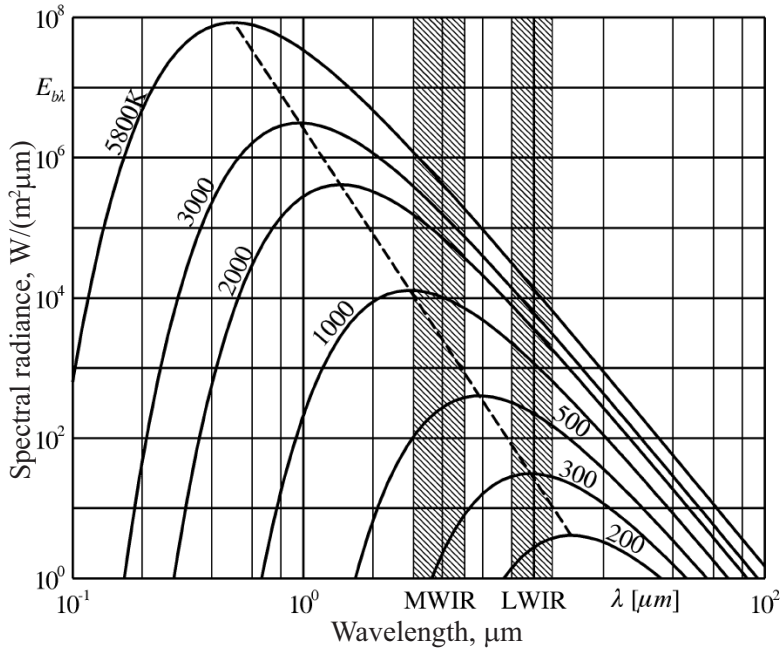

Figure 2.5: Blackbody emissive power for a range of absolute temperatures as a function of wavelength [64]

bands most commonly used in IR thermography detectors, mid-wave IR (MWIR, 3 µm - 5 µm) and long-wave IR (LWIR, 7 µm - 12 µm), are also shown. It can be observed that there is an inverse relation between the temperature and the wavelength of the emission peak. The law shows that the emission peak tends to shorter wavelengths with increasing temperatures.

In reality, materials do not behave as blackbodies and the above laws are less applicable. Their radiative properties are described relative to the blackbody, and particular attention must be paid to these to obtain accurate IR measurements.

The spectral emissivity 'ε' is defined as the ratio of the spectral radiance of the real body L_λ and the blackbody $L_{\lambda,bb}$ at the same temperature, in real bodies this is a function of wavelength λ, temperature and observation angle θ

$$\varepsilon(\lambda, T, \theta) = \frac{L_\lambda}{L_{\lambda,bb}}. \tag{2.12}$$

In a way, the emissivity can be seen as a parameter indicating the efficiency of a real body to emit compared to an ideal blackbody.

In real bodies, a fraction 'α' of the total incident energy is absorbed (absorptance), a fraction 'ρ' is reflected from the body (reflectance) and the rest passes through 'τ' (transmittance). These contributions are described by the following energy balance

$$\alpha + \rho + \tau = 1 \tag{2.13}$$

Kirchhoff's law states that the absorptivity coefficient is equal to the emissivity coefficient, i.e. $\alpha = \varepsilon$ [49]. Thus, for a non-transparent body ($\tau = 0$), as the target of the experiment could be considered, the energy balance in Equation 2.13 reduces to:

$$\varepsilon + \rho = 1 \tag{2.14}$$

This expression outlines that in order to reduce the errors due to reflection when using IR thermography, it is important to know the value of the target emissivity and

to increase it. However, being a function not only of temperature, but also observation angle θ and the material properties, including surface roughness, estimating the emissivity is not always an easy task.

Finally, the components interposed between the target and the detector, known as the optical path, affect the measurement because they interact with the radiation emitted by the target. Therefore, the transmittance and absorptance of the gases and windows have to be carefully evaluated.

In conclusion, the primary sources of error in infrared thermography arise from the assessment of target emissivity and reflectivity, as well as from the absorption of radiation before it reaches the detector. These aspects are discussed in detail in the following subsections.

2.4.1.1 Emissivity of the Target

In real bodies, ε is smaller than one and is not only a function of material properties, but also of temperature and observation angle θ [65]. Metals, which are often used in gas turbine tests, have a low emissivity and reflect a large amount of the surrounding radiance. The emitted radiance of metals increases at higher angles of incidence, and is smallest in the normal direction to the surface. The state of the component surface, for example the level of oxidation or whether a thermal barrier coating is applied [66], can change the emissivity considerably. Thus, when using an IR measurement system it is recommended to cover the parts with a very thin layer of high emissivity paint (emissivity typically between 0.93 and 0.97 [67]).

The emissivity dependence on the observation angle θ [65], conventionally measured in such a way that at 0-deg the target surface is perpendicular to the observer (detector), is known as directional emissivity and it is a function of materials properties. Only black and gray bodies emit in accordance with *Lambert's law*, which states that the emissivity is not dependent on the observation angle [63].

Previous studies have demonstrated that the variation of the emissivity is negligible in a observation angle range between 0-deg and 55-deg, and that in this range objects can be treated as Lambertian bodies. Hence, the IR camera should be positioned to keep the viewing angle within this range. When this is not possible and the viewing angle exceeds 55-deg, a calibration to account for the directional emissivity $\varepsilon(\theta)$ is required.

Referencing ISO 18434-1 [68], the general procedures to calculate the emissivity are the contact method and the reference emissivity material method. The former requires measuring the temperature of one point on the target with a contact thermometer and using this value to adjust the emissivity on the camera until the reading from the camera matches the one from the thermometer. The latter is performed in two steps. Firstly, a surface of known emissivity is applied on the target, and this emissivity is entered in the camera settings and the surface temperature recorded. Subsequently, the camera is used to measure the temperature of the target in the same conditions but without the surface-modifying material substrate. The emissivity setting in the camera is then adjusted until the temperature measured in the second step matches the first one.

2.4.1.2 Reflectivity of the Target

According to Equation 2.14, the lower the target emissivity, the higher its reflectivity. When performing IR thermography measurements, the radiation emitted by neighbouring surfaces reaches the detector after being reflected by the target surface. The target in a turbine test facility is typically surrounded by a very high temperature region, thus the errors associated with the radiation of the surroundings are not negligible. A number of past studies focused on the problem of environmental reflected radiation, which for some cases was up to 70% of the radiation reaching the detector [69, 70]. Calculating this source of error is not straightforward. Temperature distributions of the numerous surfaces are not isothermal, and the calculation of view

factors between the different objects is not trivial. The IR detector cannot distinguish between the radiation emitted by the target and the parasitic radiation that is reflected from the target but comes from the surroundings rather than the target itself. Therefore, it is imperative to set up the experiments in a way that minimises the reflected radiation and carefully estimates via calibration the amount of radiation that still reaches the detector.

Similarly to emissivity estimation, there are two common methods to measure the reflected apparent temperature: the reflector method and the direct method [68]. The former is performed by placing an infrared reflector, such as a metallic coating or an aluminium foil, in the camera field-of-view and by assuming zero distance and $\varepsilon = 1$, i.e. that the body behaves like a blackbody. The reflector temperature is then measured and considered as the reflected temperature. The direct method involves assuming $\varepsilon = 1$ and estimating the angle of reflection and of incidence with the camera at the desired location. The camera is then positioned such that it views only the sources reflected by the target. The apparent temperature of these sources is measured and considered to be the reflected temperature. For greater accuracy, the measurement can be repeated and averaged.

2.4.1.3 Absorption/Transmission of the Optical Path

The optical path (i.e. everything that is interposed between the target of the measurement and the detector) interacts with the radiation coming from the target by partially absorbing and partially transmitting it. There may also be further sources of radiation between the source and the detector. The nature of the optical path depends on the specific experimental set up, but in most turbomachinery applications is composed of gas and an IR-transparent window.

As transmittance quantifies the degree to which a medium permits the passage of radiation, a perfectly transparent medium (transmittance of 1 or 100%) would be the ideal scenario for IR measurements.

Transmission through the gas depends mainly on what is not scattered or absorbed by the gas, which varies with gas composition and temperature. For instance, the transmission spectrum of the atmosphere with a 40% of humidity, presented in Figure 2.6, highlights two main transmission regions in the long-wave ($7 - 14\,\mu m$) and mid-wave ($3 - 5\,\mu m$) infrared ranges. This behaviour of the atmosphere also explains the adoption of LWIR and MWIR bands in the development of IR detectors.

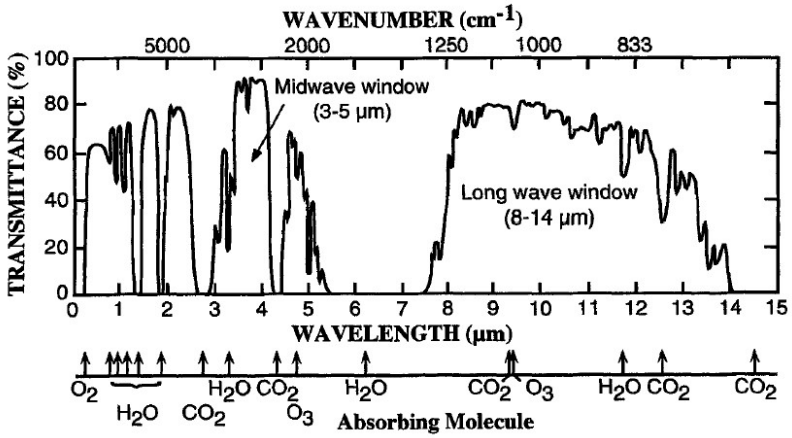

Figure 2.6: Infrared transmission spectrum of the atmosphere at Sea Level with 40% relative humidity along a 1.8 km horizontal path. Data from [71].

In the turbine stages of a jet engine the combustion gas consists of N_2, CO_2, H_2O, trace of CO, NO, SO_2, O_2 plus dust and un-burned particles [72, 73]. These can cause reflection and scattering phenomena that can occur at different wavelengths and temperatures.

Generally, monoatomic and diatomic gases such as O_2, CO, H_2, NO, N_2 exhibit minimal absorption due to the symmetrical configuration of their diatomic structure, which renders them transparent to infrared radiation. Conversely, Infrared 'opacity' comes from absorption bands of molecules such as H_2O, CO_2, CH_4 due to their asymmetric triatomic structure. A high composition of these molecules in the atmosphere will affect the results of infrared temperature measurements [74]. In literature, the most widely adopted technique to reduce the influence of the gas is to select a spectral range where there are no absorption bands, such that the gas is "transparent" (little

or no absorption) [75, 76], and to apply a filter to restrict the working wavelength of the camera [77, 78]. However, it is very difficult to select a spectral region that completely avoids the absorption of gases, and a proper calibration to compensate for these effects should be performed. The comprehensive High-Resolution Transmission Molecular Absorption Database (HITRAN) [79], can be a useful tool to simulate and predict radiation transmission and emission of specific gas compositions. The absorption of all components of the test gas should be considered, however, in most cases the main absorption of the radiation by the atmosphere is due to water vapour and CO_2. As a consequence, given the test gas in the OTRF is composed of dry air, it can be assumed that this has a transmittance equal to 1.

The second component to consider to quantify the transmission of the optical path is the optical window. In gas turbine experiments, IR transparent windows are usually used to gain optical access to the test components, adding a layer along the optical path between the target and the detector. The most adopted glasses in the field of gas turbines are germanium (Ge, which is recommended for use below 100° [80]), zinc sulphide (ZnS) and zinc selenide (ZnSe), the latter being more suitable for higher temperatures. Additionally, the windows usually require surface treatment, such as coatings to reduce back reflection, absorption and ghost image formations. This leads to more efficient transmissive optics and thus improved images [81].

To summarise, calibration is necessary to account for all these sources of error and acquire accurate IR thermography measurements. The existing calibration techniques are reviewed below.

2.4.2 Infrared Thermography Calibration Techniques

Falsetti et al. [30] presented a comprehensive review of calibration methods for IR thermography in turbomachinery applications. In the study, the authors sought to elucidate the impact of error sources on pyrometers and IR thermography measure-

ment accuracy. The primary objective of this section is to present the key findings of the cited study [30] relative to calibration procedures for IR thermography used in turbomachinery applications.

A sketch of a turbomachinery IR thermography system, which highlights the different radiation contributions captured by the IR detector, is shown in Figure 2.7.

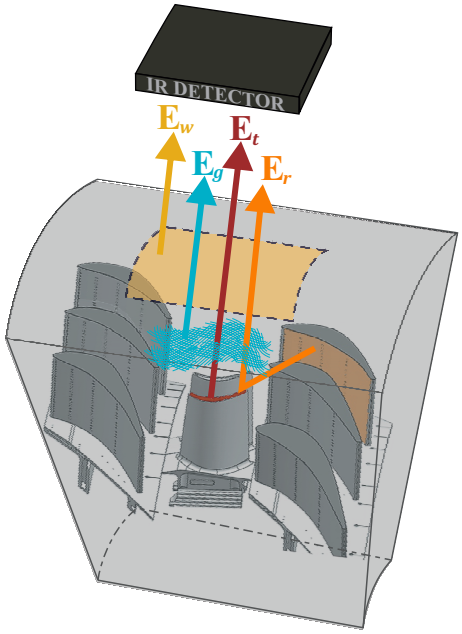

Figure 2.7: Sketch of an IR thermography system in a section of a 1.5 turbine stage (vanes, blades, vanes). The blade tip, highlighted in red, is the target of the measurement; the IR-transparent window is highlighted in yellow, the surroundings in orange, and the combustion gases are symbolized by a blue cloud. Figure from [30].

As outlined in the previous section, the radiation emitted by the target is not directly a measurement of its temperature due to non unitary emissivity ε. In addition, surroundings and optical path offset the radiation reaching the detector. Hence, the total radiation reaching the detector E_{tot} can be expressed as the sum of the radiation emitted by the target that is transmitted by the optical path $\tau_{opt}\varepsilon_t E_t$, and a certain amount of disturbance radiation E_{offset}

$$E_{tot} = \tau_{opt}\varepsilon_t E_t + E_{offset} \tag{2.15}$$

To obtain the target radiation, the target emissivity ε_t and the optical path transmittance τ_{opt} need to be determined, and to reduce the error in the measurement, the disturbance radiation E_{offset} needs to be determined and minimised or corrected.

The disturbance radiation is the sum of: i) the *radiation emitted by the surroundings* E_s, which is first reflected on the target surface due to its reflectivity $(1-\varepsilon_t)$ and then attenuated by the optical path transmittance τ_{opt}; ii) the *radiation emitted by the optical path*, which is in turn the sum of the radiation emitted by the combustion gases E_g, and the radiation emitted by the IR-transparent window E_w

$$E_{offset} = \tau_{opt}(1-\varepsilon_t)E_s + (1-\tau)E_{opt} \tag{2.16}$$

Thus, by assuming that i) the test surface is opaque and has a constant spectral emissivity ε_t, and ii) defining an effective optical path transmittance τ_{opt}, the total measured radiation can be rewritten as follows:

$$E_{tot} = \tau_{opt}\varepsilon_t E_t + \tau_{opt}(1-\varepsilon_t)E_s + (1-\tau_{opt})E_{opt} \tag{2.17}$$

This equation shows the contribution of the three main sources of error outlined in the previous section. It is essential for the calibration procedure to consider all these elements.

Calibrating an IR thermography system in order to obtain quantitative results has been a topic of discussion since 1996. Usually performed in situ, these calibration methods made use of thermocouples embedded onto the test surface. Reading from the thermocouples were used as a reference and a linear correlation was fitted to the data and compared for both the thermocouples and the IR detector; the main studies are reviewed below. Based on the pioneer study on liner-cooling designs for gas turbine combustors conducted by Meyers et al. [82], Martiny et al. [83] defined a correction procedure based on a semi-empirical equation for Planck's Law (see Equation 2.10) with a so called 'thermal value' I to represent the radiation measured by the detector

and three calibration coefficients r, b and f:

$$I = \frac{r}{e^{b/T} - f} \tag{2.18}$$

The calibration coefficients were determined in situ, as best-fit approximation between the reading from the IR detector and the object temperature. The reference temperatures from thermocouples embedded at various locations 'i' in the test surface, T_i, were recorded at the same time as the IR thermal image and under steady state conditions. The difference, X_i, between the reference temperature and the temperature derived from the IR image rearranging Equation 2.18 was computed:

$$X_i = T_i - \frac{b}{ln(\frac{r}{I_i} + f)} \tag{2.19}$$

Imposing the minimisation of the variance of X_i, a system of three non-linear equations for r, b and f was obtained and solved using the Levenberg-Marquardt method [84]. The calibration coefficients were then used to calculate the final corrected temperature field rearranging Equation 2.18. Schulz [85] applied the in situ calibration described in [83] to investigate film cooling on gas turbine components. The author pointed out that the location of the reference thermocouples on the test surface needs to be carefully evaluated. In order to ensure high accuracy, only the thermocouples located in a uniform temperature gradient area were used for the procedure. With this approach, the author succeeded in reducing the differences between reference temperatures and uncorrected infrared image data to 0.41 K.

Despite having been successfully used in several studies, the in situ calibration proposed in [83, 85] has a flaw: it is only accurate within the temperature range covered by the thermocouples. As a result, it is necessary to have enough thermocouples to cover the entire temperature range of interest, which is not always known a priori, which could lead to the instance of having to rely on extrapolated values of temperature. Furthermore, in high heat flux region thermocouples could fail to give reliable values. This limitation is particularly challenging in turbomachinery applications,

where heat flux gradients can be high and not known a priori, making it difficult to cover the entire range of temperature with thermocouple measurements. Moreover, in the studies by Martiny et al. [83] and Schultz [85] the transmittivity of the window was not taken into consideration.

Ochs et al.'s [86] novel calibration method tried to address the drawbacks in [83, 85] proposing a semi in situ calibration method to estimate r, b, f and a new coefficient I_{offset}. This new parameter allowed to take into account the signals of the hot gas, the hot window, the camera optics and the surrounding reflections that reach the IR detector, as illustrated in Figure 2.8.

The four calibration parameters r_{pre}, b_{pre}, f_{pre}, and $I_{offset,pre}$ were estimated prior to testing during an offline calibration performed at ambient temperature and the object temperature calculated as follows

$$T_{obj} = \frac{b_{pre}}{ln(\frac{r_{pre}}{I_{tot}-I_{offset,pre}} + f_{pre})} \tag{2.20}$$

The test surface was heated to cover the temperature range of interest, and a single thermocouple was used for this stage. The reference thermocouple and the detector signal were recorded at steady state conditions.

The second stage of the calibration consisted of an in situ calibration. This studied the effect of the optical setup on the total spectral transmissivity when the temperature of the entire system was raised. Among the four calibration parameters, I_{offset} always increased with temperature, hence it was always recalibrated in situ, while the other parameters depended on the total spectral transmissivity τ.

In particular, the authors identified three possible scenarios: i) if $\tau = const$, only $I_{offset,insitu}$ needs to be re-calibrated; ii) if $\tau = f(T)$, r_{pre}, b_{pre}, and f_{pre} are just scaled by a constant that has to be evaluated together with I_{offset} ; iii) if $\tau = f(T, \lambda)$, all the four calibration parameters require re-calibration. Using this modified method, the maximum error in the temperature readings was reduced from 12% [83] to 1.2% over the temperature span tested.

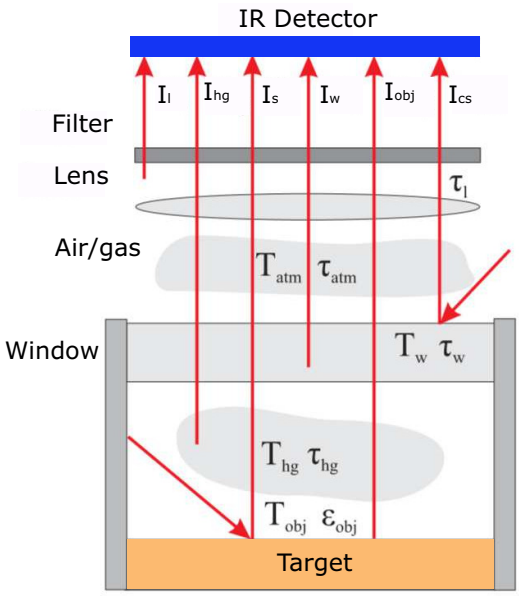

Figure 2.8: Schematic representation of the signal detected by the camera in a typical turbomachinery experiment setup [86]. The signal received by the detector is the sum of the signal emitted by the object and a disturbance signal. The disturbance signal is the sum of the radiation emitted by both the hot internal and the cold external surroundings (I_{hs}, I_{cs}) and the radiation emitted by the hot gas (I_{hg}), the hot window (I_w), the camera lenses (I_l), and the cold air.

The calibration procedures presented above has been adopted by many studies in turbomachinery research [87, 88, 89, 90, 91]. Almost all linearly correlate the values measured by embedded reference sensors (usually thermocouples) with those obtained by the IR detector. The effects of the surrounding reflections are weakened by averaging a number of thermograms at different times or by using high-emissivity paint. The target emissivity is usually evaluated by the contact method [68],but it does not take into account the viewing angle effect. Comparatively, few studies developed novel IR calibration procedures and advanced image processing techniques that resulted in higher measurement accuracy. These are reviewed below.

Morris et al. [92] presented a study focusing on the uncertainties of IR measurements for a turbofan engine on an altitude test. Differently from the previous studies, the authors experimentally characterised the IR transparent window using a SR-5000 spectroradiometer at two long wave IR bands. The transmittance, the reflectance

and the emissivity of the ZnSe window, used to shield the camera from the vibration and the heat sources, was calculated. The results showed that the window emittance is temperature invariant in a range between 20°C and 100°C. To maximise the transmittance and minimise the radiation reflected by the camera enclosure, the authors suggested to maintain the window parallel to the engine plane. In addition, a MATLAB radiometric model was developed to quantify the radiation from both the engine and the stray radiation sources, such as the exhaust collector, the window, the atmosphere and the camera enclosure. Forty thermocouples measurements were used to compare and validate the model.

Laveau et al. [93, 94], in their investigations into the impact of endwall contouring on the thermal loads in the first vane passage of a rotating turbine rig, presented an advanced method to position the camera and enhance its field-of-view (FOV) to reconstruct a real image from the infrared thermograms. In order to gain a map of the complete passage, the camera was traversed by a six axis robot arm and positioned in 38 different locations during the test. Four optical accesses were created using zinc selenide windows, coated on both sides with an anti-reflective coating in the same wavelength range of the camera to ensure a transmittance of 96%. Reference silver dots were distributed over the target and were used to create a correspondence between the dot location in the IR image and its real location. Using a single value decomposition method, a transformation matrix was obtained to link any point in the scene and its location in the infrared image. This allowed to calculate a high-resolution (20k points every 0.4 mm) two-dimensional heat transfer quantities, such as the Nusselt number and the uncertainty distribution of the adiabatic temperature on the vane surface, depicted in Figure 2.9. The uncertainty varied from 0.6 K downstream to 1.1 K at the inlet of the passage, while it was equal to $\pm\,0.3$ K for the wall temperature, thus $\pm 1\,\%$.

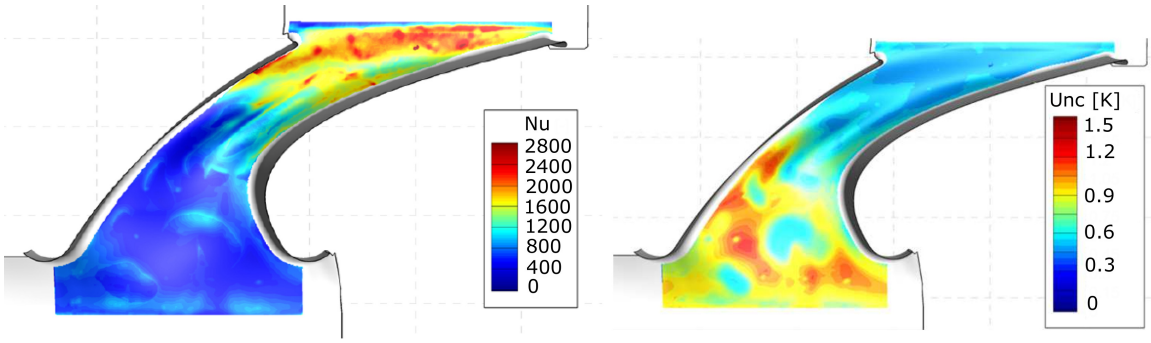

Figure 2.9: Nusselt number and uncertainty in adiabatic wall temperature distributions on the vane endwall obtained by Leveau et al. [94] using IR Thermography. The scales have been slightly modified to make them readable. The uncertainty was calculated using using the GUM Workbench software [95].

Kirollos [96] developed a two phase calibration, consisting of a blackbody calibration following by a greybody calibration. The former is done in isothermal conditions using a cavity or a hot surface with high emissivity, and the aim is to determine the coefficients a and b that appear in the equation relating the incident IR radiance $q_{cam}(x)$ in the spectral band of the camera to the pixel raw digital count $R(x)$, as follows

$$q_{cam}(x) = \sigma T_{bb}^4(x) = aR(x) + b; \tag{2.21}$$

Generally, the coefficients a and b are constant over the entire focal plane array for a specific camera and their values are provided by the manufacturer. Nevertheless, Kirollos re-calibrated them in situ using an isothermal cavity heated up to 65°C, finding a difference of 0.3 K [96] from the factory calibration. During the greybody calibration, the transmittance τ, the emissivity ε, the temperature of the surroundings T_s, and the temperature of the optical path T_{opt} were determine. The author defined a correction parameter, the *surrounding radiance* $q^*(t)$, which corresponds to the disturbance signal made of the last two terms of the summation in Equation 2.17. Furthermore, the author used the *Stefan-Boltzmann* equation (Equation 2.11) to write the radiance in terms of temperature, obtaining

$$T_{bb}^4(x,t) = \tau\varepsilon(x,\theta)T_t^4(x,t) + \tau(1-\varepsilon(x,\theta))T_s^4(x,t) + (1-\tau)T_{opt}^4(t) \tag{2.22}$$

where T_{bb} is the equivalent blackbody temperature and T_t is the target temperature.

The author assumed emissivity ε constant over the target surface and independent of camera observation angle such that $\varepsilon(x,\theta) \approx \varepsilon$, the *surrounding radiance* was then defined as

$$q^*(t) = \frac{\sigma\tau(1-\varepsilon)T_s^4(x,t) - \sigma(1-\tau)T_{opt}^4(t)}{1-\tau\varepsilon} \tag{2.23}$$

The greybody calibration was performed using a surrogate radiance correction vane that was first heated up to 65 °C using a water bath and then quickly placed in the test facility. The surrounding radiance $q^*(t)$, was measured during each run as the difference between the vane temperature T_t, measured with two embedded thermocouples during the cooling down, and the blackbody temperature T_{bb}, recorded by the IR camera at locations near the thermocouples

$$q^*(t) = \frac{\sigma T_{bb}^4(x,t) - \sigma\tau\varepsilon T_t^4(x,t)}{1-\tau\varepsilon} \tag{2.24}$$

The product $\tau \cdot \varepsilon$ was calculated by solving Equation 2.22. The temperature of the surroundings is often assumed to be uniform or equal to the atmospheric temperature to simplify the problem [97]. Kirollos also applied this assumption, considering everything but the vane at ambient temperature, then, considering unity air transmittance such that $\tau_{air} = 1$, the product $\tau \cdot \varepsilon$ was calculated as follows

$$\tau \cdot \varepsilon = \frac{T_{bb}^4 - T_{amb}^4}{T_{TC}^4 - T_{amb}^4} \tag{2.25}$$

The product was found to be approximately constant over the tested range of temperatures, thus the mean values of $\tau \cdot \varepsilon$ for the vane pressure and suction sides were adopted for the analysis.

The surrounding radiance $q^*(t)$ measured during the greybody calibration was used to evaluate the target temperature of interest as follows

$$T_t^*(x,t) = \sqrt[4]{\frac{\sigma T_{bb}^4(x,t) - (1-\tau\varepsilon)q^*(t)}{\sigma\tau\varepsilon}} \tag{2.26}$$

In a later study, Kirollos and Povey [98] described a new method to calibrate an IR system when the assumptions of spatially constant emissivity and spatially constant surroundings radiation cannot be considered valid. This method applied a reflective marker array (RMA) on the target surface and an advanced image analysis to estimate the surroundings temperature $T_s(x)$, and the emissivity $\varepsilon(\theta)$. The markers were 3 mm diameter circles of aluminium foil tape taped on a high emissivity paint as depicted in Figure 2.10a, while the ray diagram to explain the RMA method is shown in Figure 2.10b. The method implies ignoring atmospheric effects and solving Equation 2.22 for the markers and paint of differing emissivity, obtaining a set of two equations in two unknowns, T_t and T_s, as

$$T_t^4(x) = \frac{1-\varepsilon_2(x)}{\varepsilon_1(x)-\varepsilon_2(x)} T_{bb,1}^4(x) - \frac{1-\varepsilon_1(x)}{\varepsilon_1(x)-\varepsilon_2(x)} T_{bb,2}^4(x) \tag{2.27}$$

$$T_s^4(x) = \frac{\varepsilon_1(x)}{\varepsilon_1(x)-\varepsilon_2(x)} T_{bb,2}^4(x) - \frac{\varepsilon_2(x)}{\varepsilon_1(x)-\varepsilon_2(x)} T_{bb,1}^4(x) \tag{2.28}$$

where the $T_{bb,1}$ and $T_{bb,2}$ are the temperatures recorded by the camera for the paint and markers, respectively, and ε_1 and ε_2 their emissivities. The RMA method was successfully demonstrated, reducing the maximum error in the temperature from 6°C to 1.5°C in the test range of 38°C to 56°C. Thus the error was reduced from 2.8 % to 3.9 %.

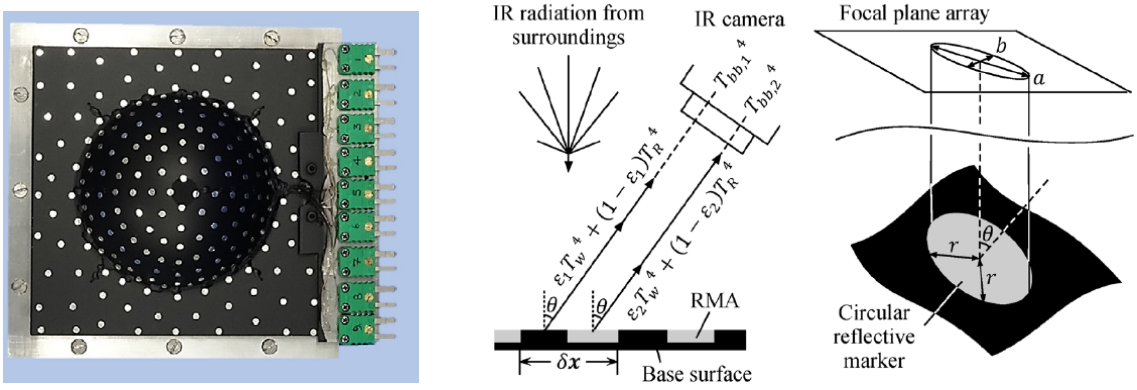

Figure 2.10: Reflective markers array study, showing (a) front view of the test piece and (b) ray diagram [98].

IR thermography was employed by Elfner et al. [99, 100] to assess rotor blade cooling effectiveness. The authors presented an advanced image processing algorithm that achieves 3D resolution by combining images at different focus using genetic optimisers, and improved the in situ calibration method of [86] to account for the change in conditions between the calibration and the actual experiments.

As in [86], the IR camera calibration was developed in two steps. Firstly, a pre-calibration to relate the radiation power and the surface temperature as in Equation 2.18 [83] was performed. Subsequently, an improved in situ calibration was performed with a calibration blade manufactured from copper and instrumented with four reference thermocouples, a linear interpolation between the four measurements was performed to obtain a temperature distribution along the blade surface.

Correction for directional emissivity was achieved with a custom bidirectional reflectance function (BRDF), suitable if the wavelength and the surface roughness have the same order of magnitude, as suggested by the study of Wen et al. [101]

$$\varepsilon(\theta) = 1 - \left(C_0 \frac{\pi}{cos(C_1\theta)} + C_2 \right) \tag{2.29}$$

where C_0, C_1, C_2 are the BRDF coefficients. The detector radiation was then corrected with $\varepsilon(\theta)$ using a linear relation: $I_D = I_{D,pre}(\theta) \cdot \varepsilon(\theta)^{-1}$.

Results showed that the maximum uncertainty on a flat surface was $\pm\,0.3$ K. The residual uncertainty for the angular dependency of emissivity was equal to $\pm\,0.67$ K at angles of view lower than 50-deg, while it increased up to $\pm\,3.19$ K at angles of 70-deg. The results confirmed what previous studies concluded about the negligible influence of observation angles below 55-deg. Results in [100] showed that the mean relative error in total cooling effectiveness was reduced from 11% to 2.4%.

Further improvements in the calibration method accounting for local variation of reflected radiation were made in a following study by the same lead author [102]. Following the approach developed by of Ochs et al. [86], they individuated the offset

radiance I_{offset} as the main source of error and they identified it with the radiation emitted by the high temperature surroundings and reflected by the target. They pointed out that in certain setups the spatial variation of I_{offset} has to be taken into consideration by the calibration procedure. To do so, they defined a non-dimensional correction field, $C = f(\overrightarrow{x})$, representing the magnitude of I_{offset}. The correction factor was computed as the sum of three irradiances:

$$C_i = \rho_{i,j}(\varepsilon T^4)_t + \tau_{i,j}(\varepsilon T^4)_{atm} + (\varepsilon T^4)_w \tag{2.30}$$

The mean value of C_i was computed at each surface location, yielding to a scalar field of correction factors, as illustrated in Figure 2.11. The corrector was then included into the calibration equation (see Equation 2.18):

$$T_t = \frac{b}{ln(\frac{r}{I_{tot} - C \cdot I_{offset}} + f)} \tag{2.31}$$

The uncertainty in the surface temperature reduced from 8% to approximately 2% at a test temperature of 350 K.

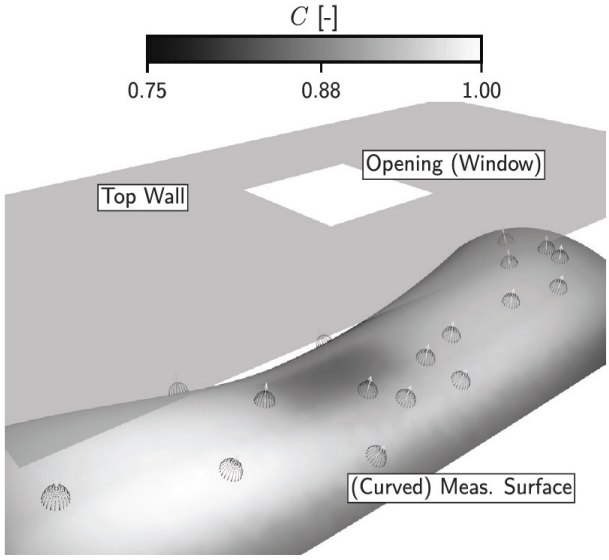

Figure 2.11: Example of the offset radiance distribution using the correction field C, which varies from 0 to 1. The presence of the window in the top wall can influence the offset radiance [102].

Aberle et al. [103] used IR thermography for heat transfer measurements on a linear cascade in a low-speed wind tunnel. As part of this work, the authors developed a calibration method to account for the angular dependency of the emissivity, the influence of the surroundings and of the IR transparent window. The process involved two in situ calibrations, global and local versions. In the global calibration, a regression of the measured IR intensities in an area close to the sensor over a range of temperatures was applied as in [85]. Instead of relying on the global calibration, an additional local calibration was performed using FEM simulations to determine the temperature distribution of the blade. It was termed local calibration since a separate regression for each mesh node was performed. The results of the simulations were validated against the reference measurements and to a high resolution temperature map of the blade. The accuracy on the temperature was equal to ± 1.5 K. The method aimed at improving the basic calibration performed with few reference sensors embedded in the target surface. It also provided an alternative solution when it is not possible to build a calibration facility reproducing the real experimental conditions in terms of target geometry and emissivity, surroundings reflections and optics transmissivity.

The majority of the past works performed in situ calibrations relying on reference sensors (usually thermocouples) embedded or attached to the target surface. As the study of Michaud et al. [104] revealed, the calibration arrangements, such as the thickness and the thermal conductivity of the paint or adhesive used to install the thermocouples, can affect the accuracy of the surface temperature measurements. The authors newly accounted for the effect of paint and adhesive layers on the thermocouple measurements accuracy, in particular for cases when there are large temperature gradients. The results showed that an increment in the paint thickness, as well as a decrease in the paint's thermal conductivity lead to an increase in the absolute magnitude of the error. As a solution, a new technique to install the reference thermocouple for in situ calibrations was proposed: bond the sensor with a disk copper and a

polymide film, and then paint it with a mat black paint, as illustrated in Figure 2.12. Using this configuration, the temperature difference between the thermocouple junction and the surface IR measurement reduced, leading to a more isothermal region in the field-of-view of the camera. Additionally, this configuration helped to protect the junction from the testing environment.

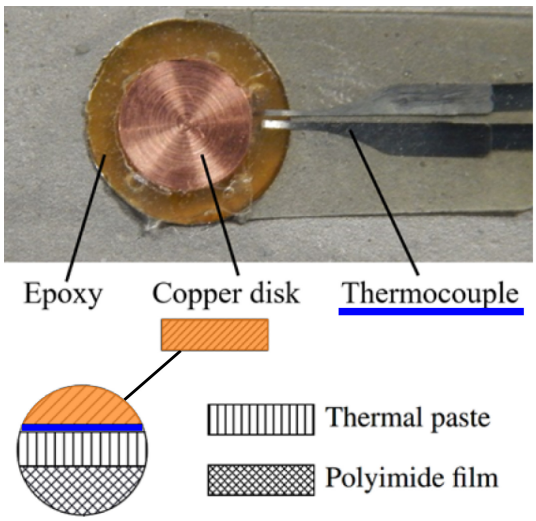

Figure 2.12: Photograph and cross-section of the thermocouple installation to reduce the instrumentation induced error, as proposed by Michaud et al. [104].

2.4.3 Turbine Heat Transfer Studies using Infrared Thermography in Engine Scale Rotating Facilities

The use of infrared thermography in high-speed rotating rigs, such as turbine rigs reaching speeds of around 10000 rpm, remains an uncommon practice. As outlined in the previous section, in situ calibration is still common practice for IR thermography experiment, however, gas turbine experimental environment presents challenges that impede the execution of these calibrations. The complex geometry and test conditions not only limit viewing access, but also complicate the temperature control essential for calibration procedures. Moreover, the high speed involved introduce the complication of motion blur, making the application of IR thermography demanding. Notably, only three research groups have contributed to the study of this area, with publications

from Lazzi Gazzini et al. [105] at the ETH Zurich, Christensen et al. [106] at the Ohio State University, and Knisely et al. [107, 108] at the PennState University.

In their study, Lazzi Gazzini et al. [105] employed IR thermography to investigate the rotor endwalls of the turbine in the long duration LISA facility, with rotor speed of 2700 rpm using a FLIR SC7300L camera. The measurement setup used is depicted in Figure 2.13.

To mitigate motion blur, the authors merged two pairs of images captured at consistent conditions but with different integration times, specifically 10 µs and 50 µs. The short integration time produces a sharper image but with higher noise level, while the longer integration time supplies a more accurate temperature level but with a higher motion blur. Their approach involved a trade-off between image sharpness and noise level, which was addressed through the application of a blind deblurring algorithm, followed by a frequency study to identify and eliminate artifacts. An overview of the image processing main steps is given in Figure 2.13b. Despite the significance of [105], which marks the first published study on IR thermography applied to the rotating frame of an engine-scale turbine rig, it is noteworthy that the facility involved operated at low speeds.

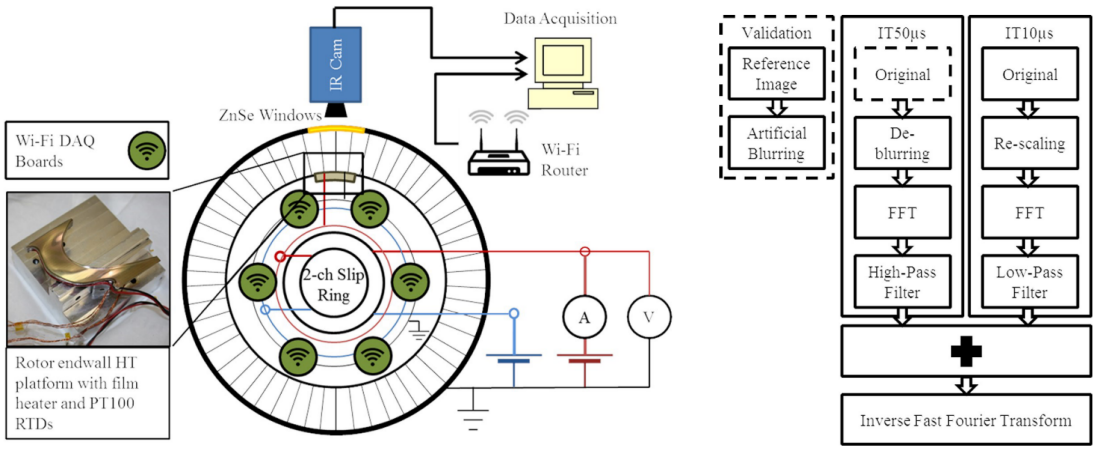

(a) (b)

Figure 2.13: Schematic of the (a) heat transfer measurement setup and (b) the image reconstruction procedure employed by Lazzi Gazzini et al. [105].

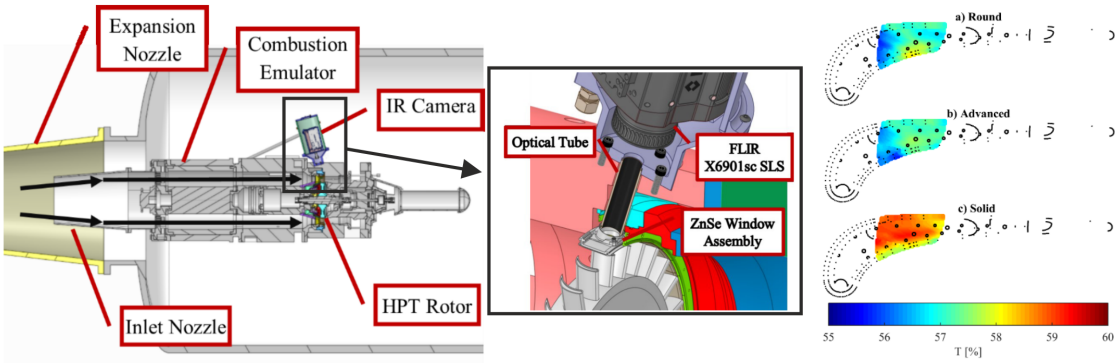

(a) (b)

Figure 2.14: Results from the Ohio State University IR thermography study by Christensen et al. [106] showing (a) the experiment setup and (b) target temperature as a percent of main flow temperature for three blade types.

Christensen et al. [106, 109] used IR thermography to assess the temperature of a cooled rotor blade tip rotating at 13000 rpm with tip speed of approximately $300\,\mathrm{m\,s^{-1}}$ using a FLIR X6901sc SLS camera. The Ohio State University Turbine Test Facility operates with a run time of 120 ms, which limits the surface temperatures to 350 K. Given the high speed and relatively low target temperature, the authors faced similar motion blur challenges. The authors selected an integration time of 47.6 µs as compromise between signal intensity and motion blur, applying a non-blind Wiener filter for deblurring based on predicted motion blur from 3-D models and particle image velocimetry software. The experimental setup employed and a sample of results in form of target temperature maps are shown in Figure 2.14.

Lastly, Knisely et al. [107] presented a methodology to assess an infrared detector for high-speed rotating tests, aiming to assess blades rotating at 10,000 rpm in the Steady Aero Research Turbine Laboratory. The authors suggested a short integration time ($1 - 2\,\mu s$) could be selected despite low target temperature level, given a minimum averaging of 100 images. In a subsequent study [108], an integration time of 2 µs and an average of 200 images were adopted to assess the overall effectiveness and lifespan. While not incorporating a deblurring technique, the authors opted for a reduced integration time alongside image averaging as an alternative approach.

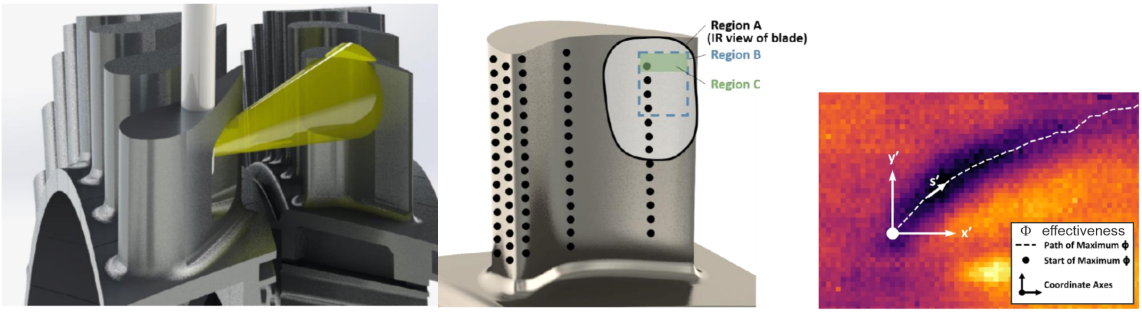

(a) (b)

Figure 2.15: Results from the Penn State University IR thermography studies by Knisely et al. [107, 108] showing (a) the experimental setup and (b) thermal image of one cooling hole including path of maximum effectiveness.

Clearly, this was achievable thanks to the continuous duration mode of the facility. The experimental setup employed and a sample of results are shown in Figure 2.15.

The literature review evidences the ongoing necessity for extensive research to comprehensively understand the applicability of IR thermography to fast-moving targets, particularly in the precise quantification and mitigation of associated errors.

2.5 Review of Blade Tip Heat Transfer Studies

Blade tips, situated at the furthest radial position of the rotating blade, consist of surfaces exposed to hot gases on all sides, presenting a challenge for effective cooling. In modern gas turbine engine, rotor blades rotate closely to a stationary casing, and the clearance between the two components is typically 1.5% of the blade span [21]. This gap enables the passage of fluid from the pressure to the suction side of the blades, driven by the pressure difference, a flow commonly known as tip leakage flow. As well as generating losses, by reducing the work that the turbine can extract from the fluid [110, 111], the hot leakage flow through the tip gap results in higher thermal loads on the blade tip, and exacerbates the tip burnout phenomenon discussed in Chapter 1 (see Figure 1.8). A diagram of the leakage flow over a flat tip is illustrated in Figure 2.16, emphasising the significant impact of pressure drop on flow migration.

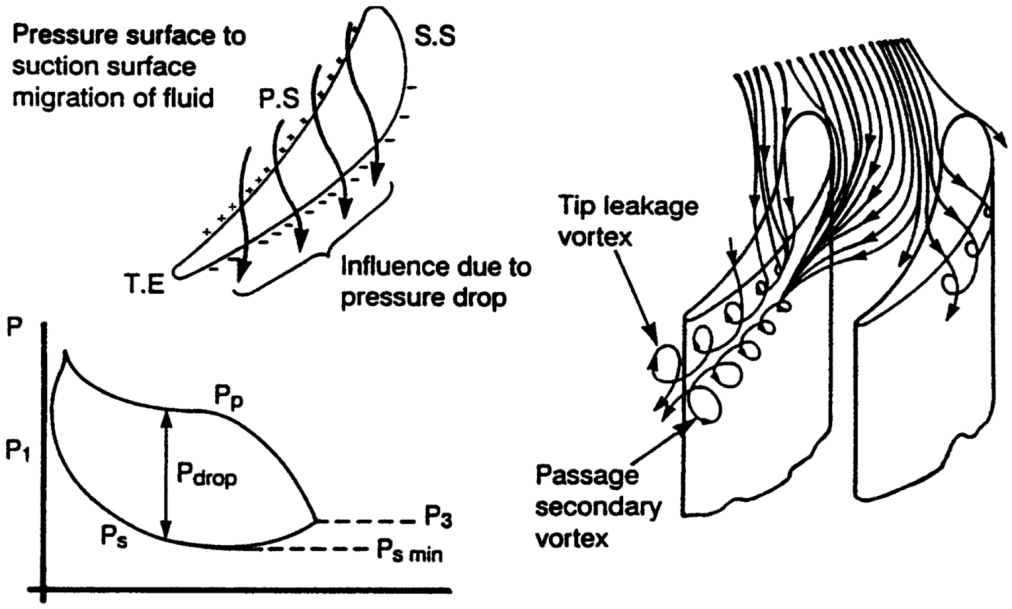

Figure 2.16: Schematic of tip leakage flow over a flat tip [112].

Further insights into tip flow patterns emerge from Bidon's 1989 study [111], where the author's finding on the flow patterns are summarised in Figure 2.17a. In this study, the author posits that the flow near the pressure side tip undergoes a rolling motion over the tip, driven by the strong pressure gradient across the tip. This rolling flow is established within the separation bubble. Subsequently, as the leakage flow interacts with the incoming suction-side flow, it separates forming a vortex. As the tip flow exits the gap the vortex grows rapidly, and it adds substantially to the overall secondary flow within the turbine blade passage, thus increasing the aerodynamic losses.

Depending on the local thickness of the airfoil, different flow regimes are individuated, this is depicted in sketch in Figure 2.17b, a representation of the blade cross-section. If the blade is thick enough, the jet formed by the flow entering the gap from the suction side mixes out over the tip. On the contrary, if a blade is thin enough the leakage flow would not reattach, this is the typical scenario close to the blade trailing edge.

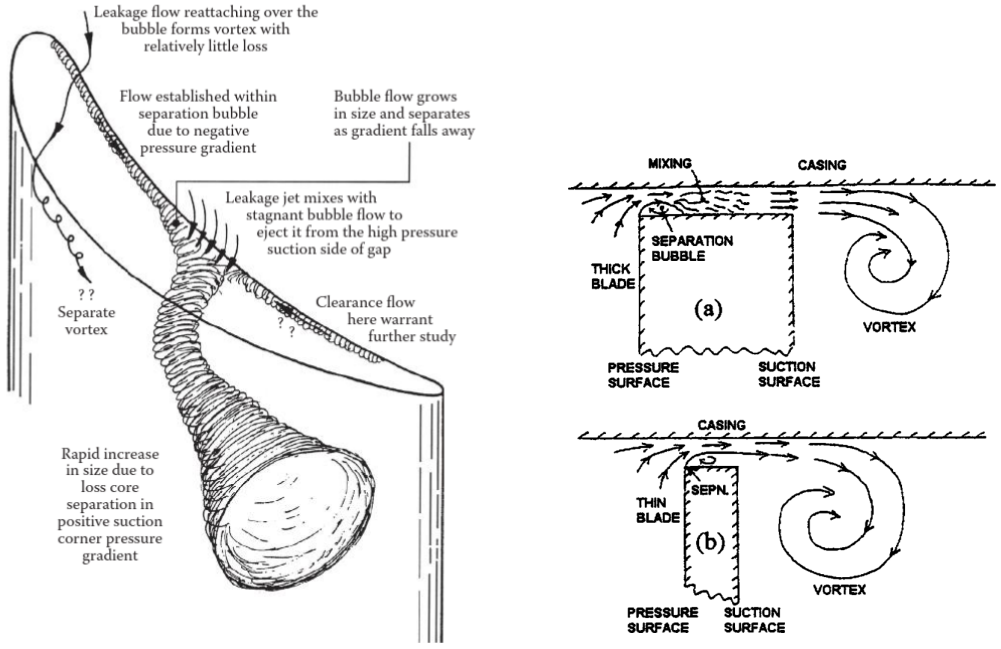

(a) (b)

Figure 2.17: Tip leakage flow (a) typical patterns for a flat tip blade as explained by Bindon [111] and (b) differences in the phenomenon between thick and thin unshrouded blade tip as explained by Denton [19].

Saleh et al. [113] discuss that when the tip experiences in-service burnout the effective tip gap increases significantly, allowing a higher leakage mass flow rate compared to a sharp-edge tip at the beginning of its operational life. As effectively cooling blade tips is challenging, the heat transfer results in material wear on the tip, leading to an increased tip gap and decreased efficiency. Simultaneously, an increased tip gap leads to higher heat fluxes [114].

One typical strategy to reduce leakage flow, which in turn reduces tip heat transfer, is the use of squealer tip geometries. A squealer is a groove that runs over the pressure and suction side and acts as a seal against the leakage flow. Flow patterns for such a geometry are shown in Figure 2.18 [115, 116]. Within the squealer, two vortices become evident. The first, a separation vortex, materializes as the incoming flow separates from the inner edge of the pressure-side rim. This vortex follows the pressure surface sidewall and exits near the blade's trailing edge. The second vortex,

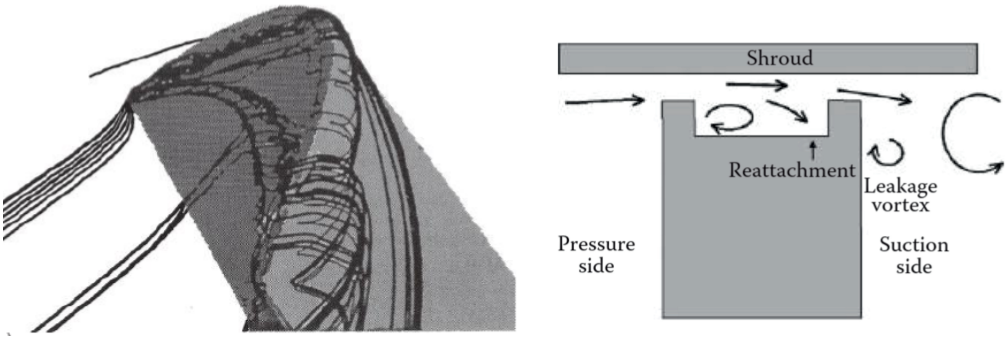

(a) (b)

Figure 2.18: Leakage flow over an unshrouded squealer tip blade, including (a) typical flow patterns [115] and (b) conceptual representation [116].

also a separation vortex, start from the stagnation region and extends over the blade's suction surface. Other vortices generate in this process, including pressure side rim, suction-side rim, and tip flow vortex [21].

Findings in the research on squealer blade tip geometried emphasised the complexity of the heat transfer and flow field. Meztger et al. [117] and Chyu et al. [118] investigated the heat transfer on a simplified rectangular model of the groove, revealing a reduction in the heat transfer at the upstream end of the cavity compared to a flat tip. Conversely, they observed higher heat transfer coefficients at the downstream end of the cavity due to flow reattachment inside the cavity. Overall research in literature demonstrated that grooved tip is beneficial in reducing the heat transfer due to leakage flow compare to a flat tip geometry [116, 119], as depicted in Figure 2.19, though attention must be paid to the entrance and exit effect on the rim. This effect was further demonstrated by Azad et al.[120, 121]. In the first study [120], the authors conducted heat-transfer experiments on the flat tip section of a turbine blade arranged in a five-bladed linear cascade; while in the following study [121] the authors compared these results to the heat transfer of a squealer tip blade. Results are summarised in Figure 2.20 for three cases of tip gaps and at two different turbulence intensities. Different heat transfer regions are identified on the cavity surface, with a higher heat transfer coefficient on the rim surface attributable to entrance and exit

effect, and on trailing edge. Tip gap size influences heat transfer, with a larger gap increasing and a smaller gap decreasing the heat transfer coefficient. Increased inlet turbulence slightly raises heat transfer along the pressure side rim and trailing edge. Despite certain localised enhancements in the heat transfer coefficient, the author's overall concluded that the squealer tip exhibited a lower heat-transfer coefficient when compared to the flat tip case.

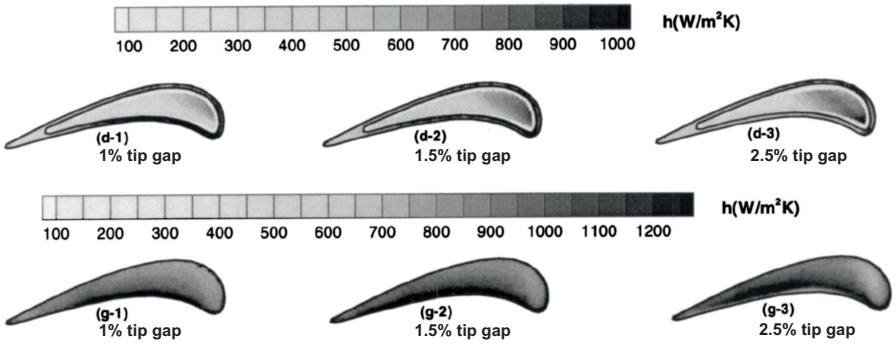

Figure 2.19: Heat transfer coefficient on a (d) squealer tip blade and (g) flat tip blade, at different tip gaps. Adapted from Kwak et al. [122, 116].

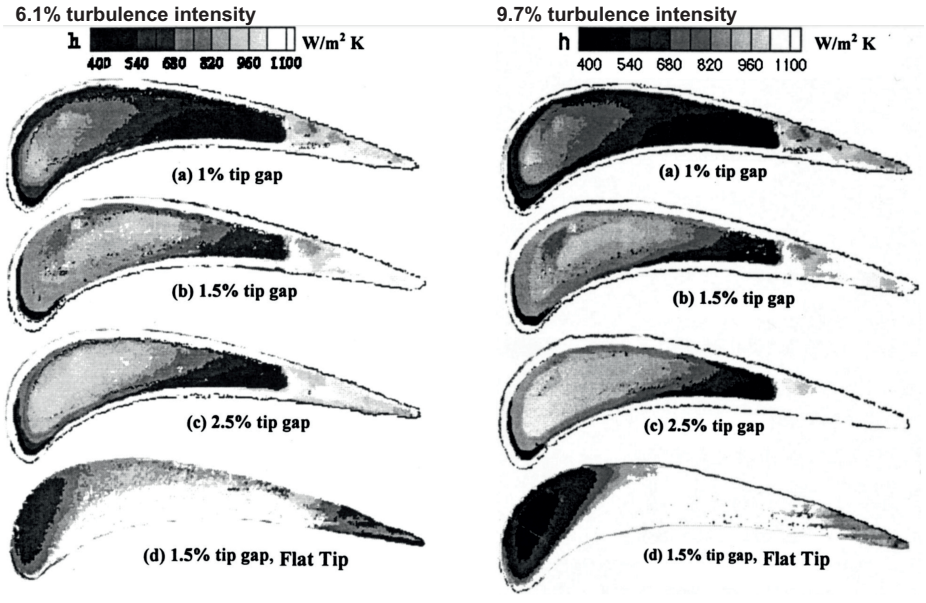

Figure 2.20: Left: heat transfer coefficient for a squealer tip blade with 6.1% turbulence intensity at the inlet, for different tip gaps and comparison with flat tip; right: results for a turbulence intensity of 9.7%. Adapted from Azad et al. [121, 120].

2.6 Summary

This chapter aimed at contextualising the use of IR Thermography for accurate heat transfer measurements in an engine scale turbine rotating facility within the existing literature. After a brief introduction to testing facilities employed in turbomachinery research, short duration facilities have been described as the more suitable for heat transfer studies. The working principles of various types, including shock tunnels, blowdown facilities, and isentropic light piston tunnel facilities, have been presented. The experiments in this study were conducted specifically in the latter type of facility.

Having established the need for highly engine-representative aerothermal experiments and affirmed the feasibility of achieving this in rotating short duration facilities, a selection of heat transfer instrumentation has been reviewed and framed for application in such facilities.

Thin-film heat transfer gauges have been introduced as they have a long history for single-point temperature measurements. Furthermore, arrays of thin-film gauges can enable increased spatial resolution and assessment of heat transfer distribution on surfaces. The theory of these instrument has been reported, and several type have been described. The use of single layer semi-infinite thin-film gauges is limited to the validity of the semi-infinite assumption. As reported by Schultz and Jones [33], this creates a constraint between substrate material, flow duration and required thickness. For instance, required layer depth for a flow duration of 1 s varies from 1 mm for a substrate made of glass materials to 3 cm for metals such as aluminum, which is excessive (see Figure 2.2). As the use of glass machined blades is restricted to stationary cascade facilities due to structural limitations, the use of single-layer thin-film gauges in fully rotating turbine test rigs is limited to flow duration shorter than 1 s. Two layer single-sided gauges are presented as they broaden the validity of the semi-infinite assumption by adding an insulating layer, typically polyamide, between the gauge and the semi-infinite substrate.

Thin-film gauges can be very accurate when used on stationary components. However, their invasive nature and wiring complications restrict their applicability on rotating components. In such cases, complicated wiring to transmit the electrical signal from a rotating frame of reference, as well as demanding time-consuming soldering are required. Moreover, the integrity of these sensors can be compromised under the high centrifugal forces experienced by gas turbine rotor blades (the gauges can be lifted off the specimens).

For these reasons, a range of optical techniques for measuring heat transfer in rotating facilities have been reviewed. The main advantage of optical techniques is their ability to obtain fully 2D resolved temperature distribution, while being non-intrusive. Thermochromic Liquid Crystals (TLCs) have been introduced as a viable technique to measure temperature in full scale rig. The TLCs respond with colour change to temperature variation, which allows researchers to visualize and map temperature gradients with relative ease, providing valuable insights into thermal behaviour. The primary drawback of this technique is the imposed limit on the maximum temperature the crystals can withstand, set at $120,^{\circ}\mathrm{C}$ [26]. This limitation restricts the application of the technique, depending on the required temperature range.

The last measurement technique reviewed is Infrared (IR) Thermography. When compared to the aforementioned techniques, infrared thermography offers several distinct advantages. Like Thermochromic Liquid Crystals, it provides high-resolution two-dimensional temperature fields for both transient and steady measurements and it is non-intrusive, while also presenting measurement capability up to $1500\,^{\circ}\mathrm{C}$. The theory of thermal radiation has been presented and the main sources of error introduced, including a thorough review of the calibration techniques. It has been highlighted that the common approach, particularly for stationary targets, involves in situ calibration using embedded thermocouples. This methodology, exemplified by Martiny et al.[83] and validated by Schulz [85], has seen further refinement by Ochs

et al. [86], resulting in a significant reduction in maximum errors in temperature readings. Recent studies developed advanced calibration, as in situ blackbody and greybody, and image restoration techniques to take into account the effect of the observation angles, the surroundings reflection and the optical path. The most advanced calibrations tried to include the influence of the geometry reproducing the specific experimental facilities geometry. Despite the success of these calibration methods for stationary targets, challenges arise when applying them to IR thermography systems for fast-moving rotating targets. Practical constraints, such as the installation of thermocouples and telemetry of data from rotating to stationary frame, present limitations. Additionally, the impact of motion blur becomes a crucial consideration, particularly when detecting temperature gradients in small features near cooling holes on a blade surface.

The most relevant studies focused on the development of IR camera calibration techniques are summarised in Table 2.1 [30].

The work found in literature involving the use of IR thermography in engine scale turbine rigs has been reported. Lazzi Gazzini et al. [105] used IR thermography in the long duration LISA facility to study rotor endwalls at 2700 rpm, addressing motion blur with an algorithm that combines images taken a two different integration times. Christensen et al. [106, 109] focused on assessing the temperature of a cooled rotor blade tip at 13000 rpm, employing am integration time of $47.6, \mu s$ and a non-blind Wiener filter for deblurring. Knisely et al. [107] presented a methodology for assessing an infrared detector in high-speed rotating tests at 10000 rpm, adopting a short integration time and image averaging to quantify effectiveness and lifespan of turbine blades. Each study faced challenges associated with motion blur, target temperature levels, and facility operating speeds.

The final section of the chapter focuses on a succinct review of the turbine blade tip heat transfer. The features of the phenomenon have been described and it has

been shown that the squealer tip geometry is proved to exhibit a lower heat transfer coefficient compared to the flat tip.

Table 2.1: Main studies on calibration techniques for IR camera measurements. The novelties and uncertainties of the past studies are outlined. From [30]

Studies	Calibration techniques/ developments	Uncertainty*
Martiny et al. [83], 1996.	Calibr. coeff. r, b, f to solve Equation 2.18; reference TCs**. Directional emissivity not considered, $\epsilon \neq f(\theta)$.	-
Morris et al. [92], 2006.	Radiometric model for surroundings reflections. Window's τ measured using spectroradiometer.	-
Ochs et al. [86], 2009.	Additional coeff. I_{offset} to include reflections; $\tau = f(T, \lambda)$; $\epsilon \neq f(\theta)$.	1.2 %
Laveau et al. [94], 2015.	Robot arm to enhance IR camera FOV. Silver markers for 3D image transformation.	$\pm$ 1%
Kirollos et al. [98], 2017.	Black and greybody calibrations, and RMA to account for $\epsilon(\theta)$, $\tau \cdot \epsilon$ and $q^*(x)$.	$1 - 2.5\%$
Lazzi Gazzini et al. [105], 2017.	Image processing with two different camera's integration times for high-speed target.	$\pm$ 1%
Elfner et al. [102], 2019.	BDRF to estimate $\epsilon(\theta)$. Local correction factor C with geometrical ray-tracing for reflections, Equation 2.31.	2 %
Aberle et al. [103], 2019.	Global and local calibrations for $\epsilon(\theta)$ and τ. Interpolation of PT100 reference sensors using FEM.	$\pm$ 1.5 K
Michaud et al. [104], 2019.	Effects of the contact path of TCs and of IR pixels selection on the temperature measurements accuracy.	-

(*) Different expression to calculate the surface temperature uncertainty were used. Please refer to the specific study.
(**) TCs stands for thermocouples.

Chapter 3

Development of an Infrared Thermography Measurement Methodology for Fast Moving Targets

This chapter outlines the development and calibration methodology of an infrared system for measuring surface temperature and heat transfer on fast moving targets, specifically gas turbine blades. The system was designed for the Oxford Turbine Research Facility, a world-leading experimental facility delivering highly engine representative, scalable heat transfer results for design code validation and technology down-selection for the aerospace sector.

The measurement system employs Infrared Thermography to capture temperature maps of high-pressure turbine blades, enabling full surface evaluation of thermal conditions, including heat transfer coefficient, adiabatic wall temperature, Nusselt number, cooling effectiveness and metal effectiveness at engine representative conditions. Overcoming challenges posed by the test environment, such as reflections from surroundings, low emissivity of metallic parts, and motion blur, the developed calibration procedures ensure accurate measurements within the accuracy of the primary measurement thermocouple.

The calibration method, validated on a fast-moving rotating geometry, demonstrates accurate correction for all the measurement disturbances.

Notably, the calibration method presented eliminates the need for a reference temperature sensor on the target, reducing technical difficulty. The development of this calibration approach involved the use of two experimental facilities: a steady calibration facility and a rotating facility with limited optical access, akin to turbomachinery conditions. The former was used to calibrate the camera detector, evaluates directional emissivity, and demonstrates the validity of the reflection correction method. The latter was employed to test the reflections correction method on a rotating system, illustrating the impact of motion blur on calibration. Detailed uncertainty analyses accompany each calibration step.

Results from this chapter, published in the papers by Sisti et al. [31, 32], contribute to the understanding of infrared measurement techniques, offering valuable guidance for developing IR measurement systems for high-speed targets.

3.1 Infrared Thermography Measurements in the OTRF

The OTRF, shown in Figure 3.1a and described in more detail in the following Chapter 4, is a transient rotating facility with a run time of approximately 500 ms, and the capability of testing high pressure turbine stages under conditions that are representative of actual engine operation. The facility can match Mach and Reynolds numbers, non-dimensional speed and gas-to-wall temperature ratio to engine conditions. Recent research studies conducted in the OTRF have been reviewed by Chana et al. [45] and Falsetti et al. [25]. An upgrade is currently being implemented which will allow a semi-transient test mode by prolonging the run time to 60 s, and enable testing at gas-to-wall temperature ratios representative of modern civil aerospace engines, increasing current capability from 1.65 to 2. The implementation of the Infrared Thermography system discussed in this thesis will also be made possible by this upgrade, enabling comprehensive surface heat transfer measurement on all rotor blade surfaces.

The various contributions of the total radiant energy reaching an IR camera imaging a typical turbine geometry are depicted in Figure 3.1b. Within this schematic representation, the focus of the measurement is marked in red and centres on the rotor blade tip. The nearby surroundings include the stator vanes; as an illustrative example, one vane is highlighted in orange. The optical path consists of the mainstream gas and the IR transparent window. The mainstream gas is shown in blue and consists of dry air in the OTRF. The IR transparent window is highlighted in a yellow hue. In addition to the radiation emitted by the target of interest (E_t), the detector also receives offsetting radiation. This disturbance signal comprises two components: i) the radiation emitted from the surroundings that reflects off the target surface, and undergoes attenuation as it travels along the optical path, and ii) the radiation emitted by the optical path, mainstream gases and IR-transparent window.

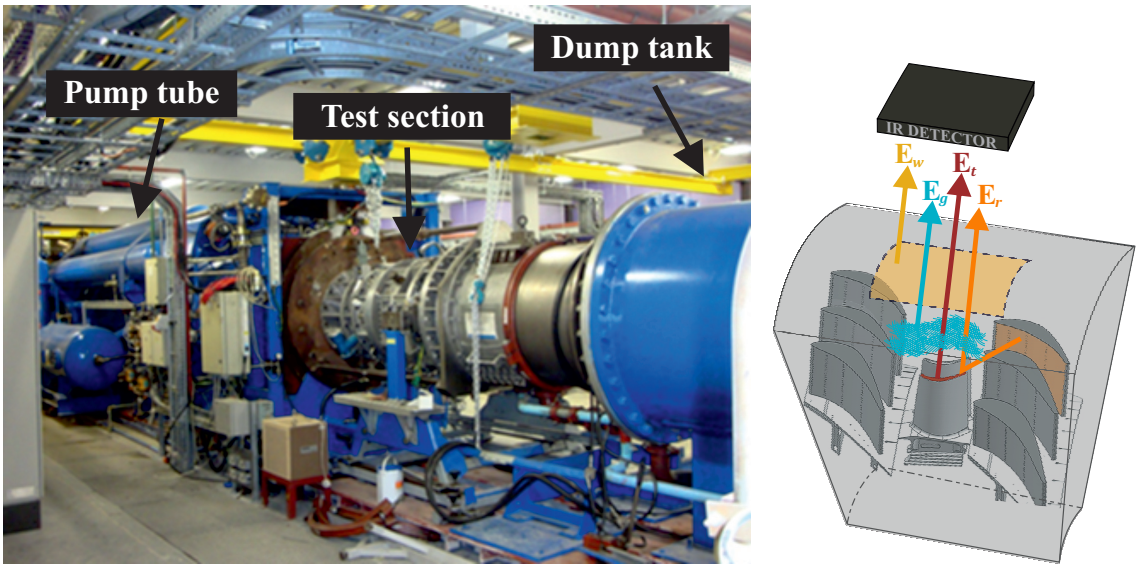

(a) (b)

Figure 3.1: (a) Photograph of the OTRF test section; (b) Schematic highlighting the energy components detected by an infrared system in a turbomachinery experiment, where E_t is the energy from the target, E_r the energy from surroundings reflected on the target, E_w the energy from the IR-transparent window, and E_g the energy from the mainstream gas [30].

Using the *Stefan-Boltzmann* equation [49], the total energy detected can be expressed in terms of temperature as:

$$T_{cam}^4 = \tau_{opt}\varepsilon_t T_t^4 + \tau_{opt}(1-\varepsilon_t)T_r^4 + (1-\tau_{opt})T_{opt}^4 \tag{3.1}$$

and solved for target temperature T_t as:

$$T_t^4 = \frac{T_{cam}^4}{\tau_{opt}\varepsilon_t} - \frac{(1-\varepsilon_t)T_r^4}{\varepsilon_t} - \frac{(1-\tau_{opt})T_{opt}^4}{\tau_{opt}\varepsilon_t} \tag{3.2}$$

The measured equivalent blackbody temperature, T_{cam}, is affected by the surroundings reflected temperature, T_r, and the optical path temperature, T_{opt}. Therefore, accurate measurement of the target temperature, T_t, requires knowledge of the above as well as of the emissivity, ε_t, the transmittance, τ_{opt}, and the calibration procedures to quantify these terms need to be optimised.

The relative contribution of the target and disturbance signals is strongly dependent on the surface emissivity. The varying contributions to the signal for a possible

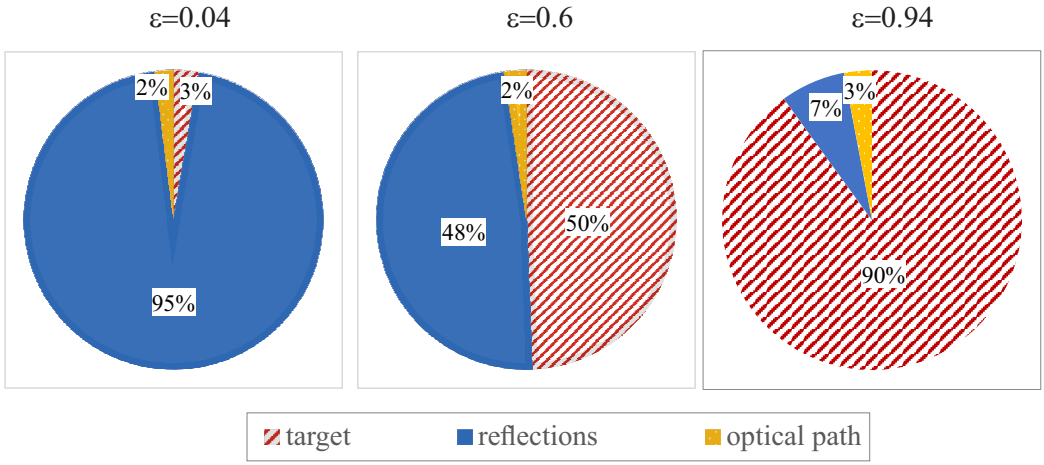

Figure 3.2: Contributions of target, surroundings, and optics spectral radiance to the total detected spectral radiance (Equation 3.1) for nominal expected values of $T_t = 500\,\mathrm{K}$, $T_r = 550\,\mathrm{K}$, $T_{opt} = 430\,\mathrm{K}$ $\tau = 0.95$ and for three emissivity value $\varepsilon = 0.04$, $\varepsilon = 0.6$ and $\varepsilon = 0.94$.

experiment in the OTRF in semi-transient mode are presented in Figure 3.2. The analysis was conducted for emissivity values varying from $\varepsilon = 0.04$, typical of polished metals, to $\varepsilon = 0.94$, obtained from the calibration of a high emissivity coating described later in this chapter. Results for an intermediate value of $\varepsilon = 0.6$ are also shown. Increasing the emissivity of the target greatly reduces the contribution of the disturbance signal, including reflections and optical transmittance, which reduces from approximately 97% with $\varepsilon = 0.04$ to 10% with $\varepsilon = 0.94$. Indeed, applying high emissivity paint on the target surface is a widely adopted practice, especially when the material has low emissivity, such as polished metals.

Table 3.1 presents the outcomes of a sensitivity analysis performed on Equation 3.2, also using expected temperature values of T_t, T_r, T_{opt} for this possible semi-transient OTRF test. Values of ε_t, and τ_{opt} were taken from calibration data presented later. The sensitivity coefficients, $C_i = (T_t - T_{t,+1\%})/(T_t) \cdot 100$, express the change in the evaluated target temperature when the corresponding parameter is varied by 1 %. The temperature detected by the camera, T_{cam}, presents the highest sensitivity coefficient with 1% error translating into 1.12% net error on T_t. It can be inferred that

to ensure an accurate measurement, particular attention must be given to the error in the evaluation of T_{cam}; thus, to the calibration from digital counts to equivalent blackbody temperature. The sensitivity coefficient for the equivalent blackbody temperature is followed by the sensitivity coefficients for emissivity and transmittance, that have approximately the same magnitude. Finally, reflected temperature and optical path temperature present the lowest sensitivity coefficients.

Table 3.1: Influence coefficients C_i of each variable to the final T_t of expected value 500 K.

Variable		Expected Values	C_i
Equivalent blackbody temperature	T_{cam}	500.5 K	1.122
Target emissivity	ε_t	0.94	0.115
Optical path transmittance	τ_{opt}	0.95	0.127
Surroundings reflected temperature	T_r	550 K	0.095
Optical Path Temperature	T_{opt}	430 K	0.031

Results from this analysis are to be considered valid for the specific temperatures and radiative conditions presented. The performance is highly interconnected and changing one variable strongly affects the results. Figure 3.3 shows the variation of sensitivity coefficients as a function of target emissivity, calculated with the same expected values for temperatures and transmittance as above. At lower emissivity values, the variable that dominates the error in target temperature becomes the reflected temperature, T_r.

As Figures 3.2-3.3 outline, increasing the target emissivity is a fundamental step in order to reduce the error. Nevertheless, calibration procedures for the detector, target emissivity, the optical path transmittance and the disturbance radiation need to be fine-tuned to the experimental conditions to obtain the best possible accuracy. In the next sections the key considerations for selecting the IR detector, the performance of the chosen camera and the IR system calibration are discussed.

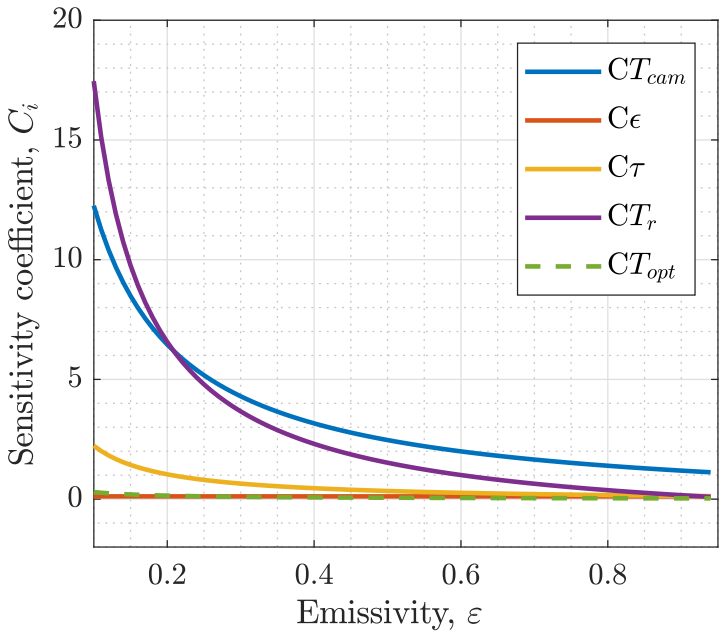

Figure 3.3: Impact of emissivity on influence coefficients C_i.

3.2 Infrared Detector Selection

Infrared thermography cameras convert spectral radiance measurements, [W sr^{-1} m^2], into temperature, [°C] or [K]. This conversion occurs at the pixel level (i.e. the sensing element), and is facilitated by two distinct detector categories found in commercial IR cameras: thermal detectors and photon detectors. Thermal detectors respond to radiant energy by inducing a change in the state of the detector material, such as alterations in resistance or capacitance, which is then converted into an electrical signal. Bolometers and microbolometers are presently the prevalent types of thermal detectors, relying on variations in the electrical resistance of the sensing element.

In contrast, photon detectors, also known as photonic or quantum detectors, operate based on quantum physics principles. Made from from semiconductive materials like indium antimony (InSb) or Type II Strained Layer Superlattice (T2SL), composed of alternating layers of indium arsenide (InAs) and gallium antimonide (GaSb), these detectors require cooling to cryogenic levels (approximately 60 K, depending on the

material) for optimal semiconductive material performance. The photons striking the sensing element cause an electronic transition, generating a photocurrent proportional to the detected incident radiation.

A crucial distinction, particularly pertinent to this study, lies in how these two detector categories capture images. Microbolometer detectors remain constantly open to incoming radiation, responding with a specific time constant. Conversely, photon detectors collect energy solely during the integration time, a parameter set through calibration. This is possible thanks to the implementation of a global shutter technology, which dictates the exposure time of the camera, also referred to as shutter time or integration time.

The thermal time constant of microbolometer detectors typically falls within the range of 7 to 12 ms. While integration time in quantum sensors can be reduced to the order of ns, enabling the capture of clean images of moving targets. Hence, with the objective of measuring temperature on rotating blades, quantum detectors are the obvious choice. The influence of the integration time on the measurements is discussed in more details below and in the following sections.

Choosing the right IR camera for a particular measurement application requires careful consideration of several factors. The following are the three key parameters that must be met for selecting an appropriate IR camera:

i) **Expected temperature range**: The expected temperature range affects the working wavelength of the IR camera based on Plank's law. As the temperature of the object increases, the peak emission wavelength shifts towards shorter wavelengths. The camera's working wavelength must be selected to correspond to the expected temperature range, ensuring that it can accurately detect the radiation emitted by the object.

ii) **Acquisition rate (Frame rate)**: The acquisition rate or frame rate of an IR camera is the number of thermal images per second that can be captured from

the camera. In a rotating set-up, this affects the number of samples that can be acquired each revolution.

iii) **Integration time/Exposure time**: Integration time or exposure time is how quickly an IR camera can capture a single frame of data. It is similar to the shutter speed of a traditional visible light camera. The exposure time for IR cameras is essential to capture the thermal signature of the target object accurately. A shorter exposure time reduces blurring for high-speed events, but may result in underexposed images. Longer exposure times allow for more light or heat energy collection, but may result in motion blur. Choosing the appropriate exposure time depends on the target object's movement speed and the desired image quality.

The expected target temperature range in the OTRF is between 300 K and 500 K, with average blade surface temperature of approximately 400 K. Plank's law is plotted in Figure 3.4 for the expected temperature range. Current IR cameras are sensitive in either the middle ($3 - 6\,\mu m$) or the long infrared wavelength ($6 - 15\,\mu m$) bands. Long wave IR cameras do not include the band between 5 µm and 7 µm because of the high atmospheric absorption in this region. Figure 3.4 depicts the highest radiance at OTRF operating temperatures in the long-wave infrared, which was therefore chosen for the camera working wavelength. Non-dimensional matching of turbine operating conditions typically results in turbine speeds ranging between $7500 - 9500$ rpm. Therefore, an acquisition rate $116 - 158$ frame/second is required to capture one frame per revolution. The camera used in this study is a FLIR A6751 SLS LWIR camera, which was chosen for its sensitivity and speed. The camera features a 640×512 pixel Focal Plane Array (FPA) and cooled Strained Layer Superlattice (SLS) detector, sensitive to the wavelength in the long infrared range, between 7.5 µm and 10.5 µm, which suits the expected experimental peak emission of 9 µm approximately. The minimum

camera integration time is 0.480 µs, and the maximum frame rate at full window is 125 Hz. The option to increase the frame rate is available by windowing down at the Focal Plane Array (FPA) level. The manufacturer specifications of the camera are summarised in Table 3.2.

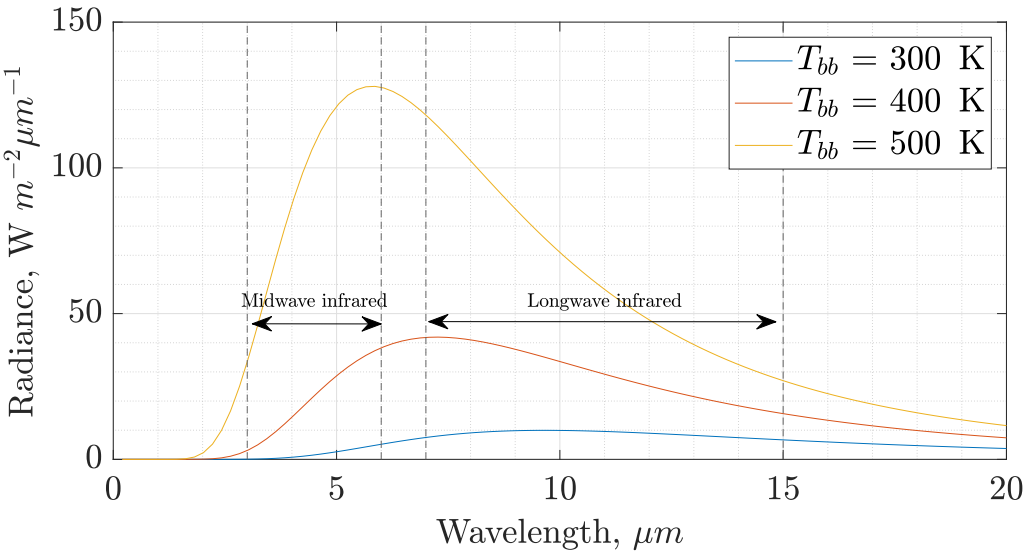

Figure 3.4: Blackbody emissive power for three absolute temperature (K) values as a function of wavelength.

Table 3.2: Infrared camera specifications.

Manufacturer	FLIR
Model	A6750 SLS
Detector Type	Strained Layer Superlattice (SLS)
Spectral Range	7.5 µm - 11 µm
Resolution	640 × 512
Frame Rate (full window)	125 hertz
Detector Pitch	15 µm
Detector Cooling	FLIR Closed Cycle Rotary

3.3 Steady System Calibration

The energy collected by the sensing element within the detector is converted into a voltage signal, which is further translated into a digital count by the system's A/D converter. To give an example, in a camera equipped with an a 14-bit dynamic range in its A/D converter, the count values range from 0 to 2^{14}. Subsequently, a detector calibration, dependent on the integration time, is necessary to correlate the digital counts and radiance values. Typically, this calibration is performed by the manufacturer and is limited to a single integration time. Performing an in-house detector calibration is recommended in scenarios where the integration time for the application is not known or when multiple integration times are being considered. Having the capability of performing a detector calibration provides the flexibility to tailor the instrument to different integration time requirements.

To this purpose, a bespoke steady-state facility was developed to perform traceable calibration of the detector, shown in Figure 3.5. The same facility was used to perform calibration of directional surface emissivity and optical path transmittance. This facility was also used to prove the concept of a novel method to correct for disturbance signal caused by reflecting radiation.

The photograph in Figure 3.5a shows the set-up for the detector calibration, where a blackbody source is placed in front of the camera at a distance of 250 mm. The enclosure, made of black Foamex PVC with a matt finish, serves to shield the calibrator and camera from extraneous radiation. The set-up used for the emissivity measurements as a function of temperature and viewing angle is shown in Figure 3.5b, where a bespoke emissivity calibrator is placed in front of the camera. A sectional view of the emissivity calibrator is shown in Figure 3.5c. The assembly includes a 5 mm thick copper plate measuring 150×100 mm sandwiched between two layers of ROHACELL®. These layers have overall dimensions of 230×180 mm and feature varying thicknesses, 40 mm at the back side and 20 mm at the front side. ROHACELL® is known for its

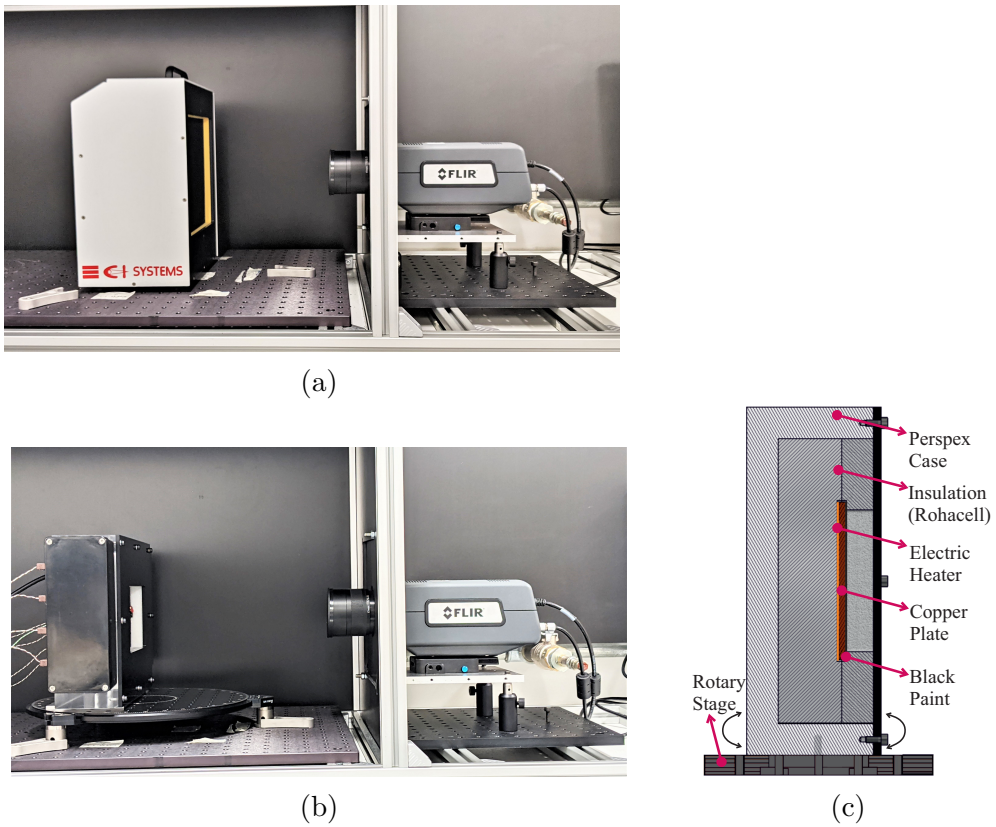

(a) (b) (c)

Figure 3.5: Steady calibration facility set-ups for (a) detector calibration, and (b-c) emissivity calibration.

thermal conductivity, approximately $0.03\,\mathrm{W\,m^{-1}\,K^{-1}}$. To further boost thermal stability, the entire assembly is encased in Perspex®. An electrical silicone heating element, powered by a variable power supply, is mounted behind the sample. Eight T-type thermocouples are surface mounted on the front and back of the copper sample to measure the temperature uniformity and serve as reference for the calibration. The signal from the thermocouples was monitored during the heating phase, and data from the thermocouples and IR camera were acquired simultaneously when steady state condition was reached, defined as a thermocouple signal standard deviation $< 0.02\,\mathrm{K}$. The emissivity of different coatings was evaluated, including black matt paint and aluminium tape. To allow measurements of directional surface emissivity, the calibrator was mounted on a rotary stage. The transmittance of a sample of ZnSe window was also determined. The window was interposed between the blackbody

source and the camera replicating the relative position of the camera, window and target relative position expected in the actual experiments.

In the following sections, the detector, surface emissivity and transmittance calibrations are described in detail.

3.3.1 Detector Calibration

To obtain a temperature map from the raw digital counts signal acquired by an IR camera, a detector calibration is required. A blackbody source was used to irradiate the Focal Plane Array (FPA) at a range of temperatures, $T_{bb,i}$. Data were averaged over 100 frames acquired at 125 Hz. Two blackbody sources, the CI-Systems SR33-7 and the Fluke 4181, were used. Both calibrators are NIST traceable. The combined uncertainty of the calibrator, which was calculated by taking the root sum square of the accuracy, uniformity, and stability errors [123, 124], is plotted in Figure 3.6 as a function of temperature. This was used to determine the ideal temperature range for each source, the CI-Systems calibrator was used in the range $293.15\,\mathrm{K} - 353.15\,\mathrm{K}$, and the Fluke 4181 in the range $353.15\,\mathrm{K} - 543.15\,\mathrm{K}$.

The approach detailed by Schulz et al. [125] was used to correct for the photoresponse non-uniformity arising in a FPA due to inherent differences in each individual

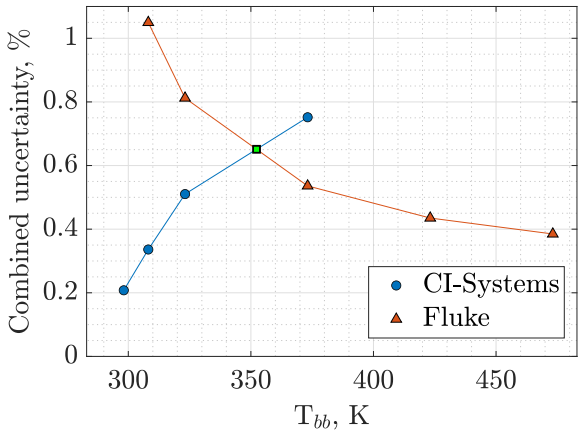

Figure 3.6: Stability, uniformity and accuracy combined uncertainty for the two blackbody sources used in the study.

detector element. A linear correction was applied pixel-wise by finding two parameters via curve fitting, the gain, m_{xy}, and the offset, q_{xy}. These identify the relationship between the deviation from the mean, $\Delta R_{x,y}$, and the mean over the entire FPA $\langle R \rangle$ as follows

$$\Delta R_{i,xy} = m_{xy} \langle R_i \rangle + q_{xy} \tag{3.3}$$

The coefficients m_{xy} and q_{xy}, namely the $gain$ and the $offset$, are calculated for each pixel by linear curve fitting. Subscript i indicates the blackbody temperature step, while the subscripts x, y indicate the pixel location in the array. Finally, the corrected digital count signal is obtained as

$$R^c_{i,xy} = \frac{R_{i,xy} - q_{xy}}{1 + m_{xy}} \tag{3.4}$$

The detector calibration and saturation are inherently a function of temperature and integration time. To capture high quality images of rotating objects a low integration time is needed, the specif value will be dependent of target speed and acceptable blur level. For instance, for a rotor speed of 4000 rpm, with a radius of 0.260 m, an integration time of 50 µs gives an estimated blur in the direction of motion of $v_t \cdot \mathrm{IT} \approx 5$ mm. Depending on the smallest feature in the image, this could be too high. For example, such level of blur would be ten times higher than a typical cooling hole overall dimension (0.5 mm). A significantly short integration time would reduce blurring and allow detection of smaller features. However, minimising the integration time decreases saturation and increases signal-to-noise ratio (SNR), possibly leading to significant measurement error. As the target temperature increases so does the detector saturation, allowing a reduction of the integration time for the same SNR.

The relationship between target temperature, integration time and detector saturation and the implications on the measurement error needs to be fully investigated to understand this limit and select the appropriate integration time. To this purpose, the detector calibration was performed and studied over a range of integration times

from 5 µs to 70 µs. For context, for a typical tangential blade velocity of 250 m/s in the OTRF, integration times of 5 µs and 70 µs would theoretically result in motion blur of 1.25 mm and 17.5 mm respectively.

A typical set of calibration data for a single pixel are shown in Figure 3.7. Figure 3.7a shows the temperature as a function of the recorded signal in digital counts for different integration time. The detector saturation lower and upper limits recommended by the camera manufacturer are represented on the graph by vertical dashed lines, with values of 12% and 82% respectively. These suggest what combination of integration time and target temperature is recommended for each specific case. For example, for temperatures between ambient and 363.15 K, an integration time above 50 µs is recommended, which corresponds to a detector saturation of 23% at 363.15 K and 11% at 293.15 K. At elevated temperatures, the minimum integration time can be reduced. For instance, temperatures exceeding 373.15 K permit an integration time of 20 µs, those exceeding 423.15 K allow for 10 µs, while for temperature higher than 513.15 K an integration time of 5 µs is permitted. Figure 3.7b shows the radiance as a function of the digital counts. This plot shows how the detector behaviour remains linear across the entire temperature range, even at the lowest integration time.

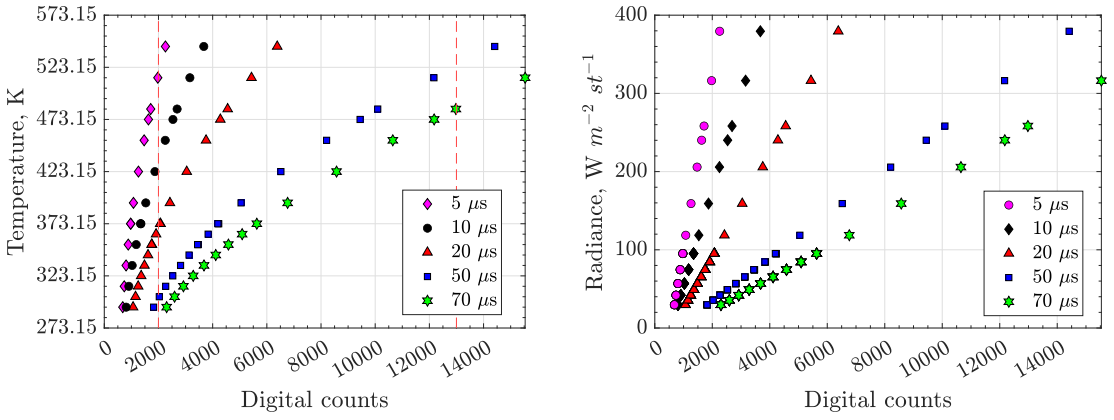

Figure 3.7: (a) Equivalent blackbody temperature and (b) Spectral radiance as a function of digital counts, for five integration times.

In the OTRF rotor speeds of $7,500 - 9,500$ rpm are typical to achieve representative test conditions. In a cooled experiment, surface temperatures below 373 K are expected in regions of high cooling effectiveness. With such high rotor speeds, a minimum integration time is desirable to minimise blur, resulting in likely undersaturated measurements at lower surface temperatures. Hence, it is fundamental to understand the implications of working in the undersaturated detector region and how this translates into measurement errors.

The signal to noise ratio (SNR) noise was evaluated over a range of blackbody temperature and integration time. Data were acquired over 100 frames and across the FPA. An example of the temporal signal of a randomly selected pixel acquired during a calibration is shown in Figure 3.8a. The calculated SNR is plotted in Figure 3.8b as a function of integration time and blackbody temperature. As expected, SNR increases with both variables, as this results in more energy (thus, higher signal), collected by the camera detector, causing an increase in SNR.

Typical temperature readings with $T_{bb} = 313.15\,\mathrm{K}$ for a range of integration times are shown in Figure 3.9a. Black lines indicate the mean temperature reading over the 100 frames, while red lines indicate the reference blackbody source temperature. Moving from the shortest to the longest integration time both the standard deviation and error in the mean value become smaller. This can be further inferred from Figure 3.9b, showing the absolute error defined as the difference between the real target temperature and the camera reading. The error fluctuates by approximately $\pm 1\,\mathrm{K}$ (2σ) around a mean of 1 K for $IT = 5\,\mu\mathrm{s}$. The fluctuation range reduces to $\pm 0.1\,\mathrm{K}$ around a mean of 0.07 K for $IT = 70\,\mu\mathrm{s}$. Finally, Figure 3.10 depicts the maximum error in temperature reading as a function of integration time and temperature of the blackbody source from the surveyed pixel. Such plot allow to quantify the balance between image quality and measurement accuracy. Image processing techniques can be required in instances where using a low integration time is unattainable.

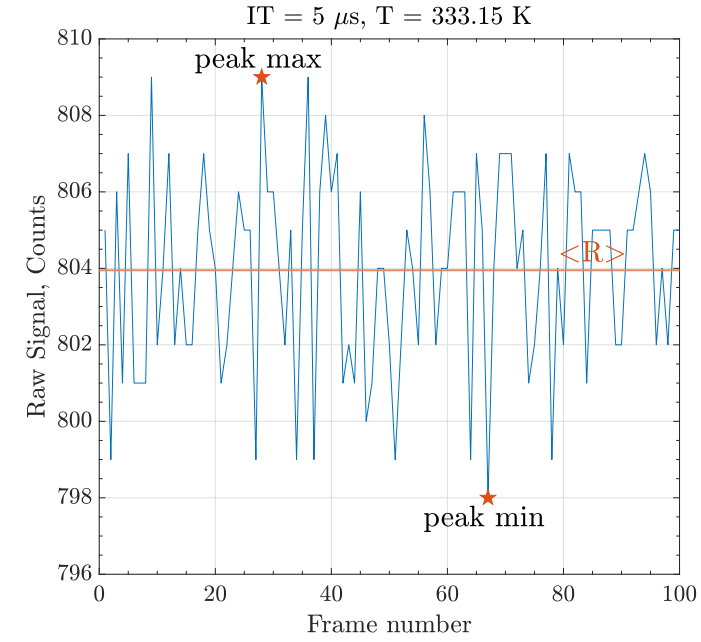

(a)

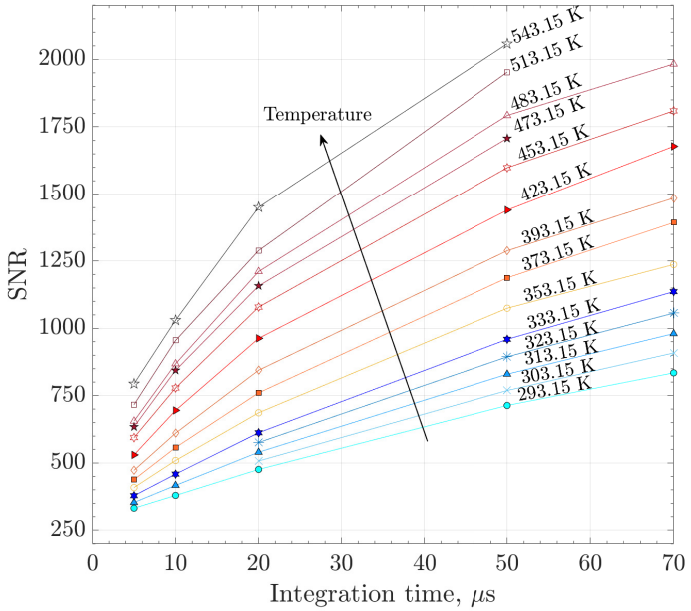

(b)

Figure 3.8: IR camera temporal noise analysis showing (a) raw signal from a randomly selected pixel, 100 frames acquired at 125 Hz, integration time of 5 µs and temperature of the blackbody source set at 333.15 K and (b) Signal-to-Noise Ratio as a function of integration time and blackbody source temperature.

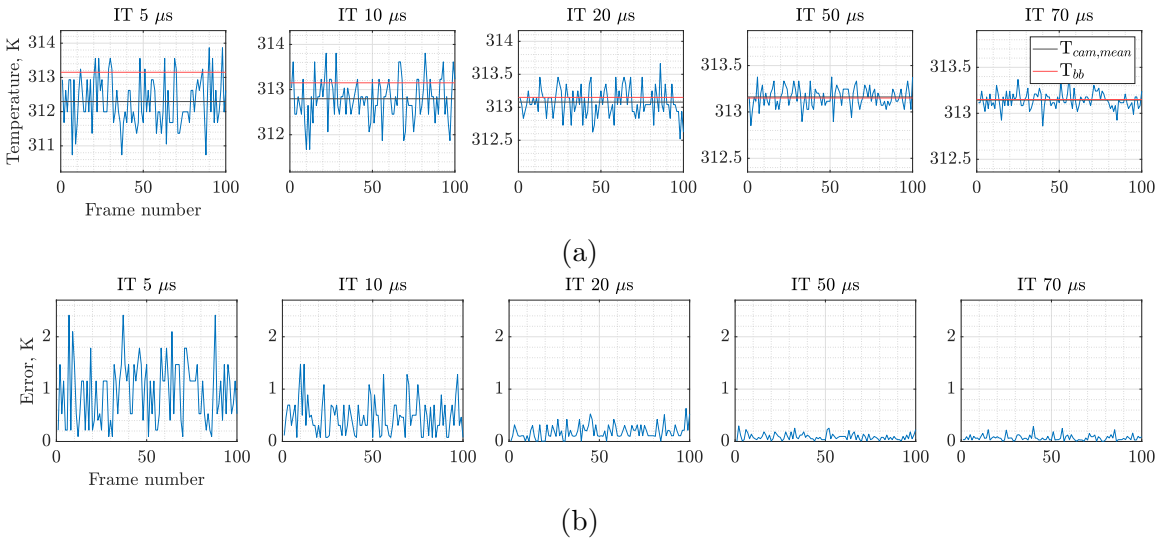

Figure 3.9: (a) Equivalent blackbody temperature reading T_{cam} and (b) absolute error in temperature reading from a randomly selected pixel, for 100 frames acquired at 125 Hz. Range of integration times from 5 µs to 70 µs.

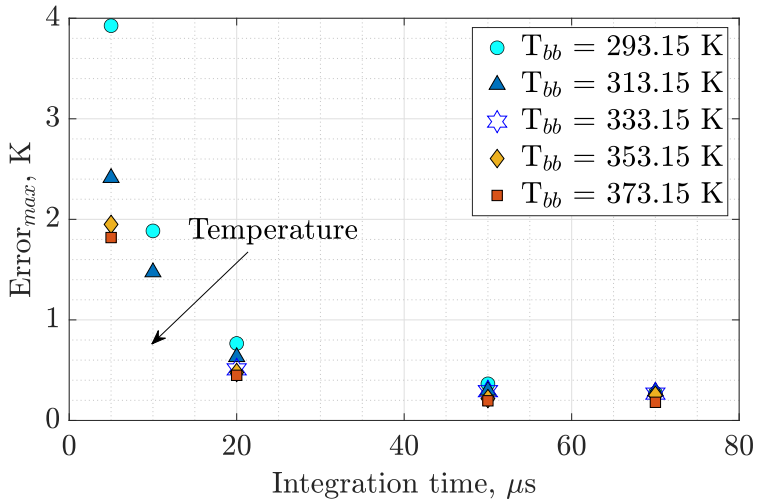

Figure 3.10: Maximum absolute temporal error in temperature reading T_{cam} of a random selected pixel as a function of integration time, for temperature between 293.15 K and 373.15 K.

3.3.2 Surface Emissivity Calibration

Accurate knowledge of target surface emissivity is a fundamental step to achieve high-accuracy IR thermography measurements. Typical emissivity values are readily available for a range of materials, however the influence of surface condition and viewing angle on emissivity should be considered. The set-up and calibrator used for

evaluating the emissivity have been described in the previous section and are depicted in Figure 3.5b and Figure 3.5c. Calibrations were performed over a range of target thermocouple temperature, T_{TC}, between 303.15 K and 373.15 K.

Two methods were used and compared for evaluating surface emissivity, both assuming an air transmittance equal to unity [74]. The first method solves Equation 3.1 for emissivity, obtaining the following:

$$\varepsilon(\theta) = \frac{T_{cam}^4(\theta) - T_r^4}{T_{TC}^4 - T_r^4} \tag{3.5}$$

The reflected temperature of the surroundings, T_r, is kept at the same level as the ambient temperature during the experiments and is measured by a K-type thermocouple.

The second method used to evaluate the surface emissivity requires two sets of data (test 1 and test 2) acquired at different target temperatures, and it is based on the assumption of consistent surroundings conditions, and hence T_r. From the energy balance, it is possible to obtain two equations in two unknowns: ε and T_r. The equations solved for ε give:

$$\varepsilon(\theta) = \frac{L(T_{cam,test2}) - L(T_{cam,test1})}{L(T_{TC,test2}) - L(T_{TC,test1})} \tag{3.6}$$

Where $L(T)$ are the spectral radiances calculated from the temperature by integrating Planck's equation.

A typical temperature map for a steady target temperature $T_{TC} = 364.15$ K, obtained applying the detector calibration is shown in Figure 3.11a (all 8 thermocouples measured within ± 0.3 K of mean). The highlighted areas A, B, C, D were used to evaluate the emissivity of the RS black matt paint, due to their proximity to thermocouple locations. The area labelled AL was covered by aluminium tape and was used as a reference for the emissivity calculation for this material.

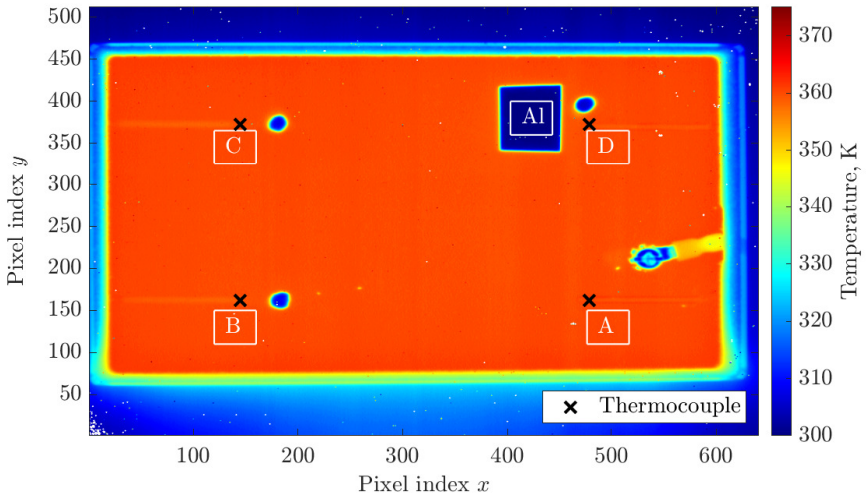

(a)

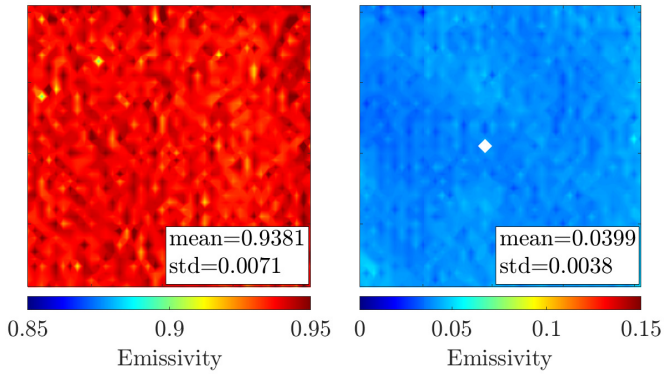

(b)

Figure 3.11: (a) Processed image of T_{cam} of the calibrator surface. The letters A, B, C, D indicate the regions used to evaluate the emissivity. Black crosses indicate the locations of the embedded thermocouples. (b) Emissivity maps for RS matt black paint (region D) and aluminium tape (AL).

The emissivity maps for the paint (sector D) and the aluminium tape (sector AL) calculated with the first method are shown in Figure 3.11b. Surface emissivity values of 0.938 ± 0.007 and 0.040 ± 0.004 were calculated respectively.

The emissivity values for the paint obtained using Equation 3.5 and Equation 3.6 as a function of target temperature are shown in Figure 3.12. The two methods agree at higher target temperatures with emissivity values of 0.94. What appears to be an emissivity temperature dependence in Figure 3.12a can be explained by measurement errors at low temperature. For target temperature close to T_r even

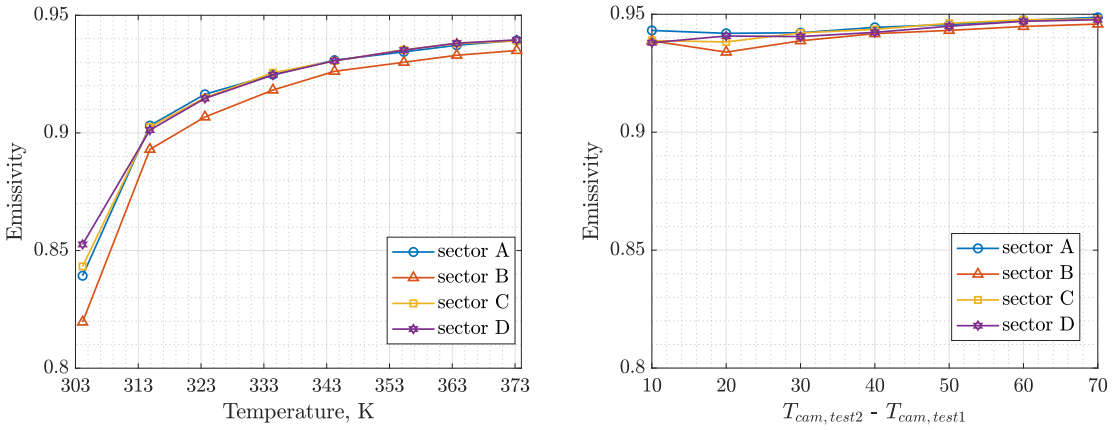

Figure 3.12: Emissivity ε of the black matt coating obtained (a) using Equation 3.5 and (b) Equation 3.6.

small measurement errors, typically 0.4% for a T-type thermocouple conforming to IEC-584-2 standards with a class 1 tolerance [126], translate into a significant error in the emissivity calculation. Both methods are valid, however, care should be taken with the first method to ensure a large enough temperature difference between T_{TC} and T_r to minimise measurement error. Results suggest a temperature difference of at least 60 K is required.

The calibration of the directional emissivity for the high emissivity paint was conducted across a range of 0° to 75°, with the corresponding trend depicted in Figure 3.13. The calibrator was rotated to adjust the angle with respect to the camera, and the measurements conducted using Equation 3.5 and setting the blackbody calibration to 320 K. It was observed that the emissivity remains almost constant and equivalent to the normal emissivity ($\varepsilon = 0.94$) up to angles of 50°. Subsequently, it gradually decreases reaching a value of 0.83. This is in general agreement with previous results in literature [127]. Whenever a large variation of viewing angle is expected, knowledge of viewing angles alongside the directional emissivity calibration curve becomes essential to assign the correct value of emissivity to each point on the surface. The anticipated viewing angles should be computed and the camera

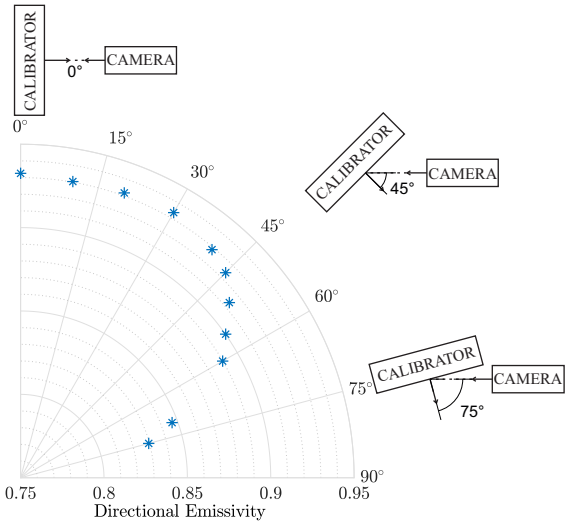

Figure 3.13: Polar plot of the measured directional emissivity.

should be aligned to ensure angles below 50° in areas of significance. In the OTRF, this analysis was addressed developing a Matlab code and results are provided in Chapter 4.

3.3.2.1 Emissivity roughness dependence

The investigation focused into understanding how coating thickness and surface roughness influence emissivity values. Four distinct paints were studied, two with high emissivity, Electrolube black and Nextel Velvet black, and two with low emissivity, Ambersil aluminium and Hycote white. Within each emissivity category, two thickness variations of the coatings were considered. Specifically, for Electrolube, Ambersil, and Nextel, the study included a 5-layer variant and a 2-layer variant. In the case of Hycote white, both samples featured two layers, but with one included a primer, and the other did not. These coatings were sprayed onto a copper plate, which was assembled in the emissivity calibrator setup shown in Figure 3.5c. The copper plate with samples of paint is shown in Figure 3.14a, and the equivalent blackbody temperature reading recorded with the IR camera is depicted in Figure 3.14b. In the image, the rectangular regions of interest (ROIs) selected for the emissivity evaluation are individuated by black lines. Equation 3.5 was used for the emissivity calculation

after setting the blackbody calibrator temperature to approximately 360 K, with ambient temperature of approximately 295 K. Figure 3.14c presents the results for surface emissivity on the selected ROIs. With an emissivity value of $0.95 - 0.97$ Nextel Velvet paint shows the highest emissivity, both in the instances of 5 and 2 layers. Hycote and Electrolube show comparable values of emissivity, varying from 0.92 to 0.95 depending of the number of layers. Finally, Ambersil shows the lowest emissivity, ranging between 0.6 and 0.66 for 2 and 5 layers respectively. Among the

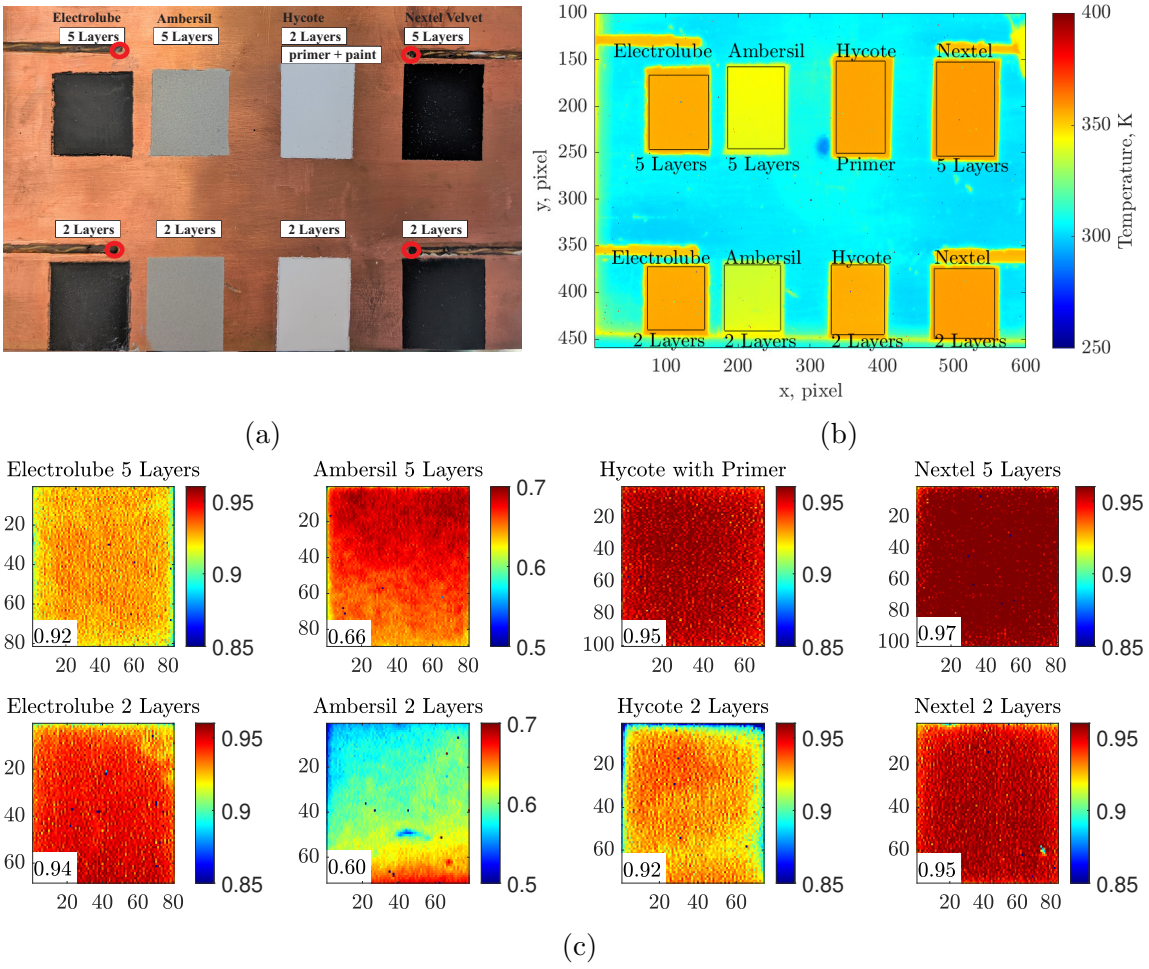

Figure 3.14: Results of the emissivity study on different samples of paint, including (a) Photograph of the copper plate used in the emissivity calibrator; (b) Equivalent blackbody temperature map with black rectangles indicating the ROIs used for emissivity calculation; (c) Surface emissivity of the selected ROIs, mean value of emissivity reported in the bottom left corner for each sample.

tested paints, only Nextel Velvet list emissivity on its data sheet, stating it as 0.98.

To better understand the influence of surface roughness on the emissivity, the copper plate was scanned using the Alicona Infinite Focus 3D Profilometer, a photograph of the setup is depicted in Figure 3.15, while the results are summarised in Tables 3.3 and 3.4. In Table 3.4, the roughness of the samples is reported in terms of S_a values, defined as the average height of the selected area in µm. The Root-Mean-Square, maximum peak height, maximum valley depth and maximum height of the selected area are also shown. The value of surface emissivity is also reported to help the comparison. From these values, it can be inferred that emissivity is not strongly affected by S_a, as even large differences in S_a corresponds to a small variation in emissivity. For instance, in the Nextel sample, a reduction in S_a from 363 µm to 20 µm leads to an increase in emissivity from 0.95 to 0.96, and the variation of 0.01 is within the uncertainty of the emissivity calculation (as shown in the uncertainty section). For all paint samples S_a decreases with increasing the number of layers. The use of the primer also appears to have a positive effect in S_a, comparing the two Hycote samples, both with two layers, it can be seen that the one with primer has a lower S_a. Furthermore, it can be inferred from the maps in Figure 3.14c that increasing the number of layer has a positive impact on the uniformity in surface emissivity.

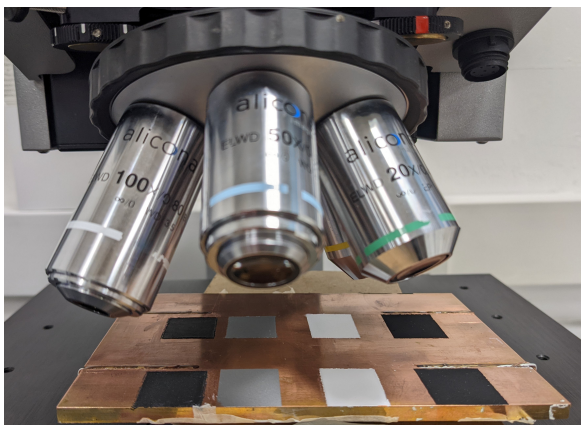

Figure 3.15: Photograph of the Alicona Infinite Focus 3D Profilometer employed to scan the samples of paint

Table 3.3: Symbols and abbreviations of quantities used to define roughness of different samples of paint.

Symbol	Description	Abbreviation	Explanation
Sa	Average height	E5L	Electrolube 5 Layers
Sq	Root-Mean-Square height	E2L	Electrolube 2 Layers
Sp	Maximum peak height	A5L	Ambersil 5 Layers
Sv	Maximum valley depth	A2L	Ambersil 2 Layers
Sz	Maximum height	HP	Hycote with Primer
		H2L	Hycote 2 Layers
		N5L	Nextel 5 Layers
		N2L	Nextel 2 Layers

Table 3.4: Results of roughness and emissivity study on different samples of paint.

	Unit	E5L	E2L	A5L	A2L	HP	H2L	N5L	N2L
Sa	µm	416	750	23	495	28	641	20	363
Sq	µm	418	750	27	496	34	641	26	363
Sp	µm	497	821	64	547	79	697	139	442
Sv	µm	-333	-691	58	-441	109	-565	70	-292
Sz	µm	163	129	122	105	188	131	209	149
ε	-	0.92	0.94	0.66	0.6	0.95	0.92	0.97	0.95

3.3.3 Transmittance Calibration

Characterisation of the optical path in terms of transmittance is also required to accurately evaluate the target temperature. The transmittance of the window was determined by placing the optical window between the blackbody source and the camera in the calibration set-up depicted in Figure 3.5a, replicating the same geometrical conditions expected in the OTRF for experiments with focus on blade tip. Using the temperature measured by the camera, T_{cam}, the blackbody source temperature, T_{bb}, and the optical path temperature, T_{opt}, the transmittance was calculated by rearranging Equation 3.1 as:

$$\tau = \frac{T_{cam}^4(\theta) - T_{opt}^4}{T_{bb}^4 - T_{opt}^4} \tag{3.7}$$

The optical path temperature is kept at the same level as the ambient temperature during the experiments and is measured by a K-type thermocouple. The transmit-

tance of the optical window used in the OTRF will be discussed in the following Chapter 4.

3.3.4 Reflection Calibration

The disturbance radiation originating from reflections from the target surface provides the most challenging calibration as it depends on geometry and temperature distribution of the environment. Some studies have considered it constant [83, 85, 86], and generally, it is advised to calibrate for this disturbance in situ [102, 98]. The method presented developed the technique proposed by Kirollos et al. [98] with the additional allowance of the optical path transmittance. The method is based on the concept that two isothermal regions of the target, each with a different surface emissivity, will radiate different magnitudes of total, emitted and reflected radiation. If the surface emissivity for each region is known, the true target and reflected temperatures can be found applying Equation 3.1 to the measurements from each region:

$$T_t^4 = \frac{1-\varepsilon_2}{\tau(\varepsilon_1-\varepsilon_2)}T_{cam1}^4 - \frac{1-\varepsilon_1}{\tau(\varepsilon_1-\varepsilon_2)}T_{cam2}^4 - \frac{1-\tau}{\tau}T_{opt}^4 \tag{3.8}$$

$$T_r^4 = \frac{\varepsilon_1}{\tau(\varepsilon_1-\varepsilon_2)}T_{cam2}^4 - \frac{\varepsilon_2}{\tau(\varepsilon_1-\varepsilon_2)}T_{cam1}^4 - \frac{1-\tau}{\tau}T_{opt}^4 \tag{3.9}$$

where subscript 1 refers to region 1, while subscript 2 refers to region 2.

The ultimate goal is to develop a calibration procedure for a rotating set-up; initially however, the method was applied to the emissivity calibrator shown in Figure 3.5b and 3.5c as proof of concept. A disturbance to enhance the reflections level was introduced by placing a hot soldering iron in proximity of the target. Results for an experimental temperature $T_{TC} = 335.8\,\mathrm{K}$ are summarised in Table 3.5. Zones D and AL on the calibrator (see Figure 3.11a) were used as high emissivity and low emissivity regions, where the recorded equivalent blackbody temperatures were 332.8 K and 296.7 K, respectively. Thus, the measurement errors before the correction, $\Delta_1 = T_{cam} - T_{TC}$, were $-3\,\mathrm{K}$ and $-39.1\,\mathrm{K}$, respectively.

Table 3.5: Emissivity and reflection correction applied to an experimental case.

ε	T_{TC}	T_{cam}	Δ_1	$T_t^{'}$	Δ_2	T_t	T_r	Δ_3
0.94	335.8	332.8	- 3.0	337.98	2.18	334.8	294.75	-1
0.04	335.8	296.7	-39.1			334.8	294.75	-1

Applying corrections for surface emissivity and reflection according to Equation 3.8 and Equation 3.9, a reflected temperature, T_r, of 294.75 K, and a target temperature, T_t, of 334.8 K were calculated. Thus, the calibration procedure was able to reduce the measurement error to within the thermocouple accuracy, from 3 K (0.9%) to 1 K (0.3%). Considering the results presented in Figure 3.2, it is clear that the regions of high and low surface emissivity provide accurate measurement of T_t and T_r respectively, allowing accurate correction to the true target temperature.

The relative magnitudes of surface emissivity and reflection corrections can be estimated by correcting for the target emissivity alone, i.e. applying Equation 3.1 with $T_r = 0$. In the high emissivity region, this results in a corrected temperature, $T_t^{'} = T_{cam}/\varepsilon^{1/4} = 337.98$ K. Hence, it is estimated that the surface emissivity and reflection corrections were same order of magnitude at $+5.18$ K$(+1.55\%)$ and -3.18 K(-0.95%) respectively, providing evidence of accurate correction for both sources of error.

3.4 Calibration Performance on High Speed Objects

The IR system capability to measure temperature of a high-speed rotating target was assessed in an experimental set-up, shown in Figure 3.16 that comprises a 450 mm diameter aluminium flat disc made of 6082 T6 alloy. An electrical motor drives the disc at a maximum speed of 4000 rpm (equivalent to approximately 66 Hz). The rotating disc is enclosed within a cylindrical chamber, with a square-shaped opening on the top cover to enable optical access. The disc is heated using a hot air blower whilst spinning, with the enclosure air temperature monitored with a K-type thermocouple.

RS Matt Black paint was applied to the disc to create a pattern that emulates the passage of 60 rotor blades, with two stripes featuring an array of holes to represent film cooling holes of 0.5 mm diameter. A 1-line optical encoder signal indicates the disc rotational speed (rpm), whilst a 60-line optical encoder enables phase lock image acquisition of the desired stripe.

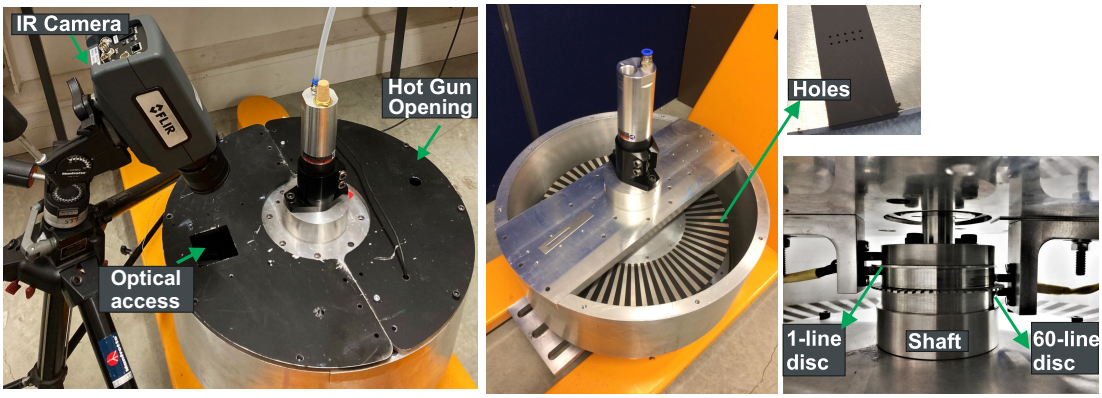

Figure 3.16: Rotating facility, with a close-up of the encoder installation (right bottom) and cooling holes of 0.5 mm diameter (right top) [31].

The aim of the experiments is to examine the degree to which velocity and blur affect the calibration procedure presented in the previous sections. Tests were performed up to 4000 rpm, corresponding to a tangential velocity of approximately 100 m s^{-1}, with integration times of 20 µs and 70 µs.

Typical infrared measurements of equivalent blackbody temperature T_{cam} are shown in Figure 3.17 for data acquired at 1500 rpm and 3000 rpm for both integration times. A few qualitative observations can be inferred from these results: i) the importance of high emissivity coating to minimise disturbance radiation is undeniable. The reflections from the optical access are clear in all images ($400 < y < 500$ & $160 < x < 450$). The areas with low emissivity, corresponding to the radial stripes of low T_{cam}, are clearly disturbed by the reflections whilst little difference is visible in the regions of high emissivity; ii) the set-up presents an intrinsic radial temperature distribution caused by the heating targeted at the disc outer radius; (iii) reducing

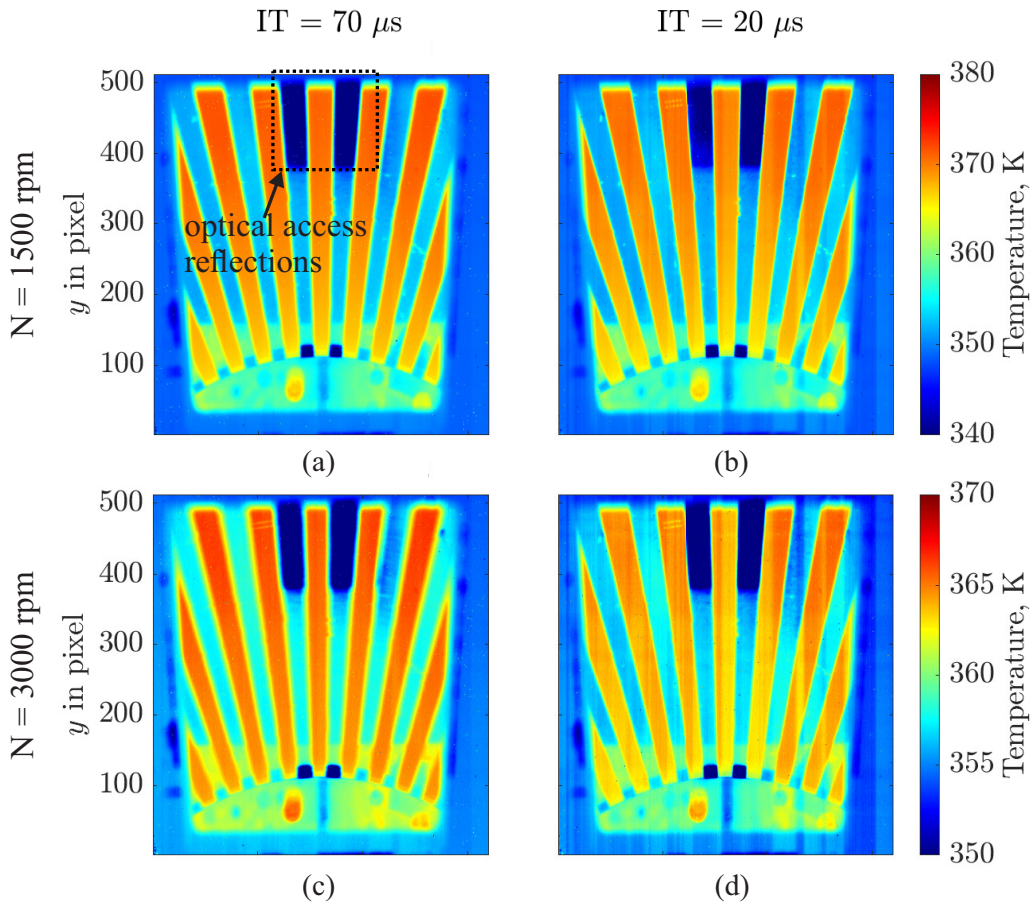

Figure 3.17: Processed images of T_{cam} at different camera integration time (IT) and disc speed (N): (a) IT=70 µs and $N = 1500$ rpm, (b) IT=20 µs and $N = 1500$ rpm, (c) IT=70 µs and $N = 3000$ rpm, (d) IT=20 µs and $N = 3000$ rpm.

integration time provides an image with sharper edges for a constant target velocity; (iv) measurement noise increases as integration time is decreased, indeed the shorter integration time limits the amount of infrared radiation detected; the phenomenon is evident as a non uniform signal even on the high emissivity regions, particularly visible for the data taken at N = 3000 rpm with 20 µs integration time on the central stripe. These observations agree with the results demonstrated previously in the steady calibration facility.

3.4.1 Emissivity and Reflections Correction with Blur

In this section the effect of rotation and motion blur on measurement accuracy is evaluated in detail. Figures 3.18a and 3.18b show the processed images of the equivalent blackbody temperature T_{cam} of the disc in the rotating facility acquired at zero speed $N = 0$ rpm and at speed of $N = 3000$ rpm respectively; both datasets were acquired with a camera integration time of 70 µs. Figures 3.18c and 3.18d depict the equivalent blackbody temperature at $y = 480$ pixel and $47 < x < 569$ pixels (range indicated with *line* in Figure 3.18). The different regions are displayed: high emissivity regions (painted part) and low emissivity regions (metallic uncoated part) alternate, with zones of blur in between for the rotating test case. The blur regions in Figure 3.18d are identified by the thresholds 'Edge' 1 and 'Edge 2'. These thresholds are defined as the temperature where the tangent to the camera signal changes. It can be inferred from Figure 3.18c that in absence of blur ($N = 0$ rpm), the signal is more similar to a square wave, where the non-perfect vertical slope is attributable to the variable paint thickness at the stripe borders, which in turns impacts the surface emissivity.

The reflections calibration requires the division of the two regions to obtain T_{cam1} (high emissivity region) and T_{cam2} (low emissivity region). Interpolation is then required to obtain the information across the entire FOV for both signals. In the case of a steady target this is a straightforward, and a simple edge detection suffices. However, separating the high emissivity signal from the low emissivity signal becomes more challenging in the case of moving target due to the presence of blur. Thus, three edge detection methods were trialled:

Method 1: The blur region was completely removed from the analysis. The high emissivity region and low emissivity regions were identified as follows:

$T_{cam1} = \{T_{cam}(x,y) \| T_{cam}(x,y) \geq Edge\,1\}$

$T_{cam2} = \{T_{cam}(x,y) \| T_{cam}(x,y) \leq Edge\,2\}$.

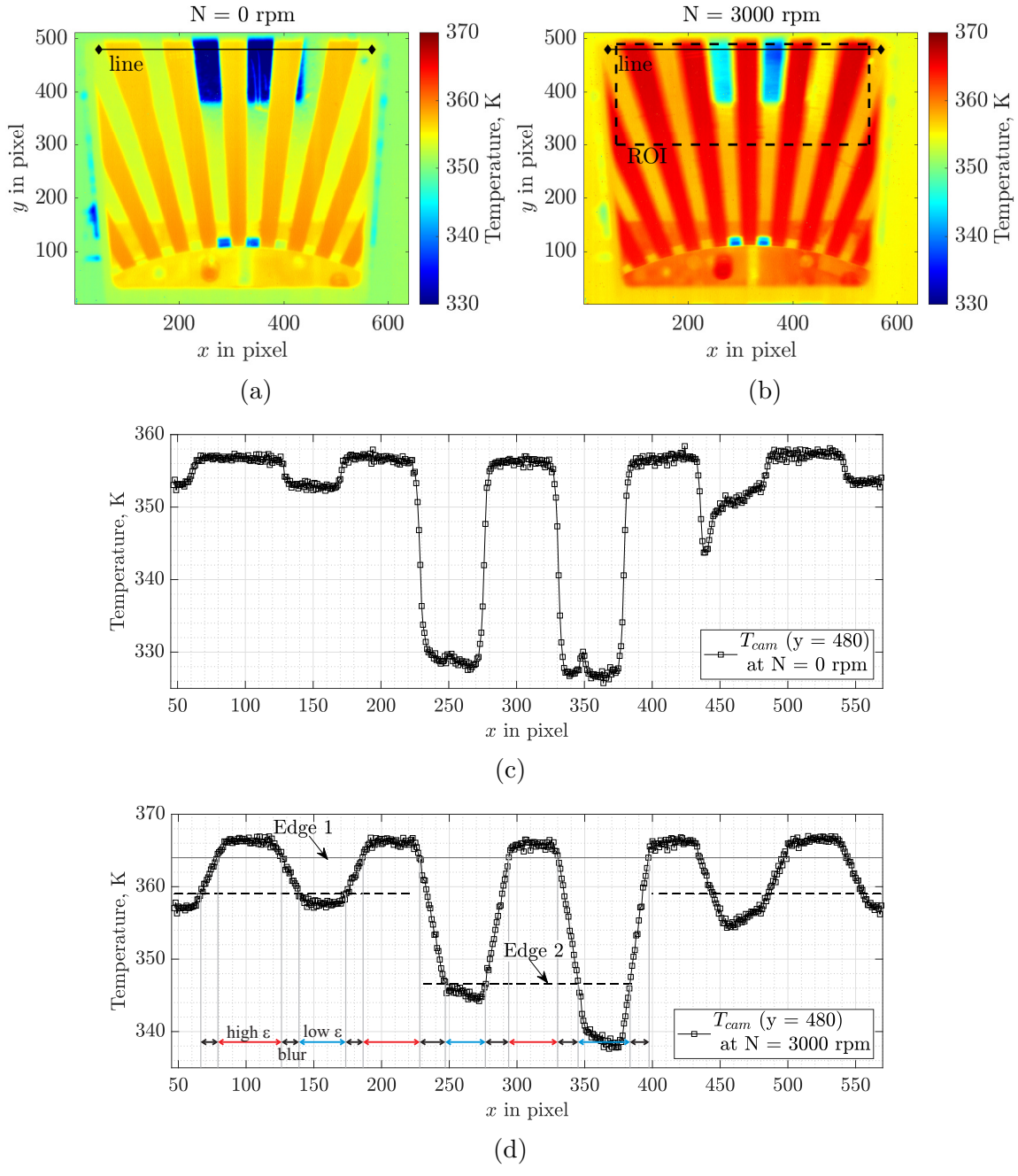

Figure 3.18: Processed images of T_{cam} for test conditions: (a) IT=70 µs and $N = 0$ rpm, and (b) IT=70 µs and $N = 3000$ rpm. Corresponding temperatures over a line for (c) IT=70 µs and $N = 0$ rpm (location $y = 480$) and (d) IT=70 µs and $N = 3000$ rpm (location $y = 400$).

Method 2: The blur was incorporated into the high emissivity region. The high emissivity region and low emissivity regions were identified as follows:

$T_{cam1} = \{T_{cam}(x,y) \| T_{cam}(x,y) \geq Edge\,2\}$

$T_{cam2} = \{T_{cam}(x,y) \| T_{cam}(x,y) \leq Edge\,2\}$.

Method 3: The blur was incorporated into the low emissivity region. The high emissivity region and low emissivity regions were identified as follows:

$T_{cam1} = \{T_{cam}(x,y) \| T_{cam}(x,y) \geq Edge\,1\}$

$T_{cam2} = \{T_{cam}(x,y) \| T_{cam}(x,y) \leq Edge\,1\}$.

A Region of Interest (ROI) was defined on the camera temperature map ($T_{cam}(x,y)$), as shown with a dashed line in Figure 3.18b. Subsequently, the signals T_{cam1} and T_{cam2} were identified by using the methods described above, obtaining Figure 3.19a with method 1, Figure 3.19b with method 2, and Figure 3.19c with method 3. Having observed the intrinsic radial temperature distribution of the rig, the interpolation of T_{cam1} and T_{cam2} was carried out radially. Finally, Equation 3.8 and Equation 3.9 were used to calculate the target temperature and the reflected temperature from the camera signal.

The calibrated signal $T_t(x,y)$ and the reflected temperature $T_r(x,y)$ are shown in Figure 3.20a, 3.20b, 3.20c for the respective edge detection methods. For all methods, T_t is found to be higher than T_{cam}. This can be explained by observing that the target is hotter than the surroundings ($T_t = 366\,\mathrm{K}$, while $335 < T_r < 360\,\mathrm{K}$), which therefore have the effect of lowering the signal reaching the camera.

With removal of the blurred region from the assessment of T_{cam1} and T_{cam2} (*method 1*), the target temperature was successfully reconstructed across the entire area. An approximately constant temperature distribution resulted, with almost no disturbance between the low and high emissivity regions (no border effects on the regions affected by reflections). This calibration method provided the best reconstructed signal.

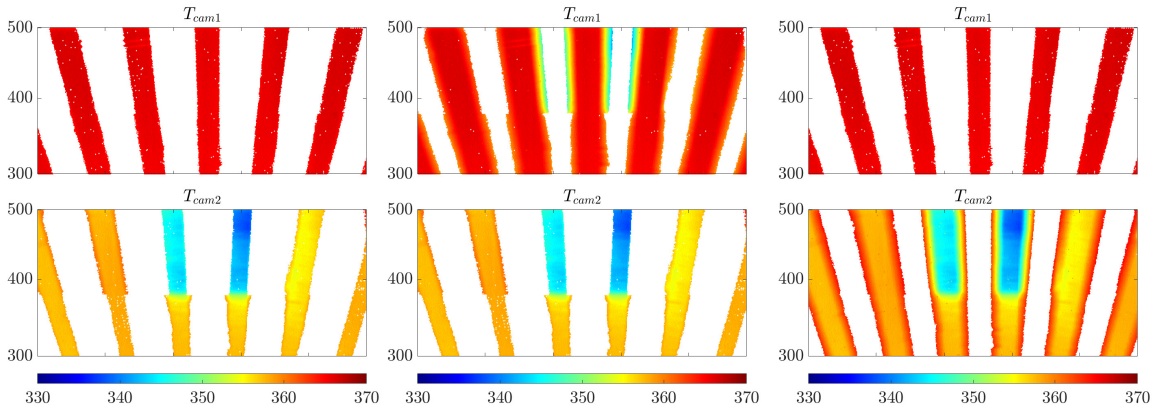

(a) (b) (c)

Figure 3.19: Identification of high and low emissivity regions, T_{cam1} and T_{cam2} respectively, on IR images of the flat disc by using (a) Method 1, (b) Method 2, and (c) Method 3.

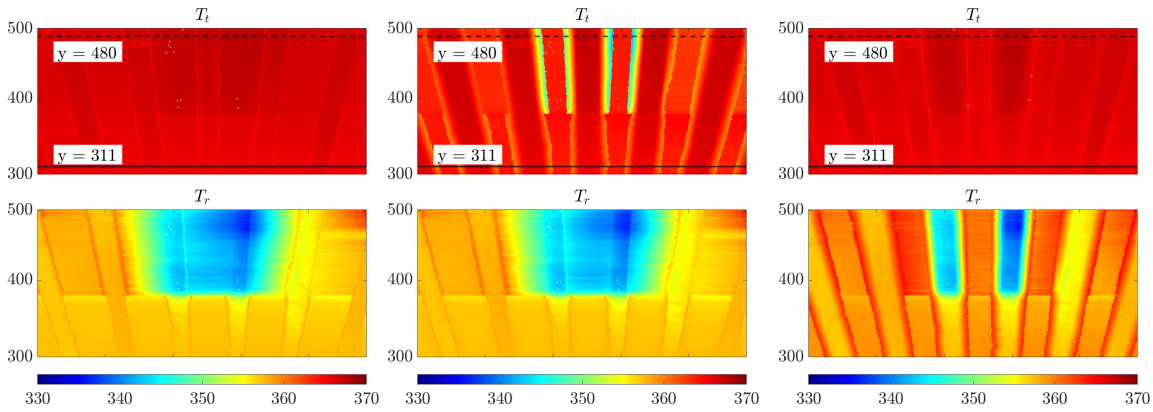

(a) (b) (c)

Figure 3.20: Maps of reconstructed target and reflected temperature, T_t and T_r, obtained with (a) Method 1, (b) Method 2 and (c) Method 3.

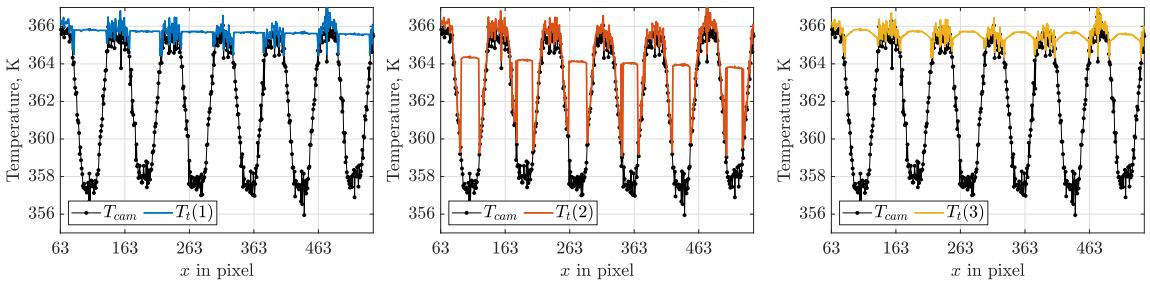

(a) (b) (c)

Figure 3.21: Equivalent blackbody and target temperatures at location $y = 311$ using (a) Method 1, (b) Method 2, and (c) Method 3.

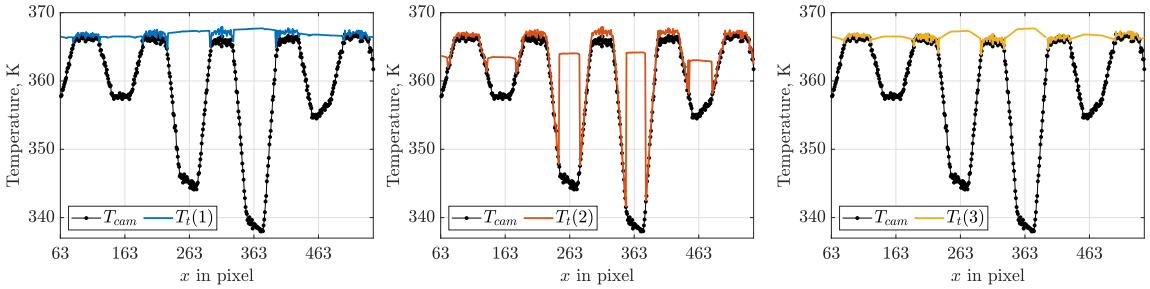

(a) (b) (c)

Figure 3.22: Equivalent blackbody and target temperatures at location $y = 480$ using (a) Method 1, (b) Method 2, and (c) Method 3.

A second comparison between the different methods is presented in Figures 3.21 and Figure 3.22, showing the calibrated target temperature and the camera temperature at locations $y = 311$ and $y = 480$, respectively. The two locations were chosen to show how the calibration performs in the ideal instance of constant reflection signal, as for $y = 311$, and in the instance of strongly spatial dependent reflection signal, as for $y = 480$ where the presence of the window causes the outside environment to affect the measurement.

The calibration carried out incorporating blurred data to T_{cam1} (*method 2*, Figures 3.21b and 3.22b) effectively calibrated the high emissivity signal, however it struggles to achieve the same degree of accuracy in the low emissivity region. The temperature difference between the high-emissivity region and the low emissivity region is approximately 2 K. In addition, a clear border effect was found in the blur region with a maximum temperature difference between the high and low emissivity regions of 7 K at location $y = 311$ and of approximately 20 K at location $y = 480$.

The calibration carried out incorporating the blurred region to T_{cam2} (*method 3*, Figures 3.21c and 3.22c) performs almost as well as the calibration achieved by removing the blurred region (*method 1*, Figures 3.21a and 3.22a). Nevertheless, a non-real parabolic temperature profile is found. The temperature difference between the high-emissivity region and the low emissivity region is approximately 0.5 K. The

border effect is still being visible, however its magnitude is reduced to a maximum temperature difference of 1 K at both locations $y = 311$ and $y = 480$.

Having concluded that calibrating using *method 1* gives the most realistic signal, a true target temperature was defined for each radius by radially averaging the signal obtained with this correction: $T_{tt}(y) = \sum_x T_{t,method1}(x, y)$. It was therefore possible to define the error resulting from blur as the difference between the true target temperature and the temperature obtained with the post-calibration, as follows:

$$Error, \% = \frac{T_{tt}(y) - T_{t,calib}(x, y)}{T_{tt}(y)} \cdot 100 \tag{3.10}$$

The errors at location $y = 311$ and $y = 480$, are shown in Figure 3.23. As expected, the highest errors appear when *method 2* is used to calibrate the signal. By including the blur into the high emissivity region, the residual error in the low emissivity region is of 0.5%, while in the blur region the error goes from 0.5% to 1.7% at $y = 311$ and from 0.5% to 7% at $y = 480$. Lower error levels are found with the use of *method 3*, where the error ranges from 0% to 0.2% at both locations $y = 311$ and $y = 480$. The errors at location $y = 311$ and $y = 480$, are shown in Figure 3.23. As expected, the highest errors appear when *method 2* is used to calibrate the signal. By including the blur into the high emissivity region, the residual error in the low emissivity region is of 0.5%, while in the blur region the error goes from 0.5% to 1.7% at $y = 311$ and from 0.5% to 7% at $y = 480$. Lower error levels are found with the use of *method 3*, where the error ranges from 0% to 0.2% at both locations $y = 311$ and $y = 480$.

The results show that careful considerations need to be taken before applying the calibration to blurred images. The first edge detection presented removed completely the blur from the analysis, and the method was successful in calibrating the target signal. In the Oxford Turbine Research Facility, measurements of reflected temperature will be acquired from a blade with low emissivity, this is described in details in Chapter 5.

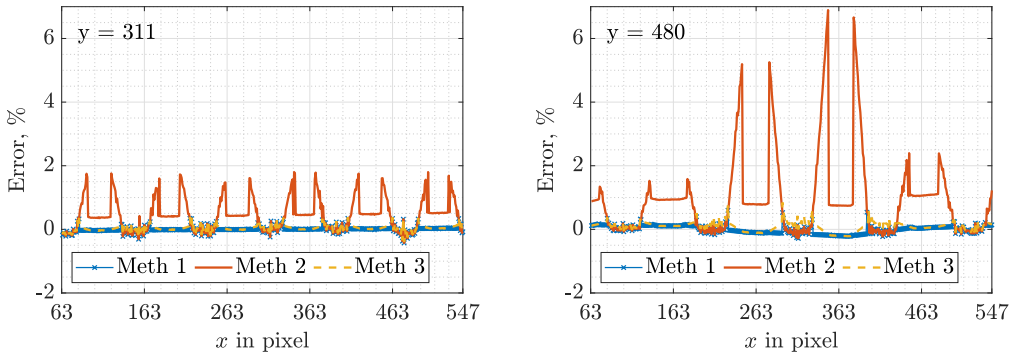

(a) (b)

Figure 3.23: Errors after calibration at locations (a) $y = 311$; (b) $y = 480$.

3.5 Quantifying Uncertainty in Target Temperature and Metal Effectiveness

The uncertainty analysis of the calibration procedure to determine the target temperature T_t are summarised in Table 3.6 and Table 3.7.

The results of the uncertainty analysis are obtained for four target temperatures, between 323.15 K and 473.15 K. The analysis is divided into: detector calibration, emissivity calibration, transmittance calibration, and target temperature. The uncertainty associated with the detector calibration, $U_{T_{cam}}$, arises from the combined errors in the reference blackbody source, $U_{T_{bb}}$, and the error from the fourth order polynomial fitting, $U_{fitting}$, which has second order influence. The uncertainty in the directional emissivity, U_{ε}, and transmittance, U_{τ}, stem from error propagation associated with Equation 3.5 and Equation 4.12, respectively. Uncertainty on reference thermocouples were taken from manufacturer specifications. Both errors reduce as target temperature increases.

To evaluate the uncertainty in the target temperature, as calculated from Equation 3.8, expected values in the OTRF were used: $T_{opt} = 430\,\text{K}$ and $T_r = 550\,\text{K}$, $\tau = 0.95$, $\varepsilon_1 = 0.94$, $\varepsilon_2 = 0.04$. The uncertainty in the calculated T_t arises from the propagation errors of the previously listed errors. Based on the analysis, target

temperature errors range from ±14 K (4.35%) for $T_t = 323.15$ K, to ±2.36 K (0.5%) for $T_t = 473.15$ K, in absolute terms. The higher error for $T_t = 323.15$ K arises from the combination of low target temperature and high reflected temperature. Indeed, if a reflected temperature of $T_r = 298$ K was used the uncertainty calculation would range from ±2.85 K for $T_t = 323.15$ K, to ±1.43 K for $T_t = 473.15$ K. It is noted that the two results differ mostly for very low target temperatures.

Table 3.6: Calibration uncertainty analysis, assuming $\tau = 0.95$, $\varepsilon = 0.95$, $T_r = 298$ K, $T_{opt} = 298$ K.

Detector					
		323.15 K	373.15 K	423.15 K	473.15 K
$U_{T_{bb}}$	blackbody calibrator, K	±1.65	±1.99	±1.84	±1.82
$U_{fitting}$	rmse, K	±0.15	±0.18	±0.18	±0.18
$U_{T_{cam}}$	IR camera, K	±1.65	±2.00	±1.84	±1.82
Emissivity					
		323.15 K	373.15 K	423.15 K	473.15 K
$U_{T_{cam}}$	IR camera, K	±1.65	±2.00	±1.84	±1.82
$U_{T_{TC}}$, U_{T_S}	T-type thermocouple, K	±1.29	±1.49	±1.69	±1.89
U_ε	Emissivity	±0.02	±0.01	±0.01	±0.01
Transmittance					
		323.15 K	373.15 K	423.15 K	473.15 K
$U_{T_{cam}}$	IR camera, K	±1.65	±2.00	±1.84	±1.82
$U_{T_{bb}}$	blackbody calibrator, K	±1.65	±1.99	±1.84	±1.82
$U_{T_{opt}}$	T-type thermocouple, K	±1.29	±1.49	±1.69	±1.89
U_τ	Transmittance	±0.01	±0.01	±0.01	±0.01

Table 3.7: Target temperature uncertainty analysis, assuming $\tau = 0.95$, $\varepsilon_1 = 0.94$, $\varepsilon_2 = 0.04$, $T_r = 550$ K, $T_{opt} = 430$ K.

		323.15 K	373.15 K	423.15 K	473.15 K
$U_{T_{cam1}}$, $U_{T_{cam2}}$	IR camera, K	±1.65	±2.00	±1.84	±1.82
$U_{\varepsilon 1}$, $U_{\varepsilon 2}$	Emissivity	±0.02	±0.01	±0.01	±0.01
U_τ	Transmittance	±0.01	±0.01	±0.01	±0.01
U_{T_t}	IR calibration, K	±14.0	±5.30	±3.14	±2.36
U_{T_t}	IR calibration, %	4.35	1.42	0.74	0.50

Another outcome from the IR measurement system is to assess cooling and metal

effectiveness in the OTRF. Metal effectiveness provides a non-dimensional surface temperature scalable to engine conditions, and it is defined as

$$\eta = \frac{T_g - T_t}{T_g - T_c} \tag{3.11}$$

The target temperature, T_t, is calculated according to Equation 3.2, T_c and T_g are coolant and gas temperatures, respectively, equal to $T_c = 290\,\mathrm{K}$ and $T_g = 473\,\mathrm{K}$.

The computed uncertainties in the measurement of metal effectiveness, η, were evaluated for blade temperatures between $100 - 200°\mathrm{C}$. The results presented in Table 3.8 were obtained using typical uncertainty in coolant and inlet gas temperatures of ± 1 K and ± 2.5 K, respectively. The bias error in η ranges from ± 0.03 to ± 0.01, in absolute terms. It is noteworthy that precision (or repeatability) errors, which indicate the capability of the measurement system to detect variations in metal effectiveness due to variations in turbine operational conditions or in blade cooling technologies, have not been considered in this preliminary analysis as they are anticipated to be significantly smaller than the reported bias errors.

Table 3.8: Metal effectiveness uncertainty analysis.

T_t	Blade temperature	373.15 K	398.15 K	423.15 K	448.15 K	473.15 K
η	Metal effectiveness	0.55	0.41	0.27	0.14	0
U_η	Metal effectiveness	± 0.03	± 0.02	± 0.01	± 0.01	± 0.01

3.6 Summary

In this chapter, a novel method to calibrate and perform high-accuracy infrared measurements on high-speed targets in the Oxford Turbine Research Facility has been developed.

The sources of error arising from the specific experimental environment have been presented, and the detector selection process based on the experimental constraints has been described, leading to the selection of a photon detector camera FLIR A6751 SLS LWIR.

The camera detector was calibrated pixel-by-pixel at various integration times, ranging from 5 µs to 70 µs, against traceable blackbody sources with a maximum uncertainty of ±0.5% of the target temperature. Analysis of the signal-to-noise ratio, as a function of integration time and equivalent blackbody temperature was performed, highlighting the importance of assessing the combination of signal intensity and integration time to ensure minimal noise effects.

A bespoke facility was developed to accurately characterise directional emissivity and transmittance; both to within ±0.01. Two post-test analysis methods to assess surface emissivity calibration methods were presented. For accurate results, the first method must be used with a significant temperature difference between the target and surroundings. A temperature difference of at least 60 K is recommended. The second method requires data at two different target temperatures and displays results that are invariant with target temperature.

To understand the impact of motion blur, a reflection calibration method was tested in a rotating facility. Three different corrections for blur were presented: the first artificially eliminates the motion blur before the correction, while the second and the last incorporate the blur in the high-emissivity and low-emissivity region respectively. The first correction is the only method that successfully calibrated the signal across the entire Field of View. However, in experiments with highly spatial temperature variation, removing data would reduce the spatial resolution of the technique, potentially leading to higher errors. In such situations, applying deblurring techniques is recommended.

The results from the calibration outlined demonstrate that the absolute uncertainty on the target temperature varies from ±5.30 K at $T = 373.15$ K to ±2.36 K at $T = 473.15$ K. These would translate into an uncertainty in metal effectiveness of approximately ±0.03 and ±0.01, respectively - equivalent to a real engine metal temperature variation of ±7 K, significantly smaller than the resolution of modern

thermal paints ($\pm 4\%$ or $\pm 50\,\mathrm{K}$). Subsequently, the presented approach is expected to yield valuable and accurate heat transfer and metal effectiveness data.

The validation of this approach on OTRF data is shown in Chapter 5, whilst the following Chapter 4 focuses on the design efforts necessary to implement the IR measurement system in the OTRF.

Chapter 4

Development of an Infrared Thermography System for Transient Heat Transfer Measurements in a Rotating Facility

This chapter outlines the development and implementation of the IR measurement system for the Oxford Turbine Research Facility, focusing on the facility and testing programme description in the initial part. The subsequent section focuses on the design requirements necessary to employ IR thermography in a short duration rotating facility capable of matching engine conditions. Two key design solutions are presented: achieving optical to the turbine stage and designing a composite blade for accurate heat transfer measurement.

The window design strategy was influenced by the effusion cooling programme and restricted optical access on the rotor due to effusion cooling segments geometry. Additionally, the maximum temperature and pressure conditions reached in facility influenced both the window geometry and material selection.

The need of composite blades was dictated by the nature of heat transfer analysis in short duration facilities, like the OTRF. The analysis of adiabatic wall temperature and heat transfer coefficient is based upon the relationship between the measured sur-

face temperature T_w and the heat flux $\dot{q}$ computed using the impulse response method by Oldfield [53]. This procedure necessitates of two conditions: a substrate for which the 1D assumption is valid, and an appreciable temperature rise on the specimen surface. In the instance of thin-film gauges application, layers of low-conductivity material, such as Kapton, are used to meet these conditions. The proposed composite blade design for IR thermography achieves similar results.

The camera synchronisation and triggering system are described. Finally, two blades were instrumented with thin-film gauges to use for IR data validation. The manufacturing and calibration procedures for these blades are described at the end of the chapter.

4.1 The Oxford Turbine Research Facility

The Oxford Turbine Research Facility (OTRF) is a short duration light piston tube facility of engine scale developed for turbine aerodynamics and heat transfer investigations. The facility is capable of testing high pressure turbine stages with or without an intermediate pressure or low pressure stator. Furthermore, the facility is able to match engine Mach and Reynolds numbers, non-dimensional speed and gas-to-wall temperature ratio.

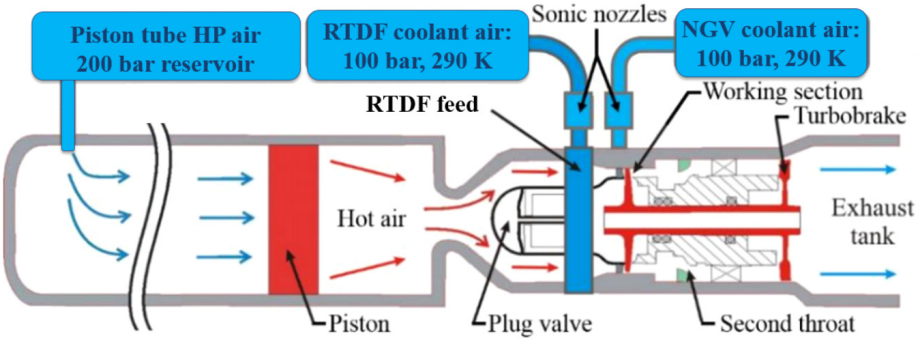

Figure 4.1: Schematic of the Oxford Turbine Research Facility.

A schematic of the OTRF is shown in Figure 4.1. The rig consists of four main sections: the pump-tube enclosing a light weight piston, a fast acting plug valve, the working section and a dump tank. Before starting a test, the plug valve is closed and air is evacuated from the working section and dump tank to attain a state of vacuum of approximately 10 mbar; this condition enables the turbine rotor to be spun by an air motor minimising windage losses and heating. Once the turbine has been spun to the desired speed, high pressure air is injected behind the free piston that travels down the piston tube, thereby isentropically compressing the test gas in front of the piston. When the desired stagnation temperature and pressure inlet conditions are achieved, the fast acting valve is triggered to allow the hot gas to flow into the test section. During this phase, the volumetric flow of gas that is injected behind the piston is matched to that leaving the tube to maintain a constant pressure and

temperature. The turbine exit pressure is regulated by the adjustable annular second throat, which is chocked to isolate the turbine from any downstream effects. Inlet and exit pressure are tuned to achieve the required stage pressure ratio and Reynolds number. Downstream of the second throat, an aerodynamic turbobrake is mounted on the rotor shaft [128]. The turbobrake permits the rotor speed to stay within ±10 rpm, thus, to remain approximately constant, enabling stable aerodynamics conditions during the test run that lasts approximately 400 ms.

In the following subsections the turbine stage, combustor simulator, instrumentation, and rig data processing in the OTRF are discussed.

4.1.1 The SILOET HP Turbine Stage

The HP turbine installed in the OTRF for this research is a single stage shroudless geometry optimised for lean burn combustor exit profile [129]. The design was funded by the SILOET 5.1 (Strategic Investment in Low-carbon Engine Technology) project. The annulus is scaled to 73% of a modern large civil aero-engine. The CAD models of NGV and rotor blades are illustrated in Figure 4.2. The turbine consists of 40 cooled nozzle guide vanes (NGV) with a subsonic exit and a transonic rotor consisting of 60 uncooled blades with 50% reaction. The NGV design features two internal cavities to feed the cooling scheme, which includes ten rows of film cooling holes, five on

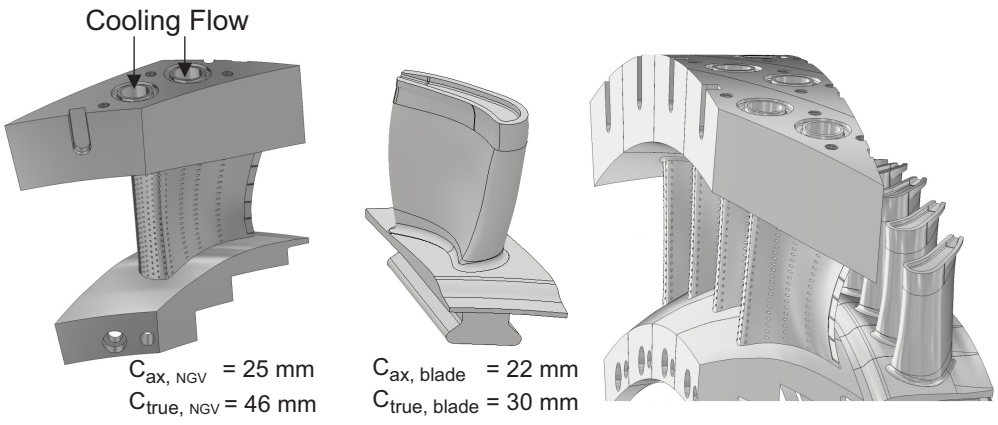

Figure 4.2: SILOET turbine NGV and blades.

the pressure side and five on the suction side. The trailing edge cooling consists of five slots extending from 4% to 96% of the blade height. The coolant, stored in an independent external reservoir as depicted in Figure 4.1, is introduced prior to the opening of the plug valve from the case of the vane and the total feed temperature is at ambient condition, approximately 290 K. The rotor blades feature a standard double squealer tip design, with a 0.6% span tip gap (tip clearance set at 0.62 mm), this representative of design tip gaps in an engine. The turbine operating conditions are summarised in Table 4.1.

Table 4.1: SILOET turbine design conditions in the OTRF.

Parameter	Symbol	Unit	Nominal value	run-to-run variability
Vane inlet total pressure	p_{01}	bar	5.4	±1%
Vane inlet total temperature	T_{01}	K	475	±2%
Vane inlet mass flow	$\dot{m}_{in}$	$\mathrm{kg\,s^{-1}}$	16.75	—
Vane cooling mass flow	$\dot{m}_{c,\mathrm{NGV}}$	$\mathrm{kg\,s^{-1}}$	1.41	±1%
Rotor exit static pressure	p_2	bar	2.05	—
Stage total-to-static pressure ratio	p_{01}/p_3	bar	2.63	±2%
Wall temperature	T_{wall}	K	290	—
Gas-to-wall temperature ratio	T_{01}/T_{wall}	K	1.64	±2%
Speed	N	rpm	8500	±1%
Corrected speed	$N/\sqrt{T_{01}}$	$\mathrm{rpmK^{-1}}$	390	±1%

4.1.2 Combustor Simulator

The facility has capability to simulate the time-average gas temperature profile at the exit of rich and lean-burn combustors thanks to a combustor simulator. The commissioning of the simulator was presented in [130] while the methodology for the designed was detailed in [131]. The simulator, shown in Figure 4.3, was conceived in a modular way, allowing the simulation of a variety of temperature distribution with different traverse profile and swirl magnitude.

Tests in the OTRF are conducted with two inlet conditions: uniform temperature T_{01} and pressure p_{01} distribution, and radial temperature T_{01} distribution with

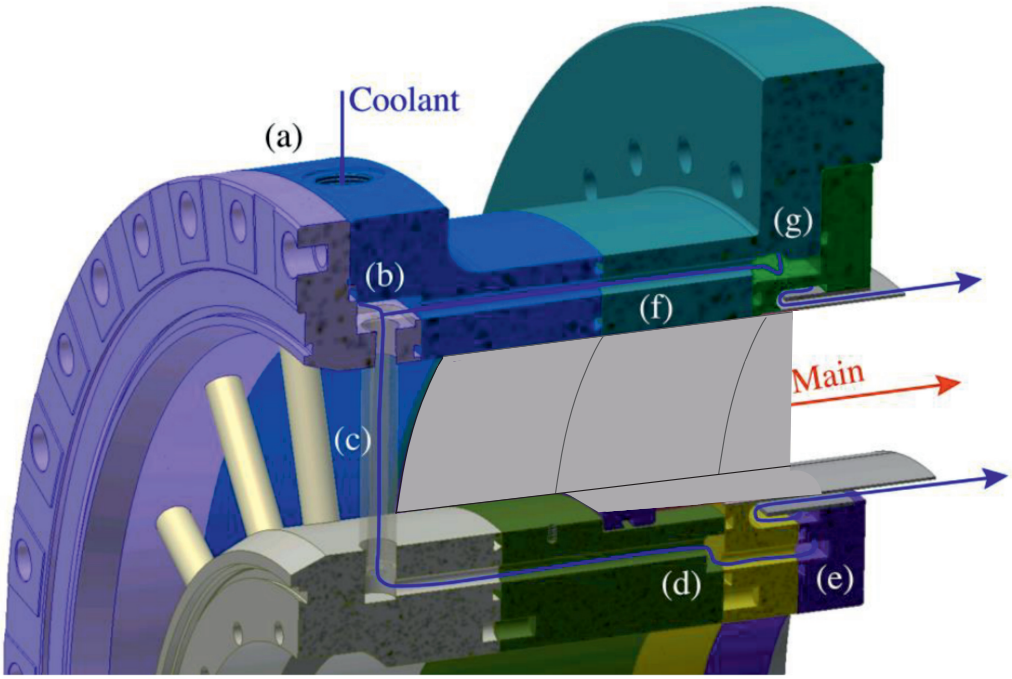

Figure 4.3: CAD model of the combustor simulator showing (a) coolant entry location, (b) coolant plenum, (c) hub feed rod, (d) hub coolant feed, (e) hub injection plenum, (f) casing coolant feed, (g) case injection plenum. Modified from [130].

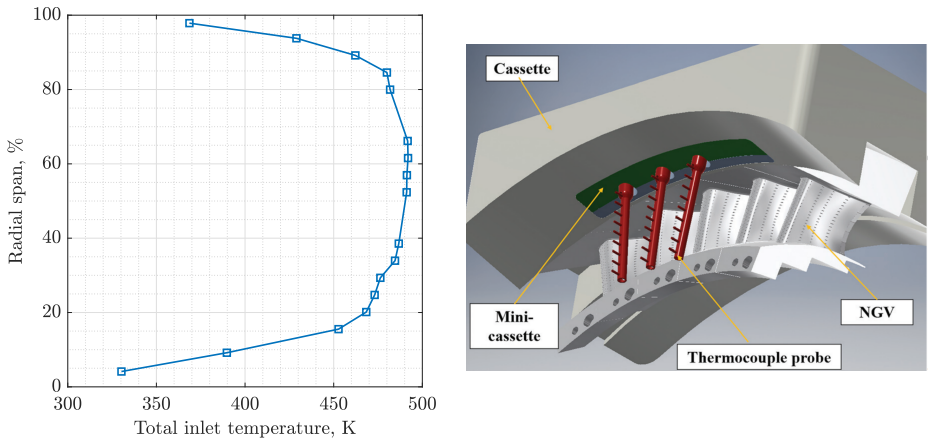

(a) (b)

Figure 4.4: (a) Radial inlet temperature profile achieved in the OTRF. (b) View of of sector of the NGV during the temperature survey [132]; thermocouple probes are radially mounted on three rakes upstream of the NGV inlet.

no swirl and uniform pressure p_{01} distribution. Achieving the radial with no swirl temperature profile involves injecting hub and casing coolant from 'e' and 'f' in Figure 4.3, namely the Radial Temperature Distortion Factor (RTDF). The RTDF cold flow is injected at ambient condition, with a temperature of approximately 290 K, from an independent external reservoir as depicted in Figure 4.1. This mass of cold flow, injected upstream of the turbine stage, mixes with the hot stream of compressed air coming from the pump tube, thus generating a radial temperature profile, like the one shown in Figure 4.4a. The amount of RTDF coolant necessary for achieving the radial distortion representative of real engine conditions was quantified in a preliminary survey carried out by Singh et al. [132]. The profile was measured one and half NGV axial chords upstream of the NGV leading edge, Figure 4.4b depicts the setup used for the the measurement campaign.

In tests with uniform inlet conditions, the simulator has a passive role, with no RTDF coolant being injected, and the hot volumetric flow of gas coming from the pump tube flows into the turbine stage unperturbed.

4.1.3 Data Acquisition and Instrumentation

Data from the facility is acquired at low speed (LS) and high speed (HS). The LS Data Acquisition system reads up to 304 signals at standard sampling rate of 2000 Hz, and primarily reads signals from thermocouples, pneumatic pressure transducers and heat transfer thin-film gauges. The HS Data Acquisition system samples up to 48 signals simultaneously at 1 MHz, and primarily acquires signals from the rotational speed optical sensors, heat transfer gauges and piezoresistive pressure sensors (kulites). At this sample rate, acquisition of blade passing events at approximately 10 kHz and turbulence spectra is possible.

The instrumentation in the facility away from the working section is schematically depicted in Figure 4.5, and a discussion of the measurements at each location is

presented below. All pressure measurements are taken with Series CTE8000 Sensor Technics transducers with a nominal accuracy of 0.05% at full-scale unless quoted.

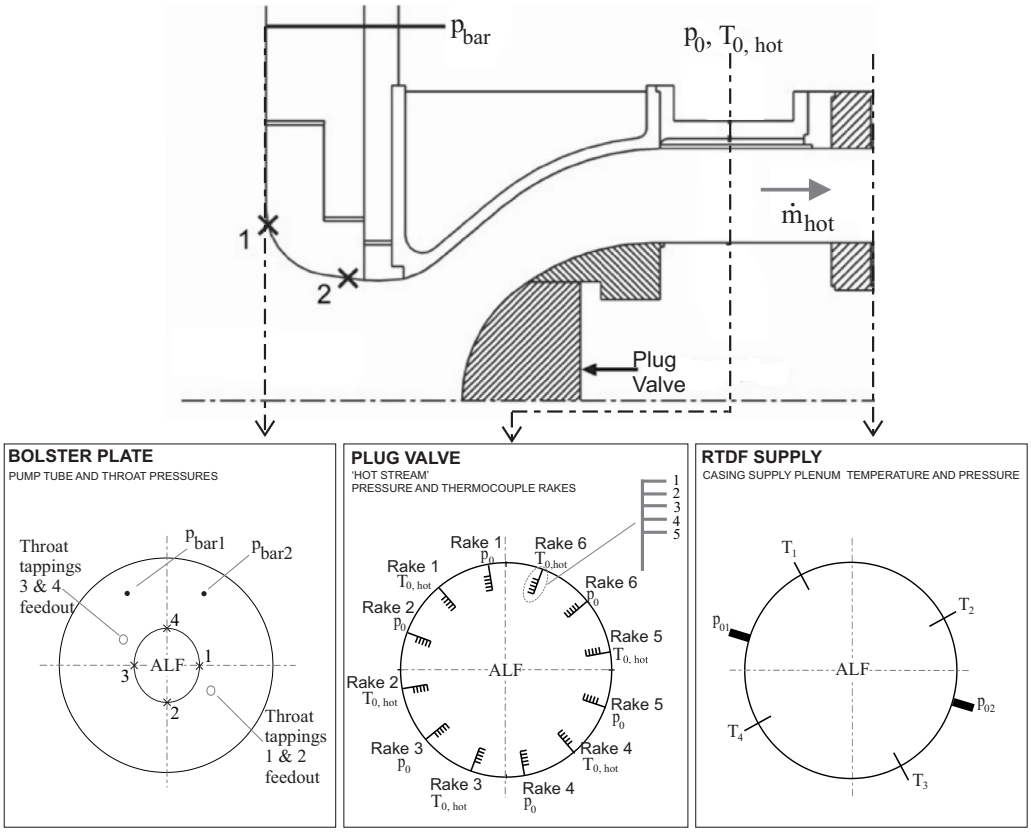

Figure 4.5: Measurement locations away from the working section in the OTRF. The acronym ALF stands for Aft Looking Front.

- Location: bolster plate plane. The pump tube total pressure p_{bar} is measured from two pneumatic tappings on the end-wall of the piston tube. The throat exit contraction is instrumented with four evenly spaced differential pressure measurements. The upstream total pressure tapping is marked '1' and the static pressure tapping is marked '2' in Figure 4.5. The pressure $p_1 - p_2$ is measured by differential Series BTEM Sensor Techniques transducers with $\pm 1\%$ nominal accuracy. The location of the static pressure tapping was optimised using CFD by Beard et al. [133] to ensure these were upstream of possible areas of flow separation. These instruments are used to measure mass flow rate through the piston tube exit contraction.

- Location: plug valve. The total temperature and pressure of the air exiting the piston tube (hot stream) is measured at the plug valve plane, upstream of the combustor simulator, using six rakes evenly distributed circumferentially for each measurement type. Each rake contains five radially distributed thermocouples or pneumatic pressure tappings, providing up to 30 measurements for each parameter. To achieve the required frequency response, 25.4 µm diameter bare bead k-type thermocouples are used. The Mach number in this region is approximately 0.05.

- Location: RTDF supply plane. Total pressure and temperature of the RTDF coolant are measured at the supply plenum on the casing. The total pressure is measured at two circumferentially evenly distributed locations, while the total temperature is measured at four circumferentially evenly distributed locations. For the temperature measurements 3″ thou (76.2 µm) diameter bare bead k-type thermocouples are used.

The instrumentation in the working section of the facility is schematically depicted in Figure 4.6, and a discussion of the measurements at each location is presented below. All pressure measurements are taken with Series CTE8000 Sensor Technics transducers with a nominal accuracy of 0.05% at full-scale unless quoted.

- Location 1: vane inlet plane, approximately 37.5 mm upstream of vane leading edge at casing. Total pressure and temperature are recorded at the vane inlet plane. Four circumferentially evenly distributed rakes of five pitot probes are used to measure the NGV inlet total pressure. Rakes of five 25.4 µm diameter bare bead k-type thermocouples are used to measure the total temperature, offset from the pressure rakes by one vane pitch (9 °).

- Location 2: vane exit plane, approximately 2 mm downstream of vane trailing edge at casing. The static pressure on the casing is measured at the vane exit

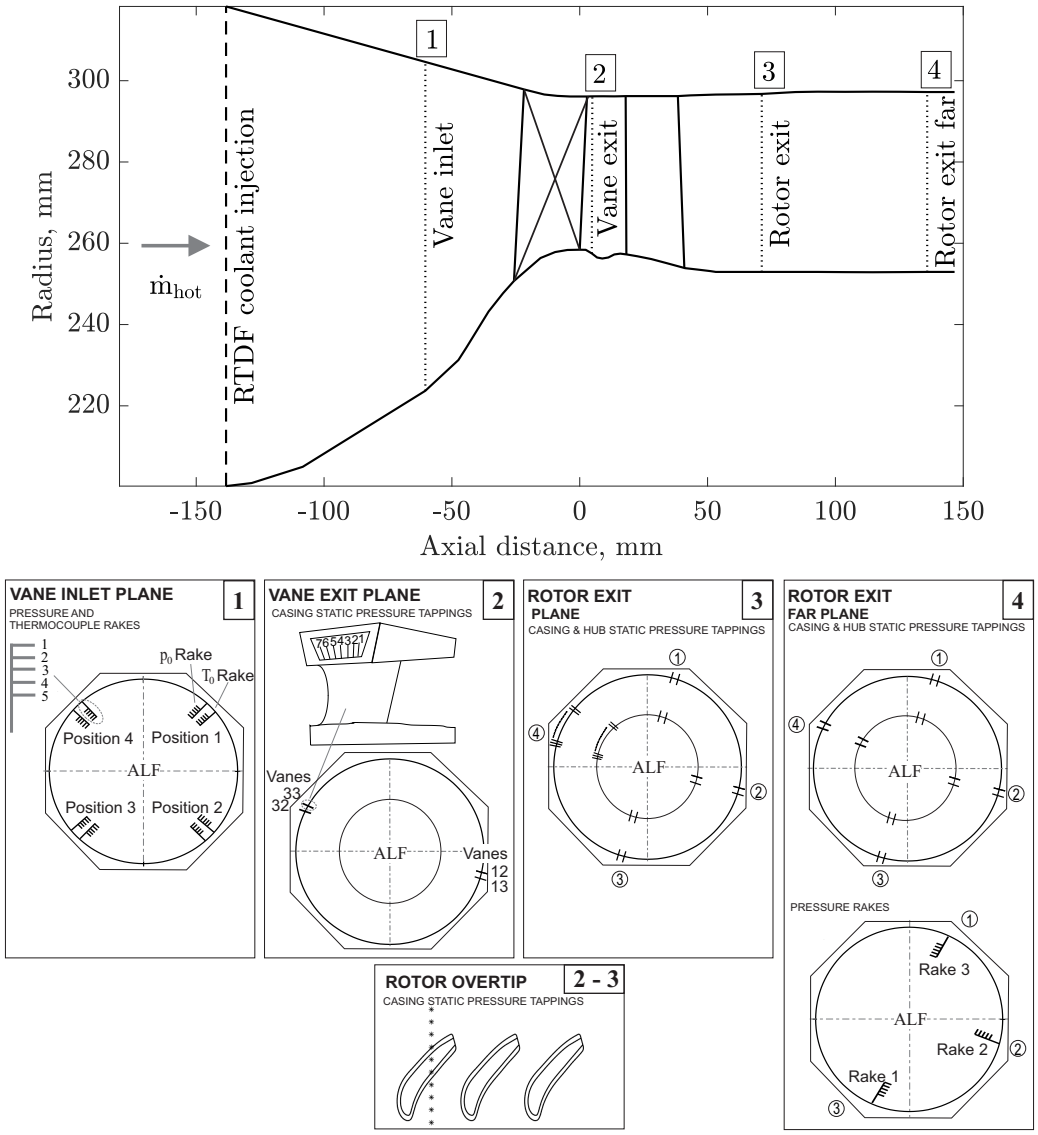

Figure 4.6: Measurement locations in the OTRF working section.

plane. Fourteen pressure tappings are evenly distributed at the exit of two vane passages (vane 12 and vane 13), seven in each passage.

- Location 2 - 3: rotor overtip. Ten tappings are axially evenly spaced over the rotor tip. These are spaced evenly, and and extend axially between −1.2mm to +40mm from rotor LE.

- Location 3: rotor exit plane, approximately 33 mm downstream of rotor trailing edge. Casing static pressure tappings are located at four circumferentially

evenly distributed locations. At circumferential location 4, 18 tappings are evenly distributed across two vane pitches on both hub and casing walls. At circumferential locations 1, 2 and offset by 90, 180 and 270 deg from location 4, two measurements are spaced by 9-deg on each wall.

- Location 4: rotor exit far plane, approximately 97 mm downstream of rotor trailing edge at casing. Casing and hub static pressure tappings at four locations evenly circumferentially spaced. Two measurements spaced by 9-deg on each wall are found at each location. In addition, three total total pressure rakes of four pitot tube each are located at three circumferential locations.

4.1.4 Rig Conditions Processing

Time traces of inlet total pressure and temperature, rotor exit static pressure, total-to-static pressure ratio and shaft speed during a typical run with uniform inlet condition in the OTRF are shown in Figure 4.7. Vacuum and ambient temperature are the conditions at the beginning of the test. The vane and RTDF cooling flows are injected prior to the opening of the plug valve, and can be seen in the pressure and temperature traces by a rise at $t = 1.9\,\mathrm{s}$. The rise in total temperature is a result of isentropic compression. At $t = 2.43\,\mathrm{s}$ the plug valve opens and the inlet total pressure and temperature increase. At $t = 2.60\,\mathrm{s}$ inlet total pressure and total temperature reach quasi-steady conditions, with mean values equal to the design ones ($p_{01} = 5.4\,\mathrm{bar}$; $T_{01} = 475\,\mathrm{K}$). The test run ends when the piston reaches the end of the piston tube at $t = 2.92\,\mathrm{s}$. As a result, the run window is approximately 300 ms. Throughout the run, the inlet total temperature mirrors the inlet total pressure almost isentropically, and the turbine speed remains approximately constant at the design value of 8500 rpm. Fluctuations in stage inlet total pressure are caused by piston oscillation at $\approx 16\,\mathrm{Hz}$ and reflection of pressure wave travelling through the facility at $\approx 70\,\mathrm{Hz}$ [134].

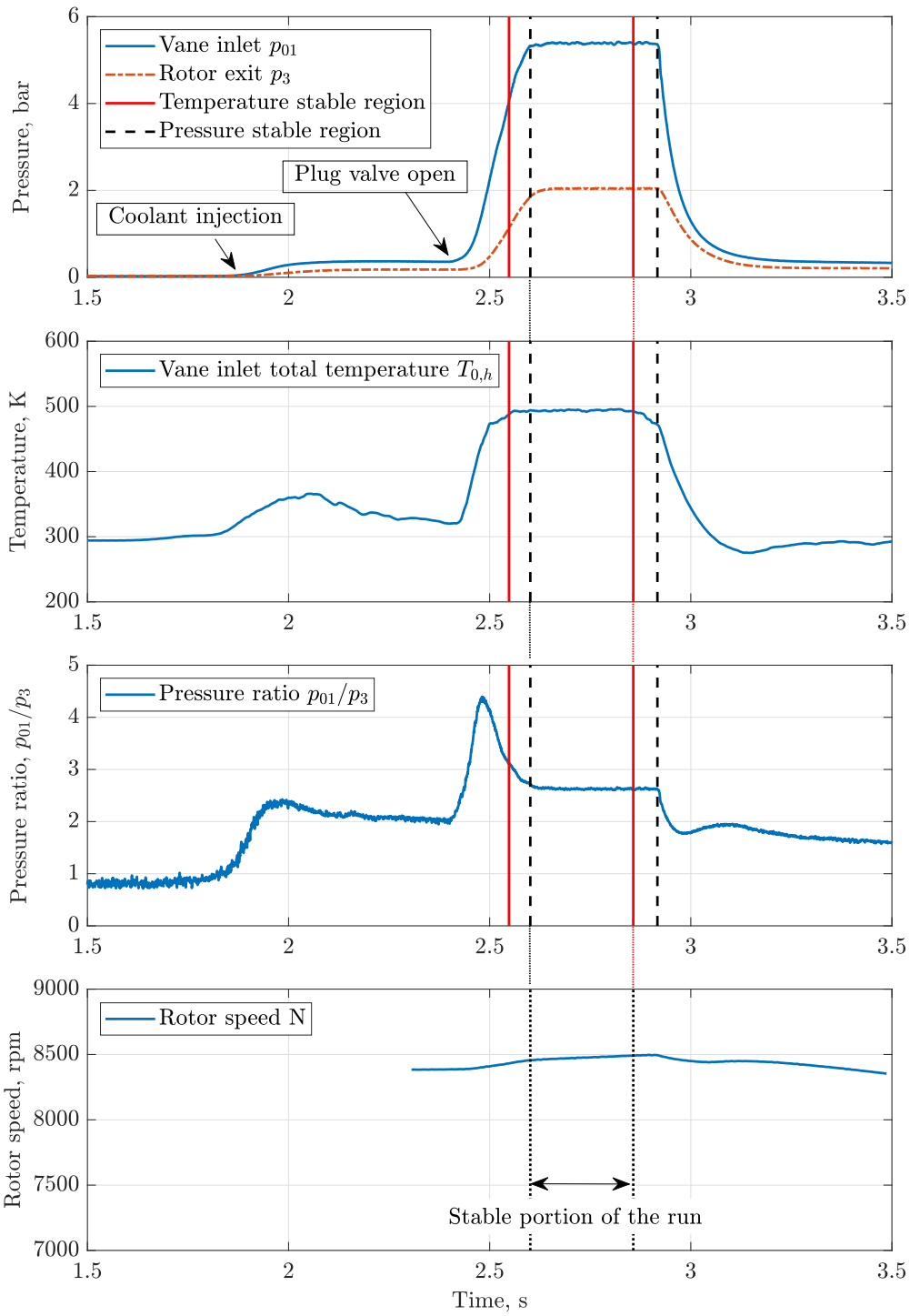

Figure 4.7: Typical traces of mean level time histories for stage inlet total pressure p_{01} and rotor exit static pressure p_3, stage inlet total temperature T_{01}, total-to-static pressure ratio p_{01}/p_3, and turbine shaft speed N. Regions of stable pressure and temperature are indicated by solid red lines and black dashed lines respectively.

The NGV inlet total pressure is used to calculate the portion of the run which is aerodynamically stable. This is done with a non linear least squares method fit to a trapezoidal function. The same approach is used to find the temperature stable region in the run, in this case the temperature signal of the hot stream is used. In Figure 4.7, the pressure and temperature stable regions are individuated by dashed and solid vertical lines, respectively, and the start and finish of the run is defined as the smallest interval of the combination of both the pressure and temperature stable regions. The total-to-static pressure ratio stays constant and equal to nominal value of 2.63 during the run. Similarly, the turbine rotor speed is approximately flat during the run, with a value close to the design intent of 8500 rpm.

The mass flow rate measurement technique in the facility was developed by Beard et al. [133]. The hot stream mass flow calculation considers the piston tube exit contraction as a subsonic converging-diverging venturi nozzle once the plug valve has opened. With this assumption, from the conservation of mass equation, the mass flow rate for a compressible flow is given by

$$\frac{dm}{dt} = \rho u \, A_{\text{eff}} \tag{4.1}$$

The effective area, A_{eff}, is a function of Reynolds number, Mach number, Prandtl number and gas-to-wall temperature, and it accounts for the displacement effect of viscous boundary layers. It also includes a correction factor for non-isentropic conditions due to heat transfer from the wall to the gas as the blowdown progresses. This was evaluated with a calibration experiment by Beard et al. [133].

Using the definition of Mach number

$$u = \mathrm{M}\sqrt{\gamma \mathrm{R}\, T} \tag{4.2}$$

the isentropic flow relationships

$$\frac{T_0}{T} = \left(\frac{p_0}{p}\right)^{\frac{\gamma-1}{\gamma}} = \left(1 + \frac{\gamma-1}{2}\mathrm{M}^2\right) \tag{4.3}$$

as well as the ideal gas low

$$\rho = \frac{p}{\mathrm{R}\,T} \tag{4.4}$$

The mass flow rate through the piston tube exit contraction can be obtained from the total pressure, total temperature and Mach number at the throat location (bolster plate plane) as

$$\dot{m}_h = \frac{dm}{dt} = p_0\, A_{\text{eff}} \mathrm{M} \sqrt{\frac{\gamma}{RT_0}} \left(1 + \frac{\gamma - 1}{2}\mathrm{M}^2\right)^{-\frac{(\gamma+1)}{2(\gamma-1)}} \tag{4.5}$$

The total pressure upstream of the piston tube contraction p_0, the total temperature T_0 of the piston tube gas, as well as the contraction static and total pressure are measured, allowing the calculation of the time-varying Mach number as

$$\mathrm{M} = \sqrt{\frac{2}{\gamma - 1}\left[\left(\frac{p_0}{p_0 - \Delta p}\right)^{\frac{\gamma-1}{\gamma}} - 1\right]} \tag{4.6}$$

Moving onto the calculation of the coolant mass flux, this follows knowing that the RTDF and NGV cooling streams are supplied from independent reservoirs and are introduced through sonic venturi nozzles. The delivery system design ensures that the nozzles remain chocked during the test run (the cold gas delivery system was designed for reservoir pressure of 100 bar and pressure downstream of the nozzle of 40 bar). The nozzles discharge coefficients are provided by a calibration traceable to the National Institute of Standard and Technology. The cold stream mass flow rate are then given by

$$\dot{m}_c = \frac{dm}{dt} = p_0 A_{\text{geo}} C_d \sqrt{\frac{\gamma}{\mathrm{R}T_0}} \left(\frac{\gamma + 1}{2}\right)^{-\frac{(\gamma+1)}{2(\gamma-1)}} \tag{4.7}$$

Figure 4.8 presents the mass flow rates in the facility: the hot stream, RTDF cooling, NGV cooling, NGV inlet and rotor inlet, for uniform inlet condition (Figure 4.8a) and RTDF inlet condition (Figure 4.8b). In the uniform inlet condition scenario, where the mass flow for RTDF cooling is zero, the vane inlet mass flow and the hot stream mass flow coincide.

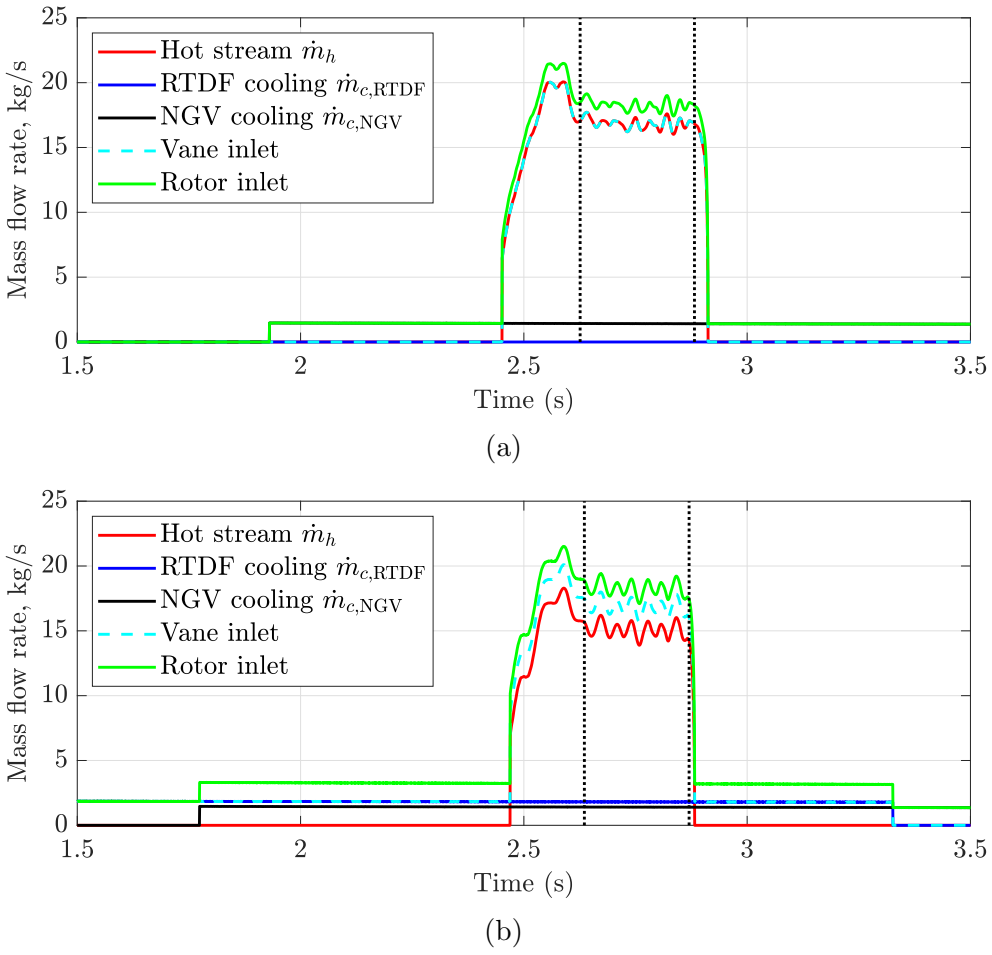

Figure 4.8: Typical mass flow rate traces during a run in the OTRF with (a) uniform inlet condition and (b) RTDF inlet condition.

4.1.5 Mass-Averaged Inlet Total Temperature

The temperatures of interest in the OTRF test section are the hot stream, the hot stream corrected, the vane inlet, and the rotor inlet total temperatures. The procedure to follow to obtain them is elucidated below.

In the OTRF, the hot stream at approximately 500 K flowing down the facility from the pump tube passes through the combustor simulator hardware, which is at ambient temperature. Thus, a temperature difference of approximately 200 K exists between the hot stream and the combustor simulator components. This results in convective heat transfer to the facility components that will cause a reduction in the

hot stream temperature. As the OTRF is a transient facility, this convective heat transfer must be considered.

Adams et al. [130] determined the correction that accounts for the temperature drop across the combustor simulator with swirler installed, while Singh et al. [132] calculated the correction for the combustor simulator with RTDF. The procedure to assess this correction consists in running a series of experiments measuring the temperature upstream and downstream of the combustor simulator, T_{0h} and T_{01} respectively, as well as the wall metal temperature T_w. These experiments allow the calculation of a correction factor, a non-dimensional heat loss across the simulator, that normalises the hot stream total temperature drop by the gas-to-wall temperature difference $\theta = (T_{01} - T_{0h})/(T_w - T_{0h})$. The heat loss factor relevant for this study amounts to 0.1035 [132].

The definition of this correction factor, enables the calculation of the hot stream corrected total temperature

$$T_{0h,corr} = \theta(T_w - T_{0h}) + T_{0h}. \tag{4.8}$$

Once the hot stream corrected temperature has been defined, the vane and rotor inlet total temperature can be determined. For tests with uniform inlet conditions, the vane inlet total temperature T_{01} is directly measured by radial rakes at the vane inlet plane. Whilst with RTDF inlet conditions, these rakes do not have the spacial resolution to determine T_{01} accurately. Instead, T_{01} is defined as mass-mean calculation [135] of hot stream and RTDF coolant stream quantities as

$$T_{01} = \frac{\dot{m}_h\, T_{0h,\mathrm{corr}} + \dot{m}_{c,\mathrm{RTDF}}\, T_{0c,\mathrm{RTDF}}}{\dot{m}_h + \dot{m}_c} \tag{4.9}$$

Similarly, the total temperature at the turbine rotor inlet can then be obtained as

$$T_{02} = \frac{\dot{m}_h\, T_{0h,\mathrm{corr}} + \dot{m}_{c,\mathrm{RTDF}}\, T_{0c,\mathrm{RTDF}} + \dot{m}_{c,\mathrm{NGV}}\, T_{0c,\mathrm{NGV}}}{\dot{m}_h + \dot{m}_{c,\mathrm{RTDF}} + \dot{m}_{c,\mathrm{NGV}}} \tag{4.10}$$

Figure 4.9 illustrates these temperature traces during a typical uniform and RTDF run in the OTRF. Notably, in tests with RTDF inlet conditions, the hot stream temperature is higher than in tests with uniform inlet condition. This is deliberate, as the aim is to achieve the same temperature level at the NGV inlet for both scenarios.

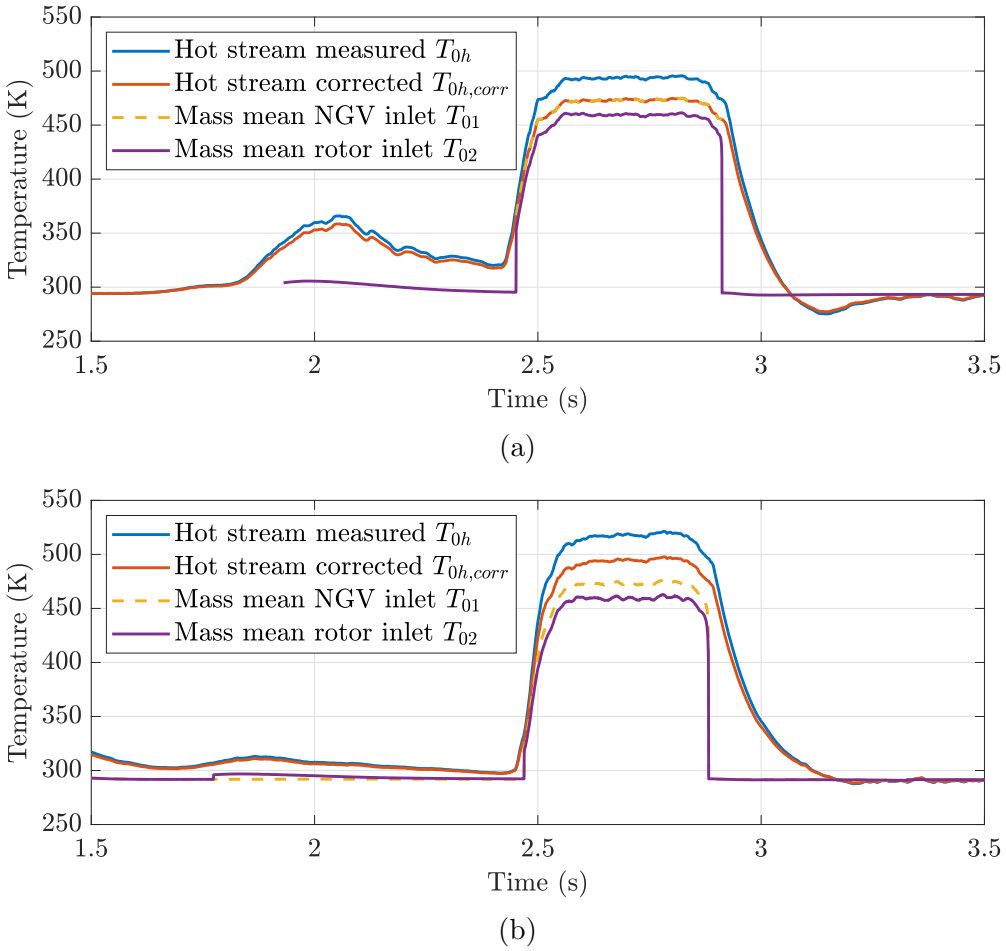

Figure 4.9: Typical mean level temperature traces during a run in the OTRF with (a) uniform inlet condition and (b) RTDF inlet condition.

4.2 Test Programme During IR Experiments: Rotor Casing Effusion Cooling

The Infrared thermography system developed in this study was tested during a rotor casing effusion cooling programme for Rolls-Royce. Although the turbine used is 73% of a large civil turbine (e.g. XWB), it is representative of defence industry at

100% scale. A brief description of the cooling system is provided, but fine details are minimised as commercially sensitive and export controlled as UK official.

4.2.1 Cooling Module

For the effusion cooling test campaign, the OTRF was fitted with 8 removable cooling modules in the overtip region, making this the first full-annulus effusion cooling configuration ever tested in this type of facility. Each module is composed of a cooling segment bolted onto an aluminium cassette which was computer numerical control (CNC) machined, as shown in photographs of Figure 4.10. The effusion cooling segments were manufactured from high temperature nickel alloy using Direct Metal Laser Sintering (DMLS) technology. This allowed to achieve the specific hole geometry using the same manufacture technique as planned for engine parts, with the tested geometry an engine geometry at 100% scale.

An illustration of the effusion cooling segment can be seen in Figure 4.11. The geometry features 10 rows of holes of 0.5 mm diameter with uniform hole spacing in the circumferential direction. One segment covers 7 blades pitches and each row lies on an axial plane between -42.27% and 134.31% of the blade axial cord at the tip ($C_{ax} = 22\,\text{mm}$). The specific geometry of the cooling holes will not be discussed here as this is Rolls-Royce proprietary, however the design was based on the results from Collins [136].

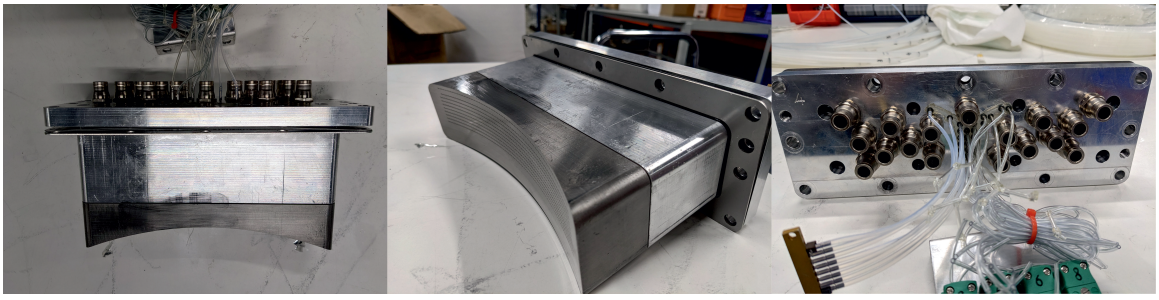

Figure 4.10: Photographs of the casing effusion cooling segment integrated within the detachable cassette of the over-tip rotor module

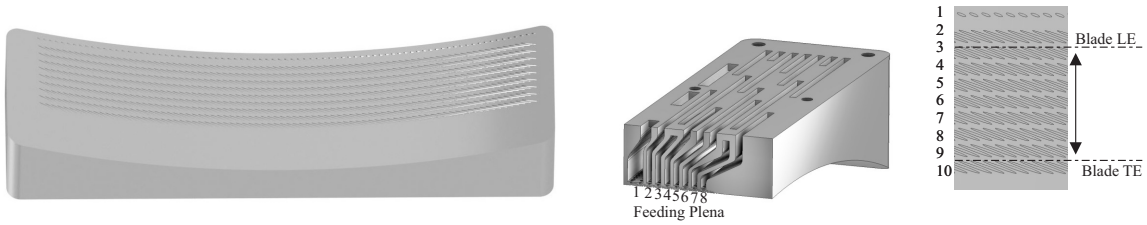

Figure 4.11: CAD model views of the effusion cooling segment geometry. The section views show the eight feeding plena and the effusion cooling rows. The blade leading and trailing edge locations are indicated with two dashed lines.

Collins studied pressure wave propagation through cooling holes and the impact of acoustic length on improving cooling efficiency. The author demonstrated that the desired mass flow rate and reduced ingestion can be achieved by shaping the hole to exploit the pressure wave propagation within the cooling duct. This study is particularly relevant in HP casing film cooling application, where the holes are subjected to large temporal variation in static pressure and heat load due to the rotor blades passing. Collins concluded that to reduce temporal fluctuation in mass flow rate the length of the hole should be designed to be between 0.15λ and 0.35λ for a hole diameter of 0.5 mm, where λ is the pressure wavelength at the speed of sound. The hole length was set within this range, and a more curved lip was preferred over a sharp edge to reduce stresses.

Due to the pressure variation caused by the power extraction by the rotor, it is desirable to have control over the mass flow for each cooling row. Eight plena feed the cooling rows; the most upstream plenum feeds rows 1 to 3, while rows 4 to 10 are fed by separate plena. The cassettes are designed to distribute the cooling flow to each plenum in a controlled manner and include pressure and temperature measurements in each plenum. The design of the effusion cooling delivery system that allowed such control is described in the following section.

4.2.2 Coolant Delivery to Effusion Segment

A schematic of the effusion cooling delivery system is depicted in Figure 4.12, and photographs featuring the different components are shown in Figure 4.13. The aim of the feed system is to provide independent control of the mass flow to the cassette plena 1-8. This is achieved by controlling the pressure and temperature upstream of calibrated choked orifices prior to distributing flow to the eight effusion cooling cassettes. The coolant is supplied at ambient temperature from a high pressure (up to 110 bar) reservoir of volume 0.73 m^3. Initially, all valves are closed and the system is vented to atmosphere. Subsequently, the main solenoid valve is opened

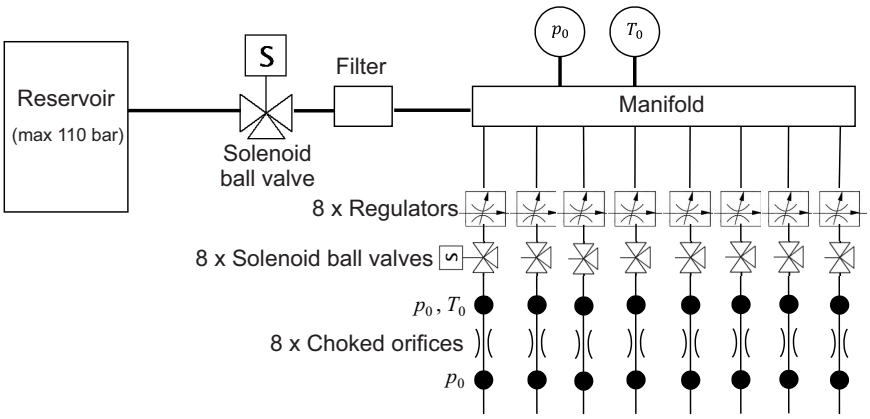

Figure 4.12: Schematic of the effusion cooling feed system.

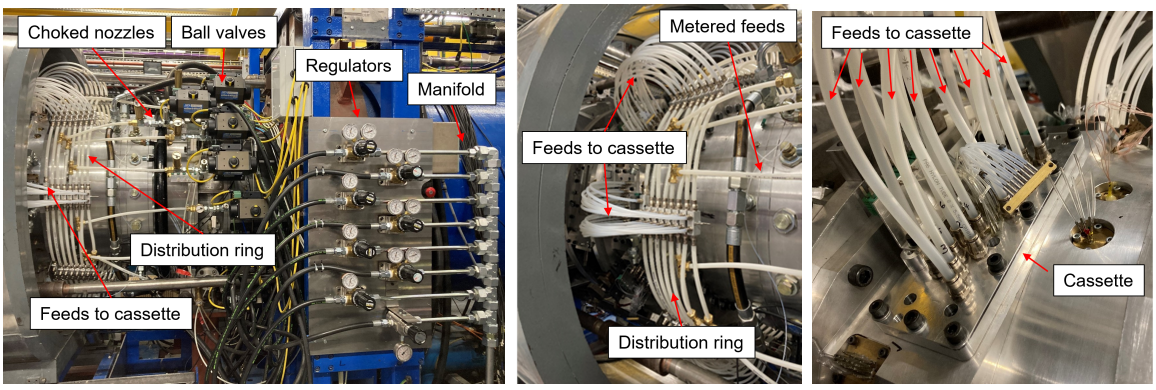

(a) (b) (c)

Figure 4.13: Photographs of effusion cooling feed system, including (a)-(b) views of the OTRF test section; (c) close-up of one effusion cooling segment installed on the facility.

to pressurise the manifold. Eight regulators (VICTOR D1G Pilot-Domeload Hybrid with maximum nominal inlet pressure of 200 bar and maximum delivery pressure of 38 bar) set the pressure upstream of eight chocked orifices. Supply of coolant to the OTRF is initated by opening the pneumatically actuated ball valves upstream of each choked nozzle. These valves are opened at the same time of NGV coolant and RTDF cold stream supplies. Pressure and temperature are measured upstream of each nozzle with Series CTE8000 Sensor Technics transducers and 3″ thou (76.2 µm) bare k-type thermocouples respectively. A measure of the pressure downstream of the nozzle is recorded to ensure the nozzle is chocked. The diameters of the feed system pipes are sized to balance the pressure drop, reduced as diameter increases, and required transient response to achieve steady conditions during OTRF test time, reduced as diameter decreases. The mass flow rate for each feed line, given the orifice choked condition and assuming an ideal compressible flow can be calculated as

$$\dot{m}_{\mathrm{ec},cavity} = p_{0c} A_{\mathrm{or}} C_{d,or} \sqrt{\frac{\gamma}{\mathrm{R}T_{0c}}} \left(\frac{\gamma+1}{2} \right)^{-\frac{(\gamma+1)}{2(\gamma-1)}} \tag{4.11}$$

where p_{0c} and T_{0c} are the coolant stagnation condition upstream of each feed nozzle, A_{or} is the sectional area of the orifices, and $C_{d,or}$ is the discharge coefficient of the orifices. Calibration curves for the discharge coefficients of each nozzle were obtained with a series of bench-top experiments, schematically depicted in Figure 4.14. Pressurised air was exhausting through each choked orifice, through a downstream calibrated mass meter before exhausting to atmosphere. The procedures for these experiments is as follows

i) Open solenoid ball valve upstream of the manifold

ii) Set pressure p_0 downstream of regulator

iii) Open solenoid ball valve upstream of the orifice

iv) Record p_0, T_0, and $\dot{m}$

Thus, knowing the orifice sectional area A_{or}, the discharge coefficient $C_d(p_0)$ was calculated. The calibration functions were found with the least mean square error method. The results for the different orifices are summarised in Fig. 4.15. To control the rig casing cooling flow rate, the pressure at the regulators were manually adjusted prior to a run targeting the desired cavity pressure, to achieve in turn the desired pressure ratio across each effusion cooling row.

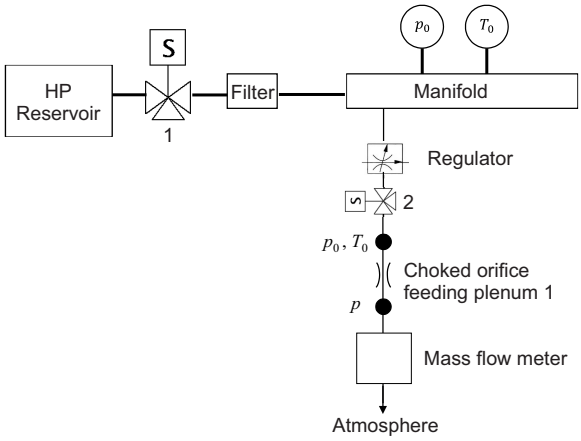

Figure 4.14: Schematic of the bench-top experiments for the orifice calibrations.

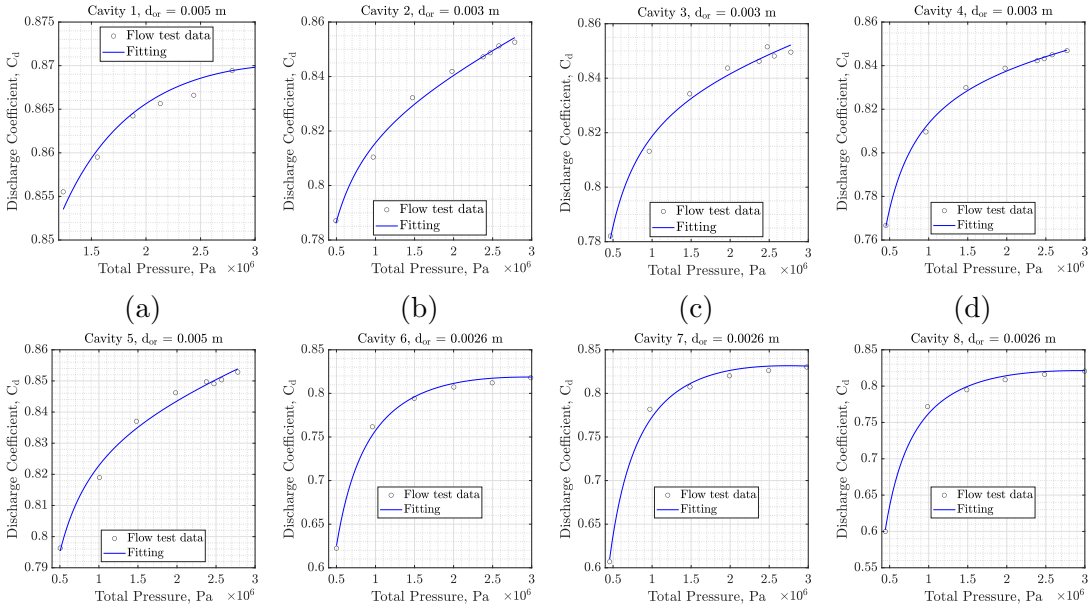

Figure 4.15: Calibration curves for effusion cooling feed orifices.

4.3 Designing the Optical Access

Infrared measurements in wind tunnel experiments require optical access, necessitating the use of windows to replace a section of the enclosure, the size of which can vary according to the specific application. The choice of material for optical access is crucial, as it must exhibit transparency to the desired infrared wavelength. However, this is not the sole requirement.

Designing an optical access for infrared thermography in a rotating engine scale facility, such as the OTRF, presents several challenges due to the operational conditions. Firstly, temperature-related challenges arise as the test gas temperature within the OTRF can reach values of 500 K. The window must withstand this thermal load while maintaining a high optical transmittance. Additionally, there are pressure-related challenges as the facility experiences a wide pressure range, fluctuating from near vacuum to a maximum inlet of 8.5 bar. Therefore, the window must fulfil the dual role of ensuring the conditions of a pressure vessel whilst withstanding the varying pressure loads at their highest levels.

To summarise, in selecting the material and designing the geometry for the optical window two fundamental aspects need to be evaluated:

i) The transmission properties of the window in the wavelength range of interest is the first factor to considerate. This is linked to the wavelength operational range of the camera. This entails examination of how the different IR substrates perform based on the specific wavelength operational range of the camera.

ii) The thermal and mechanical properties of the window must be investigated. This is especially important in facilities like the OTRF where the window is subjected to high pressure and temperature loads.

In the following sections, these key considerations will be discussed, a comparison of material properties delineates the optimal choice for the OTRF window, then

elucidations on the design choices of the window housing and mounting are given, including considerations on observation angles for the IR optical measurements in the OTRF. Finally, the transmittance of the optical material is quantified.

4.3.1 Optical Materials and the Choice of Zinc Selenide

Optical materials are substances designed to manage electromagnetic radiation across the ultraviolet, visible, or infrared spectral regions. When light encounters the boundary of a material, a fraction is reflected, another portion is absorbed, and the remaining part is transmitted. At a microscopic level, the incident photons in the electromagnetic radiation interact with the atoms in the material. These interactions govern the material's macroscopic optical properties, including how much light it transmits. As the material's response to the incident light is dependant on the interaction between its electronic configuration and the light, the optical properties crucially depend on the wavelength of the incident light, and are further influenced by factors such as material temperature and thickness.

To illustrate the absorption and transmission in optical materials and the dependency on wavelength and material structure, yttria can be considered as example. Figure 4.16 depicts the refractive index and absorption coefficient for this material [137]. It is evident how the response of the material to incident electromagnetic radiation varies dramatically across the spectrum. Yttria exemplifies two distinct absorption regions – far infrared (wavenumber 100 to 1000) and ultraviolet (wavenumber 10^5) – within these lies a transparent window in the visible/infrared spectrum. The pronounced absorption in the far infrared is attributed to the incident radiation exciting the materials vibrational modes (*lattice vibrations*). Conversely, absorption in the ultraviolet results from the incident radiation prompting electrons in the material to transition from lower to higher electronic energy levels (*electronic transitions*). In the transparent region, absorption is mainly induced by impurities, such as OH^- in

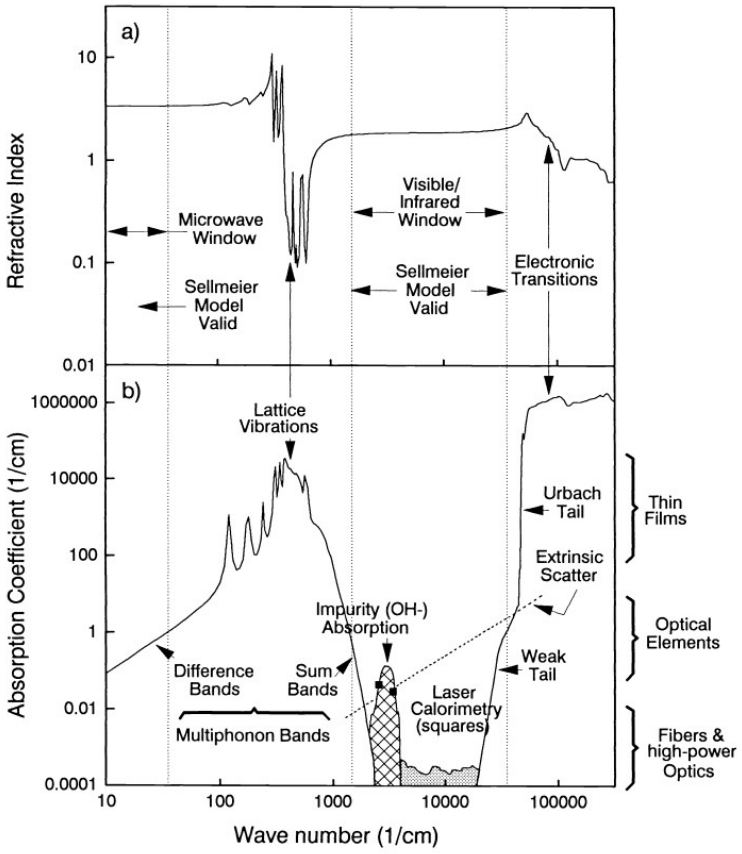

Figure 4.16: (a) Index of refraction and (b) absorption coefficient of yttria [137]

yttria. The strong absorption regions in the far infrared and ultraviolet are intrinsic properties, arising from the material's pure state. However, in the transparent region, absorption is primarily extrinsic, driven by impurities. This emphasises the need for calibration for the window material transmittance, considering potential variations among specimens.

The selection of an optical material for a specific application hinges primarily on its transmission region. Figure 4.17 summarises transmission regions for various optical materials. The wavelength range where a material exhibits appreciable transmission are shown. The limiting wavelengths, both high and low cut-off, are determined as the wavelength at which a 2-mm thick sample shows a 10% external transmittance [138]. These graphs aid selection of an appropriate optical material for a specific application.

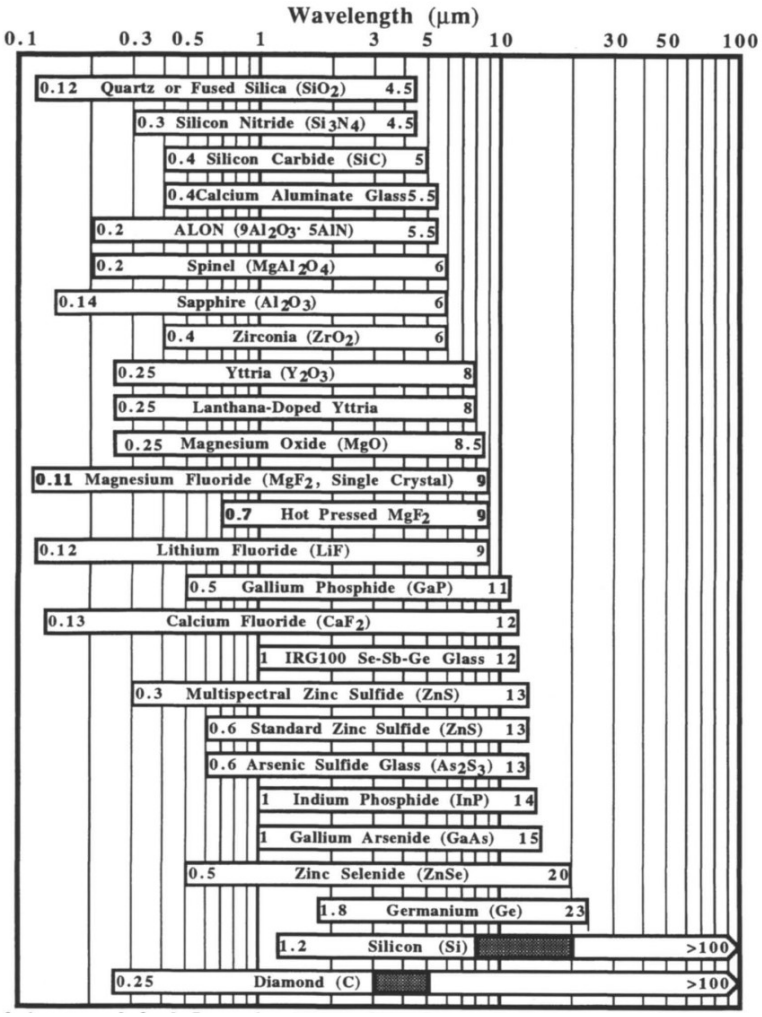

Figure 4.17: Transmission regions of optical materials (2 mm thickness) with cutoff defined at 10% external transmittance. Values are approximate and may vary based on material quality. Shaded areas for diamond and silicon indicate reduced transmission. [138]

In the OTRF experiments, given the camera working wavelength of $7.5 - 11\,\mu m$ (for further details on detector selection see Chapter 3 Section 3.2), a material with a long wave infrared transmission band is required. It can be inferred from Figure 4.17 that possible candidates of materials transmitting in the LWIR range are: zinc sulphide (ZnS), gallium arsenide (GaAs), zinc selenide (ZnSe), and germanium (Ge). Figure 4.18 present the transmission spectra in the range $3 - 20\,\mu m$ for these materials. In the graph, transmittance of silicon is also shown. However, this material cannot be considered a good candidate for OTRF experiments given the reduced

transmission bands in the wavelength range of interest.

Focusing on the wavelength band of interest for the OTRF application, 7.5 – 10.5 µm, some conclusion can be drawn. Both zinc selenide and zinc sulphide perform better than gallium arsenide, presenting a higher transmittance which make them more favourable materials. Furthermore, despite having good mechanical properties and being a durable material, germanium optical properties are strongly affected by temperature.

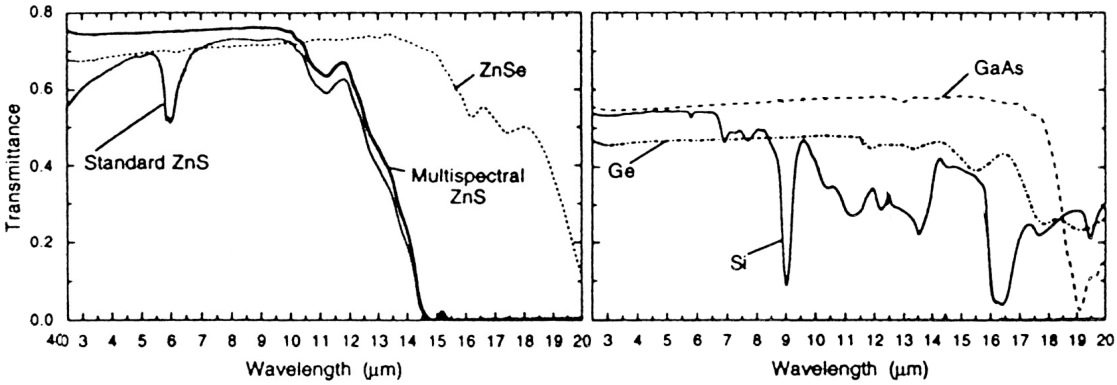

Figure 4.18: Infrared transmittance in a selection of optical materials, including standard zinc sulphide (ZnS, 6 mm thick), multispectral zinc sulphide (ZnS, 5.2 mm thick), zinc selenide (ZnSe, 7.1 mm thick), germanium (Ge, 2.8 mm thick), gallium arsenide (GaAs, 0.65 mm thick), and silicon (Si, 2.8 mm thick). Figure adapted from [139].

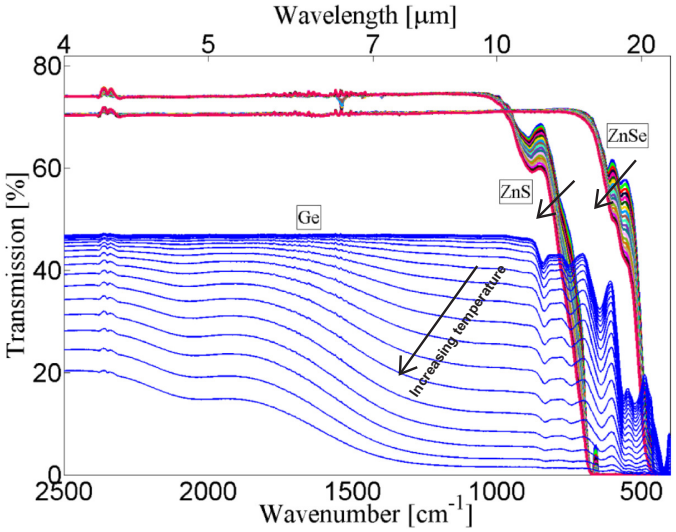

Figure 4.19: Transmission of 4 mm thick ZnS, ZnSe and Ge uncoated substrate materials at temperatures from 20 °C to 200 °C with steps of 10°C [81].

Figure 4.19 illustrates the temperature-dependent transmittance profiles for uncoated samples of the materials under consideration: germanium, zinc selenide, and zinc sulfide. The transmittance of germanium exhibits a strong temperature dependence, particularly significant in the wavelength range of interest, with transmittance falling below 20% for temperature higher than 140 °C, thus making germanium an unsuitable option for OTRF experiments. On the other hand, both zinc selenide and zinc sulphide present a transmittance insensitive to temperature. However, zinc sulphide manifests a cutoff wavelength too close to the upper limit of the wavelength band of interest for OTRF experiments. Hence, zinc selenide was selected as the optimal material for the IR transparent window.

4.3.2 Optical Access for OTRF Experiments

Once the material that provides the desired transmittance has been chosen, the challenge moved onto designing a window geometry that ensures window integrity under the temperature and pressure conditions in the OTRF and provides access to the desired field of view of at least one blade passage. In the OTRF during the effusion cooling programme limited physical space was available for the optical access on the turbine rotor overtip region. Thus, the window and its housing were designed to replace one effusion cooling segment (described in Section 4.2.1).

Figure 4.20 displays views of the CAD model for the IR transparent window geometry and the window housing. The window has a minimum thickness of approximately 16 mm, it has an external flat surface and an internal concave surface of radius equal to the turbine rotor section of the OTRF (approximately 296 mm) to match the internal casing geometry. A chamfer runs around the top side of the window to allow this to sit inside the bottom part of the housing. Two o-rings are used to ensure the sealing necessary in the rotor section to reach near vacuum conditions prior to the run. The size of the window allows optical access to two blade passages. A stress

analysis was performed on the window based on a pressure force of 5 kN, corresponding to a pressure of 10 bar. The results for Von Mises Stress and safety factor are summarised in Figure 4.21. Stresses are higher on the interface between the window and the metal, with a maximum value of approximately 44 MPa. This is also the location where the safety factor is lower, manifesting a minimum value of 1.25. These conditions were considered satisfactory.

4.3.3 Observation Angles

A photograph and CAD model of the test section instrumented for IR thermography testing is shown in Figure 4.22. During the experiments in the OTRF, the window with its housing cassette were placed in the rotor overtip region. A mounting system for the camera was designed to allow correct and repeatable positioning of the camera. The system comprises a breadboard, a rail and a rotary stage. The breadboard is bolted onto the facility and allows the camera to sit directly in front of the window.

Of crucial importance with infrared thermography measurements is the assessment of observation angles, since these have an impact on surface emissivity as discussed in Chapter 3, Section 3.3.2. In particular, a substantial decrease in surface emissivity was found for observation angles above 50°. A calculation of the observation angles under various camera positions was developed to select the ideal camera alignment, allowing angles in the regions of interest to be below the critical threshold for surface emissivity,

Target surface normals were derived from an imported surface mesh of turbine and camera 3D geometry, with viewing angles subsequently determined by the vector dot product calculations. After iterating various camera-target positions, three were found with observation angles below ±50° in the regions of measurement, i.e. rotor tip, near-tip pressure and suction sides. Figure 4.23 shows the results from the observation angle analysis, specifically the calculated viewing angles on the blade tip,

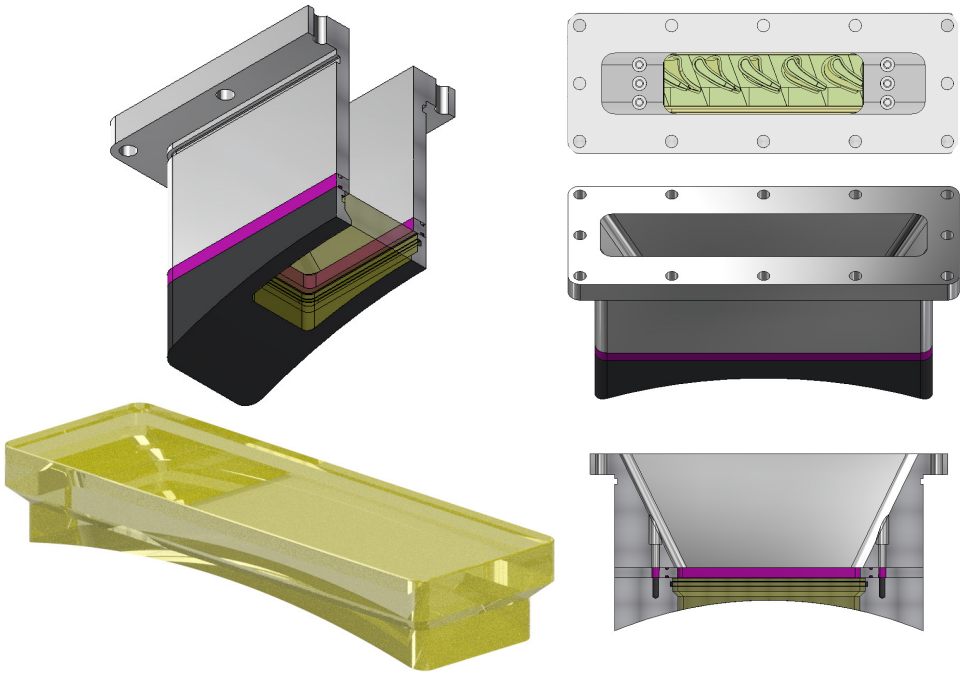

Figure 4.20: CAD model of the IR transparent window made of ZnSe designed for the OTRF effusion cooling test campaign.

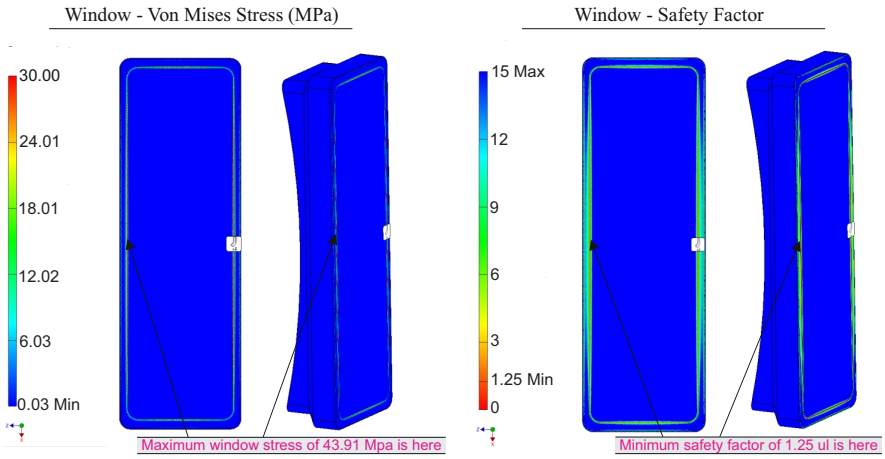

Figure 4.21: Finite Element stress analysis on window designed for the OTRF, including Von Mises Stress and safety factor.

pressure and suction surfaces for these camera positions are shown in Figures 4.23a, 4.23b and 4.23c, respectively.

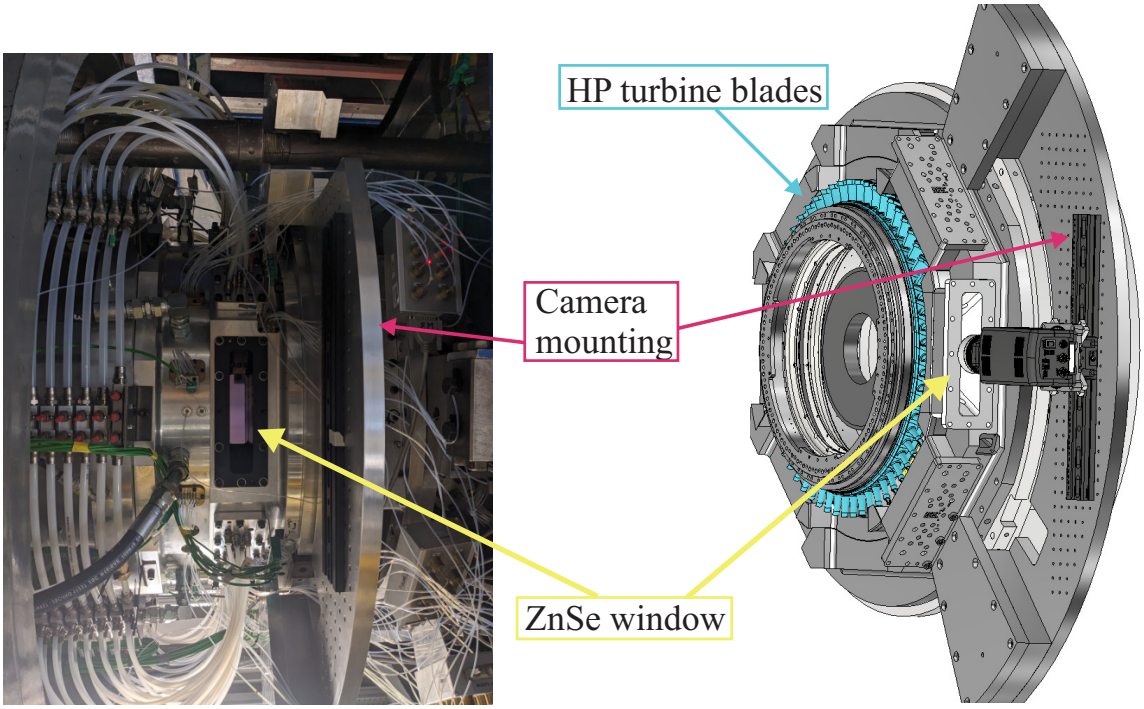

Figure 4.22: Setup of the OTRF test section for IR thermography testing, including (a) installed zinc selenide IR transparent window, and (b) 3D CAD geometry of the test section

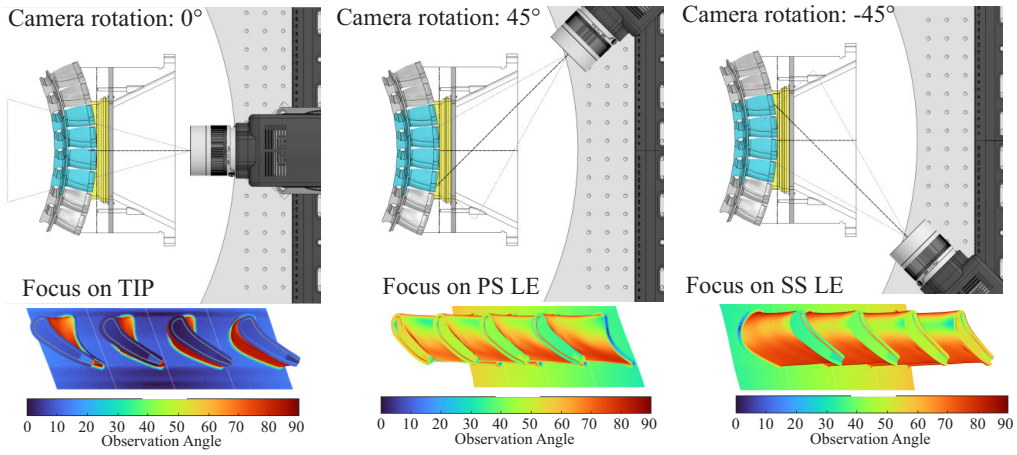

(a) (b) (c)

Figure 4.23: Analysis of the observation angles on rotor blades at camera rotation of (a) 0-deg with focus on rotor blade tip, (b) 45-deg with focus on pressure side (PS), and (c) -45-deg with focus on suction side (SS).

4.3.4 Transmittance of the Optical Path in the OTRF

In the context of infrared thermography measurements, two distinctive scenarios may arise. The first scenario involves the camera observing the target within the same enclosure or in an open space. Here, the optical path — comprising anything between the target and the camera — exclusively involves the atmosphere. In the second scenario, the one pertinent to the OTRF application, the camera observes the target through a window. In this instance, the optical path includes a gas of specific composition and an optical window. To ensure the accuracy of infrared measurements, a comprehensive investigation into the gas composition and its radiation characteristics, as well as into the radiative properties of the optical window, is required.

Within the OTRF, the optical path consists of dry air at temperature ranging from 400 to 600 K, as well as a ZnSe optical window coated with anti-reflective. According to Gao et al. [74], the gas transmittance can be assumed equal to unity for wavelength above 7 µm, and hence the transmittance of the window alone needs to be determined. As discussed earlier and visualised in Figure 4.19, the temperature of a ZnSe window has a negligible impact on the material transmittance [140]. Thus, this was kept at ambient temperature during the transmittance calibration. The transmittance was determined by interposing the window between the blackbody source and the camera in the calibration set-up presented in Chapter 3 and depicted in Figure 3.5a, replicating the same geometrical conditions expected in the OTRF.

Using the temperature measured by the camera T_{cam}, the blackbody source temperature T_{bb}, and the optical path temperature T_{opt}, which was kept at ambient temperature and was measured by a k-type thermocouple, the transmittance was calculated by rearranging Equation 3.1 as

$$\tau = \frac{T_{cam}^4(\theta) - T_{opt}^4}{T_{bb}^4 - T_{opt}^4} \tag{4.12}$$

The transmittance tested for blackbody source temperatures ranging from 323.15 K to 343.15 K was determined to be $\tau = 0.95$.

4.4 Designing the Composite Blade

Currently, in the OTRF the heat flux $\dot{q}$ is evaluated with thin-film gauges measuring the surface temperature $T_w(t)$ and computing $\dot{q}(t)$ using the impulse response method by Oldfield [53]. The method's applicability relies on assuming a semi-infinite substrate, the validity of which depends on the material properties of the substrate and the duration of the test. Furthermore, the accuracy of the impulse response method is dependant on the temperature rise ΔT achieved during the experiment, which in the OTRF is typically of 40 K. The subsequent analysis of adiabatic wall temperature T_{aw}, based upon the regression between the measured surface temperature and the heat flux, also requires an appreciable temperature rise within the steady portion of the test, typically approximately 10 K is a minimum.

Due to the high conductivity of metal, the surface temperature rise is small on metal components within 0.5 s run time, and normally walls are considered isothermal. Therefore, thin-film gauges are not deposited directly on the metal surfaces but they are sputtered on layers of polyamide with low thermal conductivity, the preferred polyamide is Kapton which has a thermal conductivity of approximtaley $0.12\,\mathrm{W\,m^{-1}\,K^{-1}}$ [141]. Hence, to implement full surface IR thermography measurements on rotor blades in the OTRF, a material with low conductivity was needed. The use of plastic blades was not feasible as they would not to withstand the stresses. The solution was to look for a full surface coating with low conductivity but also mechanical strength, thus, to design a composite blade.

The composite blade designed for IR thermography measurements consists of two parts: a metallic skeleton and a plastic coating. The manufacturing of the blade was achieved via a three step process, summarised in Figure. 4.24. Firstly, the metallic

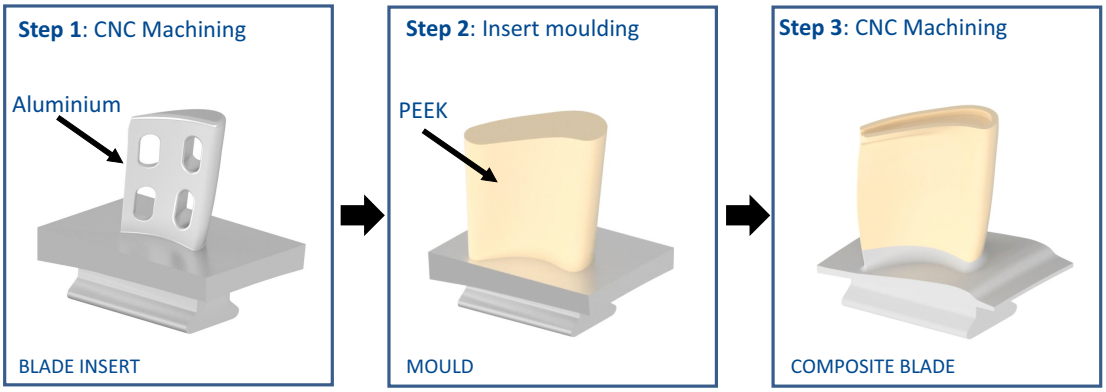

Figure 4.24: Schematic of the manufacturing process for composite blade.

insert was machined from aluminium 7075-T6 alloy, the same material used for the remaining blades. Subsequently, the insert underwent an injection moulding process, which involves injecting plastic into a mould to coat the insert. Finally, the coated blade insert was CNC machined to obtain the blade shape. The material used for the injection moulding was VICTREX Polyether ether ketone (PEEK) 450G. The choice of this material was guided by both the manufacturability with injection molding technique and the material thermal properties compared with Kapton.

The thermophysical measurements of the Vicrex PEEK 450G were outsourced to the company NETZSCH. Thermal diffusivity, specific heat capactiy and room temperature bulk density were measured to compute the thermal conductivity. The thermal diffusivity was measured using a laser flash apparatus developed by the company. The front surface of a material sample is heated by a xenon flash lamp and the consequent temperature increase on the back surface is measured using an IR detector. The specific heat capacity was measured using a differential scanning calorimeter. The density at room temperature was determined through the buoyancy flotation method, yielding a value of $1.31\,\mathrm{g/cm^3}$. Each measure was carried out three times at each temperature step. The maximum standard deviation of the three single measurements per temperature was found to be less than 3%. The results summarised in Table 4.2 and Figure 4.25 are the average values.

Table 4.2: Thermophysical properties of PEEK. Density at room temperature $\rho = 1.31\,\mathrm{g/cm^3}$

Temperature, °C	Thermal diffusivity, $\mathrm{mm^2/s}$	Specific heat, J/(g K)	Thermal conductivity, W/(m K)
25	0.177	1.101	0.255
40	0.169	1.165	0.259
60	0.163	1.238	0.264
80	0.158	1.306	0.27

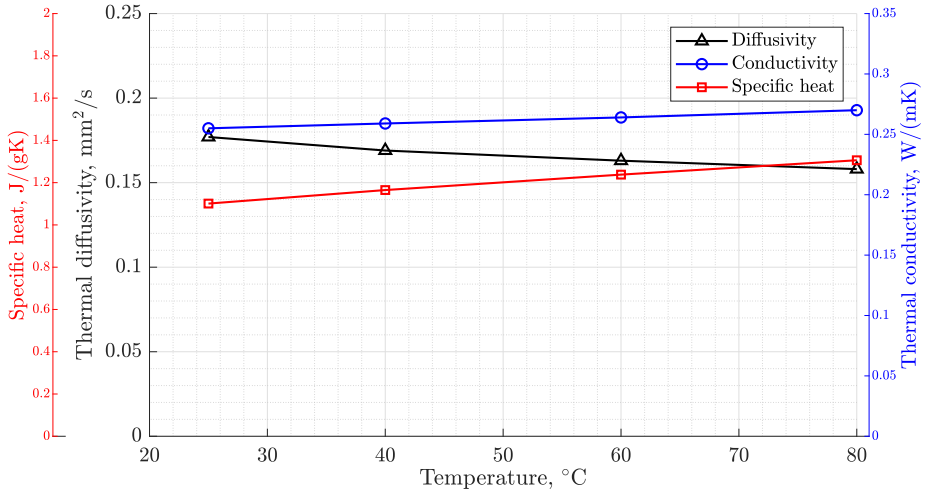

Figure 4.25: Thermophysical properties of PEEK.

4.4.1 Tensile Load and Fatigue Tests

There are some considerations to take into account when designing a part for insert molding. Designing features such as undercuts can help enhance the retention strength of the inserts within the molded part. In loads applications, it is crucial to prove the ability of the composite part to withstand the stresses and cyclic loads. However, there is not a clear way to simulate the bonding strength between the insert and the composite material in injected molded parts. Thus, tensile load and fatigue tests on a series of inserts samples were carried out.

A simplified teardrop shaped blade was used for the tests and eight different insert designs were developed. Photos and CAD model of these are shown in Fig. 4.26, their geometrical characteristics are explained below.

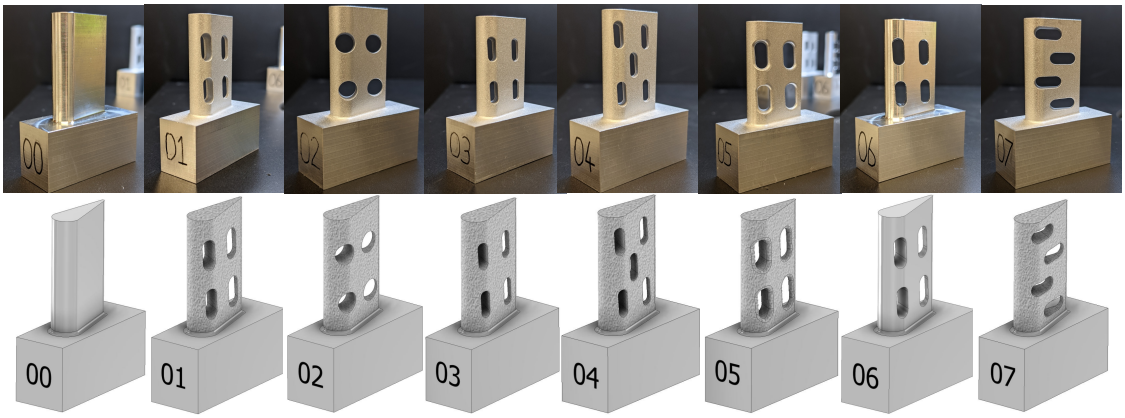

Figure 4.26: Simplified models of composite blade for tensile load and fatigue tests.

D0. This design was the baseline. The insert surface was designed to be smooth and without undercuts, representative of a case with no mechanical bond.

D1. The insert surface in this design was shot blasted to enhance surface roughness, hence the adhesive bonding between the two materials. The four undercuts were equally spaced across the volume.

D2. The undercuts volume of this design was kept the same as in design 1, while the cross sectional area was changed to circular.

D3. The shape of undercuts cross sectional area was kept the same as in design 1, while the volume was reduced by reducing the radius.

D4. The undercuts cross sectional area was kept the same as in design 3, while the undercuts volume was increased by increasing the number of undercuts to five instead of four.

D5. A fillet of 0.8 mm diameter was added to the undercuts, which have the same shape as in design 1 to help reducing the stresses. The most likely weakness is this model was assumed to be due to shear stress at the undercut entrance and exit, thus sharp edges would cause high stress concentration.

D6. The geometry was the same as design 1, whilst the surface is smooth.

D7. The undercuts shape was the same as in design 1 but rotated by 90 deg.

In the OTRF, the blade must withstand a centrifugal load generated by the rotational speed. The maximum rotational speed of the OTRF is $10,000$ rpm. Rotating components are required to withstand the forces of at least $12,000$ rpm, equivalent to +40% of the loads at the maximum rotational speed in the facility. The mass of the composite substrate was estimated to be $m = 0.020$ kg, while the radius is $R = 260$ mm. The maximum centrifugal load is as follow:

$$F_{c,max} = m\omega_{max}^2 R = 8211.51\text{N} \tag{4.13}$$

Tensile tests were performed with a 50 kN load cell. An interface was designed to grip the two extremities of the samples, as shown in Figure 4.27 depicting the set-up for the tensile load and fatigue tests. For each configuration, a speed of $100\,\mu\text{m}\,\text{s}^{-1}$ was used. The result of the tensile load test on the baseline, design D0, are shown in Figure 4.28 as force-displacement curve and photograph taken at the end of the test. The distinct feature of this design was the absence of undercuts, thus, the bonding between the metal insert and the PEEK coating is only the result of any adhesion developed during the injection molding process. The specimen was able to withstand a force of 1.3 kN before the PEEK started sliding off. At the end of the test, the aluminium insert and the PEEK had been completely separated from each other, this can be appreciated in the photograph of Figure 4.28b.

The results from the tensile load tests on designs 1 to 7 are showcased in Figure 4.29. There was no clear appreciation of the impact of different undercuts shapes, as all the various designs manifested a very similar behaviour, with maximum withstand-able loads ranging between 11 kN and 12 kN. The load-displacement curves for these tests are shown in Figure 4.29a, highlighting the different phases of the specimen deformation. The load increase almost linearly from 0 to the maximum

loads, this region equates to the elastic deformation, going from $0 - 2.5\,\text{mm}$, yielding a maximum load value of $12\,\text{kN}$ for design 7. The following region, from displacement of approximately $2 - 4\,\text{mm}$, is the plastic phase. The final fracture displacement of the various specimens ranges between $3.6 - 4.2\,\text{mm}$. Typical fractures are shown in the photographs of Figure 4.29b. The fracture is localised in the tip region were there

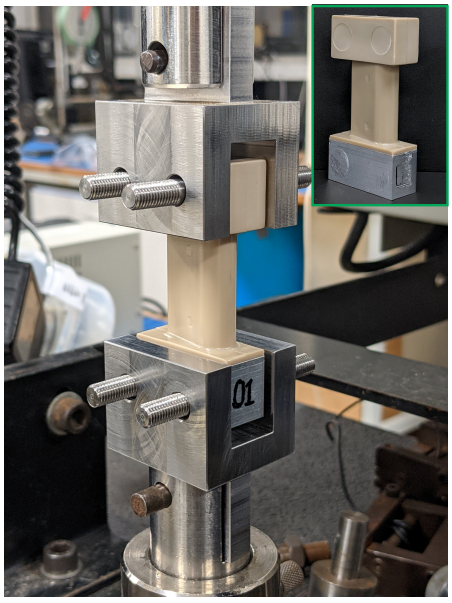

Figure 4.27: Photograph of the composite blade sample installed on the load cell for load and fatigue tests.

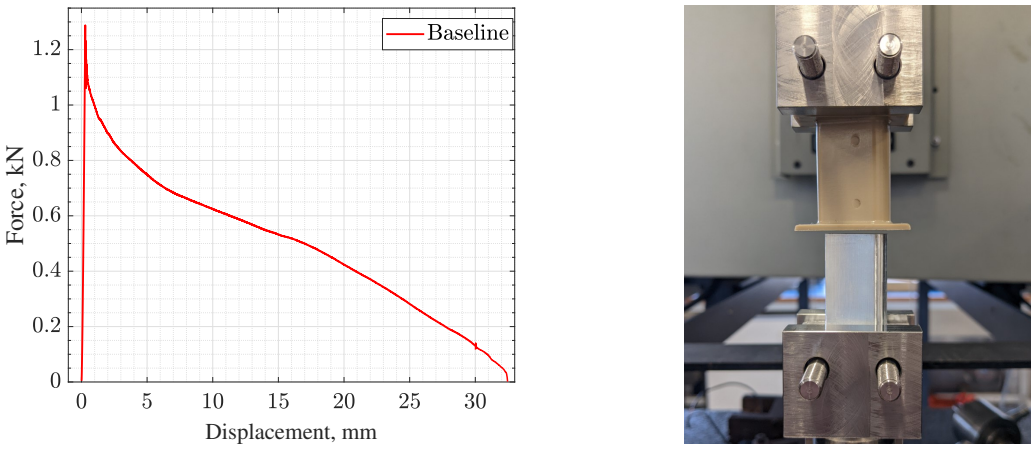

(a) (b)

Figure 4.28: Results of tensile load test on the baseline design, including (a) load-displacement curve and(b) photograph of the design at the end of the test.

is only plastic material. Time instantaneous of a typical tensile load test are depicted in Figure 4.29d.

A fatigue test was carried out on design 3. The aim of this test was to understand the behaviour of the specimen undergoing several runs in the OTRF. This was simulated subjecting the specimen to a cyclical load of 4 kN, corresponding to a centrifugal force relative to the facility nominal speed of 8500 rpm. The result for 1000

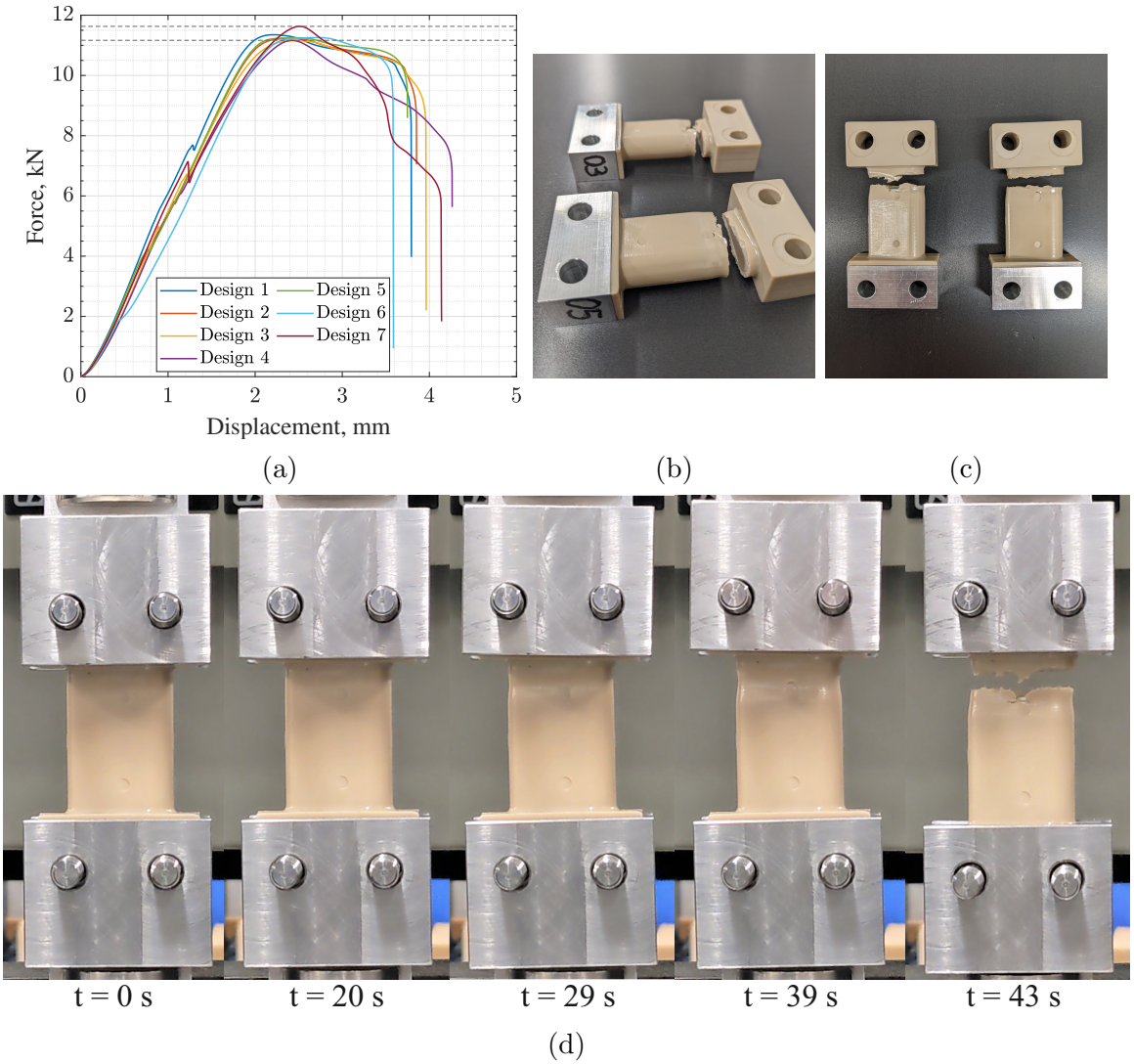

Figure 4.29: Results of tensile load tests on composite blade samples, including (a) force-displacement curves for designs 1 to 7, (b)-(c) photographs of designs 3 and 5 at the end of the test, (d) photographs of time development of test on design 1, showing subsequent instants during the tensile load test.

cycles carried out at 10 s per cycle is shown in Figure 4.30. The behaviour was very repeatable with very little hysteresis.

Despite the impossibility to appreciate different behaviour of the various undercuts design, it is evident that these provide much higher tensile strength compared to the baseline design. Furthermore, it was proved that such configurations was capable to survive stresses well above the maximum expected centrifugal load in the OTRF, thus deeming them satisfactory. The insert characteristics of design 1 were chosen for the fourteen composite blades, a photograph of the manufacturing steps is shown in Figure 4.31.

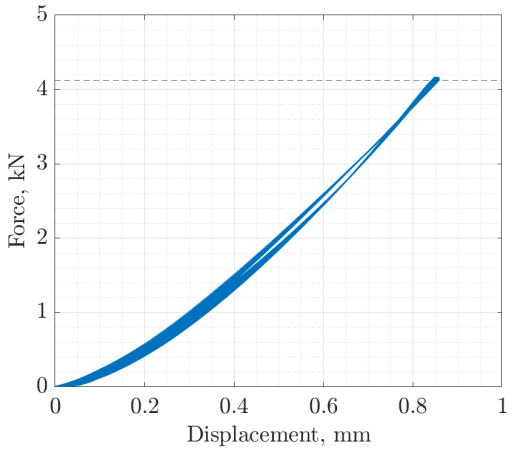

Figure 4.30: Results from fatigue test on composite blade sample D3.

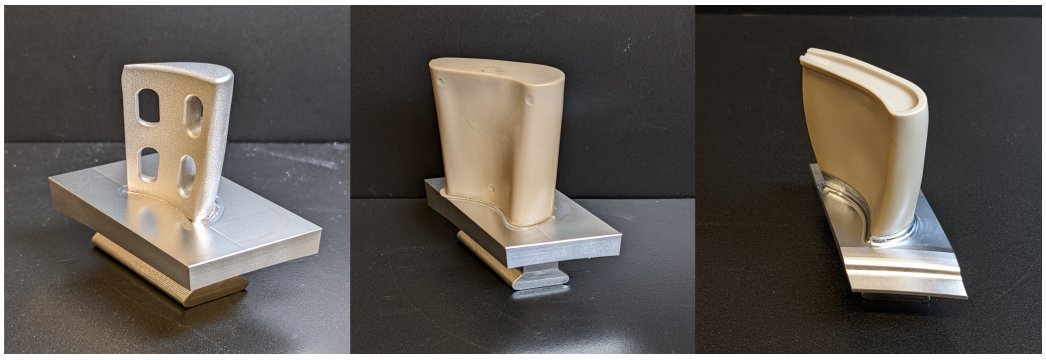

Figure 4.31: Photograph of composite blade insert, moulding and final machining.

4.5 Infrared Camera Synchronisation System

To capture blades spinning at 8500 rpm with an IR detector, there is a need for a triggering and synchronisation system. The block diagram illustrating the triggering and synchronization system developed for the IR camera in the OTRF is presented in Figure 4.32.

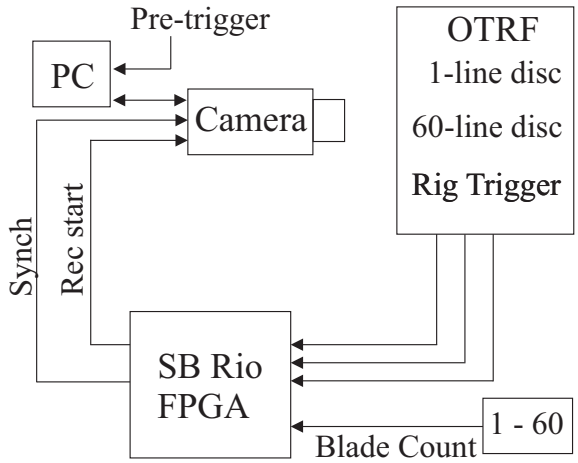

Figure 4.32: Infrared camera triggering and synchronisation system block diagram.

The IR camera is controlled through an NI sRIO FPGA digital inputs/outputs operating at 40 MHz. The FPGA reads four inputs:

i) Shaft speed signal: The turbine's shaft speed is monitored using the HOA2001 Opto Schmitt Trigger, an infrared emitting diode coupled with an Optoschmitt detector. A one-line disc, featuring a flap covering half its circumference, is coaxially mounted to the turbine shaft and aligned with the Opto Schmitt trigger. As the turbine shaft and the one-line disc rotate, the flap's interaction with the Opto Schmitt diode circuit produces a squared waveform. During one half of the rotation, the flap does not engage with the Opto Schmit sensor which therefore produces a constant 5 V output. In the consecutive half, the flap shields the diode resulting in an open circuit and a constant 0 V output. The interaction between the one-line disc and the Opto Schmitt sensor ensures the generation

of a waveform where each complete cycle corresponds to one revolution of the turbine rotor. The obtained squared wave in a typical run is depicted in blue in Figure 4.33. The maximum frequency of the signal, corresponding to the maximum frequency of the rotor, is approximately 142 Hz, with an amplitude of $0 - 5$ V.

ii) Blade passing signal: Similar to the shaft speed signal setup, the blade passing signal is obtained using a metallic disc with as many metallic flaps as the number of turbine blades (sixty for the turbine used in this study). This results in a waveform with sixty partitions within one revolution, depicted in red in Figure 4.33. One wavelength corresponds to one blade passing, and due to the high rotor speed, the shape of this signal is more akin to a sawtooth wave than a squared wave. The maximum frequency of the sixty-line disc signal is approximately 8.5 kHz, with an amplitude of $0 - 2.5$ V.

iii) Rig trigger signal: Originating from a pressure sensor at the facility NGV inlet, the rig trigger signal controls the data acquisition in the facility. The acquisition is triggered when the voltage surpasses 4 V. This signal is depicted in black in Figure 4.34.

iv) User-selected blade count: The user can select a blade number from 1 to 60 on the LabVIEW graphic user interface that controls the sRIO FPGA, corresponding to the blade's position in the turbine rotation. The first blade is identified as the one coming after the high level of the one-line disc signal.

The first three inputs are read into the 5 V sbRIO input lines using 5 V TTL logic ranges. These lines produce a low voltage output while the inputs range from -0.3 V to 0.8 V, and a high output when the inputs are between 2 V and 3.45 V. The SbRio FPGA generates two outputs controlling the camera data acquisition: the synchronisation and the record start signals.

The synchronisation output is generated by analysing the one-per-revolution signal (from the one-line disc), the sixty-per-revolution signal (from the sixty-line disc), and the user-selected blade count. The FPGA recognises the rising edge of the one-per-rev and starts counting the falling edges of the sixty-per-rev until the selected blade count is reached. At that point, a high 3 V output pulse is sent to the synch port at the back of the camera. Upon receipt of the synch, the generation of one image is initiated, allowing freeze-frame capture of the specified blade during rotation.

The record start pulse, illustrated in black in Figure 4.34, is generated when the rig trigger voltage level surpasses the 4 V threshold. This pulse is then transmitted to the Record Start port at the back of the camera. The pretrigger, necessary for recording the entire time history of the experiment, can be controlled through the camera software, where the user can specify the number of frames for pretrigger. The camera recording setting used for the test campaign were 355 frames of pre-trigger plus 2.5 s of recording post-trigger which translates to approximately 300 frames, thus each IR video has a length of approximately 630 - 635 frames, depending on turbine speed.

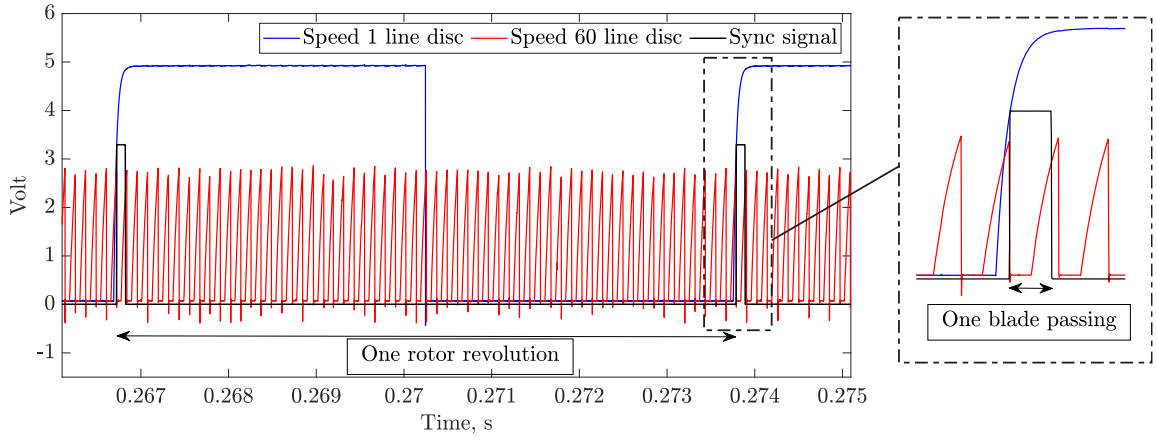

Figure 4.33: Rotor revolution, blade passing and camera synchronisation signals in volt.

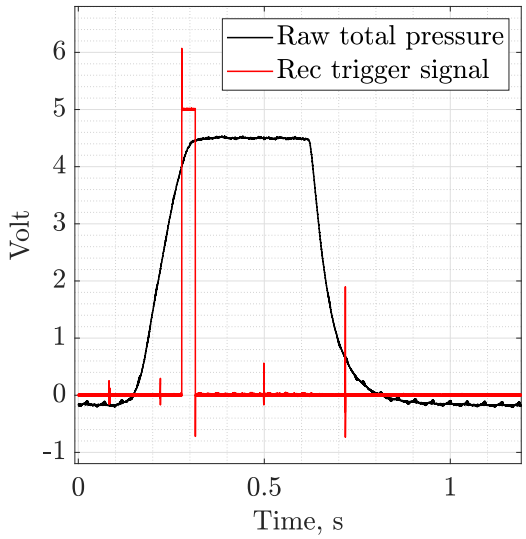

Figure 4.34: Raw total pressure and camera record trigger signals in volt.

4.6 Blades Instrumented with Thin-Film Gauges

In the test campaign, two nominal blades have been instrumented with thin-film heat flux gauges with the aim to use these for IR thermography validation. It is very challenging to instrument the blade tip with gauges, as these tend to fly off during the run and have extra complication for wiring especially on squealer tip designs. Therefore, gauges were installed near the tip, specifically at 80% span on blade suction and surface side.

The gauge manufacturing procedure follows the technique presented by Collins et al. [142]. The thin-film heat flux gauges are manufactured on a flexible polymide substrate using photolithography. First a layer of copper is sputtered on a single sided or double sided polymide film (Kapton), then copper tracks are etched on the copper layer after having applied the Photoresit and the phototool and exposed these to UV light. A second phase of Photoresist, phototool and UV exposure precede the platinum spluttering over the entire surface (layer thickness $< 0.04\,\mu m$). The platinum in excess and the developed Photoresist are removed. After designing and manufacturing, the gauges are attached to the specimen. The manufacturing

technique employed [142] allows a precision in setting the copper track thickness to around 10 microns enhancing lateral gauge density; furthermore, the quality of the copper achievable is such that allows the sheets to endure repeated folding without experiencing delamination. This aspect gains significance as the circuits, formed on the polyimide sheet, are attached to curved metallic surface of the specimen, in this study a turbine blade, using 3M film adhesive. Figure 4.35 shows a photo of one blade instrumented with thin-film gauges on the pressure and suction sides.

To translate the surface temperature history recorded with a thin-film gauge into heat flux, knowledge of the thermal properties of the substrate is necessary, as elucidated by Oldfield [53]. In this scenario, the substrate comprises polyimide and glue. To address this issue, Piccini et al. [141] have demonstrated that the polyimide and glue exhibit identical thermal behaviour, the authors measured the thermal product of both materials and showed this to be $490\,\mathrm{W/m^2/K/s^{0.5}}$ with an uncertainty of 4.2%. This equivalence allows treating the two layers as a unified entity.

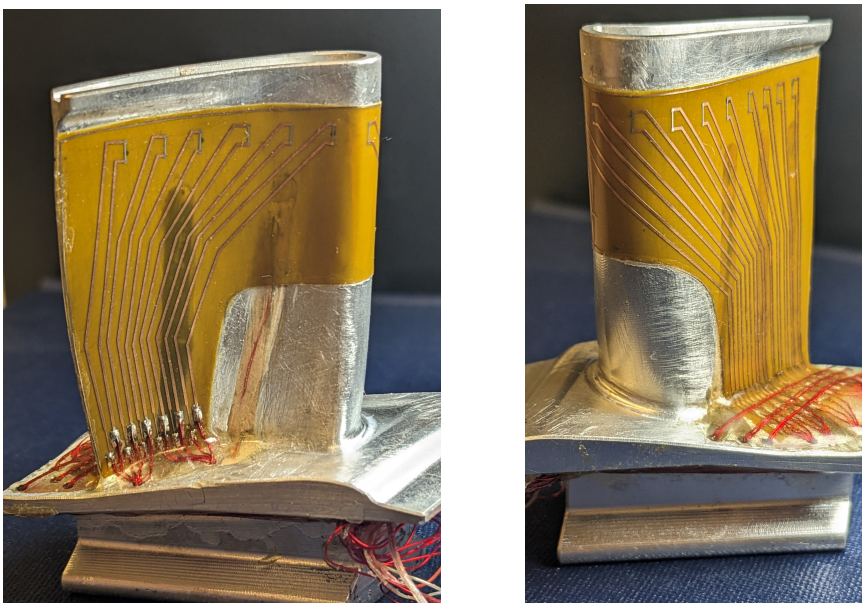

(a) (b)

Figure 4.35: Photographs of a rotor blade instrumented with thin-film heat flux gauges, showing (a) pressure surface and (b) suction surface.

After affixing the polyimide sheet onto the blade, the specimen undergoes multiple cycles of annealing. Thin-film gauges may exhibit a drift in the resistance of the sputtered thin-film resistor grid, and this effect can be mitigated by executing annealing cycles at high temperatures. These annealing cycles also enhance the film's adhesion, reducing the likelihood of failure. The annealing procedure involves two slow cycles and four fast cycles. In the slow cycles, the specimen is submerged in water at 90 °C within an insulating container. The container is then sealed, allowing the specimen to naturally cool down to ambient temperature (approximately 20 °C), this operation is repeated four times. Conversely, the fast cycles involve rapid transitions between hot and cold conditions. Initially, the specimen is submerged in hot water (approximately 90 °C) for 30 minutes, followed by a transfer to cold water (approximately 20 °C) for the same duration. An illustrative example of the annealing procedure for one of the blades is provided in Table 4.3.

Table 4.3: Example of annealing procedure for a blade with thin-film gauges

Slow cycles			
	Initial temperature	Final temperature	Elapsed time
1.1	90 °C	18.6 °C	19 hours
1.2	90 °C	22 °C	21 hours
1.3	90 °C	25 °C	15 hours
1.4	85 °C	22 °C	21 hours
2.1	90 °C	21.4 °C	21 hours
2.2	90 °C	20.3 °C	18 hours
2.3	91 °C	20 °C	21 hours
2.4	91 °C	20 °C	16 hours

Quick cycles			
1.1	90 °C	71.2 °C	30 min
1.2	18 °C	19 °C	30 min
2.1	91 °C	73 °C	30 min
2.2	14.8 °C	18 °C	30 min
3.1	92 °C	78 °C	30 min
3.2	16.5 °C	17.1 °C	30 min
4.1	86 °C	73.1 °C	30 min
4.2	15 °C	18.4 °C	30 min

The temperature coefficient of resistance α for platinum thin-film deviates from bulk platinum due to the reduced mean free path of electrons in thin-films [143], hence calibration is required. The calibration facility includes a thermostatically controlled water bath, a National Instruments PXI system, and a LabVIEW program [136]. A 22-bit National Instruments DMM with 96 channels measures gauge resistance with a 1 mΩ resolution (Figure 4.36). The test piece, equipped with thermocouples and sealed within a plastic sealed bag, undergoes resistance recording at predefined temperature steps. The automated procedure for the blade encompasses multiple cycles ranging from 25 °C to 75 °C, in steps of 10 °C ensuring hysteresis checks and generating comprehensive calibration data suitable for a linear fit.

The system ensures equilibrium has been reached by continuously monitoring both water and specimen temperatures. Upon reaching a specific tolerance range from the set point temperature, the system initiates a convergence check. This check involves monitoring the temperatures for a designed time period, typically 5 minutes. Should any measurement exceed the initial value by a predetermined tolerance, usually 0.4 °C, the temperature monitoring period resets. Once the conditions for convergence are met, the resistances of all connected gauges and all system temperatures are recorded. In Figure 4.37, the calibration data, its corresponding linear fit, and a 95% confidence interval are presented for the best and the worst thin-film gauge on the rotor blade. The α, determined to be approximately $1.7 \times 10^{-3}/°C$, is lower than the value for bulk platinum ($3.9 \times 10^{-3}/°C$), due to the reasons explained earlier [143].



Figure 4.36: Photograph of calibration facility for thin-film heat flux gauges. From left to right: PXI system, water bath, PC with LABVIEW.

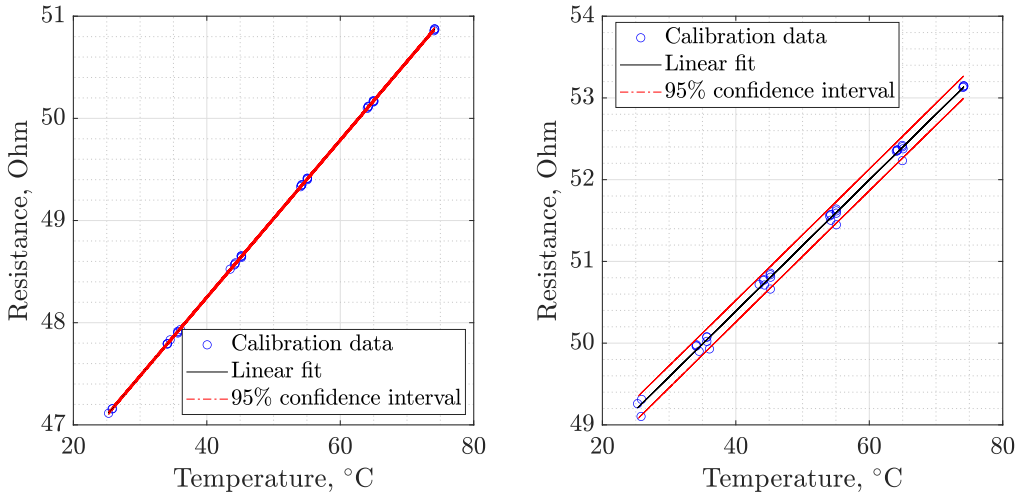

Figure 4.37: Exemplary calibration data for (a) best and (b) worst thin-film gauge on the rotor blade.

4.7 Summary

The design solution to implement an IR thermography system in the Oxford Turbine Research Facility were presented in this Chapter. Firstly, the turbine facility capable of testing high pressure turbine stages at representative engine conditions has been described. The presence of a combustor simulator allows the replication of the

temperature profile at the exit of rich and lean-burn combustors. Temperature and pressure data are recorded at different locations in the facility enabling full analysis of the turbine behavior. The test programme during the IR thermography experiments involved the presence of a casing effusion cooling system, details on this system are given in the Chapter but are limited as UK official.

The optical access design and implementation in the OTRF has been discussed. Various material optical properties have been considered, and zinc selenide was selected for its high transmissivity in the wavelength of interest and for the ideal insensitivity of the optical properties to temperature. Subsequently, pressure and temperature constraints have been considered during the design of the ZnSe IR transparent window and an FEA was performed to ensure satisfactory strength. This design encompasses a cassette that is assembled on the overtip region and provides optical access to two full blade passages

The design of a composite blade was required to perform IR thermography measurements in the OTRF. PEEK was selected for the composite substrate given its low thermal conductivity. This blade was conceived in three steps: the machining of an aluminium insert, the injection moulding of a PEEK substrate, and the post-machining to the blade airfoil shape. Tensile load and fatigue tests were performed on a range of insert designs to quantify the bond strength between the aluminium and the PEEK. These tests proved the blade is capable of withstand mechanical loads ranging between 11 kN and 12 kN, well above the maximum expected load in the facility. A fatigue test also proved the capability of the blade to withstand multiple cycles at a load of 4 kN without manifesting signs of hysteresis or cracking.

The IR camera control system, required to allow synchronisation of the image capture to the selected blade, was design using the shaft speed and the blade passing signals. The system was able to capture stable images of any selected blade on the rotor with fine adjustment of FOV possible. It also triggers the IR image acquisition

based on the facility data acquisition trigger.

Two aluminium blades were instrumented with single-sided thin-film heat flux gauges to enable comparison and validation between the results achievable with these traditional sensors and with the IR camera. As instrumenting the tip with thin-film gauges is challenging and potentially results in the gauges flying off the component, it was decided to assemble the gauges around the blade pressure and suction side close to the tip, specifically at 80% span. The instrumentation procedure and calibration of these blades is described.

Chapter 5

Infrared Thermography of Rotor Tip Heat Transfer

This chapter presents the results of a test campaign employing Infrared Thermography conducted in the Oxford Turbine Research Facility with a rotor casing effusion cooling system. These measurements mark a significant advancement in heat transfer turbomachinery research, as very few studies show comparable data in literature, these are briefly reviewed at the beginning of the chapter.

The effect of shortening the IR camera integration time on turbine tips image quality is presented, allowing deeper understanding on the nature of noise in the measurement. The data processing from raw camera digital counts to Nusselt number for an uncooled squealer tip rotor blade is described. This routine uses the calibration and correction procedures developed in Chapter 3 and also includes an image stabilisation procedure required to address limitation in the camera synchronisation system and vibrations. The outcomes of the study are presented as full field target temperature, adiabatic wall temperature and Nusselt number for a blade tip, as well as for a selected pixel. To provide confidence in the novel IR Thermography methodology, two validation cases are presented. The first compares the IR data to experimental thin-film gauges data and the second to a CFD validate simulation.

5.1 Background

The work carried out by Knisely et al. [107, 108], pioneered the implementation of infrared thermography for the START facility at PennState University. Differently from the OTRF, the START turbine test facility is continuous duration, allowing the acquisition of as many infrared images needed for reducing the RMS error (in his study from 2021, Knisely suggests a minimum of 50 frames should be averaged). Additionally, the optical access at PennState University is designed to look at the rotor blade pressure side and leading edge from the NGV, thanks to an optical custom made probe. The second group implementing IR thermography in a turbine rotating facility was the Ohio State University (OSU), and in the study by Christensen et al. [109], the authors presented their efforts to capture thermal images of turbine blade tips. The work from Ohio State University is more relevant to the present dissertation since the facility operating conditions are more similar to the OTRF ones. Firstly, the OSU turbine facility is short duration like the OTRF, and secondly the target of the measurements are blade tips. The optical access in the OSU test facility is located in the overtip region, as the one in the OTRF. However, the infrared transparent window in the OSU facility is smaller than the OTRF one, only allowing visual access to one blade tip. More details on the IR thermography research from PennState and Ohio University can be found in the literature review of Chapter 2.

5.2 Experimental Setup

The experiments were conducted in the Oxford Turbine Research Facility, the design of the experiment and a description of the facility are given in Chapter 4. The Strategic Investment in Low-Carbon Engine Technology (SILOET) turbine tested features 40 HP vanes and 60 transonic HP rotor blades, designed with 50% reaction [144]. Infrared thermography measurements concentrated on the blade tip region which fea-

tured a double-sided squealer tip with an open trailing edge. In the rotor assembly, 14 blades were coated with PEEK and allocated for IR thermography measurements, and 2 were instrumented with thin-film heat flux gauges on the pressure and suction surfaces at 80% span. Further design details on the IR thermography blades and the thin-film gauges can be found in Chapter 4, Section 4.4 and Section 4.6, respectively. The coated blades were sprayed with Nextel velvet black and Ambersil aluminium paint. The IR camera was synchronised to the blade rotation, thus working at a framerate equivalent to the rotor passing frequency and capturing one image per revolution. The rotor nominal speed of 8500 rpm is reached during the stable portion of the run, which last of approximately 0.5 s, while the speed ranges from 8350 rpm to 8500 rpm during the entire test duration. A range of camera integration times was used to investigate their impact on the measurements, the values were selected based on the expected rotor speeds.

The camera used in this study is a FLIR A6751 SLS LWIR, which was chosen for its sensitivity and speed. The camera features a 640 $\times$ 512 pixel Focal Plane Array (FPA) and cooled Strained Layer Superlattice (SLS) detector sensitive to the wavelength in the long infrared range, between 7.5 µm and 10.5 µm, which suits the expected experimental peak emission of 9 µm approximately. The camera framerate at full window of 125 Hz was increased by windowing down to match the expected rotor frequencies of 130 – 142 Hz. To maximise the field of view (FOV), an image size of 624 $\times$ 364 pixels was selected, which allowed two and a half blade tips in the FOV. Accurate positioning of the blades within the FOV. The blade positioning within the FOV was controlled by selecting the desired blade count number in the IR camera synchronisation system (described in Chapter 4, Section 4.5). A photograph of the rotor configuration used in the OTRF, as well as the schematic of the IR camera setup and typical achievable FOV with this configuration are shown in Figure 5.1. A summary of testing conditions is shown in Table 5.1.

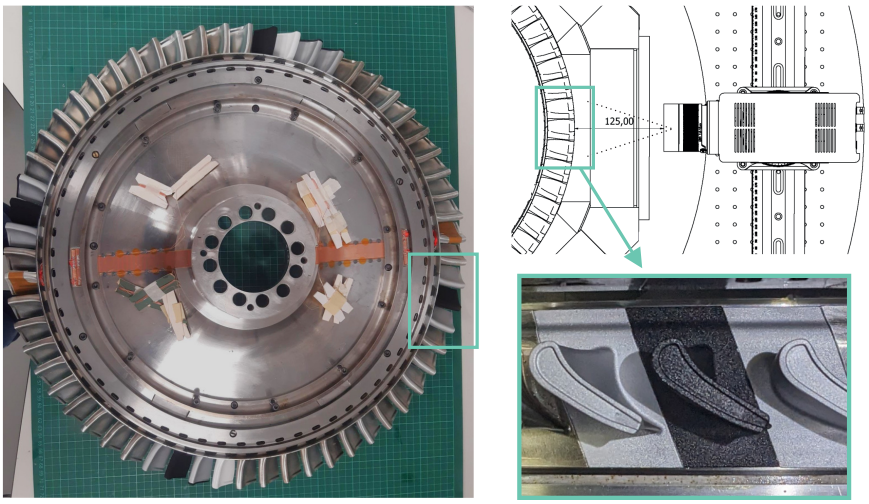

(a) (b)

Figure 5.1: Rotor assembly in the OTRF, including (a) photograph of the rotor and (b) schematic of the setup and photograph of typical achievable FOV for rotor tip IR thermography measurements.

Table 5.1: Relevant testing conditions in the OTRF during IR thermography rotor tip heat transfer measurements.

Blades	IR blades coated with PEEK	14
	Blades with thin-film heat flux gauges	2
	Nominal geometry blades	44
Rotor	Nominal rotational speed	8500 rpm
	Speed range during testing	8350 – 8500 rpm
	Tip radius	0.296 m
	Nominal absolute velocity	263.5 $\mathrm{m\,s^{-1}}$
	Nominal rotor frequency	142 Hz
	Rotor frequency range during testing	130 – 142 Hz
	Nominal blade passing frequency	8520 Hz
Temperature	Range of gas temperature at NGV inlet during testing*	295 – 475 K
Camera**	Model	FLIR A6750 SLS
	Framerate	130 – 142 Hz
	Integration time	5 µs
	Working distance	125 mm
IR dataset ***	Frames	∼630 frames
	seconds	∼4.5 seconds
Scene	pixels	624x364
	geometrical	2.5 blade tips
Window	material	Zinc selenide

* Measured by radial rakes of k-type 25.4 µm diameter bare-bead thermocouples.
** Camera synchronized to rotor frequency.
*** One frame/image captured per revolution.

5.3 Effect of Integration Time

The extent of blur in the direction of motion in an image, of particular significance when capturing fast moving targets, is dependent upon both the speed of the target and the chosen integration time of the camera detector. The blur level reduces as the integration time is shortened; however, a short integration time leads to increased error. This has been discussed in detail in Chapter 3, where the camera behaviour has been studied on a bench-top experiment. The aim of this section is to investigate the effect of integration time, error, and blur levels on measurements in the OTRF. A preliminary analysis implies the evaluation of blur as a function of integration time for nominal speed in the facility. For the calculation, the nominal rotational speed of the OTRF is of 8500 rpm, and the rotor section of the facility features a radius of approximately 0.296 m were used, giving a tangential velocity at the blade tip of

$$N = 8500\,\text{rpm} \;\rightarrow\; \omega = N \times \frac{2\pi}{60} = 890.12\,\text{rad}\,\text{s}^{-1} \;\rightarrow\; v_t = \omega \times r = 263.47\,\text{m}\,\text{s}^{-1} \quad (5.1)$$

Given an integration time, a simple estimate of blur level in millimetres is given by

$$\text{blur} = v_t \times \text{IT} \quad (5.2)$$

While to convert this value in pixel, knowledge of the camera working distance, pixel size, and focal length is necessary. In the OTRF setup, using a FLIR A6750 SLS, with a manual bayonet lens featuring 17 mm focal length and 2.5 f/number, a distance between the camera lens and the blade tip of 125 mm results in a pixel-to-mm ratio of approximately 9.067. The estimated blur on the tip in millimetres and pixels with such conditions of velocity, working distance and over a range of integration times between 20 µs and 1 µs, is detailed in Table 5.2.

The effect of the integration time on IR thermography data captured in the OTRF was studied by capturing data with the same turbine operating and inlet conditions and using a range of integration time from 20 µs to 1 µs. The detector calibration

curves shown in Figure 5.2 were used to convert data from raw digital counts to equivalent blackbody temperature T_{cam}.

Figure 5.3 presents a summary of this analysis. On the left side, infrared images of equivalent blackbody temperature T_{cam} captured in the facility are shown for a single frame selected from the stable period of each run. On the right side, the graphs display the temporal history of T_{cam} corresponding to the highlighted pixel located at a local hot spot in the blade gutter near the leading edge, indicated by a star-shaped symbol. From top to bottom, integration time decreases from 20 µs to 1 µs. Images were acquired with identical triggering settings.

Table 5.2: Blur levels as a function of integration time for nominal speed condition in the OTRF.

IT	µs	20	10	5	2	1
Blur	mm	5.27	2.63	1.32	0.53	0.26
Blur	pixel	47.78	23.89	11.94	4.78	2.39

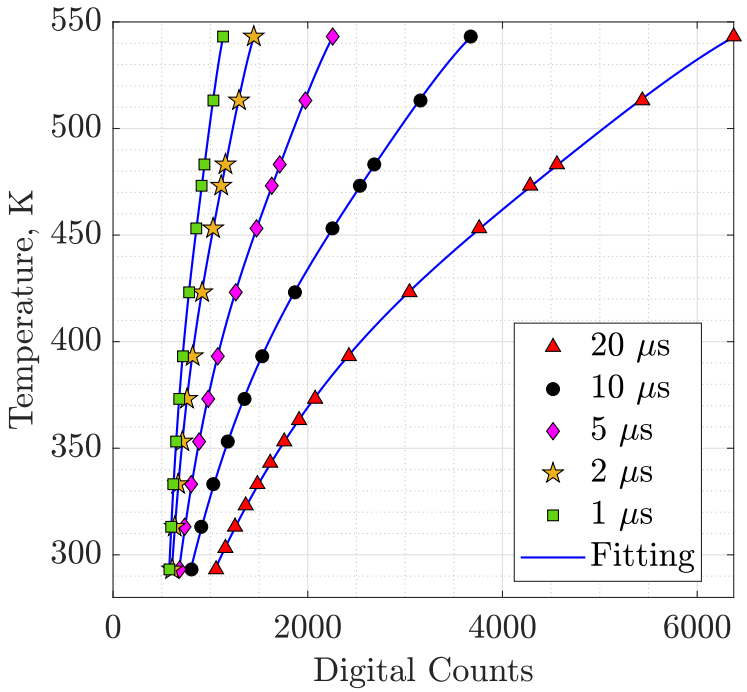

Figure 5.2: Camera detector calibration for integration times of 20, 10, 5, 2, and 1 µs.

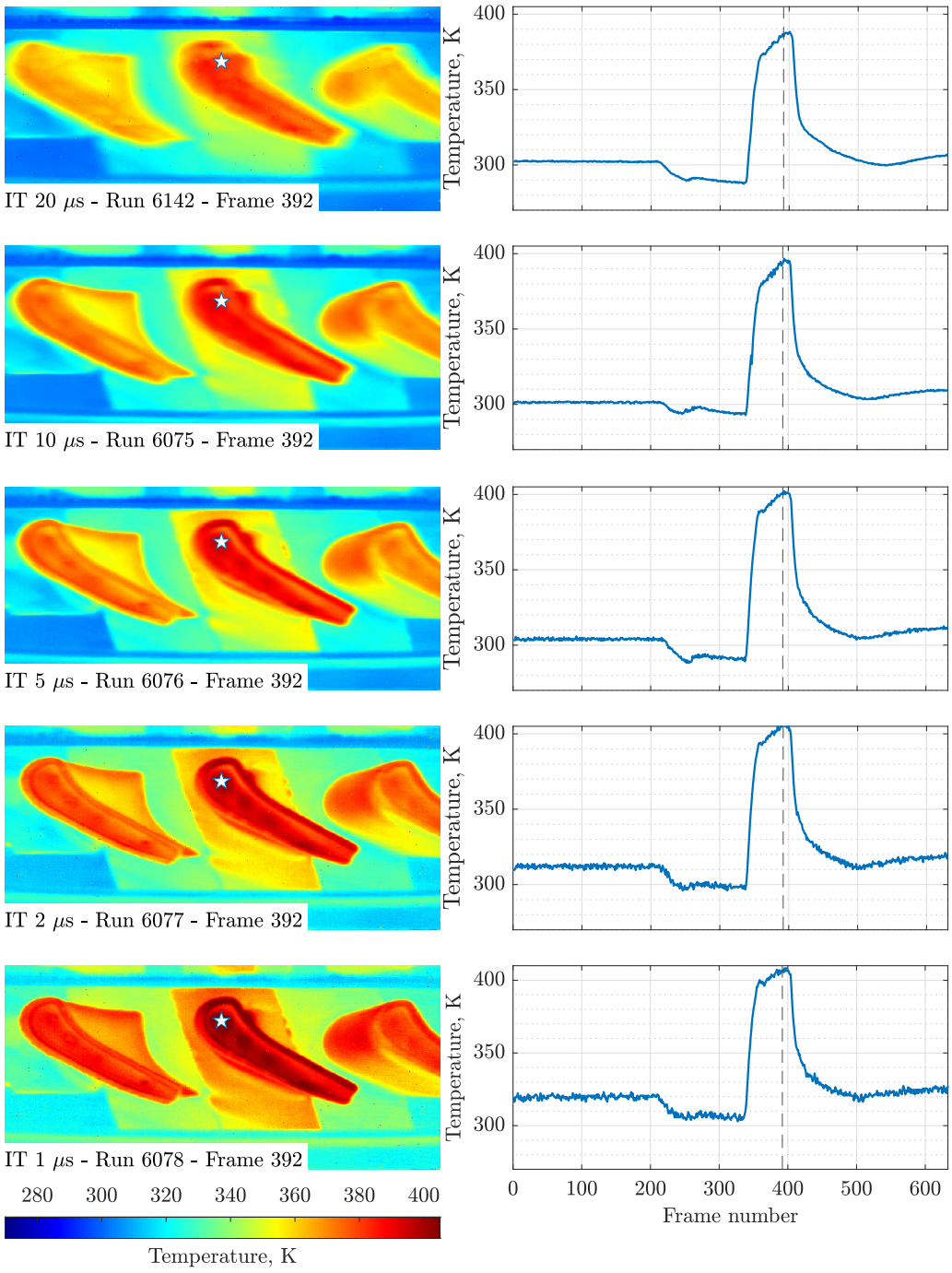

Figure 5.3: Analysis on the effect of camera integration time on image quality and signal level. On the left, infrared images of one frame of T_{cam} acquired during runs with uniform inlet condition in the OTRF. On the right, temporal history of T_{cam} for the pixel marked by a star symbol on the correspondent infrared image. Top to bottom: integration times 20, 10, 5, 2, and 1 µs.

Notably, with the longest integration time, the blade edges display considerable blur, progressively sharpening as the integration time decreases. At longer integration times, i.e. 20 µs and 10 µs, the blade displacement is large enough for the local temperature gradients (camera detector collecting energy coming from both blade tip and platform) to cause measurement error, of order 10 K, within the main test period (frame 392) at the surveyed pixel.

Although the image with the shortest integration time is clearly the sharpest, examination of the temporal history of T_{cam} for the surveyed pixel on the blade tip shows that the acquired data is also the noisier, particularly evident during the initial spin up phase of the test where the lowest temperature values are recorded. The temporal plots also reveal a discrepancy with the temperature values in the initial spin up phase (prior to frame 200). The lowest integration time dataset records a blackbody equivalent temperature of approximately 320 K compared to approximately 300 K recorded in the dataset for the longest integration time. The difference is attributable to the larger measurement error with shorter integration times, especially evident at lower temperatures. This behaviour agrees with the detector characterisation shown in Chapter 3, specifically the behaviour in Figure 3.10.

To quantify the temporal error, the characterisation was expanded to include all the integration times used in this test campaign. Figure 5.4 shows the IR camera reading and errors obtained from a dataset of 100 frames, with the IR camera looking at the blackbody calibrator set at two temperatures, 293 K in Figure 5.4a, and 353 K in Figure 5.4b. The red lines in the temperature history plots indicate the blackbody source temperature, black lines indicate the mean of the camera temperature readings across the 100 frames, and the temporal error traces are absolute errors defined as the difference between the real target temperature and the camera reading. This error decreases as the integration times and target temperature increases, agreeing with the increased error in T_{cam} at low target temperature and integration time in the OTRF

shown in Figure 5.3. By comparing the plots for the integration time of 1 µs, it can be seen that for a target temperature of 293 K, corresponding to the temperature level during the initial phase of the run in the OTRF, the temporal error goes from a minimum of 0.6 K to a maximum of 9.3 K, while for a target temperature of 353 K it goes from a minimum of 0.1 K to a maximum of 5 K.

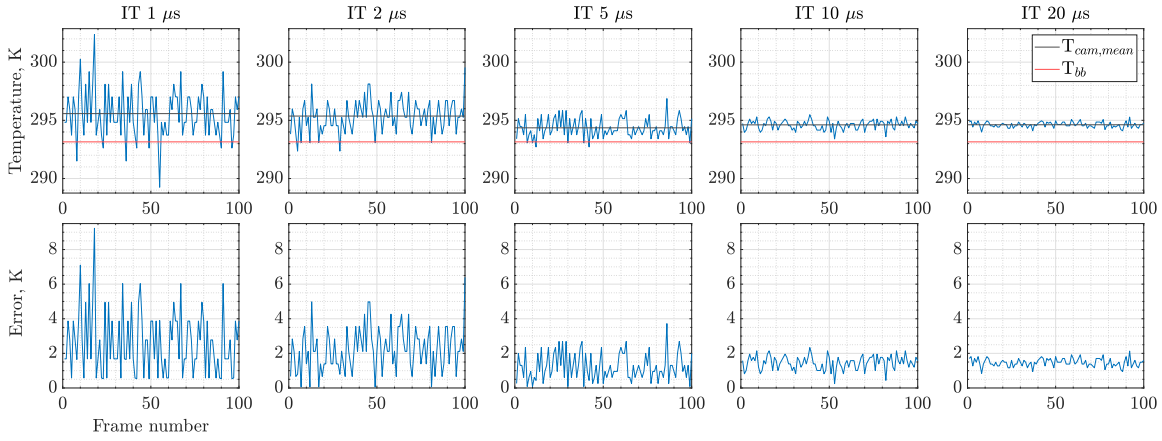

(a)

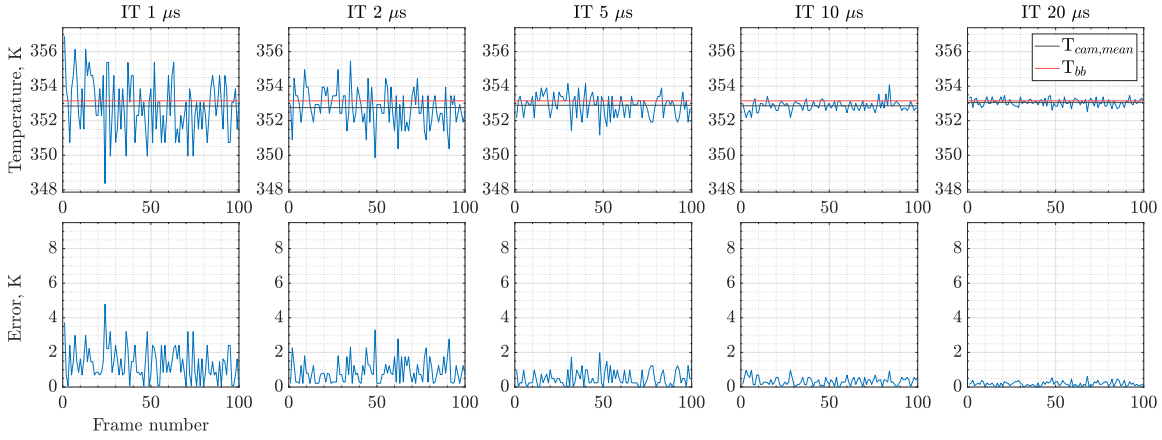

(b)

Figure 5.4: Equivalent blackbody temperature reading T_{cam} and absolute temporal error in temperature reading from a single pixel, for 100 frames acquired at 125 Hz, for blackbody calibrator temperature of (a) $T_{bb} = 293.15$ K and (b) $T_{bb} = 353.15$ K. Range of integration times from 1 µs to 20 µs.

A summary plot to better understand the influence of target temperature and integration time on the maximum temporal error is shown in Figure 5.5. The graph shows the maximum temporal error for a randomly selected pixel in the camera Focal Plane Array (FPA). A pixel, which is the detector element in a FPA, is made of two components: a photon diode and the readout integrated circuit. When the incident energy strikes the detector FPA, electrons are collected over the integrated capacitor which in turn collects energy for the duration of the set integration time. An analogy often used in the field is that of the buckets in the rain, at low temperature the buckets are filled at a lower rate as there are fewer photons. Thus, at very low integration times and low blackbody temperatures, what happens at the pixel level is that the camera is not able to differentiate between the noise level and the temperature measurement.

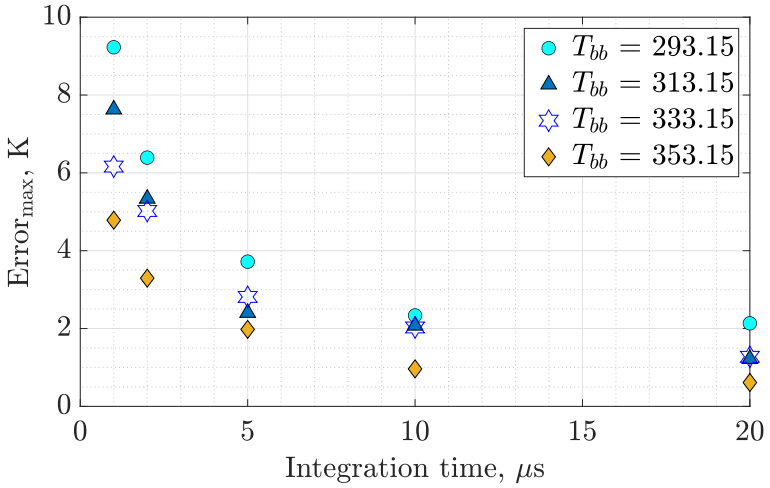

Figure 5.5: Maximum absolute temporal error in temperature reading T_{cam} from a randomly selected pixel as a function of integration time, for temperature between 293.15 K and 353.15 K.

The nature of the increased error in the camera reading for the low temperature regions in the OTRF tests shown in Figure 5.3, can be explained with the temporal error graph. This shows how errors as high as 10 K can affect the measurements acquired with an integration time of 1 µs. For this reason, an integration time of 5 µs was chosen for the OTRF tests used in the heat transfer analysis shown in the

following sections. It is worth noting that this behaviour only limits measurements of heat flux $\dot{q}$ as for this the temperature history is required. In future measurements, the emphasis will shift towards evaluating the film or metal effectiveness over extended run duration. During these evaluations only the steady conditions are required for the analysis, thereby potentially allowing for the use of lower integration times.

5.4 Processing of Thermal Data

The findings and efforts from the previous chapters are used as guideline for developing the processing of the rotor thermal data captured in the OTRF. Emphasised in Chapter 3 is the need of correction for emissivity of the target, surroundings reflection, and transmittance of the optical path to ensure accuracy in infrared temperature measurements. Correction for surrounding reflections was achieved by combining two datasets with differing surface emissivity (ε_1 and ε_2), acquired under the same aerothermal field and viewing angle conditions. During the experiments, this was achieved by acquiring IR thermal data on different rotor blades, one coated with Nextel velvet black paint (subscript 1, high emissivity) and another coated with Ambersil aluminium paint (subscript 2, low emissivity) at the centre of the Field of View (FOV).The emissivity values of the two paints were found through a traceable calibration, providing values of 0.97 for the Nextel velvet black paint and 0.6 for the Ambersil aluminium paint. The two FOVs are shown in Figure 5.6, where a red dashed line encompasses the blade of interest, thus individuating the two regions of interest (ROI). Finally, the optical path contribution was corrected calibrating the transmittance of the zinc selenide window used in the experiments and modelling the window temperature distribution during the run. Thus, a system of two equations in two unknowns stems from the IR energy balance equation, that can be solved to obtain the corrected target temperature and the reflected temperature. This workflow is schematically shown in Figure 5.7.

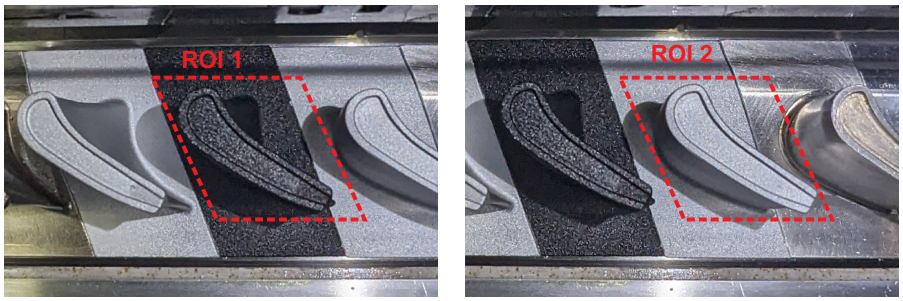

(a) (b)

Figure 5.6: Photographs of (a) FOV 1 and ROI 1 for T_{cam1} and (b) FOV 2 and ROI 2 for T_{cam2}.

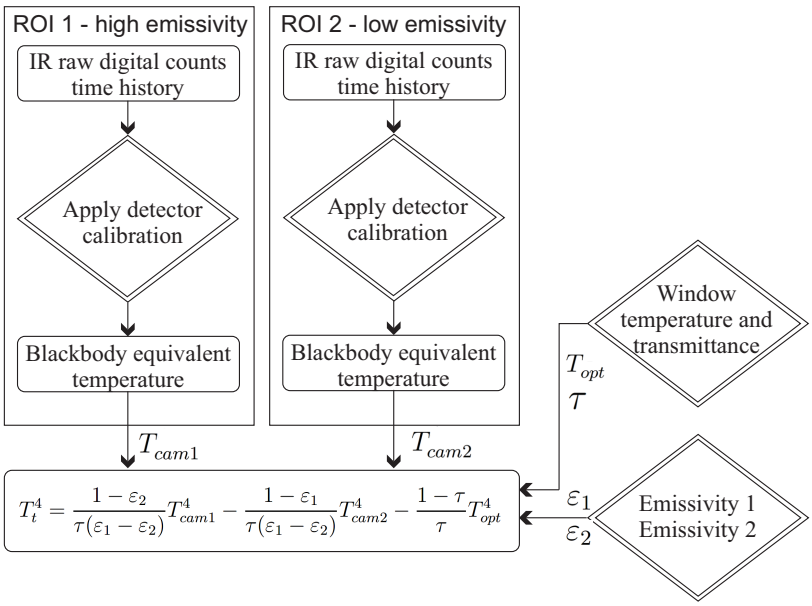

Figure 5.7: Block diagram of the workflow to process IR data from raw digital counts to target temperature.

Once the surface temperature history of the blade tip has been obtained, this can be then be processed to heat transfer quantities, specifically adiabatic wall temperature and Nusselt number. The entire processing of the OTRF thermal data can be summarised in the following steps:

Step 1: Convert raw IR data to target temperature - block diagram of Figure 5.7

- Load test and apply blackbody calibration (Section 3.3.1)

- Apply emissivity reflection and transmissivity calibration (Section 3.3.2, 3.3.3 and 3.3.4)

Step 2: Stabilise target temperature

- Export test raw image sequence in open source software Blender for image tracking
- Export video displacements in the x and y direction
- Import displacement values in Matlab and apply video stabilisation to the target temperature image sequence

Step 3: Heat transfer analysis

- Impulse response method from target temperature to heat flux.
- Adiabatic wall temperature regression.
- Nusselt number calculation

These steps will be discussed in the following sections.

5.4.1 Target Temperature and Run Characteristics

The measurement target in this study was a cavity tip, also known as a squealer tip, a configuration used to mitigate tip leakage flows, of the composite blades described in Chapter 4, Section 4.4. The thermal data was recorded in the form of raw digital counts using a FLIR A6750 SLS IR camera and converted to blackbody equivalent temperature using the detector calibration discussed in Chapter 3, Section 3.3.1 as follows

$$T_{cam} = a_4 Raw^4 + a_3 Raw^3 + a_2 Raw^2 + a_1 Raw + a_0 \tag{5.3}$$

The calibration curves as a function of integration time are reported in Figure 5.2.

It is crucial to note that the temperature obtained in this manner requires correction. As illustrated in the schematic of Figure 3.1b, various radiation sources, beyond

the radiation emitted by the target, reach the infrared detector in the OTRF infrared measurement setup. To perform a combined correction for these components, and calculate the true target temperature, Equation 3.8 was employed. This equation allows correction for surface emissivity, surrounding reflection and transmissivity of the optical path. It is reported here for ease of discussion alongside with Equation 3.9 for the calculation of the reflected temperature

$$T_t^4 = \frac{1-\varepsilon_2}{\tau(\varepsilon_1-\varepsilon_2)}T_{cam1}^4 - \frac{1-\varepsilon_1}{\tau(\varepsilon_1-\varepsilon_2)}T_{cam2}^4 - \frac{1-\tau}{\tau}T_{opt}^4 \tag{5.4}$$

$$T_r^4 = \frac{\varepsilon_1}{\tau(\varepsilon_1-\varepsilon_2)}T_{cam2}^4 - \frac{\varepsilon_2}{\tau(\varepsilon_1-\varepsilon_2)}T_{cam1}^4 - \frac{1-\tau}{\tau}T_{opt}^4 \tag{5.5}$$

Similarly to the analysis performed on the rotating flat disc facility in Chapter 3, the signal T_{cam1}, derived from the high emissivity blade, provides information about the true target temperature. This signal needs to be corrected for surroundings reflections. Using the signal T_{cam2} from the low emissivity blade is effective for this correction. The equation incorporates emissivity values to address surface emissivity correction, and, finally, correction is applied to account for the transmissivity of the optical path.

The use of this equation implies the need of two sets of measurements recorded under identical conditions: one for the high emissivity signal T_{cam1} and another for

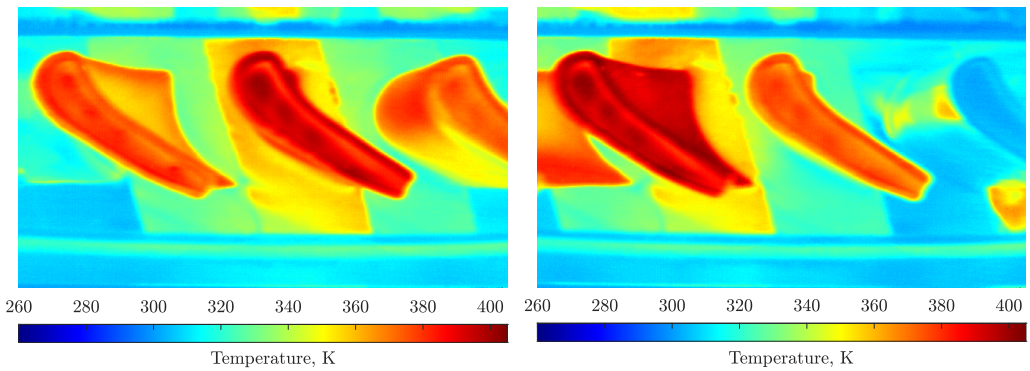

(a) (b)

Figure 5.8: Single frame camera reading, i.e. blackbody equivalent temperature, showing (a) T_{cam1} and (b) T_{cam2} for FOV 1 and FOV 2 respectively.

the low emissivity signal T_{cam2}. This was done in two runs in the OTRF, keeping the same testing conditions, but changing the camera synchronisation settings to have first the high emissivity blade at the centre of the field of view, and subsequently the low emissivity blade. Infrared images showing a map of T_{cam1} and T_{cam2} are depicted in Figures 5.8a and 5.8b. The IR images correspond to one frame during the stable portion of the run.

Figure 5.9 illustrates the temporal evolution of the blackbody equivalent temperature T_{cam1} during various stages of the test run. Positioned to the left are infrared images capturing the blade, with a specific pixel on the blade tip marked by a star-shaped marker. On the right side of each infrared image, a plot displays the temporal history of T_{cam1} corresponding to the highlighted pixel. One frame was chosen for each stage, specifically frames number 50, 250, 370 and 500. Frame 50, Figure 5.9a, is acquired during the spin up phase, where the facility is at ambient temperature, meaning very low energy detected by the IR camera, thus, low contrast in the image. In this phase, the rotor is spinning in near vacuum conditions, causing slight frictional heating on the blade tip, resulting in a slightly elevated temperature from ambient conditions on the squealer rim. Frame 250, Figure 5.9b, is acquired during the coolant injection phase where ambient temperature coolant flows are initiated and stabilised. This cools the blade back to near ambient and isothermal conditions. Horizontal 'stripes' of lower temperature result from the effusion cooling arrangement of holes situated on the static casing above the rotor tip. This demonstrates the sensitivity of the measurements, clearly detecting only a few degrees of temperature difference. As the capture of this frame is still before the plug valve opens, thus before the hot mainstream flows into the test section, the blade temperature is still close to ambient, again, resulting in a low contrast in the image. Frame 370, Figure 5.9c, is captured in the main test period, after the NGV inlet total temperature has risen to the nominal value of approximately 380 K. It is in this portion of the run that the IR images

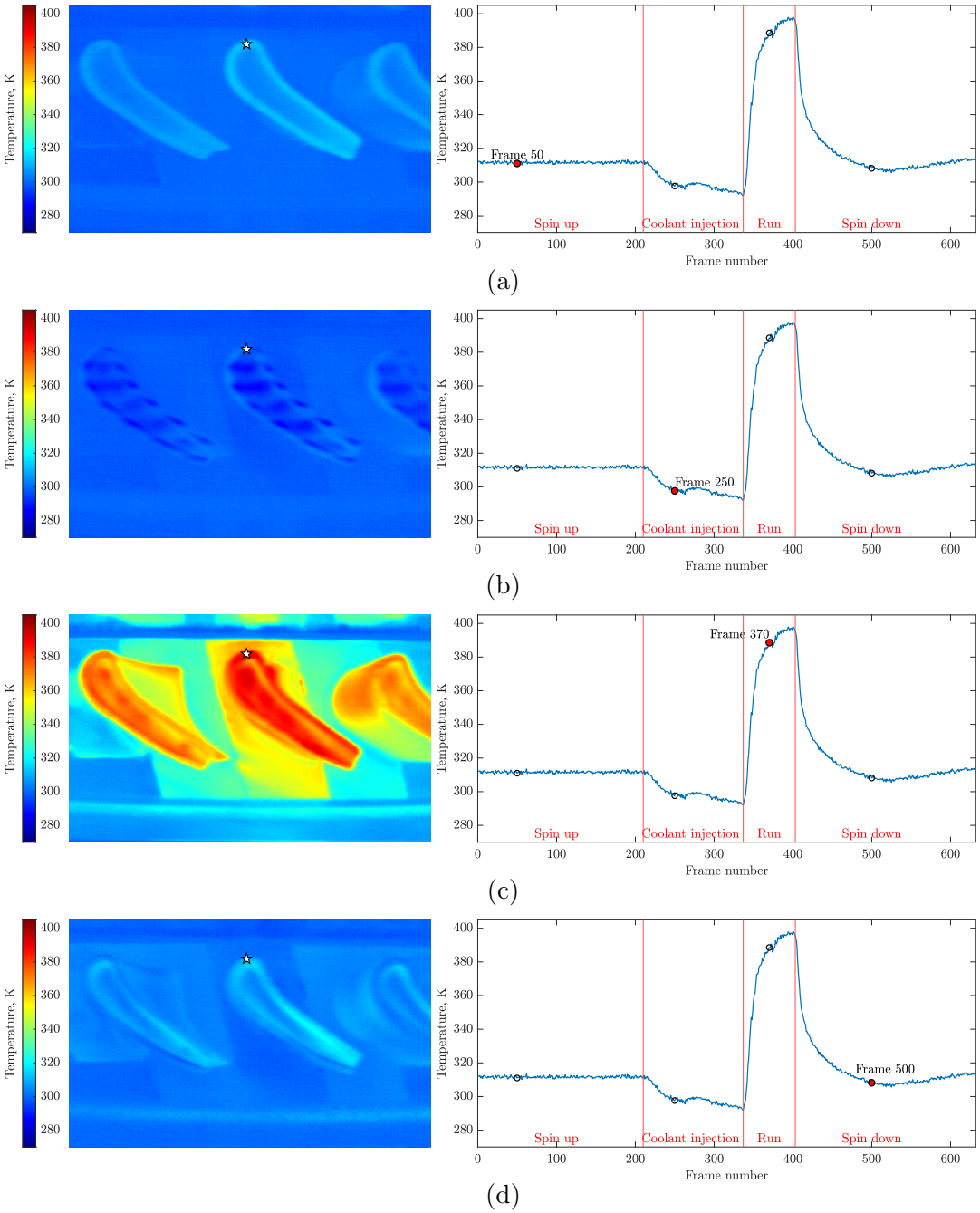

Figure 5.9: Evolution of T_{cam1} blackbody equivalent temperature during the stages of a test run with uniform inlet condition, showing (a) Frame 50; (b) Frame 250; (c) Frame 370; (d) Frame 500. Infrared images on the left with a star-marked pixel on the blade tip. The plots on the right detail the temporal history of T_{cam1} for the highlighted pixel.

are sharp and present the best contrast levels, and some qualitative observation can be drawn from this image. The three blades captured in the image are of the same

material and exposed to the same temperature field, which leads to conclude they are at the same temperature. However, the camera is reading different values from the three. This is a result of the different emissivity values and surroundings reflections from each blade. The blade at the centre has a high emissivity so the equivalent blackbody temperature is close to the true target temperature, whilst the two neighbouring blades are coated with low emissivity paint. Finally, frame 500, Figure 5.9d, is captured during the spin down, when the temperature has decreased but it still higher than ambient.

Having assumed a transmissivity of air equal to 1, the optical path temperature T_{opt}, needed for the correction of the optical path contribution in Equation 5.4, consists of the window temperature only. Given the short duration of the test in the OTRF of 0.5 s, and the window material properties [145], the window temperature increase is negligible and the window temperature stays approximately constant and equal to 295 K. This was inferred from a transient heat convection simulation conducted on the optical window, summarised in Figure 5.10. The simulation used representative (though worst case) experimental boundary conditions: internal air temperature of 477 kelvin; external air temperature of 293 K; internal heat transfer coefficient of 2000 $\mathrm{W\,m^{-2}\,K^{-1}}$, and external heat transfer coefficient of 0 $\mathrm{W\,m^{-2}\,K^{-1}}$. The internal heat transfer coefficient was extrapolated from results of experiments of casing heat transfer carried out in the facility under the same setup.

Infrared thermal images of blackbody equivalent temperatures for each blade T_{cam1} (actual $\varepsilon = 0.97$) and T_{cam2} (actual $\varepsilon = 0.60$), corrected target temperature T_t, and reflected temperature T_r are shown for frame number 392 acquired during the stable test period of the run in Figure 5.11a-d. Figure 5.11e plots the variation of these temperatures against frame number for a single pixel located in the blade tip squealer cavity towards the leading edge. The reflected temperature remains approximately equal to 295 K up until the plug valve opens letting the hot stream flowing down the

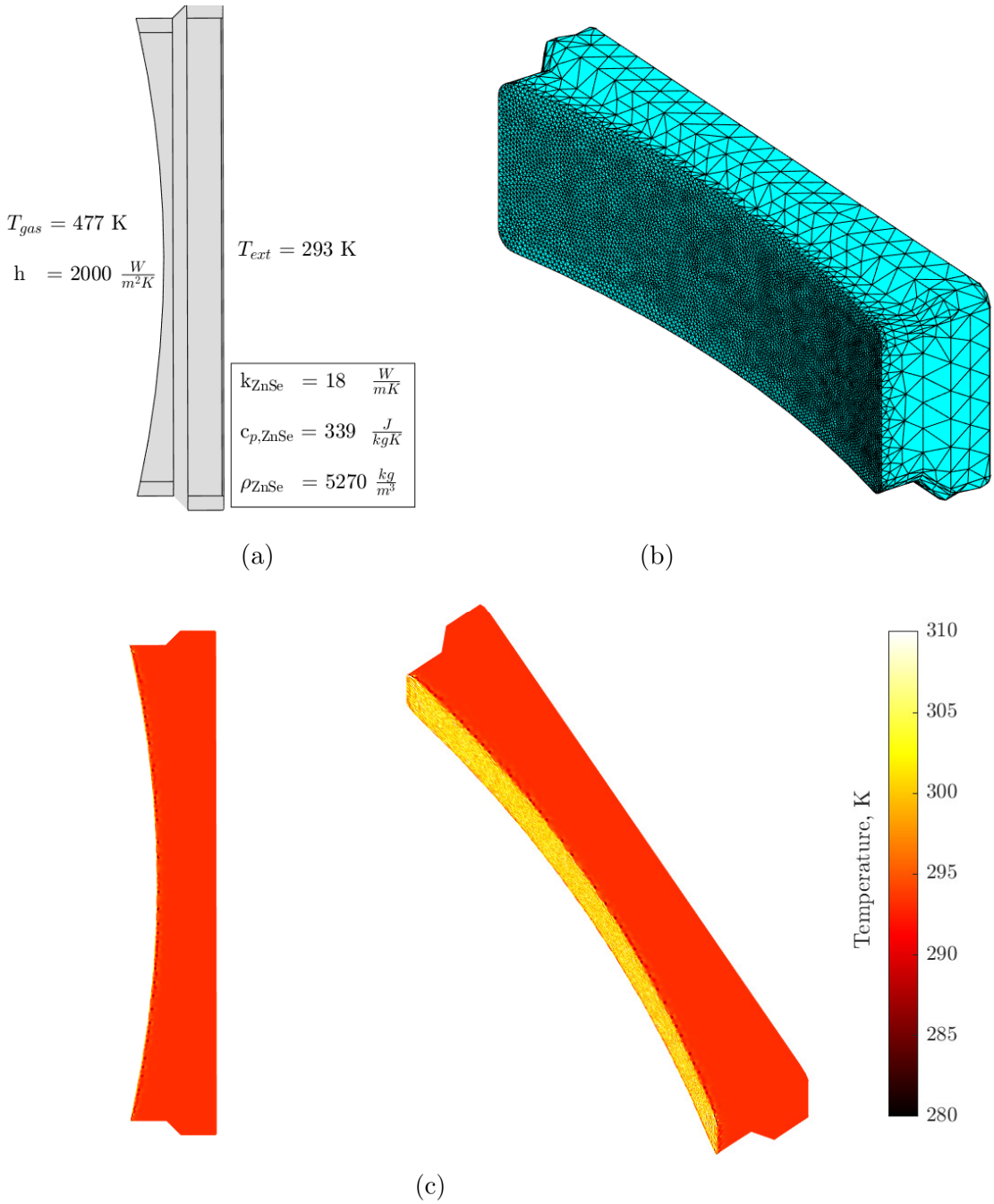

Figure 5.10: Results from the transient heat convection simulation on the IR transparent window used in the OTRF, showing (a) CAD model of the window showing the ZnSe material thermal properties and the boundary conditions; (b) mesh of the window used for the simulation; (c) temperature field of the window after 0.5 s.

test section, thus until frame number 335. The blackbody equivalent temperature T_{cam1} and target temperature T_t show a temperature slightly higher than ambient due to frictional heating of the blade tip during the spin up phase, while they return to near ambient temperature during the coolant injection phase. As the hot gas flow through the turbine test section, T_{cam1}, T_t, and T_r all increase, reaching maximum values of approximately 400 K, 405 K, and 330 K, respectively, before decreasing down to approximately 300 K at the end on the run. The camera reading T_{cam1} and target temperature T_t follow each other during the spin up and coolant injection phases of the test, staying within 1 K. On the other hand, the difference between the two increases to approximately 5 K in the stable portion of the run, identifying a total correction of approximately 1.13% between blackbody equivalent and target temperature.

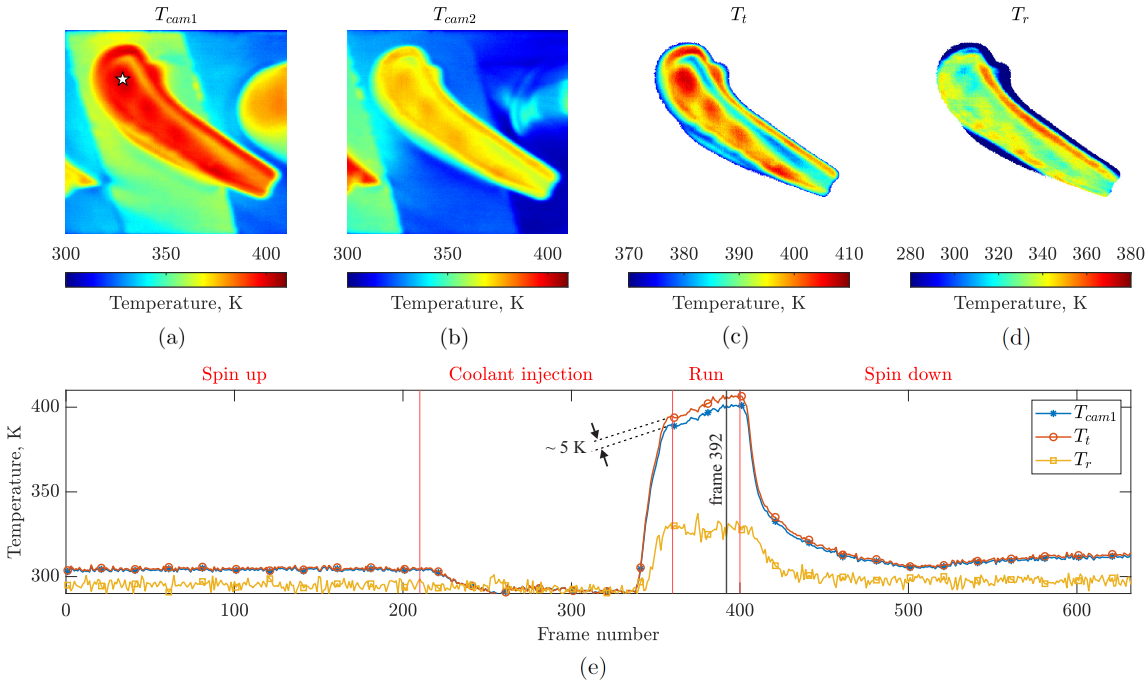

Figure 5.11: Exemplary results and correction of blade tip IR thermal data captured in the OTRF. Thermal maps during the steady test period (frame 392) showing (a)-(b) blackbody equivalent T_{cam1}&T_{cam2}, (c) target, and (d) reflected temperatures for an integration time of 5 µs. (e) Time traces for single pixel on blade tip as marked with a star.

5.4.2 Dynamic Synchronisation and Vibration Instabilities

The camera synchronisation system was able to capture stable images of any selected blade within ±5 pixels (±0.55 mm on the blade tip) on the disc with fine adjustment of FOV. Additionally, during the test period the mainstream flow induced vibrations in the camera mounting resulting in translational movement of the centre of the FOV by approximately ±9 pixels (≈ ±1 mm on the blade tip). Processing to heat transfer requires accurate time history. In areas of high gradients e.g. blade tip edges, even this instability can cause errors. To minimise the impact of the displacement on measurement accuracy, a video stabilisation procedure based on feature tracking was developed. Firstly, the IR videos captured in the OTRF were converted to a sequence of images, and their image quality enhanced to ensure sufficient contrast for the feature tracking. Notably, infrared video contrast is indicative of temperature, making features indiscernible in the initial frames of the dataset due to the uniform isothermal conditions at low temperatures characterising the beginning of the experiments. The MATLAB's function imadjust was used to uniformly improve the image contrast. The results of this enhancement are illustrated in Figure 5.12, comparing original and enhanced images at frame numbers 50, 250, 370, and 500 aligning with the different phases of the experiment and are identified in Figure 5.13, which shows the temporal history of raw digital counts corresponding to the highlighted pixel located on the leading edge.

Subsequently, the enhanced image sequence is imported into the software Blender for the tracking process. The motion tracking algorithm within the Blender software facilitates the placement of tracking markers within the scene, serving as reference points. The selection criteria for these markers prioritise distinct and high-contrast features present throughout the entire video. The algorithm uses these markers as anchor points for feature detection and matching, enabling the tracking of their movement across the video sequence. A screen shot of the Blender user interface is shown

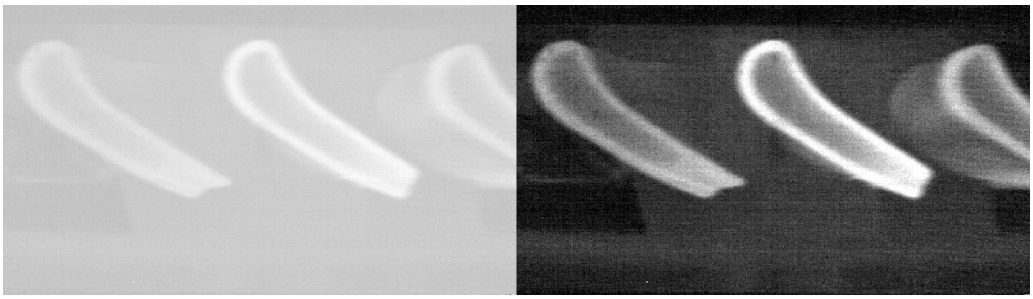

(a) Frame 50

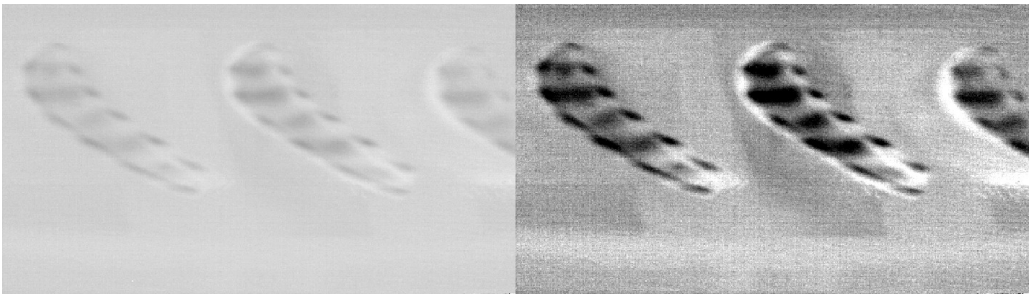

(b) Frame 250

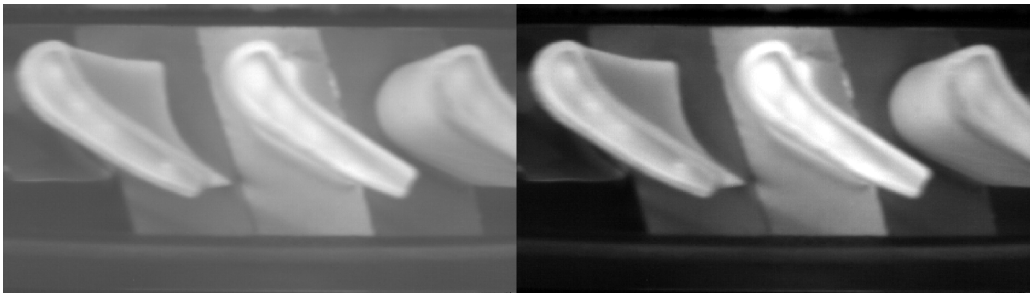

(c) Frame 370

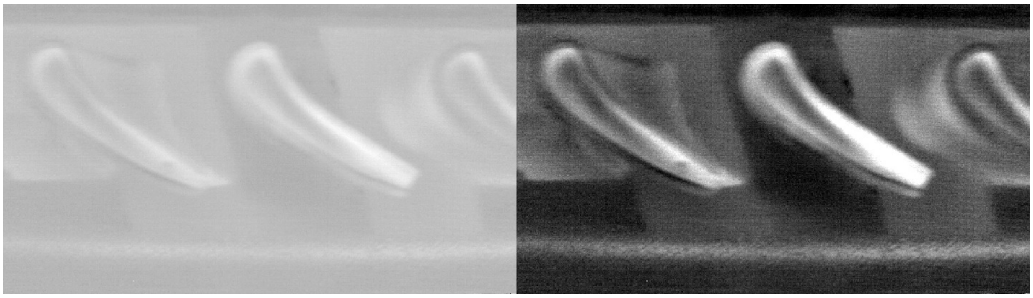

(d) Frame 500

Figure 5.12: Contrast enhancement procedure, showing original images on the left, and enhanced images on the right for (a) Frame 50; (b) Frame 250; (c) Frame 370; (d) Frame 500. The temporal location of these frames in the run is indicated in Figure 5.13.

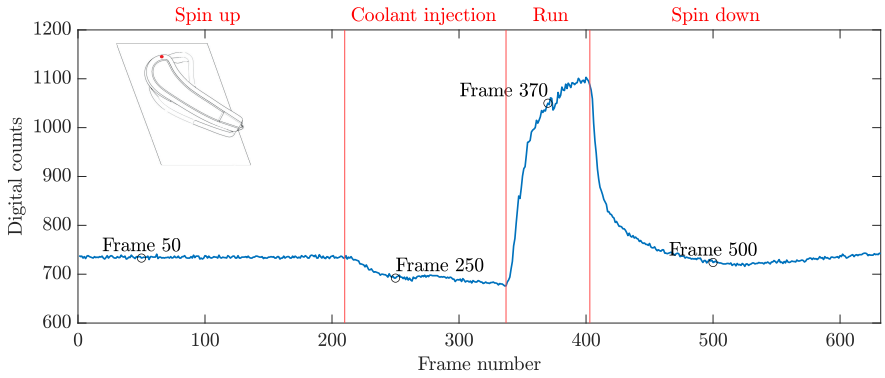

Figure 5.13: Raw digital counts history of a pixel on the blade tip for a dataset acquired with an integration time of 5 µs.

in Figure 5.14. The pattern area (i.e. the area encompassing the feature to track) encloses the blade tip, the centre of this area is individuated and its movement is tracked throughout the video, this is shown with a dark dot in the middle of the squealer tip of Figure 5.14. As the movements in the IR thermal videos captured in the OTRF are of translation nature, the *location motion* model in Blender was selected, as this model specifically focuses on linear movements along the x and y axes. The *Previous Frame* setting is selected in the motion tracking panel [146]. This setting plays a crucial role in determining the behaviour of the tracking algorithm between consecutive frames. When this setting is selected, key-frames for tracks are generated for every frame, and the tracking process occurs between a key-frame image and the subsequent frame in the video sequence. Unlike the 'Keyframe' configuration, where the tracked pattern is matched against a specific key-frame image, the 'Previous Frame' setting enables tracking between two neighboring frames. This approach provides increased flexibility in handling scenarios with substantial transformations of the feature point, like the present case. The problem with using 'Keyframe' in the present situation stems from the drastic changes of image features across the video.

The displacements detected with the feature tracking algorithm for a typical run are shown in 5.15a; the largest displacement depicted in the y-direction is of 9 px for frame number 375. The movement appears within the run interval and it is the

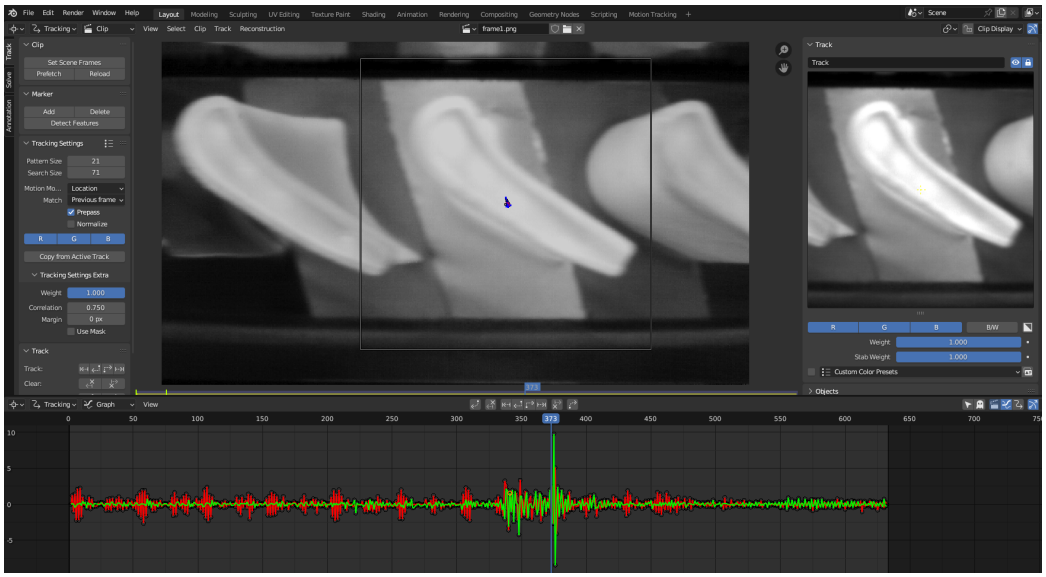

Figure 5.14: Example of feature tracking analysis in Blender.

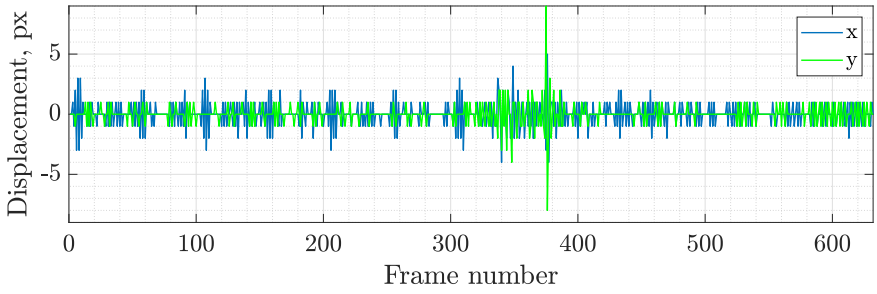

(a)

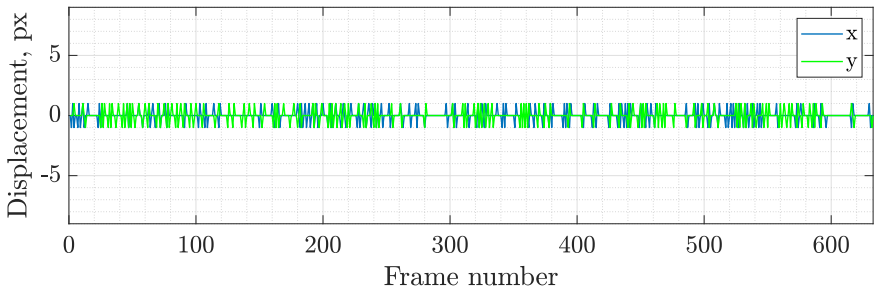

(b)

Figure 5.15: Results from the motion tracking algorithm, showing (a) level of motion before correction, i.e. first motion tracking, and (b) level of motion after correction, i.e. second motion tracking.

result of the injection of the main flow in the test section. Given the camera working distance (distance from the lens to the blade tip) of approximately 125 mm, which translates in a spatial resolution of 9.07 px/mm, a movement of 9 px corresponds to

1 mm. The displacement in the x-direction, of much lower magnitude and typically within ±3 px, is attributable to the sampling rate of the synchronisation signal.

Finally, the detected x and y displacement were exported into MATLAB, where the frames sequence was stabilised accordingly. The stabilised video was re-imported into Blender for a post-correction verification and a second motion tracking conducted. The outcomes for a typical run are plotted in Figure 5.15b, which demonstrates the displacements reduction in both directions to a maximum of ±1 px.

In a small number of test cases, instances of signal de-synchronisation occurred, which resulted in a miscounting of blades and in a much larger x-displacement. In this occasions, the frame was individuated and removed from the image sequence.

5.4.3 Heat Flux and Nusselt Number Processing

This section summarises processing of blade temperature $T_t(t)$ to heat flux $\dot{q}(t)$, as well as adiabatic wall temperature T_{aw} and Nusselt number Nu.

The processing of surface temperature measurements to heat flux involves solving the heat transfer conduction equation using the impulse response method by Oldfield [53]. The method entails determining the impulse response function $g(t)$ of the substrate from a step function in $\dot{q}(t)$ and corresponding analytical solution for transient surface temperature $T(t)$ for a semi-infinite substrate. Once known,convolution of this function with the measured temperature history provides the experimental heat flux

$$q(t) = g(t) * T(t) \tag{5.6}$$

The impulse response function can be calculated in MATLAB using the FFT based filtering, with knowledge of the substrate thermal properties. The use of this method requires the substrate to be semi-infinite. For this assumption to be valid, a penetration depth of $x = \sqrt{\alpha t}$ is suggested [33]. Following this rule, for the blade material PEEK in the OTRF, hence for a substrate with thermal diffusivity of $\alpha = 0.158\,\mathrm{mm\,s^{-1}}$ at

temperatures $T = 80\,°\mathrm{C}$ and a test duration of $t = 0.5\,\mathrm{s}$ a minimum depth of 0.28 mm must be ensured to satisfy the semi-infinite substrate assumption. The composite blade designed for these test presents a minimum thickness of approximately 3 mm on the tip, and 2 mm in the squealer tip cavity.

Having evaluated the heat flux $\dot{q}(t)$ during the steady test period, the adiabatic wall temperature T_{aw} can be found by linear regression of $\dot{q}(t)$ and $T_t(t)$, based on the thermal convection equation

$$\dot{q}(t) = h(T_t(t) - T_{aw}) \tag{5.7}$$

Corrected infrared surface temperature maps of a single frame acquired during the stable main test period of a typical run with uniform inlet conditions are depicted in Figure 5.16 for both the full FOV and the blade tip in the ROI. Note, the colormap temperature limits used in the two instances are different, purposely narrowed to maximise visibility of features for the blade tip temperature map in Figure 5.16b. The temperature on the squealer rim is hottest near the leading edge and along the pressure side, this is likely resulting from the tip leakage flow moving from pressure to suction side over the tip of the blade. In the squealer cavity, the regions of flow

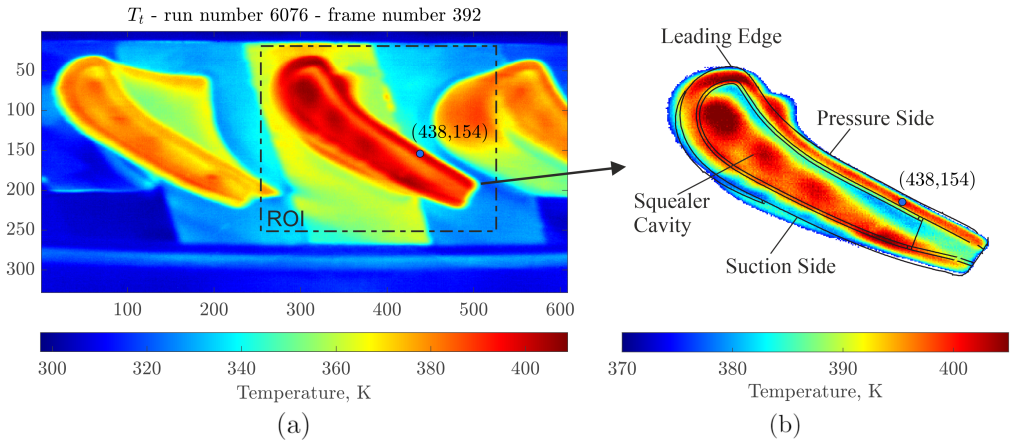

Figure 5.16: (a) Full FOV of temperature T_t at frame 392 during test 6076 corrected with test 6080. One pixel highlighted for point analysis; (b) Temperature T_t of blade tip at frame 392 during test 6076 corrected with 6080. One pixel highlighted for point analysis.

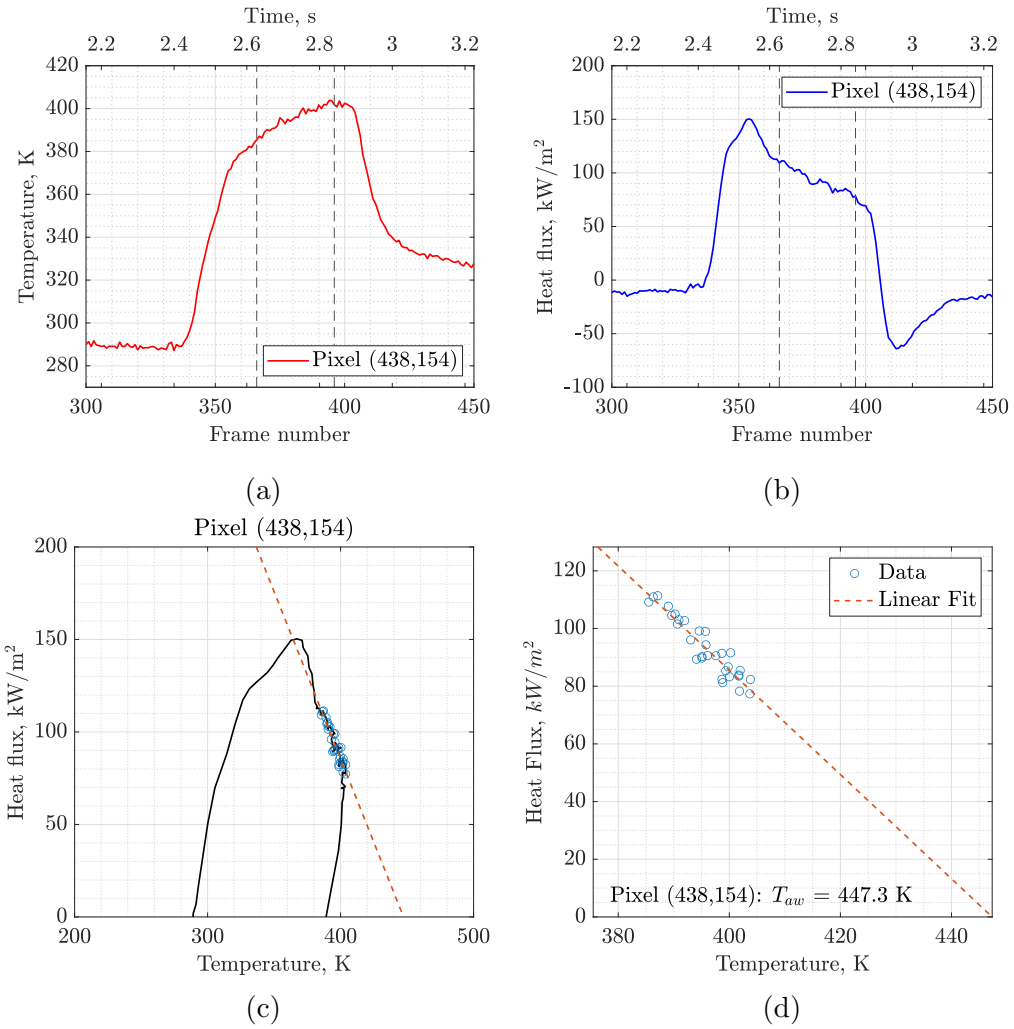

Figure 5.17: Key results from the heat transfer analysis for one pixel on the blade tip for test run 6076, including (a) temperature T_t calculated using Equation 5.4; (b) heat flux reconstructed from measured temperature; (c) reconstructed heat flux plotted against measured temperature to obtain T_{aw} by extrapolation; (d) detail of regression to obtain adiabatic wall temperature T_{aw}.

separation and reattachment could be individuated by the lower and higher surface temperature areas, respectively.

The analysis of regression to adiabatic wall temperature for one pixel (438,154 as labelled in Figure 5.16) is summarised in Figure 5.17, showing the target temperature time trace, the heat flux trace calculated using the impulse response method, and the linear regression of heat flux and target temperature. During the test period, the

heat flux initially increases sharply with the onset of the main hot test gas, and drops with time as the surface temperature rises. The stable portion of the run, over which regression to determine adiabatic wall temperature and heat transfer coefficient is appropriate, is indicated in Figure 5.17a and 5.17b by vertical dashed lines. In this window, the surface temperature rises by approximately 35 K going from 370 K to 405 K, allowing a stable regression to obtain the local adiabatic wall temperature. The regression is shown in Figure 5.17c, and a detailed view is depicted in Figure 5.17d. The adiabatic wall temperature for the examined pixel is 447.3 K. The calculation for adiabatic wall temperature can be extended to the entirety of the FOV, obtaining the two-dimensional map depicted in Figure 5.18a. The hottest regions are the squealer rim on the pressure side and towards the trailing edge. The minimum and maximum adiabatic wall temperature values were 387 K and 479 K, respectively.

Finally, the adiabatic wall temperature was used to reduce the heat flux data to Nusselt number, based upon the rotor true chord

$$Nu = \frac{hc_{true}}{k_{air}} = \frac{\dot{q}(t)c_{true}}{k_{air}(T_{aw} - T_t(t))} \tag{5.8}$$

where the blade true chord is $c_{true} = 0.037\,\text{m}$. The map of Nusselt number for the squealer tip, averaged over the stable portion of the run is shown in Figure 5.18b.

These measurements represent an important leap forward in the field of turbomachinery research. Never before was this type of measurement possible with thin-film gauges in the OTRF. The significance of this achievement becomes evident when considering the abundance of insights now accessible, and the simplification of the system compared to the historical approach used for the thin-film gauges.

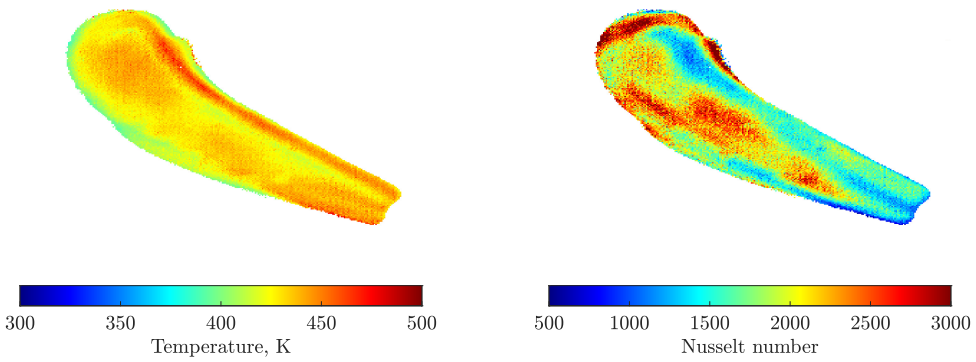

(a) (b)

Figure 5.18: Results for (a) adiabatic wall temperature and (b) Nusselt number on the rotor blade tip, obtained with data captured at turbine uniform inlet condition, and camera integration time 5 µs.

5.5 Validation Cases

Two cases were used for validation. The first compares IR data with experimental thin-film gauges data while the second compares to a CFD validated simulation.

5.5.1 Comparison with Heat Flux Gauges

With the scope of validating the heat transfer measurements captured via IR thermography, a blade was instrumented with single sided thin-film heat transfer gauges, described in Section 4.6. As instrumenting the tip with thin-film heat transfer gauges is challenging and potentially results in the gauges flying off the component, it was decided to assemble the gauges around the blade pressure and suction side close to the tip. Specifically, the platinum resistance gauges consisting of an insulating Kapton layer on a thermally semi-infinite layer of aluminium [48], were located at 80% span. More details on the development of these sensors can be found in Chapter 4 Section 4.6. A photograph of the pressure side of the blade instrumented with thin-film heat transfer gauges is shown in Figure 5.19; the results from the first gauge of the pressure side, identified by a circle, were used for the validation. The thin film gauges data was compared with thermal data captured inclining the camera to focus

on the pressure surface. The map of target temperature obtained with uniform inlet condition is shown in Figure 5.20. As the region of interest was within an observation angle $< 50°$, normal emissivity values were used for the corrections. A black ellipse is used in the figure to encompass this region. The pixel marked corresponds to the location of the first gauge on the pressure side.

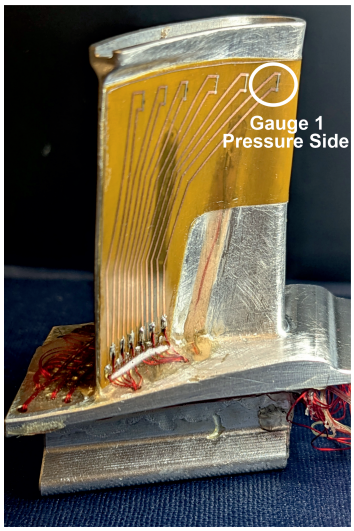

Figure 5.19: Photograph of the blade instrumented with thin-film heat transfer gauges. The gauge used for comparison with the IR thermography results is individuated by a white circle.

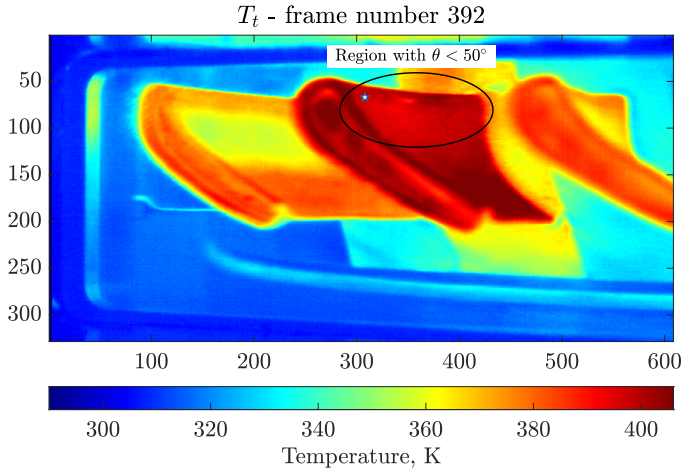

Figure 5.20: IR thermography data looking at the blade pressure side corrected to target temperature using runs 6104 and 6108. Data was captured with a camera integration time of 5 µs, at turbine uniform inlet condition. The region of interest is the pressure surface of blade in the middle of the field of view. One pixel highlighted corresponding to first gauge location on pressure surface for point analysis.

The heat transfer analysis for the thin-film gauges on the rotor is a multi-step process that goes from the recorded voltage signal to Nusselt number. Thin-film gauges instrumentation on the rotor requires a slip-ring to transmit the signal from the rotating to stationary frame. To eliminate noise interference from the slip-ring, data is acquired by an in-shaft data acquisition system. This system includes analogue signal conditioning prior to data storage in-shaft for digital download once the run is complete and the rotor is stationary. Signal pre-conditioning includes high frequency boost which counteracts the decreasing thin-film gauge frequency response in order to avoid digitisation errors at high frequency, as described by Anthony et al. [147]. The system also supplies the gauge current and allows data acquisition for approximately 4 s at a sample rate of 1 MHz. Thus, the first step of the post-processing analysis consists in signal debosting to restore the original signal. Subsequently, the α coefficients obtained from the calibration are used to convert the measured voltage to temperature, while the heat flux is determined from the measured surface temperature using the fast Fourier transform method [53]. Figure 5.21a and 5.21b depict the temperature and heat flux traces respectively, obtained from the first gauge on the pressure side. Notably, the temperature trace is approximately flat over the stable portion of the run. This behaviour, arising from the inability of the Kapton substrate to manifest adequate insulation, precluded the use of the regression technique described in Section 5.4.3 to calculate the adiabatic wall temperature. As a consequence, the usual practice (e.g. in Qureshi et al. [148]) is used to process the heat flux to Nusselt number using the relative total temperature at the rotor T_{02rel}, as

$$Nu_{T_{02rel}} = \frac{\dot{q}(t)\, \mathrm{c}_{\mathrm{true}}}{k_{T_{02rel}}(T_{02rel} - T_w)} \tag{5.9}$$

where T_w is the wall temperature from the thin-film gauges, $\dot{q}$ is the heat flux reconstructed from T_w, and T_{02rel} was calculated based on the design angles and velocity triangles at the specific span. The thermal conductivity of air k was evaluated at this

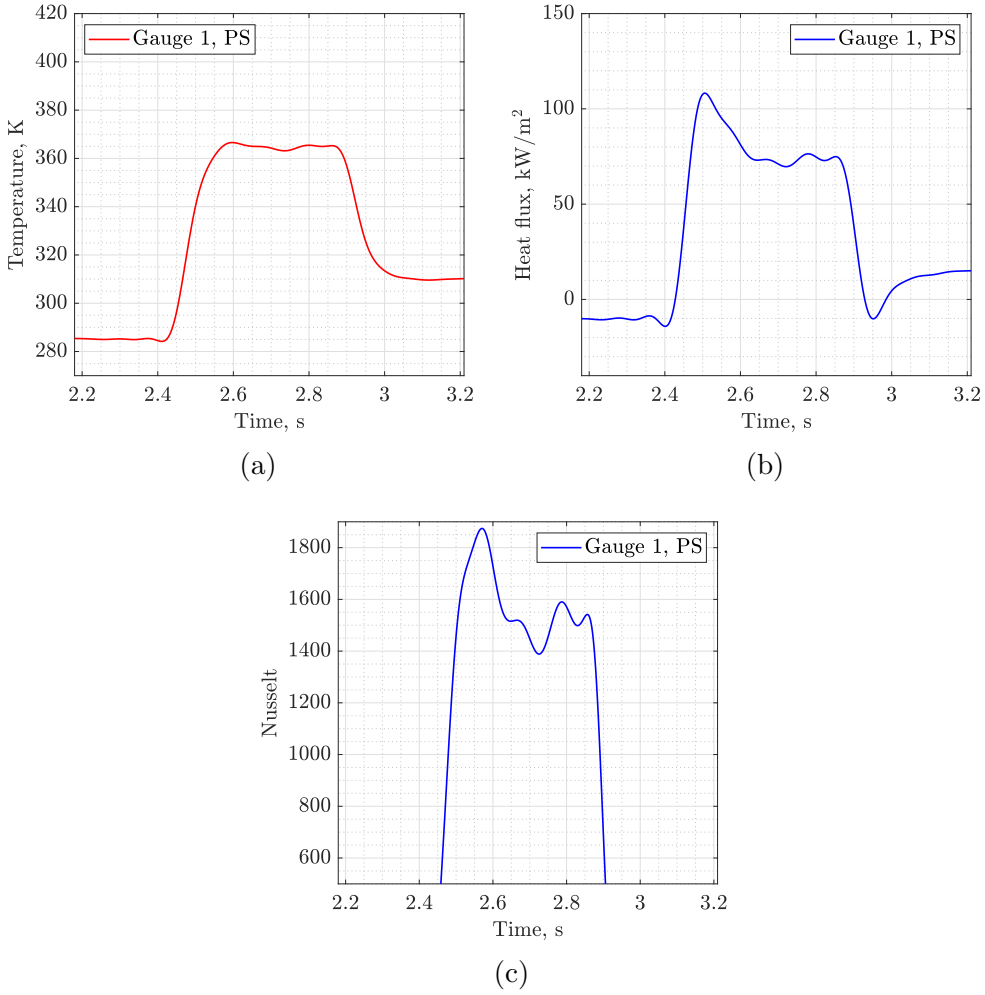

Figure 5.21: Key results from heat transfer analysis at turbine uniform inlet conditions from gauge 1 on the blade pressure side. Including (a) measured temperature; (b) heat flux reconstructed from measured temperature; (c) Nusselt number obtained with the relative temperature and the chord at 80% span.

temperature. The time history of Nusselt number obtained with this calculation is depicted in Figure 5.21c. This inconvenience appears frequently when thin-film gauges are used on the blade aerofoil, in this instance, the kapton layer is too thin and the aluminium is too diffusive. This behaviour limits the application of thin-film gauges data on the rotor as validation of CFD rather then process to adiabatic wall temperature T_{aw} and scaleable Nusselt number Nu. The developed IR system overcomes this issue using the composite blade. Achieving the measurement of adiabatic wall

temperature on the rotor, made possible by this system, represents a groundbreaking accomplishment not previously achieved in the OTRF. A possibility to explore for future experiments is to instrument the composite blade with thin-film gauges.

The heat transfer analysis on the IR thermal data was carried out as explained in the previous sections, and the temperature and heat flux time histories, as well as the regression to adiabatic wall temperature and the Nusselt number time history

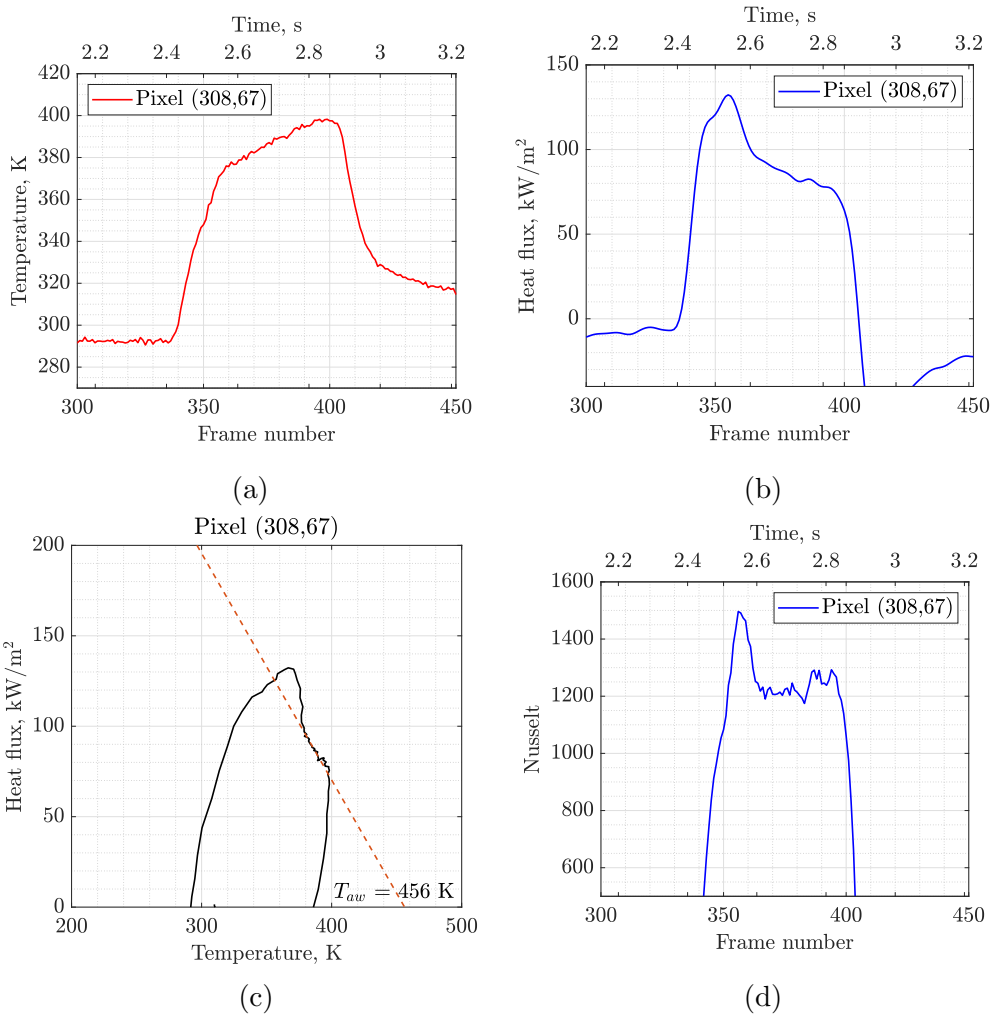

Figure 5.22: Key results from heat transfer analysis at turbine uniform inlet conditions from IR thermography data for one pixel on the blade pressure side. Including (a) temperature T_t; (b) heat flux reconstructed from measured temperature; (c) reconstructed heat flux plotted against measured temperature to obtain T_{aw} by extrapolation; (d) Nusselt number obtained with the adiabatic wall temperature and blade true chord at 80% span.

for the pixel corresponding to the position of the first thin-film gauge on the pressure side are shown in Figure 5.22. Comparing Figures 5.21 and 5.22, some conclusions can be drawn. As mentioned above, the temperature trace recorded by the thin film gauge remains flat during the stable portion of the run while the one recorded with the IR camera presents the desirable temperature rise that allows for the regression to adiabatic wall temperature. As the recorded temperature values are different, due to this inherent issue with the thin-film gauges setup, comparing temperature and heat transfer traces is not conclusive. However, both representations of Nusselt number are approximately flat, with an average value of 1496 from the thin-film gauges and 1250 from the IR thermography, agreeing to within ±16%.

5.5.2 Comparison to validated CFD

The CFD simulation employed for this comparison has been validated against casing heat transfer data for uncooled conditions and for three effusion cooling flow rates. The agreement on the adiabatic wall temperature on the casing was within 15 K. The simulation was run internally at Rolls-Royce and a brief description of the setup is given below. To capture the effect of the moving rotor and stationary casing, an interface plane was position within the tip clearance. This represents the 'sliding plane' approach in the Rolls-Royce in house solver HYDRA. Using this interface plane, the domain was divided into two subdomains: blades and the casing segment. Figure 5.23 shows the sliding plane and subdomains for both cooled and uncooled simulations. The boundary condition types used are summarised in Table 5.3. Radial total pressure, temperature, and turbulence profiles at the NGV trailing edge, taken from a throughflow Q263 solution that was calibrated to the turbine operating point, were used as boundary conditions at the domain inlet. Static pressure profiles at the rotor exit were also taken from the throughflow Q263 solution used as boundary conditions at the domain exit. The effusion cooling mass flux at the exit of each row

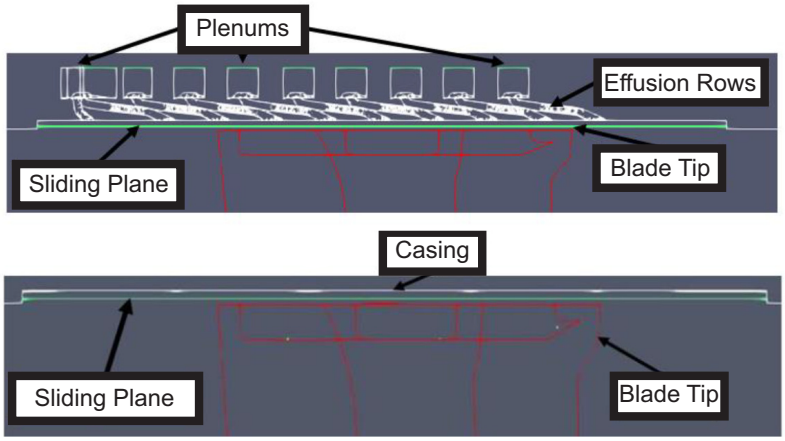

Figure 5.23: View of the domain used for the CFD simulation for the cooled and uncooled case.

Table 5.3: Boundary conditions types used for CFD simulation.

Station	Boundary Condition
Domain inlet	Subsonic inflow
All walls	Viscous walls
Blade/casing interface	Sliding plane
Domain exit	Non-reflecting subsonic outflow
Plenum inlet	Subsonic inflow

were matched to experiment. Given the inability of CFD to model the roughness of cooling holes manufactured with ALM, to match the mass flux on the effusion cooling boundaries an iterative procedure on the plena pressures was required. Using values of total pressure and temperature in the cavities from the experiments, these values were varied until the effusion cooling mass flux was matched. The $k-\omega$ SST plus wall functions were used to model turbulence and perfect gas behaviour was imposed.

The comparison between adiabatic wall temperature for uniform inlet conditions obtained with experiments and CFD is shown in Figure 5.24. The colour bar limits for the two maps do not match to allow a qualitative comparison flow features in both. The same flow features can be appreciated, with a higher temperature on the pressure side (PS) rim and lower in the cavity towards the PS where the flow could be separating, and higher again at the downstream end of the cavity and trailing

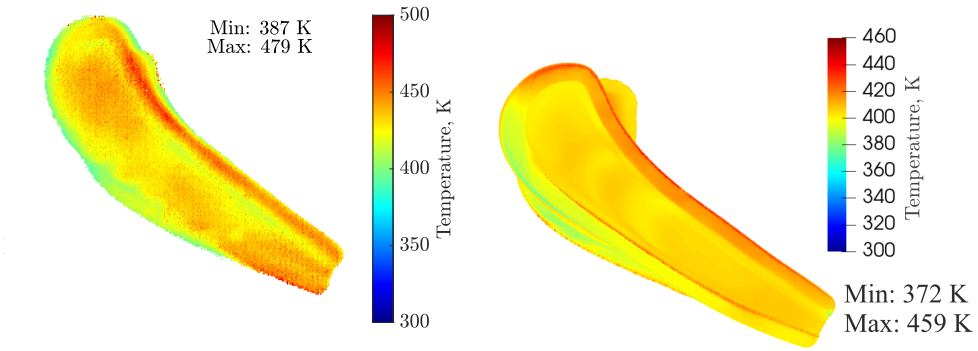

(a) (b)

Figure 5.24: Adiabatic wall temperature at turbine uniform inlet condition, obtained with (a) IR thermography and a set integration time of 5 µs and (b) CFD simulation.

edge possibly due to flow reattachment inside the cavity. Experiments show higher values compared to CFD, with temperature ranging from 387 K to 479 K, compared to the 372 K to 459 K obtained with CFD. Thus, a difference of approximately 20 K was found. These values mostly agree to within the CFD validation range of ±15 K.

5.5.3 Uncertainty Comparison

The following discussion aims to quantify the uncertainty in surface temperature measurement and conversion to heat flux for the two experimental techniques: thin-film heat flux gauges and IR thermography.

5.5.3.1 Uncertainty of Surface Temperature Measurement

Employing thin-film gauges, the wall temperature is calculated with the following equation

$$T_w = T_{ref} + \frac{(V - V_{ref})\,[1 + \alpha_{cal}(T_{ref} - T_0)]}{\alpha_{cal}\,V_{ref}} \tag{5.10}$$

where α_{cal} is the temperature coefficient of resistance calibrated in the water bath, referenced to condition $T_0 = 0\,°C$. The voltages in the equation are the signals measured by the thin-film gauge. The wall temperature is referenced to the isothermal condititions before the start of the run using T_{ref} and V_{ref}, where T_{ref} is a temperature

reading from a k-type thermocouple in the rig, and V_{ref} is the thin-film gauge voltage reading before the start of the run. Thus, the uncertainty of surface temperature measured with thin-film gauges mostly arises from the coefficient of resistance α_{cal}, estimated to have confidence interval of $\pm 1\%$ [149], and T_{ref}, measured by a k-type thermocouple and estimated to have uncertainty of $\pm 0.43\%$ [134].

Employing Infrared Thermography, the surface temperature is calculated with the following equation

$$T_t^4 = \frac{1-\varepsilon_2}{\tau(\varepsilon_1-\varepsilon_2)} T_{cam1}^4 - \frac{1-\varepsilon_1}{\tau(\varepsilon_1-\varepsilon_2)} T_{cam2}^4 - \frac{1-\tau}{\tau} T_{opt}^4 \tag{5.11}$$

where ε_1 and ε_2 are the surface emissivity values, T_{cam1} and T_{cam2} the blackbody equivalent temperature readings from the IR camera τ the IR transparent window transmissivity, and T_{opt} the temperature of the window. Thus, the uncertainty of surface temperature measured with IR Thermography mostly arises from the calibration of the system described in Chapter 3, as well as the temporal error on the IR camera detector presented in Figure 5.5. For a typical pixel on the blade tip, reading a temperature of approximately 400 K and a set integration time of $IT = 5\,\mu s$, these were ± 0.01 arising from the emissivity and transmissivity calibration, ± 1.8 K arising from the blackbody detector calibration, and ± 2 K arising from the temporal error in the detector.

The most significant sources of uncertainty affecting surface temperature measurements for thin-film gauges and IR camera are given in Table 5.4. These can be combined to give an overall figure of uncertainty of $\pm 1.09\%$ for thin-film gauges and $\pm 1.08\%$ for IR camera measurements.

Table 5.4: Comparing the uncertainty in surface temperature between thin-film gauges and IR camera.

Thin - film heat flux gauges		IR Camera	
variable	T_w **Uncertainty,** %	**variable**	T_t **Uncertainty** %
α_{cal}	1	T_{cam1}	1.03
T_{ref}	0.43	T_{cam2}	0.06
		T_{opt}	0.01
		ε_1	0.22
		ε_2	0.02
		τ	0.25
Total	**1.09**	**Total**	**1.08**

5.5.3.2 Uncertainty of Heat Flux Calculation

The measured wall temperature signal is processed to heat flux using the impulse response method for a two layered substrate developed by Oldfield [53]. This method requires knowledge of the substrate thermal properties.

In the case of the thin-film gauges, the two-layer model needs to be employed as the top layer comprising polyamide and glue is not thick enough to be considered semi-infinite. Thus, knowledge of the material thermal product $\sqrt{\rho ck}$ of the top layer (polyamide), in addition to the thickness-to-thermal conductivity ratio k/a of the upper insulating layer is required. The uncertainty in these quantities are of $\pm 4\%$ and $\pm 2\%$ respectively, as calibrated by Piccini et al. [141].

In the case of the composite blade used for the IR thermography measurement, the thickness of the top layer is enough to be considered semi-infinite. Thus, only knowledge of the thermal product $\sqrt{\rho ck}$ of the top layer (PEEK) is required. The uncertainty in this quantity was quoted by NETZCH to be $\pm 6\%$ (2σ).

The most significant sources of uncertainty affecting heat flux calculation measurements are given in Table 5.5. These can be combined to give an overall figure of uncertainty of $\pm 5\%$ for thin-film gauges and $\pm 6\%$ for IR camera measurements. The largest source of uncertainty arises from the definition of the thermal product. It is suggested that future experiments will focus on calibrating the PEEK thermal

product to a better accuracy.

Table 5.5: Comparing the uncertainty in heat flux between thin-film gauges and IR camera

Thin - film heat flux gauges		IR Camera	
variable	$\dot{q}$ **Uncertainty,** %	**variable**	$\dot{q}$ **Uncertainty** %
T_w	1.09	T_t	1.08
$\sqrt{(\rho ck)_1}$	4.2	$\sqrt{(\rho ck)_1}$	6
a/k_1	2		
Total	**4.78**		**6.09**

5.6 Summary

In this chapter, the experimental IR thermography data of rotor tip in the Oxford Turbine Research Facility have been presented. An investigation of the impact of IR camera integration time on blade tip displacement, image quality, and temperature accuracy at turbine nominal speed of 8500 rpm demonstrated that the IR camera temporal error on temperature reading can be as high as ±10 K, for a set integration time of 1 µs, corresponding to almost no blur. This error is also a function of the temperature of the scene, decreasing as temperature increase. A 5 µs camera integration time was selected for the subsequent heat transfer analysis, these conditions allow a limited blade tip displacement, of 1.32 mm and introduce a contained temporal error, ranging from ±4 K to ±2 K for temperatures between 290 K and 353 K.

The IR thermography dataset of a squealer tip rotor blade captured in the OTRF was processed from raw digital counts data to target temperature employing the methodology detailed in Chapter 3. Emissivity, reflection and transmissivity corrections were quantified thanks to this methodology, and a maximum total correction of 1.13% was identified between blackbody equivalent and target temperature for a run at uniform pressure and temperature inlet conditions. A transient convection analysis on the ZnSe optical window, necessary to estimate the temperature of the optical

path required for the IR data corrections, showed the insensitivity of the window temperature to the exposure to the high temperature gas in the facility.

An image stabilisation procedure was developed to correct for the movements induced in the video by the limited resolution of the image synchronisation system and the mainstream flow induced vibration. The combination of these two factors caused a movement of the image within ± 5 pixels, and the developed procedure reduced this to ± 1 pixel. This procedure enables an accurate processing to heat transfer, where accurate time history is required and even this instability can cause error, particularly in areas of high temperature gradients.

The surface temperature was process to heat flux, adiabatic wall temperature and Nusselt number. Results were shown for the entire field of view as well as for one pixel on the blade squealer rim. The composite blade PEEK substrate achieved a satisfactory temperature rise during the stable portion of the run. This rise, of approximately 35 K, allowed a stable regression to adiabatic wall temperature.

Measurements of adiabatic wall temperature on the rotor was made possible by the IR Thermography system developed in this thesis, and had never been accomplished in the OTRF before. This was further proved by comparing IR thermography data with experimental thin-film gauges data. Unfortunately, instrumenting the tip with thin-film heat flux gauges is challenging and potentially results in the sensors flying off. Thus, gauges were installed in the near-tip region (i.e. 80% span). Data from one gauge close to the leading edge on the blade pressure side and from one pixel at the same location in the IR data were compared.

The temperature trace recorded by the thin-film gauge results approximately flat over the stable portion of the run, hindering the regression to adiabatic wall temperature and as a consequence the evaluation of a Nusselt number. This is a common issue of thin-film gauges rotor heat transfer measurements. The usual practise is then to calculate a Nusselt number based on a relative total temperature at the ro-

tor obtained from the design angles and velocity triangles. However, this limits the experimental data to a simple validation of CFD rather than a Nu scalable to engine condition. On the other hand, the IR camera achieves a stable regression to adiabatic wall temperature, hence outperforming the traditional point-based thin-film gauges. Even though the two experimental datasets had to be processed to Nusselt number using a different procedure, these agreed within ±16%.

A second comparison of IR data to validated CFD simulation gave further confidence in the capability and accuracy of the IR Thermography methodology. The computational fluid dynamic simulation has been run by Rolls-Royce using the internal solver HYDRA, and has been validated against casing heat transfer experimental data. From a qualitative point of view, the adiabatic wall temperature map of the blade squealer tip obtained with the two techniques show similar flow features, capturing the expected higher temperature on the PS rim and trailing edge, lower temperature in the separation regions in the cavity, just behind the rim on the pressure side and higher temperature in the region where the flow reattaches. However, experiments show higher values, with a maximum of 20 K difference found between experiment and simulation results. This value is within the same level as the difference between the simulation and the casing thin-film gauges data of ±15 K.

The final section of the chapter presents an uncertainty analysis and comparison between accuracy in surface temperature and heat flux achievable with thin-film gauges and IR Thermography. A consistent overall uncertainty of approximately ±1.09% in surface temperature was revealed for both thin-film gauges and IR thermography data. The uncertainty in heat flux transformation is mostly affected by the uncertainty in the thermal product. Notably, the thin-film gauges present a more accurate measure for this quantity, leading to a lower overall uncertainty of approximately ±5%, as opposed to the ±6% observed in the IR thermography data.

Chapter 6

Conclusions

There is significant potential for improving gas turbine engines, possibly leading to a 30% increase in overall efficiency compared to current best-in-service engines [8]. The consequent reduction CO_2 emissions would have a positive impact on climate change. Achieving such level of progress requires advancement in various fields, including targeting higher TET. This however leads to high aerothermal loads on engine components, particularly on the high-pressure turbine rotor. Novel cooling solutions and better design procedures are necessary to ensure survival of these components. This is only achievable by studying the flow physics at engine conditions and the role of rotating engine scale facilities, such as the UK National Oxford Turbine Research Facility, is pivotal in this endeavour.

In the historical examination of heat transfer in such facilities, quantities such as surface temperature, heat flux, adiabatic wall temperature, and Nusselt number were traditionally investigated using point-based techniques. However, these methods involve cumbersome wiring access and time-consuming soldering procedures. Recognising the need for improvement, in particular in terms of efficiency and accuracy, the current work focuses on implementing Infrared Thermography in the OTRF. This technique was chosen for its superiority over conventional point-based methods and for its ability to provide two-dimensional information of true surface temperature, ensuring a short response time, high sensitivity/resolution, and being non-intrusive.

Implementing IR thermography in an engine-scale turbine facility holds significance not only due to its novel application in the OTRF but also because it addresses a notable gap in the existing literature. Few studies have presented comparable data [107, 108, 109], making this endeavor a valuable contribution to the field.

The challenges of employing IR Thermography in a turbomachinery environment to capture images of a blade moving at rotational speed of approximately $300\,\mathrm{m\,s^{-1}}$ include accurate evaluation of surface emissivity, surroundings reflection, optical path transmissivity, and motion blur.

The first part of this thesis focused on understanding the physics behind these sources of error and test a methodology to minimise their impact on the accuracy of the measurement. This methodology is developed in details in Chapter 3, and can be summarised in the following key-points

i) **Detector selection and calibration**:

   Based on the specific application, the most suitable IR detector needs to be selected. This involves understanding the expected temperature range, to select the correct camera working wavelength, and the expected speed, which affect the camera integration time and framerate requirements. Subsequently, a study and calibration of the detector needs to be carried out. This entails correlating the camera raw digital count to blackbody equivalent temperature, as well as revealing the relationship between the camera integration time and noise. It is understood that lowering the camera integration time enables sharper images, however a low integration time leads to a noise increase. The relationship between camera integration time and noise is also connected to the scene temperature level.

   In this thesis, for tests in the OTRF happening at turbine nominal speed of 8500 rpm, an integration time of 5 µs was selected. This allowed a predicted

blade tip displacement of approximately 1.32 mm, with a temporal error due to camera noise ranging between ±1 K and ±4 K.

ii) **Emissivity and transmittance calibration**:

Increasing the target emissivity and optical path transmission is paramount to achieve accurate IR thermography measurements. It is also crucial to have knowledge of these value to a high degree of accuracy. A bespoke calibrator and facility were designed for this purpose, which enabled to calibrate the two parameters within ±0.01. A selection of paints were tested for emissivity, with the Nextel velvet black paint showing the highest emissivity ($\varepsilon = 0.97$). This paint was therefore selected for the tests in the OTRF.

iii) **Reflection correction**:

The reflectivity of the target substrate will result in reflected radiance due to the presence of the surroundings. This is possibly the most challenging component to quantify in IR thermography measurements. The proposed method develops on the work presented by Kirollos et al. [98] and involves the use of a low emissivity substrate on the target surface, which together with the high emissivity substrate allows to solve the energy balance equation (Equation 3.1) providing a system of two equations in two unknowns (Equations 3.8 and 3.9). For this thesis, employing this method entailed the use of a low emissivity paint. The Ambersil aluminium, providing an emissivity of 0.6, was selected.

iv) **Impact of blur on calibration**:

The impact of motion blur on the calibration was investigated and three methods were presented. The first artificially eliminates the motion blur before the correction, while the second and the last incorporate the blur in the high-emissivity and low-emissivity region respectively. The first correction is the only method that successfully calibrated the signal across the entire Field of View. However,

in experiments with highly spatial temperature variation, removing data would reduce the spatial resolution of the technique, potentially leading to higher errors. Furthermore, the features of interest could be of dimension comparable to blur level. In such situations, applying deblurring techniques is recommended.

The design solutions for implementing an IR thermography system in the Oxford Turbine Research Facility were outlined in Chapter 4. The chapter encompassed the description of the turbine facility, highlighting its capability to test high-pressure turbine stages under representative engine conditions, aided by a combustor simulator for temperature profile replication. The optical access design using zinc selenide, the development of a composite blade with PEEK substrate, and the design of the IR camera control system for synchronised image capture were detailed. Zinc selenide was chosen for its high transmissivity in the wavelength of interest and for the ideal insensitivity of the optical properties to temperature. The composite blade design was proven to be able to withstand mechanical loads ranging between 11 kN and 12 kN before failure, and multiple cycles at a load of 4 kN without manifesting signs of hysteresis or cracking. The camera synchronisation system enabled capture of stable images of any selected blade within ±5 pixels. The instrumentation of two aluminium blades with thin-film heat flux gauges was discussed, with the aim of using these instrumentation to validate the IR thermography measurements in the OTRF.

The IR Thermography methodology developed in this study was used in a test campaign on the rotor tip in the Oxford Turbine Research Facility. The investigation focussed on a squealer tip design. Tests were captured with a camera integration time of 5 µs and at turbine uniform pressure and inlet conditions. The methodology lead to a maximum total correction of ±5 K between blackbody equivalent and target temperature in the stable portion of the run, translating to a 1.13% correction. An image stabilisation procedure was developed to correct for the movements induced

in the video by the limited resolution of the image synchronisation system and the mainstream flow induced vibration. The developed procedure was able to reduce the movement in the sequence of images to ± 1 pixel.

The processing of IR data from raw digital counts to heat transfer quantities has been described and results of adiabatic wall temperature and Nusselt number have been shown for the entire field of view. A temperature rise of approximately 35 K was achieved in the composite blade over the stable portion of the run, allowing stable regression to adiabatic wall temperature. The IR data were compared to the experimental thin-film gauges data. This comparison emphasised the superiority of IR thermography for heat transfer measurements on the rotor. The thin-film gauges on the airfoil present a flat temperature trace hindering the regression of adiabatic wall temperature. A Nusselt number based on relative rotor inlet temperature was evaluated for the gauges, as this is the usual practice to overcome the inability of the gauges to achieve regression to adiabatic wall temperature [148]. Despite the necessity of processing the two experimental datasets for the Nusselt number using different procedures, they exhibited a good agreement, within a range of $\pm 16\%$.

A second comparison of IR data to validated CFD simulation gave further confidence in the capability and accuracy of the IR Thermography methodology. The comparison shows adiabatic wall temperature maps obtained with the two techniques, which exhibit the same qualitative flow features: higher temperature on the pressure side squealer rim and regions of high and low temperature in the squealer cavity corresponding to regions of flow separation and reattachment. Experimental data exhibit higher values than CFD, with a maximum of 20 K difference. This is still within the level of validation of the CFD of ± 15 K.

Finally, a comparison between the uncertainty arising from thin-film gauges and IR thermography revealed a consistent overall uncertainty in surface temperature of approximately $\pm 1.09\%$ in both instances. For the heat flux, in both cases the

uncertainty is mostly affected by the accuracy in the thermal product. The thin-film gauges present a more accurate measure for this quantity, leading to a lower overall uncertainty in heat flux of approximately $\pm 5\%$, as opposed to the $\pm 6\%$ observed in the IR thermography data. Nevertheless, an improvement of accuracy in the PEEK thermal properties measurements will result in the IR thermography surpassing the thin-film gauges for the precision in heat flux calculation.

These values give confidence on the validity of the experimental methodology developed in this study, paving the way for further significant progress. This marks a substantial leap forward and a valuable contribution to the field.

Further improvements in the methodology presented in this thesis could be achieved investigating the following areas

i) Low scene temperature/camera integration time error

ii) De-blurring techniques

iii) Camera mounting design

iv) PEEK thermal product accuracy

i-ii) The facility is currently undergoing an upgrade which will allow testing at higher temperature, permitting the use of lower integration time. However, given the target speeds and the interest in visualising feature of small dimensions, such as cooling holes, it will continue to be beneficial to further understand the nature of the temporal error that rises at low scene temperature and low camera integration time and potentially find a solution to calibrate this out. Alongside this type of investigation, de-blurring techniques could enhance the capability of the methodology. With a full IR dataset now available at different camera integration times, two approaches could be investigated: a de-blurred result reconstructed from two datasets one at long integration time and one at short integration time (similarly to the method proposed

by Lazzi Gazzini et al. [105]), or the implementation of more standard de-blurring filters such as the Wiener filter. iii) The camera mounting design in the OTRF lead to a small level of vibration visible in the IR scene. This movement arises during the stable portion of the run, corresponding to the high pressure gas flowing into the test section. Although it was possible to correct for this moment in post-processing with a stabilisation algorithm, it would be beneficial to redesign the mounting to eliminate or reduce the movement. A possible solution could be the implementation of a robot arm, this solution could aid in improving the repeatability of the camera alignment, which in the present campaign was entirely manual. iv) Improving the accuracy in the thermal properties measurements of the substrate used in the composite blade, PEEK, would results in an improved accuracy in the calculated heat transfer quantities.

Bibliography

[1] International Civil Aviation Organization (ICAO). CO_2 standard for new aircraft, 2014. https://www.icao.int/newsroom/pages/icao-council-adopts-new-co2-emissions-standard-for-aircraft.aspx [Accessed: 8 January 2024].

[2] International Energy Agency. Tracking Aviation, 2014. https://www.iea.org/energy-system/transport/aviation [Accessed: 8 January 2024].

[3] European Commission, Directorate General for Mobility, Transport, Directorate General for Research, and Innovation. *Flightpath 2050 – Europe's vision for aviation – Maintaining global leadership and serving society's needs*. Publications Office, 2011.

[4] International Civil Aviation Organization. Views on a long-term aspirational goal for international aviation CO_2 emissions reductions. Technical report, 2022.

[5] International Civil Aviation Organization. ICAO Environmental Report 2022. Technical report, 2022.

[6] P. Su-ungkavatin, L. Tiruta-Barna, and L. Hamelin. Biofuels, electrofuels, electric or hydrogen?: A review of current and emerging sustainable aviation systems. *Progress in Energy and Combustion Science*, 96:101073, 2023.

[7] A. Ficca, F. Marulo, and A. Sollo. An open thinking for a vision on sustainable green aviation. *Progress in Aerospace Sciences*, 141, 2023.

[8] National Academies of Sciences, Engineering and Medicine. *Commercial Aircraft Propulsion and Energy Systems Research: Reducing Global Carbon Emissions*. The National Academies Press, Washington, DC, 2016.

[9] R. Blockley, R. Agarwal, F. Collier, A. Schaefer, and A. Seabridge. *Green Aviation*. John Wiley & Sons, 2016.

[10] Rolls-Royce. The Trent XWB, 2019. `https://www.rolls-royce.com/media/our-stories/discover/2019/the-trent-xwb-let-me-count-the-ways.aspx` [Accessed: 23 October 2023].

[11] Pratt & Whitney. GP7200 Engine, 2014. `https://www.prattwhitney.com/en/newsroom/multimedia/gp7200-engine` [Accessed: 7 January 2024].

[12] A.H. Epstein. Aeropropulsion for commercial aviation in the twenty-first century and research directions needed. *AIAA Journal*, 52(5):901–911, 2014.

[13] B.L. Koff. Spanning the globe with jet propulsion. *AIAA 21st Annual Meeting and Exhibit*, 1991.

[14] H.I.H. Saravanamuttoo, G.F.C. Rogers, H. Cohen, and P.V. Straznicky. *Gas Turbine Theory*. Pearson Prentice Hall, Harlow, England; New York, 2009.

[15] J.C. Han and A.P. Rallabandi. Turbine Blade Film Cooling Using PSP Technique. *Frontiers in Heat and Mass Transfer*, 1(1), 2010.

[16] J. Goeing, H. Seehausen, L. Stania, N. Nuebel, J. Salomon, P. Ignatidis, F. Dinkelacker, M. Beer, B. Berend, J.R. Seume, and J. Friedrichs. Virtual process for evaluating the influence of real combined module variations on the overall performance of an aircraft engine. *Journal of the Global Power and Propulsion Society*, 7:95–112, 2023.

[17] X. Guo, W. Zheng, C. Xiao, L. Li, S. Antonov, Y. Zheng, and Q. Feng. Evaluation of microstructural degradation in a failed gas turbine blade due to overheating. *Engineering Failure Analysis*, 103:308–318, 2019.

[18] J.C. Han. Advanced Cooling in Gas Turbines 2016 Max Jakob Memorial Award Paper. *Journal of Heat Transfer*, 140(11):113001, 07 2018.

[19] J.D. Denton. Loss Mechanisms in Turbomachines. In *Proceedings of the ASME 1993 International Gas Turbine and Aeroengine Congress and Exposition*, volume 2: Combustion and Fuels; Oil and Gas Applications; Cycle Innovations; Heat Transfer; Electric Power; Industrial and Cogeneration; Ceramics; Structures and Dynamics; Controls, Diagnostics and Instrumentation; IGTI Scholar Award of *Turbo Expo: Power for Land, Sea, and Air*, page V002T14A001, 05 1993.

[20] R.J. Clifford. Rotating heat transfer investigation on a multi-pass cooling geometry. *AGARD*, Heat Transfer and Cooling in Gas Turbines(AGARD-CP-390):2–1 2–12, 1985.

[21] J.C. Han, S. Dutta, and S. Ekkad. *Gas Turbine Heat Transfer and cooling Technology*. CRC Press, 2012.

[22] C. Hirsch, editor. *Advanced methods for cascade testing*, volume AG-328. AGARD, August 1993.

[23] F. Papa, U. Madanan, and R.J. Goldstein. Modeling and Measurements of Heat/Mass Transfer in a Linear Turbine Cascade. *Journal of Turbomachinery*, 139(9):091002, 04 2017.

[24] A. Messenger, J. Cartlidge, N. Chowdhury, F. Goenaga, and T. Povey. ECAT+: A Second-Generation High-Temperature Engine Component Aerothermal Facility at the University of Oxford. In *Proceedings of ASME Turbo Expo 2023:*

Turbomachinery Technical Conference and Exposition, volume 13B: Turbomachinery - Axial Flow Turbine Aerodynamics, page V13BT30A023, 06 2023.

[25] C. Falsetti, P.F. Beard, D.N. Cardwell, and K.S. Chana. A Review of High-Speed Rotating HP Turbine Heat Transfer and Cooling Studies Over the Last Decade in the Oxford Turbine Research Facility. In *Proceedings of the ASME Turbo Expo 2022: Turbomachinery Technical Conference and Exposition*, volume 10B: Turbomachinery - Axial Flow Turbine Aerodynamics; Deposition, Erosion, Fouling, and Icing; Radial Turbomachinery Aerodynamics, page V10BT30A016, 06 2022.

[26] P.T. Ireland and T.V. Jones. Liquid crystal measurements of heat transfer and surface shear stress. *Measurement Science and Technology*, 11(7):969–986, 2000.

[27] Z. Gao, D.P. Narzary, and J.C. Han. Film cooling on a gas turbine blade pressure side or suction side with compound angle shaped holes. *Journal of Turbomachinery ASME*, 131, 2009.

[28] N. Gurram, P.T. Ireland, T.H. Wong, and K.P. Self. Study of film cooling in the trailing edge region of a turbine rotor blade in high speed flow using pressure sensitive paint. In *Proceedings of the ASME Turbo Expo*, volume 5C-2016, sep 2016.

[29] M. Héder. From NASA to EU: the evolution of the TRL scale in Public Sector Innovation. *The Innovation Journal*, 22:1, 2017.

[30] C. Falsetti, M. Sisti, and P.F. Beard. Infrared thermography and calibration techniques for gas turbine applications: A review. *Infrared Physics & Technology*, 113:103574, 2021.

[31] M. Sisti, C. Falsetti, P.F. Beard, and K. Chana. Infrared temperature measurements on high pressure turbine blades in the Oxford Turbine Research Facility:

calibration and image processing techniques. In *Proceedings of 14th European Conference on Turbomachinery Fluid dynamics & Thermodynamics*, 2021.

[32] M. Sisti, C. Falsetti, and P.F. Beard. Infrared temperature measurements on fast moving targets: A novel calibration approach. *Measurement*, 225:113870, 2024.

[33] D.L. Schultz and T.V. Jones. Heat-transfer measurements in short duration hypersonic facilities. *AGARD-AG-165*, AG(165), 1973.

[34] D.L. Schultz, R.W. Ainsworth, and C.T.J. Scrivener. The role of short duration facilities in gas turbine research. In *8th Symposium of ISABE*, number Paper No. 87-7031, Cincinnati, 1987.

[35] M.G. Dunn and M. Randall. History of short-duration measurement programs related to gas turbine heat transfer, aerodynamics, and aeroperformance at calspan and osu. In *Proceedings of the ASME Turbo Expo 2013: Turbine Technical Conference and Exposition*, volume 3C: Heat Transfer, 2013.

[36] A. Hertzberg. A shock tube method of generating hypersonic flows. *Journal of the Aeronautical Sciences*, 18(12):803–804, 1951.

[37] M.G. Dunn and F.J. Stoddard. Studies of heat transfer to gas turbine components. Technical Report AD-A048 551, Calspan Corp, Buffalo New York, 1977.

[38] M.G. Dunn and A. Hause. Measurement of heat flux and pressure in a turbine stage. *Journal of Engineering for Power*, 104(1):215–223, 1982.

[39] A.H. Epstein, G.R. Guenette, and R.J.G. Norton. The MIT Blowdown Turbine Facility. In *Proceedings of the ASME 1984 International Gas Turbine Conference and Exhibit*, volume 4: Heat Transfer; Electric Power, 1984.

[40] R.J. Anthony and J.P. Clark. A review of the afrl turbine research facility. In *Proceedings of the ASME Turbo Expo 2013: Turbine Technical Conference and Exposition*, volume 3C: Heat Transfer, 2013.

[41] T.V. Jones, D.L. Schultz, and A.D. Hendley. On the flow in an isentropic light piston tunnel. Technical Report 3731, Aeronautical Research Council Reports & Memoranda, 1973.

[42] D.L. Schultz, T.V. Jones, M.L.G. Oldfield, and L.C. Daniels. A new transient cascade facility for the measurement of heat transfer rates. Technical Report Cp-229, NATO AGARD High Temperature Problems in Gas Turbine Engines, 1977.

[43] A.J. Brooks, D.E. Coldbourne, E.T. Wedlake, T.V. Jones, M.L.G. Oldfield, D.L. Schultz, and P. J. Loftus. The isentropic light piston cascade facility at rae pyestock. Technical Report CP-390, NATO AGARD Heat Transfer and Cooling in Gas Turbine, 1985.

[44] M.A. Hilditch, A. Fowler, T.V. Jones, K.S. Chana, M.L.G. Oldfield, R.W. Ainsworth, S.I. Hogg, S.J. Anderson, and G.C. Smith. Installation of a turbine stage in the pyestock isentropic light piston facility. In *Proceedings of the ASME 1994 International Gas Turbine and Aeroengine Congress and Exposition*, volume 4: Heat Transfer; Electric Power; Industrial and Cogeneration, 1994.

[45] K.S. Chana, D.N. Cardwell, and T.V. Jones. A Review of the Oxford Turbine Research Facility. In *Proceedings of the ASME Turbo Expo*, volume 3C: Heat Transfer, 06 2013.

[46] G. Paniagua, C.H. Sieverding, and T. Arts. Review of the von karman institute compression tube facility for turbine research. In *Proceedings of the ASME Turbo Expo 2013*, volume 3C, 2013.

[47] R.J. Vidal. Model instrumentation techniques for heat transfer and force measurements in a hypersonic shock tunnel. Technical Report AD-917-A-1, Cornell Aeronautical Laboratory, 1956.

[48] J.E. Doorly and M.L.G Oldfield. The Theory of Advanced Multi-Layer Thin Film Heat Transfer Gauges. *International Journal of Heat and Mass Transfer*, 30(6):68, 1987.

[49] F. Incropera, D. Dewitt, T. Bergman, and A. Lavine. *Fundamental of Heat and Mass Transfer*. John Wiley & Sons, New York, 2006.

[50] M.L.G. Oldfield, T.V. Jones, and D.L. Schultz. On-line computer for transient turbine cascade instrumentation. *IEEE Transactions on Aerospace and Electronic Systems*, AES-14(5):738–749, 1978.

[51] G.T. Skinner. Analog network to convert surface temperature to heat flux. Technical Report CAL-100, Cornell Aeronautical Laboratory, 1960.

[52] M.L.G. Oldfield, H.J. Burd, and N.G. Doe. Design of wide-bandwidth analogue circuits for heat transfer instrumentation in transient tunnels. In *Heat & Mass Transfer in Rotating Machinery, Proceedings 16th Symposium of the International Centre for Heat and Mass Transfer*, 1984.

[53] M.L.G. Oldfield. Impulse response processing of transient heat transfer gauge signals. *Journal of Turbomachinery*, 130(2), 2008.

[54] Jane E. Doorly. *The Development of a Heat Transfer Measurement Technique for Application to Rotating Turbine Blades*. PhD thesis, University of Oxford, Oxford, 1985.

[55] D.E. Van Zante and T.H. Okiishi. Visualization of boundary-layer development on turbomachine blades with liquid crystals. Technical Report NASA-CR–190433, NASA, 1991.

[56] P.T. Ireland and T.V. Jones. The response time of a surface thermometer employing encapsulated thermochromic liquid crystals. *Journal of Physics E: Scientific Instruments*, 20(10):1195, 1987.

[57] P.T. Ireland, A.J. Neely, D.R.H. Gillespie, and A.J. Robertson. Turbulent heat transfer measurements using liquid crystals. *International Journal of Heat and Fluid Flow*, 20 (4):355–367, 1999.

[58] Z. Wang, P.T. Ireland, and T.V. Jones. An advanced method of processing liquid crystal video signals from transient heat transfer experiments. *Journal of Turbomachinery*, 117(1):184 – 189, 1995.

[59] T. Kim, H.P. Hodson, and T.J. Lu. Fluid-flow and endwall heat-transfer characteristics of an ultralight lattice-frame material. *International Journal of Heat and Mass Transfer*, 47(6-7):1129 – 1140, 2004.

[60] T. Kim. Chapter 7 - surface heat transfer mapping using thermochromic liquid crystal. In Tongbeum Kim, Tian Jian Lu, and Seung Jin Song, editors, *Application of Thermo-Fluidic Measurement Techniques*, pages 191–214. Butterworth-Heinemann, 2016.

[61] M. Parsley. *An Introduction to Thermochromic Liquid Crystal Products*. Hallcrest Liquid Crystal Division, 1987.

[62] Y. Yan and J.M. Owen. Uncertainties in transient heat transfer measurements with liquid crystal. *International Journal of Heat and Fluid Flow*, 23(1):29–35, 2002.

[63] R. Siegel and J.R. Howell. *Thermal Radiation Heat Transfer, 4th edition*. Taylor and Francis Group, 2002.

[64] T. Astarita and G.M. Carlomagno. *Infrared Thermography for Thermo-Fluid-Dynamics*. Springer, 2013.

[65] A. Pantinakis and N. Korstsalioudakis. A simple high-sensitivity radiometer in the infrared for measurements of the directional total emissivity of opaque materials at near-ambient temperatures. *International Journal of Thermophysics*, 22:1843–1854, 2001.

[66] R. Siegel and C.M. Spuckler. Analysis of thermal radiation effects on temperatures in turbine engine thermal barrier coatings. *Materials Science and Engineering: A*, 245(2):150 – 159, 1998.

[67] W. Minkina and S. Dudzik. *Infrared Thermography: Errors and Uncertainties*. Wiley, New York, 2009.

[68] ISO18434-1. Condition monitoring and diagnostics of machines — thermography — part 1: General procedures, 2008.

[69] W.H. Atkinson and R.R Strange. Turbine pyrometry for advanced engines. *AIAA/SAE/ASME/ASEE 23rd Joint Propulsion Conference, San Diego, USA*, 1987.

[70] E. Suarez and H.R. Przirembel. Pyrometry for turbine blade development. *Journal of Propulsion and Power*, 6:584–589, 1990.

[71] H.A. Gebbie, W.R. Harding, C. Hilsum, A.W. Pryce, and V. Roberts. Atmospheric transmission in the 1 to 14 µm region. In *Proceedings of the Royal Society London*, volume A206, pages 87–107, 1951.

[72] M. De Lucia, R. De Sabato, P. Nava, and S. Cioncolini. Temperature measurements in a heady duty gas turbine using radiation thermometry technique: error evaluation. *Journal of Engineering for Gas Turbines and Power*, 123:333 – 339, 2001.

[73] A.H. Lefebvre. *Gas Turbine Combustion*. CRC Press, 2010.

[74] S. Gao, L. Wang, C. Feng, and K.D. Kipngetich. Analyzing the influence of combustion gas on a gas turbine by radiation thermometry. *Infrared Phys. Technol.*, 73:184–193, 2015.

[75] D.P. DeWitt and G.D. Nutter. Theory and practice of radiation thermometry. *Wiley*, New York, 1988.

[76] H. Li, G. Wang, N. Nirmalan, S. Dasgupta, and F. Edward. Passive absorption/emission spectroscopy for gas temperature measurements in gas turbine engines. In *Proceedings of ASME Turbo Expo 2011: Turbine Technical Conference and Exposition GT2011*, volume Vancouver, Canada, pages 1–14, 2011.

[77] T. Taniguchi, R. Tanaka, Y. Shinoda, M. Ryu, N. Mortiz, and K. Kusterer. Application of an optical pyrometer to newly developed industrial gas turbine. In *Proceedings of ASME Turbo Expo 2012: Turbine Technical Conference and Exposition GT2012*, 2012.

[78] W.F. Mohr and P. Ruffino. Experimental investigation into thermal behaviour of steam turbine components: Part 1 - temperature measurements with optical probes. In *Proceedings of ASME Turbo Expo 2012: Turbine Technical Conference and Exposition GT2012*, 2012.

[79] Harvard. The HITRAN Database, 2015. `http://www.cfa.harvard.edu/HITRAN` [Accessed: 07 December 2023].

[80] Edmund Optics. *Germanium windows datasheet*. 2018.

[81] T. Stolberg-Rohr, J. Gary, and D. Hawkins. Spectral design of temperarture-invariant narrow bandpass filters for the mid-infrared. *Optics Express*, 23:580–596, 2015.

[82] G. Meyers, J. Van Der Geest, J. Sanborn, and F. Davis. Comparison of advanced cooling concepts using color thermography. *AIAA*, 1985.

[83] M. Martiny, R. Schiele, M. Gritsch, A. Schulz, and S. Wittig. In situ calibration for quantitative infrared thermography. *QIRT 96 - Eurotherm Series 50 Stuttgart, Germany*, 1996.

[84] W. Press, B. Flannery, S. Teukolsky, and W. Vetterling. Numerical recipes. *Cambridge University Press*, 1987.

[85] A. Schulz. Infrared thermography as applied to film cooling of gas turbine components. *Measurement Science and Technology*, 11:948, 2000.

[86] M. Ochs, T. Horbach, A. Schulz, R. Koch, and H.J. Bauer. A novel calibration method for an infrared thermography system applied to heat transfer experiments. *Measurement Science and Technology*, 20:075103, 2009.

[87] R.S. Reilly. Advanced film cooling rig development and test results. *NASA Contractor Report 204136*, Aug. Limited distribution, 1996.

[88] P.C. Sweeney and J.F. Rhodes. An infrared technique for evaluating turbine airfoil cooling designs. *Journal of Turbomachinery*, 122:170–177, 2000.

[89] S.V. Ekkad, S. Ou, and R.B. Rivir. A transient infrared thermography method for simultaneous film cooling effectiveness and heat transfer coefficient measurements from a single test. *Journal of Turbomachinery*, 126:597–603, 2004.

[90] A. Mensch and K.A. Thole. Overall effectiveness and flowfield measurements for an endwall with non-axisymmetric contouring. In *Proceedings of ASME Turbo Expo 2015: Turbine Technical Conference and Exposition, Montreal, Canada*, pages 1–12, 2015.

[91] H. Ma, Z. Wang, L. Wang, and Q. Zhang. Ramp heating in hig-speed transient thermal measurement with reduced uncertainty. *Journal of Propulsion and Power*, 32:1190–1198, 2016.

[92] T.A. Morris, M.A. Marciniak, G.C. Wollenweber, and J.A. Turk. Analysis of uncertainties in infrared camera measurements of a turbofan engine in an altitude test cell. *Infrared Physics & Technology*, 48:130–153, 2006.

[93] B. Laveau, R.S. Abhari, M.E. Crawford, and E. Lutum. High resolution heat transfer measurements on the stator endwall of an axial turbine. In *Proceedings of ASME Turbo Expo 2014: Turbine Technical Conference and Exposition GT2014*, pages 1–14, 2014.

[94] B. Laveau, R.S. Abhari, M.E. Crawford, and E. Lutum. High resolution heat transfer measurement technique on contoured endwall with non-uniform thermal resistance. In *Proceedings of ASME Turbo Expo 2015: Turbine Technical Conference and Exposition GT2015*, pages 1–14, 2015.

[95] International Organisation for Standardisation. ISO: Guide to the Expression of Uncertainty measurement. *(Gum), Geneva*, 1995.

[96] Benjamin Kirollos. *Aerothermal optimisation of novel cooling schemes for high pressure components using combined theoretical, numerical and experimental techniques*. PhD thesis, University of Oxford, 2015.

[97] FLIR Systems. The ultimate handbook for R&D professionals, 2012.

[98] B. Kirollos and T. Povey. High-accuracy infrared thermography method using reflective marker arrays. *Measurement Science and Technology*, 28:095405, 2017.

[99] M. Elfner, A. Schulz, H.J. Bauer, and K. Lehmann. A novel test rig for assessing advanced rotor blade cooling concepts, measurement technique and first results. *Proceedings of ASME Turbo Expo 2017: Turbomachinery Technical Conference and Exposition, Charlotte, USA*, pages 1–12, 2017.

[100] M. Elfner, A. Schulz, H.J. Bauer, and K. Lehmann. A comparative experimental investigation of leading edge cooling concepts of turbine rotor blades. In *Proceedings of ASME Turbo Expo 2018: Turbomachinery Technical Conference and Exposition, Oslo, Norway*, pages 1–12, 2018.

[101] C.D. Wen and I. Mudawar. Modeling the effects of surface roughness on the emissivity of aluminum alloys. *Int. J. Heat and Mass Transf.*, 49:4279–4289, 2009.

[102] M. Elfner, T. Glasenapp, A. Schulz, and H.J. Bauer. A spatially resolved in situ calibration applied to infrared thermography. *Measurement Science and Technology*, 30(8):085201, 2019.

[103] S. Aberle, M. Bitter, F. Hoefler, J.C. Benignos, and R. Niehuis. Implementation of an in-situ infrared calibration method for precise heat transfer measurements on a linear cascade. *International Journal of Rotating Machinery*, 141:1–7, 2019.

[104] M. Michaud, F. Ornano, N.H.K. Chowdhury, and T. Povey. Methodology for high-accuracy infrared calibration in environments with through-wall heat flux. In *Proceedings of Global Power and Propulsion Society, Beijing Conference*, pages 1–10, 2019.

[105] S. Lazzi Gazzini, R. Schader, A.L. Kalfas, and R.S. Abhari. Infrared thermography with non-uniform heat flux boundary conditions on the rotor endwall of an axial turbine. *Measurement Science and Technology*, 28(2):025901, 2017.

[106] L. Christensen, R. Celestina, S. Sperling, R. Mathison, H. Aksoy, and J. Liu. Infrared temperature measurements of the blade tip for a turbine operating at corrected engine conditions. In *Proceedings of the ASME Turbo Expo*, volume 7, 9 2020.

[107] B.F. Knisely, R.A. Berdanier, K.A Thole, C.W. Haldeman, J.R. Markham, J.E. Cosgrove, A.E. Carlson, and J.J. Scire. Acquisition and processing considerations for infrared images of rotating turbine blades. *ASME Journal of Turbomachinery*, 143(4):041013, 2021.

[108] B.F. Knisely, R.A. Berdanier, K.A Thole, and C.W. Haldeman. Effects of part-to-part flow variation on overlall effectiveness and life of rotating turbine blades. In *Proceedings of ASME Turbo Expo 2022*, volume Volume 6A: Heat Transfer — Combustors; Film Cooling, page V06AT12A042, 2022.

[109] L. Christensen, R. Celestina, S. Sperling, R. Mathison, H. Aksoy, and J. Liu. Infrared Temperature Measurements of the Blade Tip for a Turbine Operating at Corrected Engine Conditions. *Journal of Turbomachinery*, 143(10):101005, 05 2021.

[110] D.W. Peters and J. Moore. Tip leakage loss development in a linear turbine cascade. *AGARD-CP-571*, AG(571), 1995.

[111] J.P. Bindon. The Measurement and Formation of Tip Clearance Loss. *Journal of Turbomachinery*, 111(3):257–263, 1989.

[112] T. Arts and Von Karman Institute for Fluid Dynamics. *Turbine Blade Tip Design and Tip Clearance Treatment: January 19-23, 2003*. Lecture series. Von Karman Institute for Fluid Dynamics, 2004.

[113] Zainab J.S., Eldad J.A., and Theodosios K. Effect of in-service burnout effect on the transonic leakage flows over cavity tip model. In *Proceedings of the Institution of Mechanical Engineers, Part A: Journal of Power and Energy*, volume 235, pages 1847–1863, 2021.

[114] J. Vieira, J. Coull, P. Ireland, and E. Romero. Aerothermal Effect of Cavity Welding Beads on a Transonic Squealer Tip. *Journal of Turbomachinery*, 143(11):111009, 06 2021.

[115] A.A. Ameri, E. Steinthorsson, and David L. Rigby. Effect of Squealer Tip on Rotor Heat Transfer and Efficiency. In *Proceedings of the ASME 1997 International Gas Turbine and Aeroengine Congress and Exhibition*, volume 3: Heat Transfer; Electric Power; Industrial and Cogeneration, page V003T09A016, 06 1997.

[116] J.S. Kwak, J. Ahn, J.C. Han, C.P. Lee, R.S. Bunker, R. Boyle, and R. Gaugler. Heat Transfer Coefficients on the Squealer Tip and Near-Tip Regions of a Gas Turbine Blade With Single or Double Squealer. *Journal of Turbomachinery*, 125(4):778–787, 2003.

[117] D.E. Metzger, R.S. Bunker, and M.K. Chyu. Cavity Heat Transfer on a Transverse Grooved Wall in a Narrow Flow Channel. *Journal of Heat Transfer*, 111(1):73–79, 1989.

[118] M.K. Chyu, H.K. Moon, and D.E. Metzger. Heat Transfer in the Tip Region of Grooved Turbine Blades. *Journal of Turbomachinery*, 111(2):131–138, 04 1989.

[119] F.J.G. Heyes, H.P. Hodson, and G.M. Dailey. The Effect of Blade Tip Geometry on the Tip Leakage Flow in Axial Turbine Cascades. In *Proceedings of the ASME 1991 International Gas Turbine and Aeroengine Congress and Exposition*, volume 1: Turbomachinery, page V001T01A052, 1991.

[120] Gm.S. Azad, J.C. Han, S. Teng, and R.J. Boyle. Heat Transfer and Pressure Distributions on a Gas Turbine Blade Tip. *Journal of Turbomachinery*, 122(4):717–724, 02 2000.

[121] Gm.S. Azad, J.C. Han, and R.J. Boyle. Heat Transfer and Flow on the Squealer Tip of a Gas Turbine Blade. *Journal of Turbomachinery*, 122(4):725–732, 2000.

[122] J.S. Kwak and J.C. Han. Heat transfer coefficient on a gas turbine blade tip and near tip regions. *8th AIAA/ASME Joint Thermophysics and Heat Transfer Conference*, 2002.

[123] CI Systems. SR-33N Integrated Compact Extended Area Blackbody, 2023. last accessed 17 August 2023.

[124] Fluke. Fluke calibration 4180/4181 precision ir calibrators, 2023. Last accessed 17 August 2023.

[125] M. Schulz and L. Caldwell. Nonuniformity correction and correctability of infrared focal plane arrays. *Infrared Physics & Technology*, 36(4):763–777, 1995.

[126] LabFacility. Temperature handbook, 2023. Last accessed 17 August 2023.

[127] J. Manara, M. Zips, T. Stark, M. Arduini, H.P. Erbert, A. Tutschke, A. Hallam, J. Hanspal, M. Langley, D. Hodge, and J. Hartmann. Long wavelength

infrared radiation thermometry for non-contact temperature measurements in gas turbines. *Infrared Physics & Technology*, 80:120–130, 2017.

[128] M.I. Goodisman, M.L.G. Oldfield, R.C. Kingcombe, T.V. Jones, R.W. Ainsworth, and A.J. Brooks. An Axial Turbobrake. In *Proceedings of the International Gas Turbine and Aeroengine Congress and Exposition*, New York, NY, June 1991. ASME.

[129] S. Shahpar and S. Caloni. Aerodynamic Optimization of High-Pressure Turbines for Lean-Burn Combustion System. *Journal of Engineering for Gas Turbines and Power*, 135(5):055001, 04 2013.

[130] M.G. Adams, T. Povey, B.F. Hall, D.N. Cardwell, K.S. Chana, and P.F. Beard. Commissioning of a combined hot-streak and swirl profile generator in a transonic turbine test facility. *ASME Journal of Engineering for Gas Turbines and Power*, 142(3):031008–1–16, 2020.

[131] B.F. Hall, K.S. Chana, and T. Povey. Design of a Nonreacting Combustor Simulator With Swirl and Temperature Distortion With Experimental Validation. *Journal of Engineering for Gas Turbines and Power*, 136(8):081501, 02 2014.

[132] D. Singh, P.F. Beard, D. Cardwell, and K.S. Chana. Investigation of a high-pressure turbine stage in a high-speed rotating transient test facility for rotor tip study and a parametric study for improved heat transfer calculation. *ASME. Journal of Engineering for Gas Turbines and Power*, 144(12), 2022.

[133] P.F. Beard, T. Povey, and P.T. Ireland. Mass flow rate measurement in a transonic turbine test facility with temperature distortion and swirl. *Flow Measurement and Instrumentation*, 19(5):315–324, 2008.

[134] Paul F. Beard. *On Transient Turbine Efficiency Measurements with Engine Representative Inlet Flows*. PhD thesis, University of Oxford, 2010.

[135] N.A. Cumpsty and J.H. Horlock. Averaging Nonuniform Flow for a Purpose. *Journal of Turbomachinery*, 128(1):120–129, 02 2005.

[136] Matthew C.J. Collins. *Casing Effusion Cooling*. PhD thesis, University of Oxford, 2015.

[137] W.J. Tropf and M.E. Thomas. Models of the optical properties of solids. In Paul Klocek, editor, *Window and Dome Technologies and Materials III*, volume 1760, pages 318 – 328. International Society for Optics and Photonics, SPIE, 1992.

[138] D.C. Harris. *Materials for Infrared Windows and Domes: Properties and Performance*. 1999.

[139] D.C. Harris. Durable 3–5 μm transmitting infrared window materials. *Infrared Physics & Technology*, 39(4):185–201, 1998.

[140] H. Qi, X. Zhang, M. Jiang, C. Liu, Q. Wang, and D. Li. Optical properties of zinc selenide slabs at 373 and 423 K in the wavelength $2 - -15\,\mu m$. *Optik*, 127:5576–5584, 2016.

[141] E. Piccini, S.M. Guo, and T.V. Jones. The development of a new direct-heat-flux gauge for heat-transfer facilities. *Measurement Science and Technology*, 11(4):342, apr 2000.

[142] M. Collins, K. Chana, and T. Povey. New technique for the fabrication of miniature thin film heat flux gauge. *Measurement Science and Technology*, 26(025303), 2015.

[143] C.A. Neugebauer and M.B. Webb. Electrical Conduction Mechanism in Ultrathin, Evaporated Metal Films. *Journal of Applied Physics*, 33(1):74–82, 06 1962.

[144] S. Shahpar and S. Caloni. Aerodynamic Optimization of High-Pressure Turbines for Lean-Burn Combustion System. *Journal of Engineering for Gas Turbines and Power*, 135(5):055001, 04 2013.

[145] Crystran. Zinc selenide material properties, 2023. Last accessed 26 August 2023.

[146] Blender. Blender 4.0 reference manual, 2023. `https://docs.blender.org/manual/en/latest/index.html` [Accessed: 17 December 2023].

[147] R.J. Anthony, M.L.G. Oldfield, T.V. Jones, and J.E. LaGraff. Development of high-density arrays of thin film heat transfer gauges. In *Proceedings 5th ASME/JSME Thermal Engineering Joint Conference*, San Diego, CA, March 15–19 1999.

[148] I. Qureshi, A.D. Smith, K.S. Chana, and T. Povey. Effect of Temperature Nonuniformity on Heat Transfer in an Unshrouded Transonic HP Turbine: An Experimental and Computational Investigation. *Journal of Turbomachinery*, 134(1):011005, 05 2011.

[149] Deepanshu Singh. *Aerothermal Study of High-Pressure Turbine Rotor Tips and Casing at Engine Representative Conditions with High-Speed Rotation*. PhD thesis, University of Oxford, Michaelmas Term 2022.